SIMULATION OF EROSION PHENOMENA USING COMPUTATIONAL FLUID DYNAMICS COUPLED WITH MESH MORPHING AND DISCRETE ELEMENT METHOD

A Dissertation

by

MOSTAFA BAHMANI SHOORIJEH

Submitted to the Office of Graduate and Professional Studies of
Texas A&M University
in partial fulfillment of the requirements for the degree of

DOCTOR OF PHILOSOPHY

Chair of Committee,	Jean-Louis Briaud
Committee Members,	Hamn-Ching Chen
	Marcelo Sanchez
	Mary Jo Richardson
Head of Department,	Robin Autenrieth

December 2020

Major Subject: Civil Engineering

ABSTRACT

Erosion is responsible for a tremendous economic loss in different parts of the world, particularly the US annually. Many dams in the world and the US are earth dams, which are susceptible to internal erosion due to their old ages. All around the world, about 46% of dams suffer a risk of internal erosion. In France, nearby 70 critical cases have already been detected (Monnet et al. 2012). In addition, vast distances of shores in the US are prevented from floods with levees, which can lose their functionality in surface erosion due to overtopping (Briaud et al. 2008). A large number of bridges can be in danger due to scour in floods. Scour has been the number one cause of bridge failure in the United States, with an average annual rate of 22 bridges collapsing or closed due to severe deformation (Briaud et al. 2014). These treats emphasize the importance of continuing research on erosion. Different researchers have proposed different test methods to quantify the magnitude of erosion due to water flow. Some other researchers utilized numerical methods to tackle erosion problems. Still, due to new advances in numerical methods and the necessity to apply these new methods in the study of erosion, more research is needed. This dissertation intends to utilize numerical approaches to model erosion tests and indicates the application of numerical simulation in erosion modeling.

The first goal is to start modeling well-known erosion tests using mesh morphing technique (computational fluid dynamic (CFD) domain with erodible boundaries). By utilizing erosion function (EF), resulted from Erosion Function Apparatus (EFA) (Briaud et al. 2001), other erosion tests and even practical models of erosion can be modeled with this

technique. Results of different erosion tests, including Borehole Erosion Test (BET) (Briaud et al. 2016), Hole Erosion Tests (HET) (Wan 2006, Wan 2004a, Wan 2004b), Jet Erosion Tests (JET) (Hanson 1990, Hanson 1991) have been compared with the results of numerical simulation with mesh morphing technique to verify the applicability of this method.

The tests mentioned above are intended to be modeled with this new technique to extend the research from macro to micro by parallelizing CFD with the discrete element method (DEM) (CFD-DEM technique). One of the problems in soil erosion that needs to be investigated is the particles' incipient motion. Results of CFD-DEM simulation of EFA will be compared with the result of video analysis on EFA tests to investigate the incipient motion of particles in the erosion process. Accelerations, velocities, drag forces, and shear stresses extracted from the two approaches will be compared to study the incipient motion more precisely.

Application of the two numerical approaches (Dynamic mesh technique and CFD-DEM) in practical problems is another goal, followed in this research. Scour and infilling in erosion are two practical applications that can be more investigated using these CFD techniques.

DEDICATION

I dedicate this dissertation to my beloved wife, Maryam. Words are powerless to express my gratitude for your unconditional love, constant support, and encouragement throughout this endeavor.

ACKNOWLEDGEMENTS

First and foremost, I would like to express my sincere acknowledgment to my mentor and supervisor, Professor Jean-Louis Briaud. Prof. Briaud facilitates this endeavor for me by his superior knowledge, insight, wisdom, and understanding. At the start of Ph.D., this path was impossible for me. Still, Prof. Briaud elaborately converted this to an opportunity of constant learning and empowering the research skills for me, which shaped my future as an authentic researcher and professional engineer. He oriented me in the right direction and kept me focused and, at the same time, motivated by his advice in our weekly meetings and cut the research's wrong directions. Aside from an academic perspective, I learned from him how striking a work-life balance is essential and how, in every condition, research ethics, attention to the details, and a different system of thinking can change the game. I was very fortunate to have had the opportunity to work as a research assistant with Prof. Briaud, and I am forever grateful to him.

My deepest appreciations go to my committee members Prof. Chen, Prof. Sanchez, and Prof. Richardson, for their contributions and guidance throughout this research. Prof. Chen helped me grasp the Computational Fluid Dynamics method's basics and answered my questions each time I knocked on the door, patiently and elaborately. With his exceptional insight towards the CFD method, Dr. Chen provided tremendous help to the dissertation's progress. I learned the Physical and Engineering Properties of Soil from Prof. Sanchez, where he meticulously and enthusiastically explained each topic in the wonderful world of soil mechanics. His valuable advice on the contributions of the dissertation illuminated the path of this research. I also express my sincere gratitude to Prof. Richardson for serving on my

advisory committee and dedicating her time to overseeing my research and providing valuable advice. I wish to thank Prof. Aubeny for his support and help. Prof. Aubeny wasn't in the dissertation committee. Still, the knowledge he transferred through two courses, Numerical Methods in Geotechnical Engineering and Advanced Numerical Methods in Geotechnical Engineering, indirectly enriched the research quality.

My warm gratitude goes to my friends and colleagues at Zachry Department of Civil Engineering at Texas A&M University, who helped me fulfill this achievement; Iman Shafii, Anna Shidlovskaya, Anna Timochenko, and Zihan Zhang. I would like to thank the staff and lab coordinators in the geotechnical engineering program at Texas A&M University who, with their support, made this study possible. Finally, I would appreciate my former teachers at Shiraz University and the Isfahan University of Technology, who paved the road for my endeavors as a civil and geotechnical engineer.

Last but not least, I am affectionately beholden to my supportive family and my beloved wife, Maryam. Their spiritual support was my everyday source of motivation to pursue my goals. I sincerely appreciate them for continually correcting me and motivating me to push my limits.

CONTRIBUTORS AND FUNDING SOURCES

The work was supported by a dissertation committee consisting of Professor Jean-Louis Briaud of the Department of Civil Engineering, Professors Hamn-Ching Chen and Marcelo Sanchez of Department of Civil Engineering, and Professor Mary Jo Richardson of the Department of Oceanography at Texas A&M University.

Chapter 3 of this dissertation was initially performed for NCHRP Project 24–43 by the Texas A&M University Transportation Institute (TTI), which supports one year of funding support for this research. Consortium for Education and Research in Geoengineering Practice (CERGEP) provided two years of funding support for this research

TABLE OF CONTENTS

LIST OF FIGURES

LIST OF TABLES

Page

1. INTRODUCTION

Laboratory experiments, field experiments, and numerical simulation can be implemented to efficiently and precisely investigate the erosion process. Several experimental methods were applied to study the susceptibility of soils against external and internal erosion, including Erosion Function Apparatus (EFA) (Briaud et al. 2001), Borehole Erosion Test (BET) (Briaud et al. 2016), Pocket Erosion Test (PET) (Briaud et al. 2012), Hole Erosion Tests (HET) (Wan 2006, Wan 2004a, Wan 2004b), Jet Erosion Tests (JET) (Hanson 1990, Hanson 1991) Slot Erosion Tests (SET) and Rotating Cylinder Tests (Lim 2006).

Different numerical methods can also be used to simulate the erosion process in geotechnical engineering, including the Finite Element Method (FEM), Computational Fluid Dynamics (CFD), Lattice Boltzmann Method (LBM), Finite Difference Method (FDM), Discrete Element Method (DEM), Smoothed Particles Hydrodynamics (SPH) and so forth.

These methods can be categorized into continuum methods and discrete methods. FEM, CFD, and FDM are continuum methods that can be empowered by dynamic methods like mesh morphing technique to simulate erosion problems. DEM and SPH are discrete methods that use the Lagrangian approach to model the materials.

The complex behavior of erosion phenomenon needs a method that can consider many aspects, including particle size and distribution, void size and distribution, the angularity of particles, soil matrix arrangement, and method of specimen preparation. The interaction between fluid flow and solid particles, granular materials, and porous rocks is a vast and complex topic. The discrete element method is well suited to study these systems' mechanical behavior (Galindo-Torres et al., 2013). Since 1990, many modeling techniques have been utilized to solve fluid-solid problems by combining fluid-flow models with the discrete element method (DEM). These new methods can be benefitted from the advantages of both approaches. These methods have been applied to a broad spectrum of application areas (Galindo-Torres et al., 2013).

This dissertation focuses on a CFD with mesh morphing technique and CFD-DEM technique to explore the fundamental mechanisms of erosion in the Erosion Function Apparatus (EFA) test, Jet Erosion Test (JET), Hole Erosion Test (HET), and Borehole Erosion Test (BET). In the next step, CFD-DEM is used to model the EFA simulation to derive velocity-based and shear stress based erosion functions. The effect of several parameters of the derived erosion function from EFA is also studied. Furthermore, to extend the numerical modeling to the real applications of erosion, two forms of internal instabilities, including contact erosion and suffusion, are studied. The CFD-DEM method is also utilized to study the backfilling phenomena. In the first procedure, CFD with mesh morphing technique in STAR-CCM+ software will be utilized. In the coupled CFD-DEM method, the fluid will be modeled using computational fluid dynamics, and the particles will be modeled at the microscale level by using DEM.

1.1. Research Objectives

The general objectives of this dissertation are:

- Constructing CFD models enabled by the Mesh Morphing technique to investigate the scour and erosion. By application of an erosion function (EF) derived from the

EFA test on the erodible boundaries, current erosion tests, including JET, HET, BET, are simulated, and their results are compared with the experimental results.

- Investigation of the shear stress evolution with time in the tests mentioned in the above.
- Comparison of erosion functions, critical shear stresses, and critical velocities derived in the laboratory for gravel samples with the erosion functions, critical shear stress, and critical velocities derived from the CFD-DEM simulation of the numerical samples.
- Investigation and comparison of acceleration, velocity, drag force, and lift force contributions in the incipient motion of particles with CFD-DEM simulation and video analysis of EFA test in the laboratory.
- Comparing average shear stress on the sample calculated from the Moody chart, average shear stress on the sample from CFD, and average shear stress on the particle from the particle acceleration.
- Constructing fully coupled CFD-DEM models for EFA to investigate the erosion process and erosion function and its contributing parameters more precisely.
- Exploring the potential and applications of CFD-DEM coupling in simulating the erosion process, including infilling and two types of internal instabilities; contact erosion and suffusion.

1.2. Research Plan

Figure 3 demonstrates the final outline of the dissertation. The dissertation has been organized into six chapters to achieve overmentioned goals. In the following, the final plan for the whole research, and each chapter has been presented.

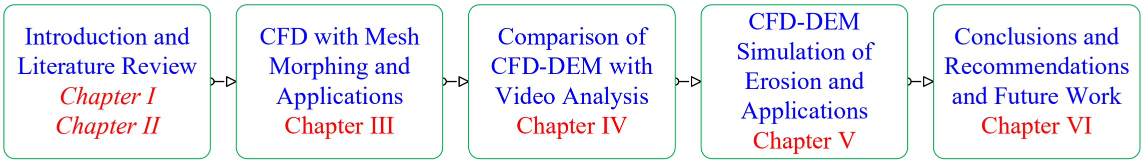

Figure 1-1. Final outline of the dissertation

1.2.1. Chapter 2

An in-depth literature review on the start of erosion, the forces involved in the erosion process, and quantification of the magnitudes of the erosion in the current erosion tests should be performed to accomplish the proposed objectives in this dissertation. The mechanism of erosion, definition, and phases, types of erosion, the progression of erosion, control parameters for the likelihood of erosion, geometric criteria to access the potential of erosion, constitutive models for soil erosion, current laboratory and field tests for the erosion will be presented.

To cover the background of numerical techniques implemented in the numerical simulations, a more in-depth and more detailed literature review in line with the main objectives of this dissertation will be discussed. In the first section, a literature review on the current continuum methods emphasizing on mesh morphing technique will be covered. Current research on discrete modeling of erosion mainly, CFD-DEM, will be investigated in the second section. The procedure for the CFD-DEM technique in STAR-CCM+ will also be demonstrated in this chapter. The basic concept behind a discrete element method and the interactions between the particles, including the Hertz-Mindlin relationship to manage the vertical and tangential behavior between the particles. The definition of bonds and cohesion between the particles is also presented in this chapter.

In the third section, different methods and apparatuses to measure the hydrodynamic forces on the incipient motion of particles will be covered.

1.2.2. Chapter 3

The CFD approach with mesh morphing technique in software STAR-CCM+ will be more implemented to model different erosion tests. In this technique with field function ability in STAR-CCM+, an erosion function derived from the EFA test in the laboratory will be applied on the boundaries to move the mesh depends on the value of shear stress on the boundaries (soil sample). The erosion function, which acts as a constitutive model for the soil erosion, summaries all erosion properties in one equation, which can work for all types of the soils and enable CFD software like STAR-CCM+ to simulate different hydraulic structures which are susceptible to erosion. With this technique, several erosion tests, including JET, HET, and BET, have been simulated, and their results will be compared with the laboratory results. Furthermore, the shear stress evolution on these tests will be studied.

1.2.3. Chapter 4

The validation of the CFD-DEM approach will be provided by simulating an experimental case. The procedure to derive erosion function from the numerical results is also illustrated.

Finally, the erosion functions, critical velocities, and critical shear stresses extracted from the numerical results have been compared with the laboratory tests.

The basic techniques of video analysis applied in this dissertation will be presented in this chapter. The procedure of Video analysis with Tracker software has been performed, and the process to calculate velocity, acceleration, drag, and lift forces from movies of EFA tests will be demonstrated. At the same time, numerical models of the same samples will be constructed in STAR-CCM+ software to compare the numerical results with the experimental results.

Velocity and acceleration versus time curves obtained from the numerical simulations have been compared with the laboratory results. Average horizontal and vertical accelerations from numerical simulations and laboratory tests for samples with different sizes (5 samples) have been examined. The results of this chapter can be utilized as a benchmark to verify the efficiency of the CFD-DEM technique to model the erosion phenomenon.

1.2.4. Chapter 5

By modeling Erosion Function Apparatus (EFA) test, a sensitivity analysis of the essential parameters of the Erosion Function will be investigated in this chapter. The effect of different sizes of particles, the density of particles, friction between the particles, rolling resistance of particles, dry density of the sample, abrasion effect of the suspended particles on the surface of the sample, and cohesion between particles on Erosion Function are investigated. In the next section, after validation of drag models and boiling condition problem in CFD-DEM, applications of the CFD-DEM in erosion problems, including contact erosion, suffusion and, infilling, will be investigated and presented. In the study of contact erosion, nine samples (four samples constant diameters and five samples with particle size distributions) will be simulated to check the efficiency of the Terzaghi criterion (1932) in filter design and contact erosion. For the suffusion process, the efficiency of several geometric criteria (Istomina (1957), Kezdi (1969), Kenny and Lau (1985), Burenkova (1993), Li and Fannin (2008)) to prevent erosion will be examined with twelve samples with particle size distributions by CFD-DEM technique. For the infilling, the effect of several essential parameters on the magnitude of infilling is also studied. These parameters are the diameter of particles, depth, the slope of the scour hole, coefficient of rolling resistance, friction coefficient, and cohesion between particles.

1.2.5. Chapter 6

The essence of the dissertation, including the conclusions and recommendations for further work, will be provided in this chapter.

1.3. Contribution to New Knowledge

In this dissertation, with the help of the dissertation committee, the following contributions are pursued and fulfilled:

1. The Erosion Function (EF) obtained from the Erosion Function Apparatus (EFA) and input in Computational Fluid Dynamics (CFD) method coupled with the Mesh Morphing (MM) technique gives reasonable predictions of time-dependent erosion problems including the Jet Erosion Test, the Hole Erosion Test, and the Borehole Erosion Test. This proves that EF is a fundamental constitutive law of soil erosion.
2. The CFD method, coupled with the Discrete Element Method (DEM), predicts reasonably well the movement vs. time, velocity vs. time, and acceleration vs. time

measured in the EFA test on large gravel particles and Teflon balls. This proves that dem is able to predict soil particle movement.

3. The CFD method, coupled with the Discrete Element Method (DEM), can be utilized to derive erosion functions (velocity or shear stress vs. erosion rate) for sand and gravel particles. This proves that DEM is a sound simulation method for erosion of soil particles.
4. The CFD-DEM simulation method shows the influence of particle size, friction, rolling resistance coefficient, dry density, abrasion of suspended particles in the fluid on the settled particles, and cohesion on the erosion function. Between these parameters, the effect of cohesion dominates other effects, then rolling resistance coefficient (shape), static friction coefficient (angularity), particle diameter, and abrasion effect. The effect of dry density is minimal.
5. The erosion through the soil is simulated by CFD-DEM, and it is shown that the Terzaghi filter criterion is valid. Although when the density is low, lower values of $D_{15coarse}/D_{85fine} < 4$ should be considered.
6. The suffusion process in the soil is simulated by CFD-DEM, and the validity of several criteria in the assessment of internal stability was shown. The most reliable methods are Li and Fannin (2008) and Kenney and Lau (1985). Burenkova (1993), Kezdi (1969) are conservative methods, and Istomina results are not accurate.
7. The CFD-DEM simulation of the infilling process showed the influence of the shape of the scour hole (depth and slope), size of particles, shape and angularity of particles, and dry density and cohesion between particles. The depth and slope of the scour hole

are not important, while D_{50} of particles, their shape, angularity, and cohesion are important parameters.

2. BACKGROUND KNOWLEDGE

2.1. Porous Media Flow Problems

The fluid flow through porous media is a two-phase system, i.e., the solid grain skeleton and the pore space, filled with stationary or moving fluids (air, gas, water, etc.). Porous media flow involves the mechanical interaction between neighboring grains comprising the porous matrix, the hydrodynamic evolution of fluids within the transport channels formed by connected pore spaces, and the hydro-mechanical interaction along with fluid-solid interfaces. These processes are coupled with each other. The momentum energy transferred by fluid flow along the fluid-solid interfaces introduces additional forces and moments on the solids, which may disrupt the equilibrium state existing between contact forces, body forces, and bonding strengths, possibly causing the grains to translate and rotate. Translational and rotational movement of solid grains will change the local boundary conditions of fluid flow in the pore spaces. Movements of solids also cause changes in the connectivity and geometry of pore spaces. Porous media flow is of great interest and extensively studied in many science and engineering fields, such as soil and rock mechanics, geophysics, hydraulics, petroleum engineering, etc. The principal exploration means in porous media flow research and practice include field tests, laboratory experiments, and theoretical (mainly numerical) analysis.

2.2. Erosion Definition

Three main components contributing to the erosion process are erodible material, which is soil or rock, an erodible fluid, which is water, and the geometry of the erodible material.

The resistance of soil or rock against erosion is described by its erodibility, which depends on hydraulic, mechanical, and geometric conditions. Hydraulic conditions are fluid velocity and chemical properties of the fluid. Mechanical conditions can be related to properties of the erodible material include the degree of compaction and cohesion. Geometric conditions of erodible material are grain size distribution, pore size distribution, roughness, grain, and pore shapes.

Briaud (2008) divided the erodible materials into three categories. Soil which are earth elements which can be classified by the Unified Soil Classification System (USCS), rock, which are materials with unconfined compressive strength of the intact rock core of more than 500 kPa with the joint spacing of at least 0.1 m and Intermediate geomaterials which are any Earth material intermediate between rock and soils.

Figure 2-1 shows the free body diagram of a soil particle at the interface surface between the water and the soil. When the velocity is zero, the static equilibrium in horizontal and vertical directions between the support forces, weight, and Archimedes forces govern. When the fluid starts to flow, the condition will change due to the effects of viscous shear stress on the particles, positive and negative pressures in areas around the particles. These pressure changes can cause turbulent fluctuation of the shear and normal forces (drag and lift forces).

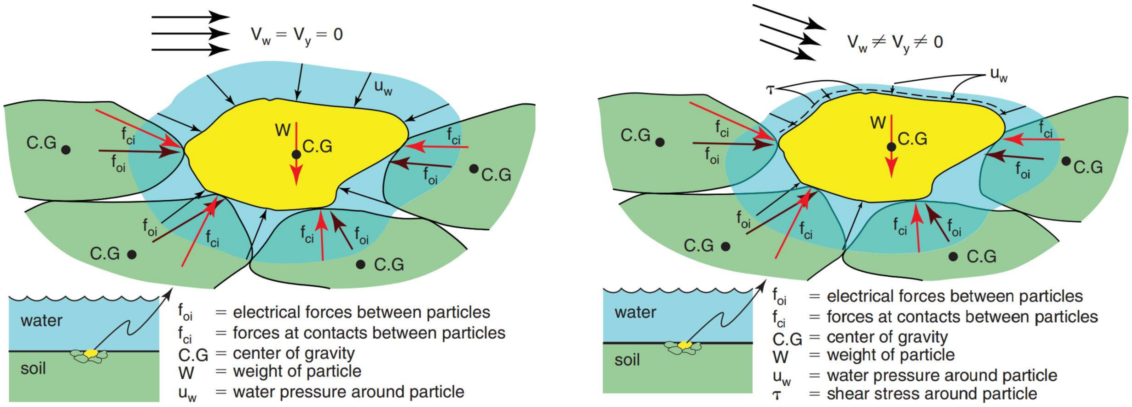

a) No-flow condition b) With the water flow

Figure 2-1. Free body diagram of a soil particle or rock block in two different stages a) no-flow condition, b) with the water flow (reprinted from Briaud, 2008)

The erosion process can be classified into internal and surface erosion. Seepage through embankment dams, levees, canal-side embankments can cause internal erosion due to high flow gradient, improper design, and ill-suited maintenance. Surface erosion, which is due to water's surface flow on the erodible material, can cause bridges to scour, overtopping of levees, dams, highway embankments, and meander migration.

2.2.1. Surface Erosion

Surface erosion is a phenomenon that happens on the soil surface, such as in river beds, during the overtopping flow of levee and embankments, and bridge scours. Similar to the erosion shown in Figure 2-1, Three main stages of surface erosion occur are:

1) Due to drag force on the soil surface, which at the interface between the erodible material (soil particles /rock block) and water, resulting shear stress is developed.

2) The eroding fluid decreases in the induced normal stress on the surface of the erodible material (soil particle/ rock block). In other words, with the increase of velocity in the vicinity

of soil particles, based on the rule of conservation of energy and Bernoulli's principle, the induced normal pressure by the eroding fluid decreases to maintain the flow.

3) The turbulence energy in the water causes the normal stress, and the induced shear stress fluctuates on the interface between the eroding fluid and soil. At high velocities, these fluctuations create cyclic loading of the soil particle, which makes erosion easier to occur (Croad, 1981; Hofland et al., 2005). When the combination of normal uplift force and drag shear force and their fluctuations due to turbulence energy overcome the resisting forces, the surface erosion process starts.

As mentioned earlier, surface erosion is an essential factor in bridge scour. One of the most common causes of bridge failure is scouring around bridge supports (Arneson, 2013).

More than 80 percent of all bridges in the United States (approximately 500,000 bridges) are located over water, highlighting the significance of studying surface erosion. Studies have shown that in 60 percent of the bridge collapse cases, the failure was due to the bridge scour (Briaud et al., 1999). Bridge scour is a severe and costly problem for the environment and leads to severe disasters such as the one reported in 159 counties of Georgia in 1994 (CDC, 1994).

2.2.2. Internal Erosion

The other type of erosion responsible for many failures in a variety of structures is internal erosion. In this type of erosion, soil particles are migrated within the body of the hydraulic structure, such as embankment dams and levees, from a location with a hydraulic gradient to another location with a lower hydraulic gradient, by the eroding fluid, is known as internal erosion (Wan and Fell, 2002).

Due to the importance of internal erosion, the mechanism, different stages, and different internal erosion types are presented in the following sections.

2.2.3. Mechanisms of internal erosion

In this section, a brief review of the mechanisms of internal erosion initiated by suffusion is presented. The review focus on nine aspects: (a) definitions and phases of internal erosion; (b) progression of internal erosion; (c) control parameters for the likelihood of internal erosion; (d) susceptibility of soils to internal erosion; (e) the critical hydraulic gradient controlling the onset of erosion; (f) effect of stress state on the erosion process; (g) the coupling among geometric, hydraulic, and mechanical conditions; (h) the mechanical consequence of soils suffering from internal erosion; and (i) seepage induced failure of soils to internal erosion.

2.2.4. Definitions and phases of internal erosion

Internal erosion is one of the most common failure modes in embankment dams (Fell et al. 2003; Zhang et al. 2009). It refers to the loss of soil particles within a hydraulic structure (embankment dam) or its foundation by seepage forces. The entire internal erosion process of a dam can be generally divided into four phases: initiation, continuation, progression, and development. Internal erosion can be classified into four different categories; concentrated leak erosion, backward erosion, soil contact erosion, or suffusion (Fell and Fry 2007). Figure 2-2 illustrates these four initiation modes for internal erosion.

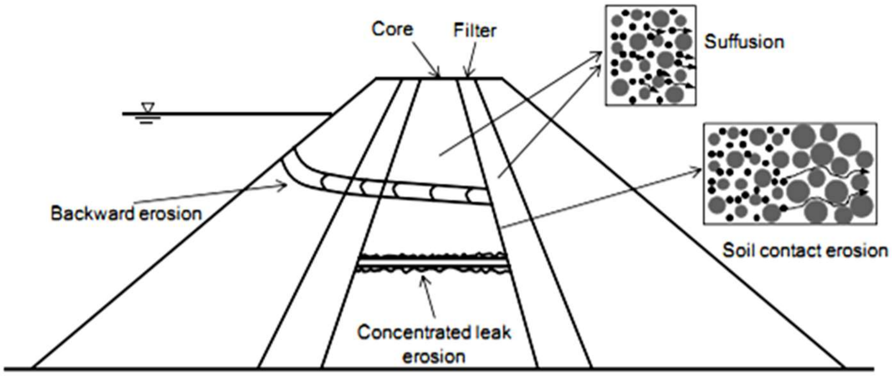

Figure 2-2. Four modes of internal erosion: suffusion, backward erosion, concentrated leak erosion, and soil contact erosion (reprinted from Zhang et al. 2016)

Concentrated leak erosion: erosion in a concentrated leak which can occur in cracks in an embankment dam (core) caused by differential settlement, hydraulic fracture, or desiccation, arching phenomenon, void adjacent to a concrete wall, or in a continuous permeable zone containing coarse and/or poorly compacted materials which form an interconnected voids system.

Backward erosion involves soil particles' erosion at the exit end of a seepage path due to a high exit velocity there, which continues in a backward direction. The exit of the seepage path may locate at a free surface, such as the ground surface downstream of a soil foundation or the downstream face of a homogeneous embankment, or the interface between the clay core and the downstream filter of central core earth or rock-fill embankment dam (Wan 2006). The loosen particles from the exit area are carried out by the seepage flow, and the erosion process gradually propagates towards the upstream side (backward) following the critical seepage paths.

Soil contact erosion is often called filtration, which involves selective erosion of fine-grained particles in the base materials at the base-filter interface under seepage flow.

Suffusion involves selective erosion of fine particles within the matrix of coarse soil particles (migration) in a soil whose particle size distribution does not satisfy self-filtering conditions under seepage flow. Soils that are susceptible to suffusion are considered internally unstable.

Whether internal erosion continues or not depends on whether the exit point is exposed or filtered. If it is filtered, the materials in the filters should satisfy several filter criteria (mainly based on geometric properties of grains) (e.g., USBR 2004; Sherard and Dunnigan 1989; GEO 1993; ICOLD 1994; USACE 1953). Otherwise, the continuation of internal erosion may occur and continue until failure.

When erosion has been initiated, and the filters are absent or unable to prevent erosion, internal erosion will form the pipe. For different initiation modes (four modes mentioned above), the progression is not the same. For internal erosion initiated by backward erosion, the initiation and development of a pipe depend on the hydraulic gradient, the flow rate inside the pipe, and the soil properties. For internal erosion initiated by concentrated leaks, the hydraulic shear stress and the soil erodibility within the hole control the rate of enlargement in the hole. For the internal erosion initiated by suffusion, the hydraulic and mechanical responses of the soil can increase due to the loss of fine particles within the coarse matrix. In severe cases, the loss of fine particles could induce concentrated flow and lead to piping failure eventually (Schuler 1995).

Several possible breach mechanisms for internal erosion involve the gross enlargement of pipe diameter, dam settlement, sinkhole on the crest leading to overtopping, and instability of the downstream slope (Foster et al. 2000).

The initiation of internal erosion by suffusion requires a soil particle to detach from its parent material and migrated through sufficiently large voids and constrictions between particles. Detachment and migration of soil particles need a hydrodynamic force against the inter-granular friction. For internal erosion to start and continue, it requires large seepage forces to drag the relatively stable fine particles within the pores and large soil constrictions to permit further movement of the fine particles. During the suffusion process, the microstructure and the mechanical response of the soil particles change continuously.

2.2.5. Progression of erosion in the element level

Internal erosion incorporates variations in erosion rate, permeability, and deformation during the entire erosion process. Several laboratory tests were conducted to study internal erosion progression by applying a constant large hydraulic gradient (e.g., Honjo et al. 1996; Tomlinson and Vaid 2000; Bendahmane et al. 2008).

The maximum erosion rate is influenced by the applied hydraulic gradient and clay contents. It generally increases with the increase of hydraulic gradient and decreases with the increase of the clay content. The progression of internal erosion was also investigated by applying hydraulic gradient in steps in the laboratory tests (e.g., Adel et al. 1988; Skempton and Brogan 1994; Tomlinson and Vaid 2000; Moffat and Fannin 2011). The progression of internal erosion is a progressive process until complete failure.

Tomlinson and Vaid (2000) investigated the influence of the rate of gradient increase on filtration failure. The hydraulic gradient was applied in two ways: incremental, increase in steps of 0.5 per 10 minutes and single step, increase in one step of 23 in 1 minute. The hydraulic failure gradient for the one-step case is only one-third of that of the multi-step case. This indicates that the soil that may typically be stable at a given gradient may become unstable if the same gradient was imposed rapidly.

Moreover, the initiation of internal erosion of internally unstable soil is usually under a low hydraulic gradient. Thus, the hydraulic gradient should be applied in multiple steps to efficiently characterize the hydraulic information of the initiation of internal erosion. This procedure is followed in the numerical simulations of this research.

2.2.6. Control parameters for the likelihood of erosion

Internal erosion of a soil is affected by the geometric conditions of soil, hydraulic conditions, and mechanical conditions (Sherard et al. 1984; Kenney et al. 1985; Schuler 1995; Tomlinson and Vaid 2000; Wan and Fell 2004a; Lim 2006; Richards and Reddy 2007; Indraratna et al. 2011; Moffat and Fannin 2011). However, the control variables for different modes of internal erosion are different. For backward erosion, the essential factors are hydraulic gradient, seepage in the exit location, the relative density of the soil, and grain-size distribution. After the formation of a pipe within a dam or its foundation, the hydraulic shear stress induced by the pipe flow and the soil's erodibility are the two most critical parameters affecting the enlargement of the pipe and its stability. In the case of concentrated leak erosion, the soil properties (i.e., fines content, dispersivity, degree of compaction, water content, and plasticity index), and hydraulic parameters, including the hydraulic gradient, hydraulic shear stress within the crack, crack orientation, and diameter and chemical property of the fluid are the most critical parameters. For filtration failure (contact erosion), important control variables are grain-size distribution and constriction size of the filter, thickness of the filter layer, hydraulic gradient, and dispersivity of the base materials.

Suffusion usually occurs in gap-graded granular soils and broadly graded soils with a steep slope in the coarse fraction and a gentle slope in the fine fraction. Table 2-1 summarizes the main parameters influencing the susceptibility of soil in suffusion.

Table 2-1- Parameters influencing the susceptibility of a soil to suffusion (reprinted from Schuler 1995)

Conditions	Parameters
Geometric conditions	Grain size and their distribution, pore size and their distribution, grain shape, pore shape
Mechanical conditions	Degree of compaction, cohesion, effective stress
Hydraulic conditions	Hydraulic gradient, seepage direction, pore fluid velocity, chemical property of the fluid

From a geometric perspective, grain-size distribution and pore-size distribution are the two most important factors. Grain shape and pore shape also affect the transport of the fine particles. Rounded particles are more comfortable passing through the constrictions. From a mechanical standpoint, the degree of compaction is the most critical parameter. Compaction effort affects the pore size and its distribution, and especially the constriction size. In the case of drag forces that trigger the process of suffusion, the hydraulic gradient and seepage direction are two important parameters. Under a low hydraulic gradient, suffusion may not occur even if the soil is internally unstable because the seepage forces may not overcome the resistance of the fines. Under the upward flow conditions, the critical hydraulic gradient would be more extensive than those in downward and horizontal flow cases (Adel et al. 1988). The effective stress in the soil is also an important factor for the development of suffusion (Moffat and Fannin 2011) because the stress influences the microstructure of the soil and, in turn, the hydraulic response.

2.2.7. Geometric criteria for assessing the potential of erosion

The geometric information of the soil controls the potential of internal erosion. Gain-size distribution is one of the essential geometric factors. A large number of laboratory tests were conducted to investigate the potential of internal erosion of different soils. The testing conditions for most previous internal erosion tests are summarized in Table 2-2.

Table 2-2- Summary of laboratory experiments of internal stability of soils (reprinted from Zhang et al. 2016)

References	Soil properties				Testing information				Test results	
	C_u	$(H/F)_{\min}$	$(d_{15c}/d_{85f})_{\max}$	P	i	Vibration	Flow direction	Saturated	No. of stable cases	No. of unstable cases
USACE (1953)	11–24	0.07–0.73	2.6–8.1	0	0.5–16.0	Y	D	Y	3	1
Kenney and Lau (1985)	3–71	0.49–3.08	1.7–51.0	0	—	Y	D	—	8	6
Adel et al. (1988)	17–57	0.25–1.02	6.2–41.0	0	0–0.7	N	H	—	1	1
Lafleur et al. (1989)	7–19	0.23–0.65	3.5–6.3	0	2.5–6.7	Y	D	—	2	1
Sun (1989)	3–7000	0–0.55	10.6–37.0	7–43	20.0	N	U	Y	6	10
Aberg (1993)	3–30	0.34–1.91	1.4–8.9	0–12	21.6	Y	D	—	6	2
Burenkova (1993)	3–109	0.17–0.77	8.1–82.0	0	2.5	N	D	N	4	4
Skempton and Brogan (1994)	4–24	0.14–2.70	4.0–10.9	0	0–1.0	N	U	Y	2	2
Chapuis et al. (1996)	18–32	0.35–0.99	2.3–10.6	0	9.8	Y	D	Y	2	1
Honjo et al. (1996)	2–13	0–2.75	1.2–7.4	0	9.8, 13.0	Y	D	Y	5	4
Liu (2005)	18–152	0.3–1.00	3.3–25.3	0	0–1.0	N	U	—	2	7
Mao (2005)	20–54	0–0.80	5.0–22.0	0	—	N	U	—	0	8
Moffat (2005)	73–85	0.30	13.7–14.3	0–4	1.0–62.0	N	D & U	Y	0	2
Fannin and Moffat (2006)	4–21	0–2.20	2.4–7.4	0	0.1–18.5	Y	D	Y	2	0
Lafleur and Nguyen (2007)	12–24	0.08–0.18	2.7–12.8	16–27	10.0–11.0	N	D	Y	3	0
Bendahmane et al. (2008)	42–173	0–0.03	19.3	10–30	5.0–140.0	N	D	Y	1	2
Li (2008)	6–36	0–1.30	2.8–19.0	0–19	0.08–31.0	N	D & U	Y	1	6
Wan and Fell (2008)	21–5709	0–0.62	5.0–99.0	3–40	8.0	N	D & U	—	10	9
Cividini et al. (2009)	32	0.07–0.56	8.6–11.3	25–31	0.2–0.99	N	U	Y	2	0
Total									60	66

C_u: coefficient of uniformity; H: mass fraction between grain size d and $4d$; F: mass fraction at any grain size d; d_{15c}: diameter of the 15% mass passing in the coarse part; d_{85f}: diameter of the 85% mass passing in the fine part; P: fines content; i: hydraulic gradient.

Y: yes; *N*: no; *D*: downward; *U*: upward *H*: horizontal

Based on the testing results, several geometric criteria (

Table 2-3) was developed to assess the internal stability of the soil. This section mainly focuses on geometric criteria.

Table 2-3- Summary of common geometric criteria for soil internal stability (reprinted from Zhang et al. 2016)

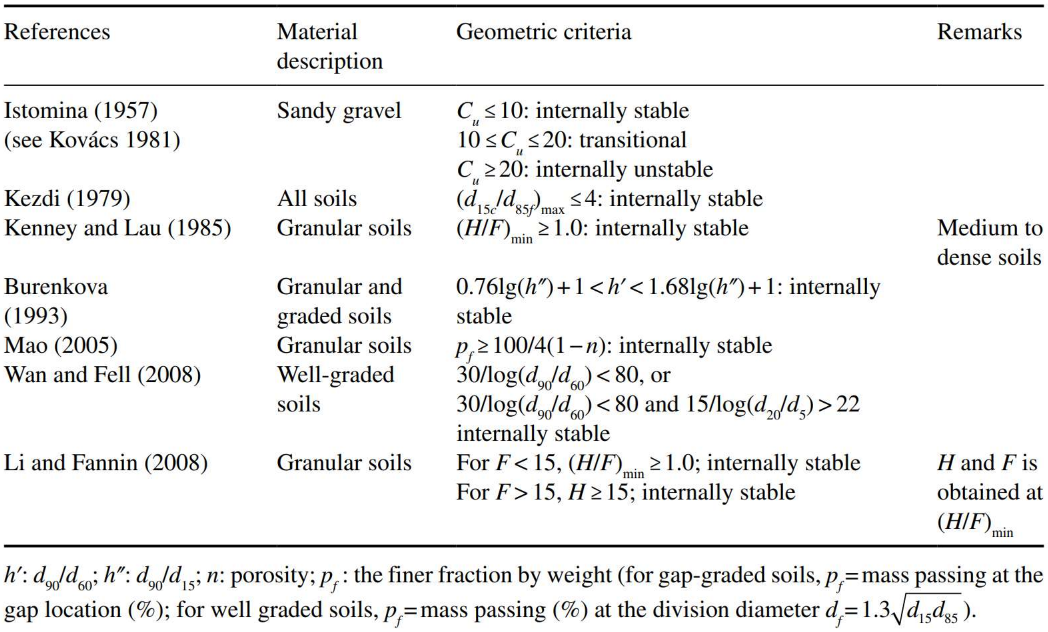

References	Material description	Geometric criteria	Remarks
Istomina (1957) (see Kovács 1981)	Sandy gravel	$C_u \le 10$: internally stable $10 \le C_u \le 20$: transitional $C_u \ge 20$: internally unstable	
Kezdi (1979)	All soils	$(d_{15c}/d_{85f})_{\max} \le 4$: internally stable	
Kenney and Lau (1985)	Granular soils	$(H/F)_{\min} \ge 1.0$: internally stable	Medium to dense soils
Burenkova (1993)	Granular and graded soils	$0.76\lg(h'') + 1 < h' < 1.68\lg(h'') + 1$: internally stable	
Mao (2005)	Granular soils	$p_f \ge 100/4(1-n)$: internally stable	
Wan and Fell (2008)	Well-graded soils	$30/\log(d_{90}/d_{60}) < 80$, or $30/\log(d_{90}/d_{60}) < 80$ and $15/\log(d_{20}/d_5) > 22$ internally stable	
Li and Fannin (2008)	Granular soils	For $F < 15$, $(H/F)_{\min} \ge 1.0$; internally stable For $F > 15$, $H \ge 15$; internally stable	H and F is obtained at $(H/F)_{\min}$

h': d_{90}/d_{60}; h'': d_{90}/d_{15}; n: porosity; p_f: the finer fraction by weight (for gap-graded soils, p_f = mass passing at the gap location (%); for well graded soils, p_f = mass passing (%) at the division diameter $d_f = 1.3\sqrt{d_{15}d_{85}}$).

F: mass fraction particles finer than grain size d; H: mass fraction of particles between grain size d and $4d$

2.3. Laboratory and field erosion tests simulated in this research

2.3.1. Erosion function apparatus (EFA)

The Erosion Function Apparatus (EFA) basic idea was first developed, established, and patented by Briaud at Texas A&M University In the early 1990s (Briaud et al., 1999, 2001a, 2001b). Today, the EFA is manufacturing by Humboldt, Inc. and utilizes extensively by many engineering organizations. This EFA test was initially designed to evaluate the erodibility of a wide range of cohesive and non-cohesive soils from gravels to clay and silt. Figure 2-3 shows a schematic diagram as well as a photograph of the EFA device.

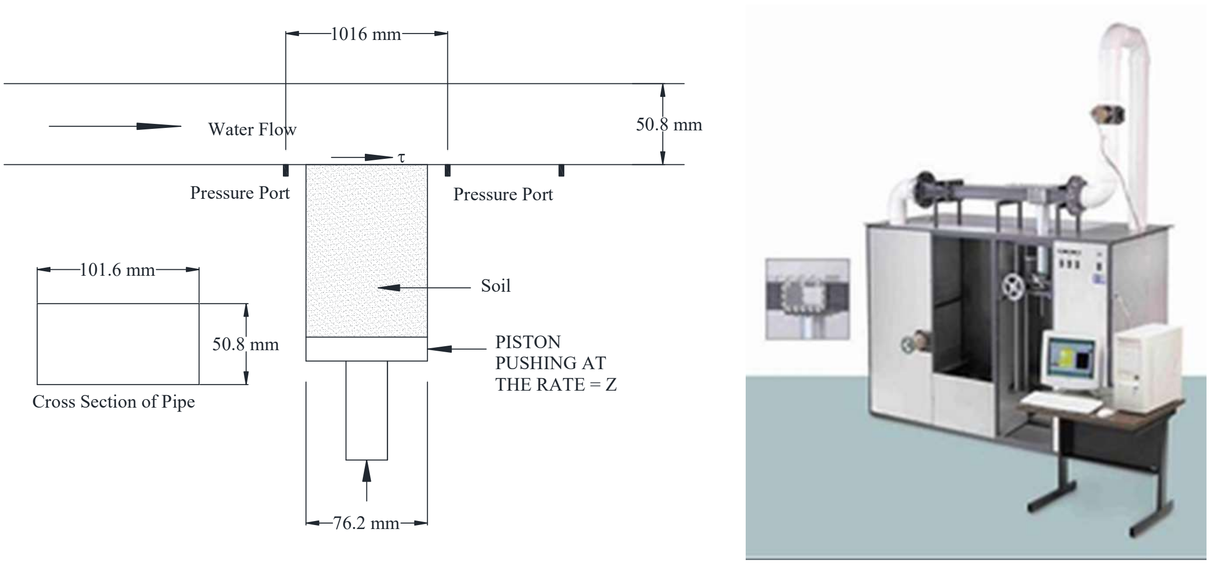

Schematic diagram of the EFA

EFA photograph

Figure 2-3. Schematic diagram of the Erosion Function Apparatus (EFA) and a photo of the Humboldt apparatus

Soil samples are taken using ASTM standard Shelby tubes with an outside diameter of 76.2 mm (3 inch) (ASTM, 2015). Similarly, for soft rocks, a rock core sample can be extracted and placed into a Shelby tube for rock erosion testing. As the eroding fluid, water is driven using a pump into a 1.2 m long rectangular cross-section 101.6 × 50.8 mm, as shown in Figure 2-3. The water flow can be adjusted using a valve, and a flow meter measures the average water velocity in line with the flow. The Shelby tube's tip is placed on the bottom of a circular plate, which is connected to a pushing piston. The piston pushes the sample up into the flow when it is necessary. The sample's upward movement is continued until it becomes flush with the bottom of the rectangular cross-section pipe.

The step by step test procedure is as follows (Briaud et al., 2001):

1) Place the Shelby tube's tip on the circular plate piston, push the piston up to become flush with the bottom surface of the rectangular channel.
2) Fill the rectangular channel with water and wait for one hour
3) Initiate the flow with small flow velocity, typically 0.2 m/s.
4) Start recording time. Hold the sample surface flush with the bottom of the rectangular pipe during the induced flow velocity. The test operator needs to make sure that the soil surface is kept flush all the time by pushing the soil with the piston as the water erodes it and maintains a level interface. Continue this until 50 mm of the soil is eroded, or 30 mins have passed. Read the protrusion height by observing the change in the height of the bottom of the piston.
5) Redo step 3 and 4 for a new and higher flow velocity (i.e. 0.2 m/s, 0.6 m/s, 1 m/s, 1.5 m/s, 2 m/s, 3 m/s, 4.5 m/s, and 6 m/s).

The scour rate versus flow velocity is plotted. The shear stress on the soil's eroded surface is calculated by using the Moody chart (Moody, 1944).

$$\boldsymbol{\tau = \frac{1}{8} f \rho v^2} \qquad 2\text{-}1$$

Where, τ refers to the shear stress (pa), ρ is the density of water (1000 kg/m^3), and v is the flow velocity (m/s). f is the friction factor obtained using the Moody chart.

Advantages

1) Minimize the sample disturbance effect, as it takes the sample directly from the field using Shelby tubes.
2) Can be used for natural samples as well as human-made samples

3) Gives the critical velocity and the critical shear stress. It can give the erosion function directly.
4) EFA test results are directly used as input to the TAMU-SCOUR method for bridge scour depth predictions (Chapter 6 of HEC-18).
5) EFA can test the soil's erodibility at any depth as long as a sample can be recovered.
6) While the EFA test is a surface erosion test, it can be used to evaluate internal erosion because the EFA erosion function represents the soil's erodibility at the element level.
7) Can test very soft to very hard soils. Extensive applications.

Drawbacks

1) Shear stress is indirectly measured from velocity using Moody charts, which might not be accurate. Also, the average flow velocity is used in the calculations instead of the actual velocity profile.
2) In some cases, that field samples are required, obtaining samples is difficult and costly. The test needs to be done on the sample before the sample is affected by long storage periods.
3) Particles larger than 40 mm in size cannot be tested confidently as the sampling tube's diameter is 75 mm.
4) The EFA is a reasonably expensive device (around $50k).

2.3.2. Hole erosion test (HET)

Fell (2002) introduced an experimental erosion test in Australia (Wan and Fell, 2002; Wahl, 2009; Benahmed and Bonelli, 2012) (Figure 2-4). It is derived from the older Pin Hole test and consists of drilling a 6 mm diameter hole at the soil sample center. Water flows through the hole with a hydraulic gradient and a specified velocity from the upstream side to the downstream. The mass removal rate per unit area as a function of time can be used to determine the erosion rate (kg/s/m^2).

The soil is compacted in a 100 mm (4 in.) diameter standard compaction mold. A tank provides the pressure head with a head ranging from 50 to 800 mm. The tank is connected to the sample chamber. The flow can be controlled through a control valve before the inlet.

The mass removal rate per unit area can be calculated as $\frac{\rho_d}{2} \times \frac{d\phi}{dt}$, where $d\phi$ is the change in diameter of the hole, and ρ_d is the dry unit weight of the sample. Since the hole diameter cannot be monitored during the test, this value is indirectly predicted using the measured flow rate, the hydraulic gradient, and Eqs. 2-4 and 2-5. Eq. 2-4 refers to laminar flow conditions, while Eq. 2-5 refers to turbulent flow. Turbulent flow is associated with Reynold's number higher than 5000.

$$\boldsymbol{\phi_t} = \left(\frac{\mathbf{16} \times \boldsymbol{Q_t} \times \boldsymbol{f_{Laminar,t}}}{\boldsymbol{\pi \rho_w g s_t}}\right)^{\frac{1}{3}} \qquad 2\text{-}2$$

$$\boldsymbol{\phi_t} = \left(\frac{\mathbf{64} \times \boldsymbol{Q_t^2} \times \boldsymbol{f_{Turbulant,,t}}}{\boldsymbol{\pi^2 \rho_w g s_t}}\right)^{\frac{1}{5}} \qquad 2\text{-}3$$

where Q_t is the flow rate at time t, $f_{Lamiliar,t,}$ and $f_{Turbulance,t}$ is the estimated friction factors at time t, ρ_w is the water unit weight, g is the ground gravity acceleration, and s_t is the hydraulic gradient obtained from the manometers at both ends of the sample. In these equations, the friction factors are estimated using the recorded hole diameter before and after the test.

The test results link the rate of mass removal per unit area to the net shear stress above critical; the shear stress on the hole wall is estimated using Eq. 2-6. This equation is obtained after considering force equilibrium on the body of the eroding fluid along the pre-formed hole at a particular time, t.

$$\boldsymbol{\tau = \rho_w \times g \times s_t \times \frac{\phi}{4}} \qquad 2\text{-}4$$

Where, ρ_w is the density of water, s_t is the hydraulic gradient across the hole, and ϕ is the diameter at time t. The equation used for the erosion function is linear

$$\dot{m} = C_e\left(\tau - \tau_c\right) \qquad 2\text{-}5$$

The parameter C_e is called the erosion coefficient. The erosion rate index is then defined as

$$I_{HET} = -\log_{10}\left(C_e(s/m)\right) \qquad 2\text{-}6$$

Wan and Fell went on to propose some erosion categories based on I_{HET} (Table 2-4).

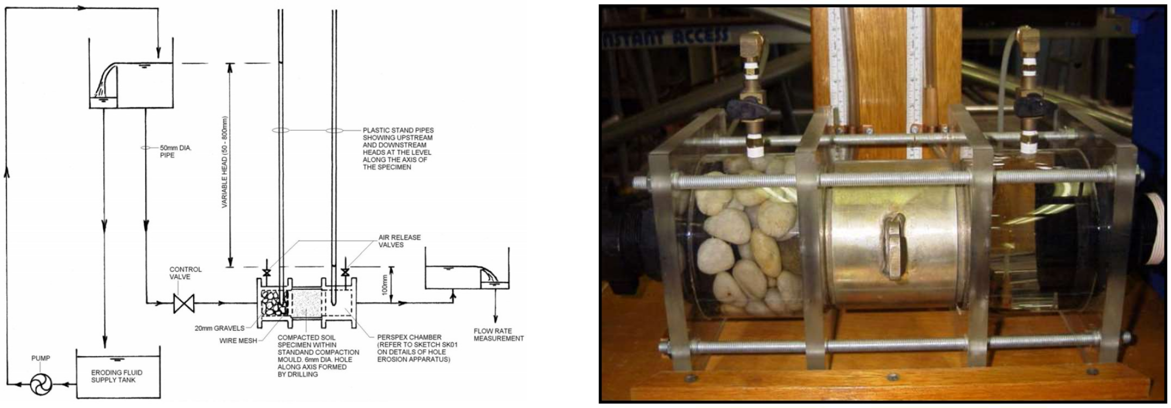

Schematic diagram of the HET

Photograph of the HET sample setup (Wan and Fell, 2002)

Figure 2-4. A schematic diagram of the HET and a photograph of the sample setup

Table 2-4. Hole Erosion Test – Fell's classification according to the erosion index (reprinted from Wan and Fell, 2002)

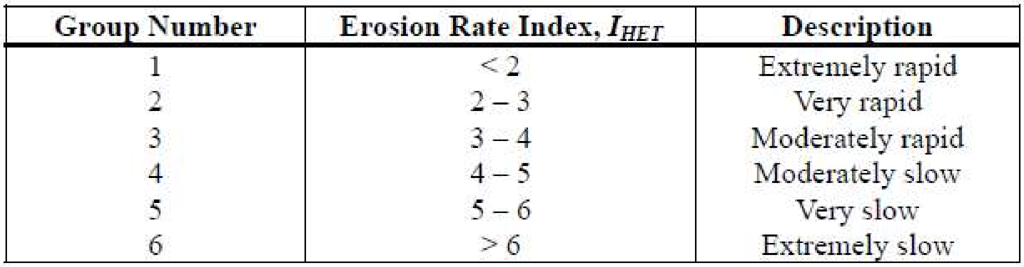

Group Number	Erosion Rate Index, I_{HET}	Description
1	< 2	Extremely rapid
2	$2 - 3$	Very rapid
3	$3 - 4$	Moderately rapid
4	$4 - 5$	Moderately slow
5	$5 - 6$	Very slow
6	> 6	Extremely slow

Advantages

1) A direct similitude with piping erosion in earth dams
2) It can apply a wide range of pressure heads and, therefore, a wide range of hydraulic shear stress at the soil-water interface.

Drawbacks

1) The sample needs to be cohesive and strong enough to stand under its weight. Therefore, the test cannot be run on cohesion-less samples.
2) Very difficult to run on intact samples in Shelby tubes from the field. Better for remolded samples in the lab.
3) Difficult and time-consuming preparation of the test
4) No direct monitoring of the erosion process. The erosion rate needs to be extrapolated and inferred.
5) The hydraulic shear stress is inferred and not directly measured.
6) The data reduction process is very subjective.
7) The flow within the eroded hole and at the soil boundary is complex and challenging to analyze.

2.3.3. Jet erosion test (JET)

The JET is an erosion test which can be credited to Hanson and developed at the USDA-ARS (Hanson, 1990). Hanson (1990) first developed this testing device to measure the soil erodibility in situ. The JET test was standardized as ASTM D5852 in 1995 and included both the in-situ and the JET test lab version. It included a nozzle with a diameter of 13 mm, which was held 22 cm away from the center of the soil surface. Figure 2-5 shows a schematic diagram of the in-situ version of the JET apparatus. To read the change in the hole's depth made in the soil by the jet, a pin profiler is used after each jet sequence (Hanson, 1990).

The JET test has been modified since its inception. Hanson and Hunt (2007) developed a new laboratory version of the JET apparatus. The circular jet submergence tank in this version has a 305 mm diameter, and its height is 305 mm. The scour readings are made using a point gauge aligned with the orifice and measures the scour in the specimen's center. The soil specimen is compacted in a 4" standard compaction mold, centered in the jet submergence tank, and placed below the jet nozzle. The distance between the nozzle and the soil surface in the standard compaction mold is 33 mm. Some DOTs and engineering firms currently use JET.

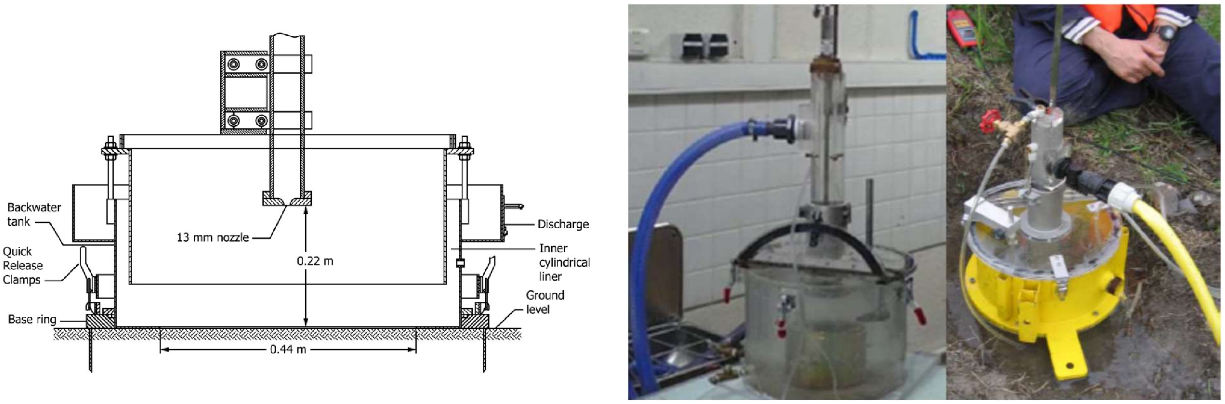

a. b.

Figure 2-5. a. Schematic diagram of submerged JET apparatus for field testing (ASTM D5852-95) b. The photographs of the lab version and in-situ version of JET (reprinted from Hanson and Hunt, 2007)

The step by step procedure of a JET test in the laboratory is (Hanson and Hunt, 2007):

1) Compact the sample in the 4" standard compaction mold, and trim the top surface.
2) Center the specimen in the submergence tank right below the jet orifice. Fill the tank with water.
3) Adjust the pressure head at the jet orifice to be 775 mm.
4) Direct the water jet at a given velocity perpendicularly to the soil surface and record the depth of the hole made by the jet as a function of time (not more than 2 hours), while holding the jet in a stationary position.

The last version of the JET test is a miniature of the original JET apparatus, called the mini JET. It was first used in the field by Simon et al. (2010) at 35 sites in Oregon (Al-Madhhachi et al., 2013). Compared to the previous versions, it is easily portable and can be used both in the field and the lab on the 4" standard compaction mold sample. The submergence tank in the mini JET has a dimension of 101.6 mm, and a height of 70 mm. The adjustable mini JET nozzle is 3.18 mm in diameter, and the head pressure at the nozzle is typically 450 to 610 mm.

Figure 2-6 shows the stress distribution at the soil surface proposed by Hanson and Cook (2004). The erosion rate is calculated as the slope of the curve linking the hole's depth to the time of jetting. The shear stress associated with the jetting process is calculated as a function of the maximum stress due to the jet velocity at the nozzle using the following equation:

$$\boldsymbol{\tau = \mathrm{C_f} \times \rho \times U_0^2 \times \left(\frac{J_p}{J_i}\right)^2} \qquad \text{2-7}$$

Where, C_f is the coefficient of friction (typically 0.00416), U_0 is the velocity of the jet at the origin ($\sqrt{2gh}$), ρ is the fluid density, J_i is the initial jet orifice height from the soil surface, and J_p is called the potential core length (6.3 × nozzle diameter). The critical shear stress, τ_c, is defined as the stress which exists when the hole is deep enough that the jet is no longer adequate to cause additional downward erosion (Hanson and Cook, 2004). To describe the relationship between the JET erosion rate and the jet velocity or calculated shear stress (erosion function), Hanson used a linear relationship and called the slope of the line the erosion coefficient K_D (Hanson, 1991 and 1992; Hanson and Cook, 2004):

$$\dot{z} = K_D\left(\tau - \tau_c\right) \qquad \text{2-8}$$

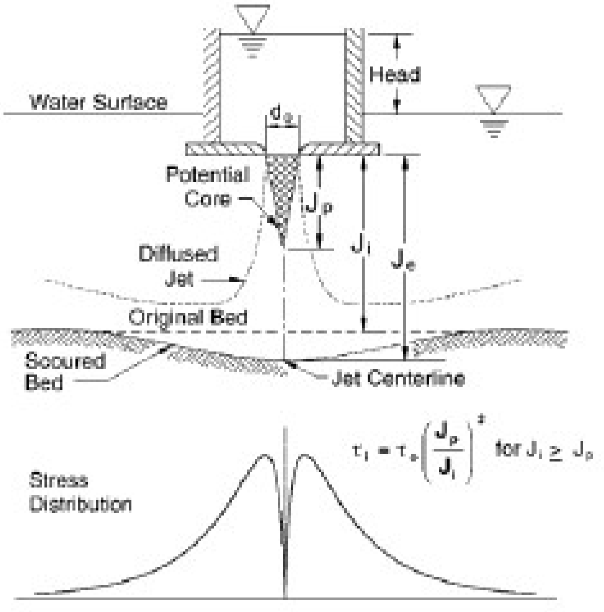

Figure 2-6. Stress distribution at the soil surface in the Jet Erosion Test

Based on many JET performed over time, Hanson classified the soils' erodibility according to their K_D value, as shown in Figure 2-7.

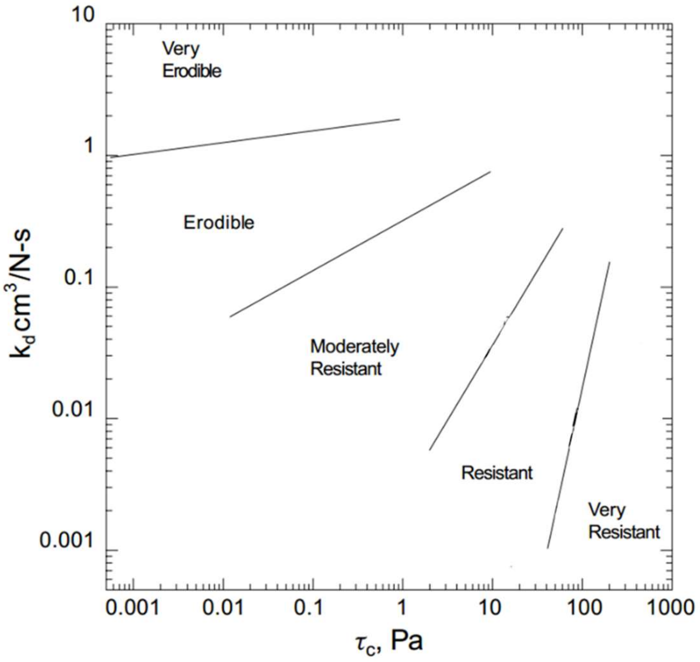

Figure 2-7. Jet Erosion Test: Hanson's classification according to the erosion coefficient (reprinted from Hanson and Simon, 2001 and Chedid et al., 2018))

Advantages

1) The JET can be run both in the field and in the lab.
2) The JET is simple, quick, and inexpensive compared to other types of erosion tests.
3) The JET can be performed on any surface, vertical, horizontal, and inclined (Hanson et al., 2002).

Drawbacks

1) For cohesive soils with a large coarse grain fraction, the JET might not be appropriate, as the submerged JET typically is not strong enough to move the coarse particles out of the eroded hole.

2) The JET is limited to testing the soil at the ground surface and cannot measure the soil's erosion properties at depth.
3) The flow within the eroded hole and at the soil boundary is complex and difficult to analyze

Before Hansen (1990), a few scholars had conducted some studies on the erodibility of soils by shooting jet into the soil's surface. Here is a summary of some of that work.

2.3.4. Borehole erosion test (BET)

The Borehole Erosion Test (BET) is an in-situ test developed by Briaud at Texas A&M University (Briaud et al., 2016). This test aims to quantify the erodibility of the soil layers as a function depth as follows. Figure 2-8 shows the schematic diagram of the BET and fieldwork photographs.

1) Drill a hole into the ground, say 100 mm in diameter, 10 m deep.
2) Remove the rods and measure the initial diameter of the borehole with a borehole caliper.
3) Re-insert the rods to the bottom of the hole and circulate water down the rod and up the hole's outside annulus for a given time, say 15 minutes.
4) Remove the rods and measure the diameter of the hole with the borehole caliper.
5) The increase in the borehole diameter at a certain depth given by the calipers divided by the flow time is the erosion rate of the soil at that depth for the flow velocity applied during the test.
6) Profiles of erosion rate for different velocities can be prepared in that fashion.

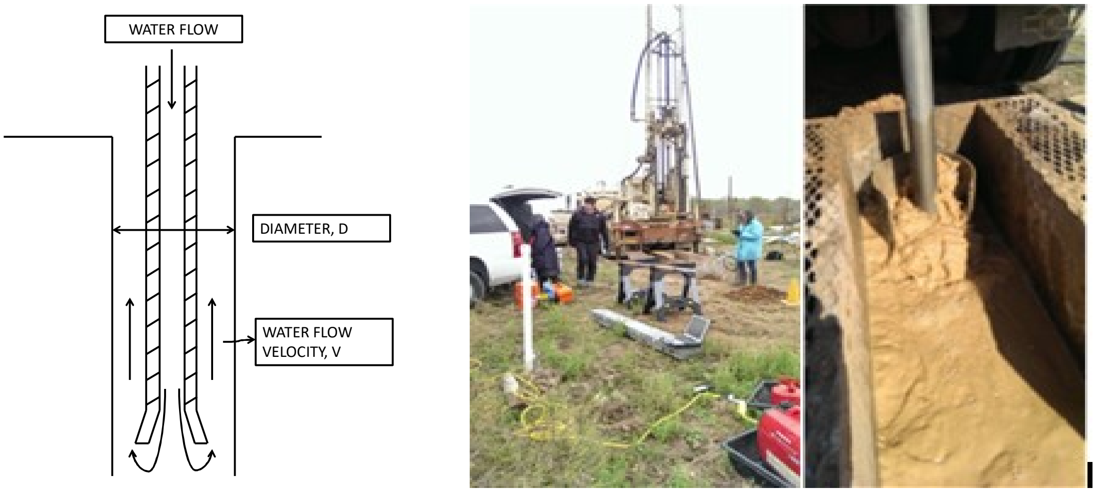

a. b.

Figure 2-8. a) A schematic diagram of the Borehole Erosion (BET) test and b) photographs of the test at the Riverside campus at Texas A&M University (reprinted from Briaud et al., 2016)

The advantages and drawbacks of this test are below.

Advantages

1) Only typically available field equipment (common drilling rig for wet rotary boring, flow meter in line with the drilling rig pump, and borehole caliper) is used to perform a BET test. Therefore the BET can be performed by many.
2) Each test gives the erosion function for all layers traversed since a complete borehole diameter profile is obtained from the caliper. This would require many tests on many samples if laboratory tests were to be conducted.
3) It has two component tests: the lateral erosion test associated with the increase in the borehole diameter and the bottom erosion test associated with the increase in depth below the bottom of the drilling rods during the flow. The latter one is much like an in-situ jet erosion test.
4) It can be used in any soil or rock where a hole can be drilled.

Drawbacks

1) The shear stress is obtained from the Moody chart.
2) Limited by pump flow available on the drill rig.
3) Fairly expensive setup.
4) In sand boreholes, Bentonite's addition during drilling needs to be controlled not to impact the erosion resistance.

2.4. Constitutive models for soil erosion

There are many different kinds of erosion models that are used for different purposes. It is always easier to measure the velocity of the flow; however, the velocity measurement is limited to the mean-depth velocity of the flow. Indeed, the velocity profile reaches a value of zero at the interface between the water and the soil. A better model definition of erosion is the relationship between the erosion rate and the shear stress at the soil-water interface (Briaud et al., 2017).

Previous erosion models in the literature do not incorporate both shear stress and normal stress effects in one single erosion model. Shafii et al. (2016) presented a comprehensive erosion model by incorporating the effects of turbulence-driven fluctuations in normal, and shear stresses acting on a particle (Equation 2-9):

$$\frac{\dot{z}}{v} = \alpha\left(\frac{\tau - \tau_c}{\rho v^2}\right)^m + \beta\left(\frac{\Delta\tau}{\rho v^2}\right)^n + \gamma\left(\frac{\Delta\sigma}{\rho v^2}\right)^p \tag{2-9}$$

Where v, is the flow velocity, τ refers to the hydraulic shear stress, τ_c Is the critical shear stress (the threshold shear stress associated with 0.1 mm/hr erosion rate), $\Delta\sigma$ refers to the net uplift normal stress fluctuations, and $\Delta\tau$ is the shear stress turbulent fluctuations. Any other parameter in Equation 2-9 is the unit-less erosion model parameters. Determining all the parameters required in Equation 2-9 is not practical at this time; therefore, a more practical erosion model is presented in this study (Equation 2-10):

$$\frac{\dot{z}}{0.1} = \left(\frac{\tau}{\tau_c}\right)^{\alpha} \times \left(\frac{\sigma}{\sigma_c}\right)^{\beta} 2 \qquad 2\text{-}10$$

Where, $\dot{z}$ is the erosion rate (mm/hr), τ_c (Pa) and σ_c (Pa) are the critical shear stress and critical normal stress associated with 0.1 mm/hr erosion rate, and α and β are the unit-less erosion model parameters. Equation 2-2 is expected to capture the influence of both shear and normal stresses during erosion.

This research has tried to compare the results of video analysis with CFD-DEM simulation, which can give more insight into the micromechanisms of the incipient motion of large particles. Formerly a video analysis has been done on the incipient motion of large particles by Briaud's research team on erosion in soil erosion laboratory (SEL) (Shafii, Zhang, and Briaud (2018)). To prove the efficiency of the CFD-DEM approach in predicting accelerations, velocities, displacements, and forces (lift, drag), it has been tried to modify the quality of video analysis and compare them with the results of EFA modeling in DEM.

2.5. Experimental modeling of measuring hydrodynamic forces in erosion

One of the vital problems in erosion is the prediction of a particle's incipient motion, including acceleration, velocity, and drag force or lift force at which the particle starts to move.

Many researchers have tried to measure the hydrodynamic force by using different methods. Shan et al. (2011) used an innovative direct force gauge in an ex-situ scour testing device (ESTD) to study forces acting on cohesive soil samples and analyze the incipient erosion of cohesive soils. They used a direct force gauge and a sensor disk to measure the acting horizontal and vertical forces on the soil's surface during the erosion process. The direct force gauge is separated into wet and dry parts by a rubber membrane, and on top of the core, the platform sits the sensor disk so that the normal and shear force acting on the soil specimen from the flow is directly measured.

Dwivedi et al. (2011) carried out a fixed ball experiment to measure the hydrodynamic forces and velocity on the particle at the entrainment condition. This experiment was performed using a force sensor in a flume and aimed to replicate conditions similar to a flow condition. The target spherical particle is fixed to a hollow rod attached to the force sensor so that the sensor will measure the forces that acted on the target particle. Their results indicate that both the drag force and lift force fluctuate during the test; the specific values are not given.

Maali et al. (2012) used a colloidal probe Atomic Force Microscopy (AFM) to quantify the slip length and drag-force on microstructured surfaces in a drainage experiment. The AFM is in contact mode during this test. The hydrodynamic drag force is given by the cantilever's deflection when the particle is subjected to a constant velocity flow. The particle used in this test was a spherical borosilicate particle with a 52.5 μm diameter. Their results demonstrate that measured hydrodynamic forces decrease sharply with increasing separation distance. Also, the amounts of force are higher on pillars than between pillars.

2.6. Infilling Phenomenon

During major flood events, the presence of scour holes around the bridge supports are probable. After the flood peak velocity, the water slows down, and the river, if it transports a lot of sediments or if the velocity is still sufficient to move the soil at the bottom of the river, may deposit some loose soil in the scour hole. When the inspector comes to measure the depth of the scour hole after the flood, the depth of the in-filled scours hole z_i, which may be different from the depth of the scour hole at the height of the flood z_f (Figure 2-9). How much difference is there between z_i and z_f is a critical question.

The infilling process comprises two components: vertical deposition and horizontal deposition (Figure 2-10). Vertical deposition comes from the fall of suspended soil particles by vertical settling in the scour hole. This is due to the natural downward movement by the particles' gravity and the fact that the velocity slows down after the flood. The fall velocity is given by Stokes Law, which relates the diameter of a sphere and its unit weight to its fall velocity in a liquid:

$$v_v = \left(\frac{\gamma_s - \gamma_f}{18\mu} \right) D^2 \tag{2-11}$$

Where γ_f is the fall velocity of the sphere, γ_s the unit weight of the sphere, γf the unit weight of the fluid (soil plus water), μ the viscosity of the liquid, D the sphere diameter.

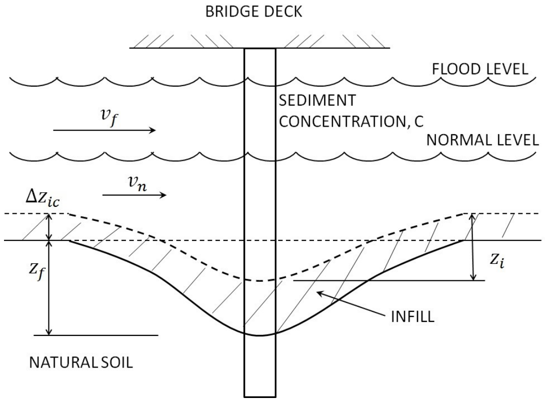

Figure 2-9. Definitions of infilling scour depths

One would think at first glance that the same amount of soil would fall in the scour hole as would fall everywhere else on the river bottom. If that were the case, then this part of the infilling process would not lead to reading an erroneous scour depth (relative measurement) but merely a wrong elevation (absolute measurement) (Figure 2-9). This is not entirely true for the following reason. At the peak of the flood, the water has to accelerate around the pier to maintain the flow. As a result, the velocity around the pier is about 1.5 times larger than the approach velocity (Figure 2-11). However, after the flood, the velocity is lower above the scour hole (larger depth for the same flow) than in the approach section (Figure 2-11). These differences in velocity over the scour hole contribute to a differential deposition process around the pier compared to the approach channel.

The horizontal deposition is called bedload transport or live bed scour. For the deposition to occur, the approach flow velocity must be higher than the soil critical velocity. This critical velocity v_c is given by Figure 2-12 after Briaud (2008). For coarse-grained soils

$$v_c(m/s) = 0.35\left(D_{50}(mm)\right)^{0.45} \qquad 2\text{-}12$$

Where D_{50} is the mean grain size of the soil on the river bed. For fine-grained soils, the critical velocity is not proportional to the mean grain size but can be bracketed by the two following relationships (Figure 2-12):

$$v_c(m/s) = 0.03(D_{50}(mm))^{-1} \qquad 2\text{-}13$$

$$v_c(m/s) = 0.1(D_{50}(mm))^{-0.2} \qquad 2\text{-}14$$

The particles infill the scour hole by bedload transport because they roll down the front slope of the scour hole and do not have enough energy to climb back up the back slope, thereby getting trapped in the scour hole infilling it. Bedload transport or horizontal deposition likely is the most prevalent of the two mechanisms for infilling. The difference in velocity in the open channel and around the pier affects the horizontal deposition and the vertical deposition.

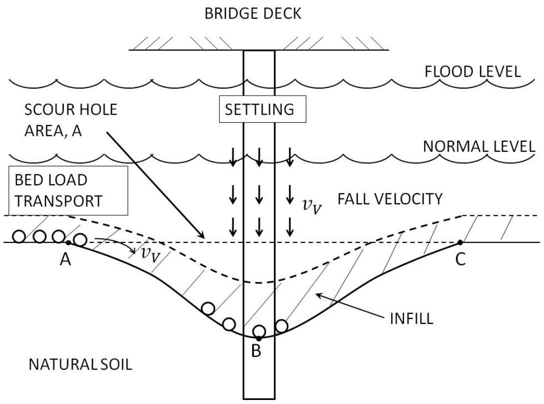

Figure 2-10. Infilling phenomenon

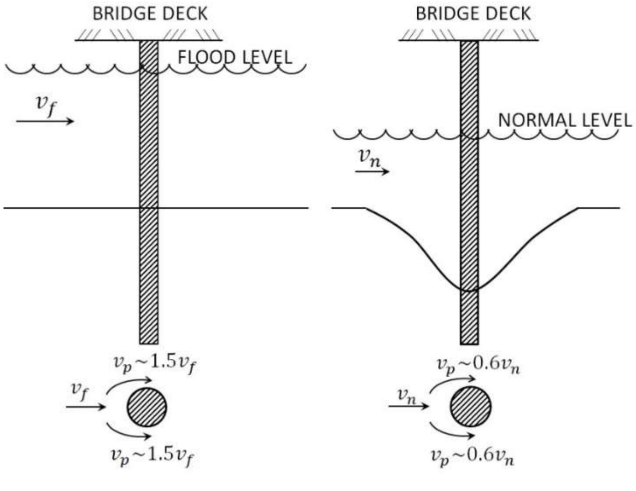

Figure 2-11. Comparison of velocities near the bridge pier

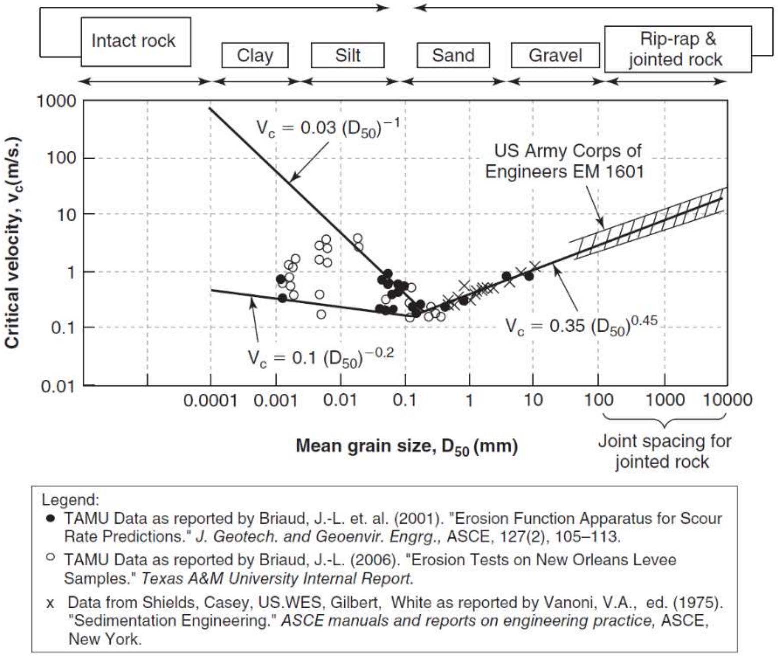

Figure 2-12. Critical velocity as a function of mean grain size (reprinted from Briaud, 2013)

The factors influencing the infilling process are identified in Table 2-5.

The transported or suspended sediment concentration C is essential as it contributes directly to the infilling process. Yet, it does so by differential deposition between the main channel and around the pier. This concentration C typically varies between 0.1 and 5 g/l (Heimann et al., 2011), and the grain size of the transported sediments typically varies between 0.01 mm and 0.2 mm (Walling and Moorehead, 1989).

The flood velocity V_f is critical as it is responsible for the depth of the scour hole during the flood, the sediment concentration in the flow, and the movement of particles on the river bed, called live bed transport, during the flood.

The average flow velocity V_n is crucial as it controls the continuation of the amount of sediment being transported in suspension and as a live bed under normal flow condition. The flow hydrograph of the receding flood is also essential as the sediment concentration and the live bed process will decrease during that period along with the infilling rate.

The grain size of the natural soil D_{50n} in the upstream reach of the river and the grain size of the suspended sediments D_{50t} in the flow are both important as they impact the erosion and deposition process, including the fall velocity of the soil particles and the critical velocity of the soil grains on the river bottom directly. A distinction is made between infilling by vertical deposition or settling and infilling by horizontal deposition or bedload transport (Figure 2-10).

The obstacles in front of the water flow (flood plain, main channel) are indirectly significant through the velocity difference as the flow velocity is typically lower in the flood plain than in the main channel.

The size of the obstacle has a significant influence on the depth of scour during the flood but not likely on the infilled depth after the flood.

The water depth does not seem to have a particularly significant influence on the infilling process.

Table 2-5. Factors influencing the infilling process

FACTOR	LEVEL OF INFLUENCE
Sediment concentration C	Important
Flood velocity V_f	Very important
Normal flow velocity V_n	Very important
The grain size of natural soil D_{50n}	Important
The grain size of transported sediment D_{50t}	Important
Location of obstacle (main channel, flood	Important
Size of obstacle (Pier, contraction,	Not very important
Water depth H	Not very important

2.6.1. *Analytical elements of infilling*

Vertical deposition or sediment settling comes from the vertical settling of the soil particles in the water column. We can establish the following simple model to represent the contribution of this part of the infilling process. If the fall velocity is V_v then the weight of soil ΔW_{sv} per unit time Δt entering the scour hole due to vertical deposition will be

$$\Delta W_{sv} / \Delta t = A\ V_v\ C \qquad 2\text{-}15$$

where A is the horizontal area of the scour hole through which the soil particle can enter, and C is the soil concentration in the water (kN/m^3). Simultaneously, the weight of soil entering the scour hole per unit time will occupy a volume equal to A times the infill thickness ΔI_v . Therefore the weight of soil entering the scour hole per unit time is also given by

$$\Delta W_{sv} / \Delta t = A\ \Delta I_v\ \gamma_d / \Delta t \qquad 2\text{-}16$$

Where γ_d is the dry unit weight of the soil in the scour hole. Combining equations 2-15 and 2-16 gives

$$\Delta I_v / \Delta t = V_v\ C / \gamma_d \qquad 2\text{-}17$$

Equation 2-17 gives the infill rate due to vertical deposition. Note that the infill rate is a function of the concentration of soil in the flow, which depends on the flow velocity V which varies with the time t (Figure 2-13). Therefore the total infill thickness after a flood will be given by:

$$I_v = \frac{V_v}{\gamma_d} \int_0^t C(t)dt \qquad 2\text{-}18$$

Horizontal deposition comes from the rolling velocity or bedload transport velocity of the soil particles on the river bottom at the flood stage. This velocity must be larger than the soil critical velocity, which is given in Fig. 45. The critical velocity is the velocity at which the soil particles resting on the river bottom start rolling and moving forward with the flow. We can establish the following simple model to represent this part of the infilling process. If the horizontal velocity is V_h then the weight of soil ΔW_{sh} per unit time Δt entering (falling in) the scour hole due to horizontal deposition will be

$$\Delta W_{sv} / \Delta t = b \ D_{50} \ \gamma_d \ V_h \ \Delta t \qquad \text{2-19}$$

Where b is the width of the scour hole perpendicular to the flow, D_{50} is the mean grain size of the rolling particles, and γ_d is the soil's dry density. Simultaneously, the weight of soil entering the scour hole per unit time will occupy a volume equal to A times the infill thickness ΔI_v. Therefore the weight of soil entering the scour hole per unit time is also given by

$$\Delta W_{sv} / \Delta t = A \ \Delta I_v \ \gamma_d / \ \Delta t \qquad \text{2-20}$$

Where γ_d is the dry unit weight of the soil in the scour hole. Combining equations 2-19 and 2-20 gives

$$\Delta I_v / \Delta t = V_h \ b \ D_{50} / A \qquad \text{2-21}$$

Equation 2-21 gives the infill rate due to horizontal deposition. Note that the infilling rate is a function of the flow velocity V_h. Therefore the total infill thickness after a flood will be given by:

$$I_v = \frac{bD_{50}}{A}\int_0^t V_h dt \qquad \text{2-22}$$

The total infill is I_t given by

$$I_t = I_v + I_h \qquad \text{2-23}$$

Combining the two models would lead to the scour depth as a function of time, including the process of infilling (Figure 2-14).

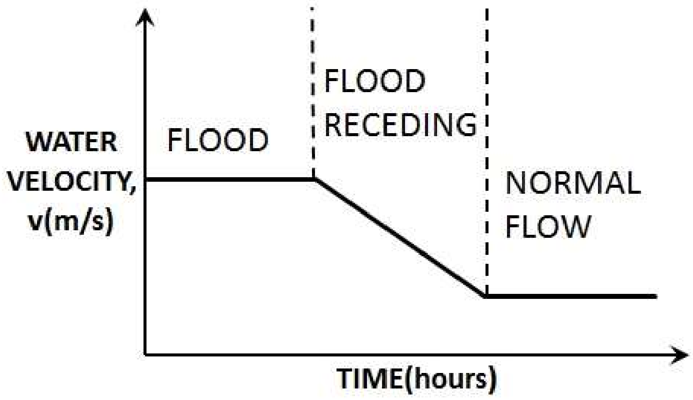

Figure 2-13. Evolution of flow velocity during and after the flood.

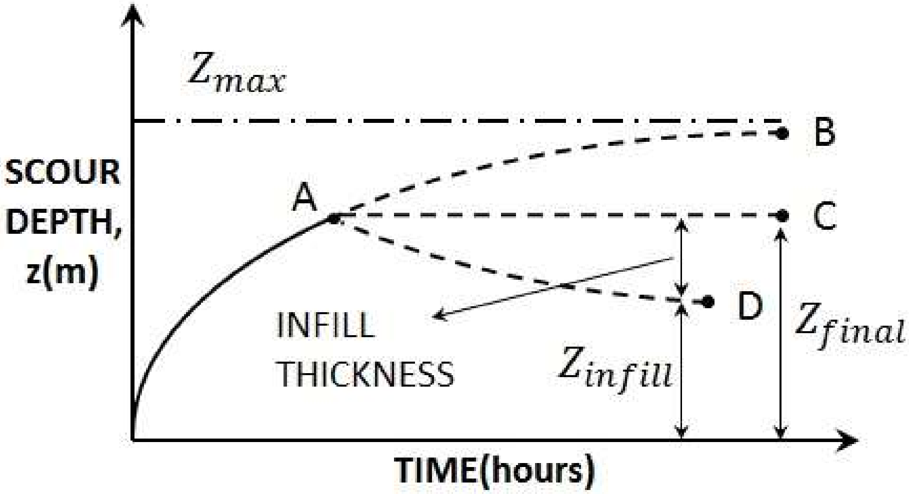

Figure 2-14. Evolution of scour depth during and after the flood.

2.6.2. A short literature review on infilling of scour holes

A search of the literature indicated that the amount of published work on the infilling of scour holes is very limited. While there are some early studies (Culbertson et al. (1967)), studies by Benedict and his colleagues (Benedict, 2003; Benedict and Caldwell, 2009) have the most amount of measured data. They state the following: "The issue of predicting and/or defining infill is quite challenging. For clear-water scour on the floodplain (Benedict, 2003), we found that the amounts of infill in abutment scour holes were typically small. In the Coastal Plain of South Carolina, we collected scour data at 109 abutments, and infill ranged from 0 ft to 4.6 ft with a mean of 0.7 ft and a median of 0.3 ft. In the clayey over Piedmont banks, we collected 100 measurements of abutment scour and found infill to be minimal and typically considered nonexistent. For live-bed scour in the channel (Benedict and Caldwell, 2009), infill is much more challenging to define. The database for Benedict and Caldwell (2009) contains estimated infill for the scour holes based on GPR data and may be of some help in understanding scour. However, the complexities of the field and the limitations of field data should be kept in mind."

Figure 2-15 shows an example of GPR data collected at a site in South Carolina by Stephen Benedict. This GPR graph shows a relatively uniform deposition of looser soil (lighter color) across the river profile. While the scour hole due to contraction is 3.6 m deep, the infilling is only 0.6 m thick or 20% of the observed depth of the scour hole. It is known that GPR works better in coarse grain soils than in fine grain soils and that the conductivity of the water further impairs it. A seismic method called Chirp or frequency sweep is much more likely to be successful in fine grain soils.

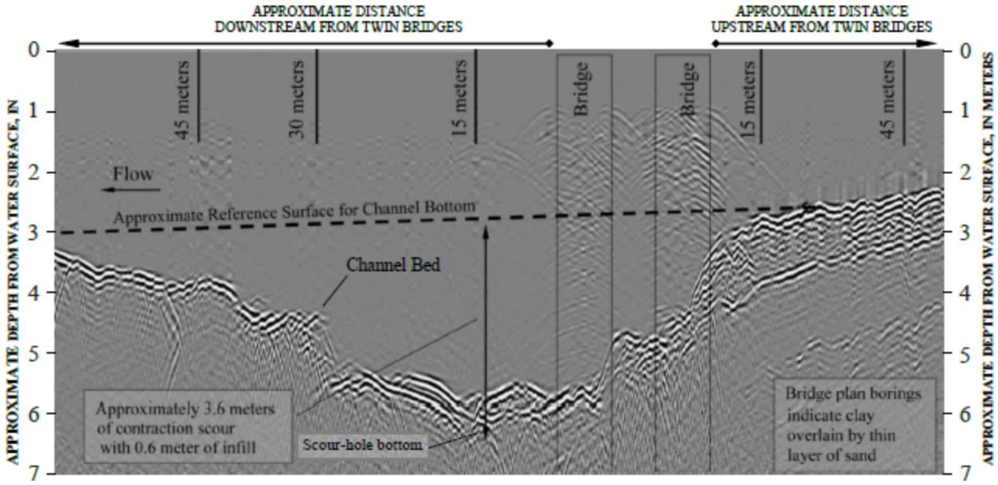

Figure 2-15. Example of GPR sounding

2.7. Numerical Simulation of Erosion

Two approaches can be utilized to simulate the fluid flow, distribution of velocities and shear stresses, and the scour depth in erosion problems. A Computational Fluid Dynamics (CFD) approach with moving boundary and a CFD approach with the Discrete Element Method (DEM).

In the first approach, the CFD technique can be applied to model the fluid flow. To model the bed's erosion process, the boundaries should be moved, which can be handled by applying several methods. The boundary movement is proportional to the erosion rate, which is a function of shear stress on the boundaries. This function, called erosion function, which can be determined by the scour data from the laboratory or the field. The erosion function can be programmed in the CFD program to change the boundaries. This movement can be done by direct application of scouring data in a similar scheme. The advantage of this method is the efficiency of the scheme compared to the CFD-DEM approach or other coupled approaches.

2.7.1. Numerical simulation of erosion by continuum modeling

Several researchers utilized the mesh morphing technique to investigate surface erosion. This research focuses on the investigation of surface erosion and scour and infilling around the bridge piers. In the following, a summary of this researches is presented.

Farimani et al. (2011) proposed a computational model to simulate the morphological changes due to wind erosion. They modeled a sinusoidal sand pile in a laboratory and CFD solver to compare the results. They have considered an analytical morphological model to incorporate avalanche, saltation, creep, and mass flux in the CFD solver. The surface morphology comparison of CFD results with the experimental modeling indicates good agreement.

Edwards et al. (2013) introduced three physics-based models for scouring non-cohesive sand in STAR-CCM+ with mesh morphing techniques. They proposed a critical shear stress model to account for the uphill and downhill of particles during the erosion process. By application of this model, the scour will happen normally to the scoured bed. Also, they incorporated the slope failure in the model. By utilizing a remeshing technique, they tried to keep the quality of mesh excellent during the erosion process. Their results showed that with the new model, the value of scour was overpredicted by 35 percent at the deepest point. Although the model correctly predicts the shape of the scour hole for non-cohesive sand.

Kim et al. (2016) coupled a CFD solver, FAN3D, with a morphological model to simulate scour, infilling, and sediment transport around a circular pier. They have considered two constant velocities and one time-variant hydrograph. Two sizes of particles considered to incorporate the effect of particle size on scour and infilling. This morphological model has been implemented by Khosronejad et al. (2011), which considers the critical shear stress form shield diagram. This model also accounts for slope failure and sand slide. Results showed that after 3 hours of simulation, the equilibrium was not reached, but infilling was observed in the transition flow case. Scour was formed at the early stages of scouring and infilled in the average velocities.

The research mentioned above applied different analytical methods to consider different aspects of erosion problems. Still, the drawback of all these analytical methods is the lack of a direct link to the experiment. In these methods, based on different general methods, it has been tried to simulate the erosion accurately. The best trend for simulation of erosion is performing an erosion test on samples extracted from the different depths of the exact location and using the results to estimate the amount of scour in that specific location. Among the current experimental erosion tests, EFA is one of the extensive tests in the US and worldwide. EFA captures the erosion function, which explains the relationship between erosion rate and shear stress. The erosion function is simple and adequately describes the behavior of soil in the erosion process. Using erosion function derived from the same sample that is intended to do the simulation could be the best way to simulate the hydraulic structure in CFD software. This research has tried to apply erosion function in CFD software STAR-CCM+ and simulate other erosion tests, including JET, HET, and BET. Since this scheme (CFD-Mesh Morphing) is utilized in Chapter 3, the basics of this scheme are presented in Chapter 3.

2.7.2. Numerical simulation of erosion by discrete modeling

By applying CFD, fluid and soil phases can be explained as the Eulerian-Eulerian approach, which indicates the motion of fluid and particles with a continuum point of view. Eulerian viewpoint capture precise solution for the fluid but less accurate results for the particulate domain. Despite the Eulerian approach, the Lagrangian approach could be an excellent tool to simulate the motion of particulate media. In this approach, the motion of particles is defined in space and time.

The discrete element method, which was first proposed by Cundall in 1971, uses the Lagrangian approach to locate the position of particles in space and time. This approach can complete the Eulerian approach to use as the Eulerian-Lagrangian approach. Many industrial applications can be considered as multiphase and can be simulated by the Eulerian-Lagrangian approach.

In CFD-DEM, the motion of the fluid phase is assumed as a continuum in mesoscale. In this scale, the motion of a fluid can be described by the volume-averaged Navier-Stokes equations. For the DEM part, the motion of the particulate domain can be described as micro-scale by Newton's and Euler's second laws (Figure 2-16). Fluid-particle interaction and data exchange from the particulate phase to the fluid phase (miro to meso) work based on total interaction per unit volume of the fluid cell. While from the fluid phase to the particulate phase (meso to micro) is based on force (drag forces) acting on any individual particle.

The limitation of this technique concerning continuum techniques is the high computational cost of this method with current computational power. Still, the advantage of this method is the ability to capture the micro behavior of individual particles. In each time step, displacements, velocities, and accelerations for particles can be derived, enabling the researcher to study the motion of particles in the CFD-DEM technique deeply. Considering the vast applications of this technique in different engineering fields, the future of this technique is promising.

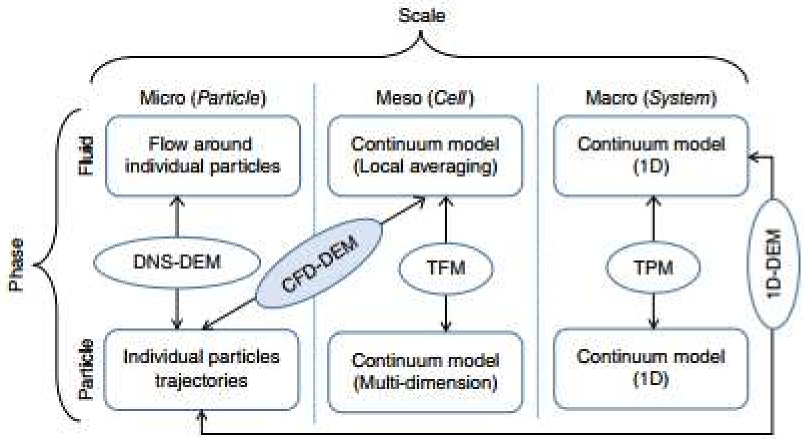

Figure 2-16. Different scales in modeling fluid phase and particulate phases (reprinted from Norouzi et al. 2016)

In recent years, different fields of engineering applied CFD-DEM az an effective technique to investigate different phenomena. Liquid fluidized bed reactors, Fluidized bed dryers are two applications in Chemical Engineering. In Geotechnical Engineering and Ocean Engineering, this approach is used by different researchers to simulate phenomena like sediment erosion, internal erosion, suffusion, and piping. In the following, a summary of this researches is presented.

Abdelhamid and Shamy (2014) utilized an LBM-DEM (mesoscale-microscale) to study surface erosion. They indicated that particle spinning affects the tendency of particles against lift, and spinning facilitates the lift action. They also showed that there is a small distance in the surface known as a sheet-flow layer for a packed bed of particles, which depends on flow velocity and particle size. They concluded that the relative velocity between the fluid penetrating the bed and initially, static particles contribute to drag and lift forces, which cause the incipient movement of particles. With increasing the velocity of flow, the erosion depth will increase, and the effect of lift force in erosion becomes more highlighted.

Abdelhamid and Shamy (2015) used an LBM-DEM approach to investigate the mechanism of fine particle migration in granular filters. By changing the values of D_{15F}/D_{85S}, (D_{15F} is the diameter of the filter particles for which 15% of particles are finer and D_{85} is the diameter of the soil particles for which 85% of particles are finer). They studied the efficiency of the Terzaghi criteria for filter design (1922). They showed that for the value of $D_{15}\ /D_{85}\ \leq 4$ led to stable filters with high-pressure buildup in the filter zone while with $D_{15F}/D_{85}\ > 4$ filter design will be unstable with no pressure buildup. When $D_{15}\ /D_{85S} \leq 4$, the migration of particles starts but will stop after clogging. The clogging effect will occur before the migration of 20% of particles. In this case, most of the soil particles will be trapped between the filter particles in the first third of the filter zone. They also indicate that with $D_{15}\ /D_{85}\ > 4$, around 80% of particles were eroded, and the permeability was increased.

Sun and Xiao (2016) investigated dune formation and morphological evolution by a CFD-DEM scheme. They successfully predicted the dune formation of sand particles with the CFD-DEM technique, which is comparable to experimental results. They also showed the capability of the CFD-DEM approach in the prediction of small dunes (Re = 840), vortex dunes (Re = 6500), and suspended particles in high Reynolds numbers (Re = 48000).

Tao and Tao (2017), with a CFD-DEM approach, investigated the piping erosion. They studied the effect of hydraulic gradient on piping progression. They investigated the evolution of contact force, hydraulic force, contact number, and porosity during the piping process. They showed that hydraulic forces could rearrange the particles under a small hydraulic gradient and change the void ratio. While In a high hydraulic gradient, the contact force between the particles becomes weaker and weaker until piping is initiated. A decrease of overburden due to the erosion of top particles will cause more erosion until the total heave. During this process, the orientation of forces changes from being vertically oriented to horizontally oriented. They compared the internal erosion of uniform sand with Ottawa 20-30 sand. They indicated that in uniform sand, porosity is more significant, and it is easier for water to release pressure and seep upward and create a clear progression of piping. In contrast, for Ottawa sand, only a bottom-up dilation occurs.

Guo and Yu (2018) applied a CFD-DEM approach using COMSOL and PFC3D to investigate the effect of grain shape on the erodibility of non-cohesive soils. They have indicated no critical velocity for the spherical particle, contributing to the low rolling resistance of particles. However, ellipsoidal particles show a critical velocity, which is due to the angularity of particles. They showed that the CFD-DEM approach is an efficient tool in understanding soil erosion mechanism and incipient motion of particles in the erosion process.

Guo and Yu (2018) applied the CFD-DEM method to investigate surface erosion. They deposited particles inside a pipe to investigate the surface erosion. They investigated the effects of particle size, interparticle bond, and turbulence of flow on the erodibility of soil particles. They also determined critical shear stress by dividing external force into an effective cross-sectional area of particles. They showed that critical shear stress increases linearly with the grain size. They indicated that the increase in particle bond strength decreases the amount of erosion. By applying $k-\varepsilon$ turbulence model (k is turbulence kinetic energy and ε is its dissipation), they showed that flow turbulence aggravates the erosion rate of particles.

Zheng et al. (2018) applied a CFD-DEM approach to investigate sediment erosion. Based on their simulations, they found out that the sediment could be divided into four layers from top to bottom. In the top layer, saltation of particles occurs, and particles have leap motion (Salting layer). The next layer shows only the rolling of particles, and particles slipped and rotated (Rolling layer). The third layer is a thin layer, in which the only creep of particles will happen (Creeping layer).

Beneath the third layer, particles are in a static condition (Static layer). At low shear velocities, particle erosion is intermittent, while in high velocities, the erosion is continuous and linear.

In the rolling layer, particle velocity increases linearly from bottom to top. In the saltation layer with low shear velocities, successive migration of particles happen. In high shear velocities, an abrupt increase in migration velocity cause the particles to remove from the surface faster. In low shear velocities, particle trajectory follows the morphology of the surface, while in high shear velocities, particles are removed from the surface. In low Reynolds numbers, the viscous effect plays a role in the erosion of particles, while high Reynolds number turbulence governs.

Zhang, Gao, and Yin (2019) studied the mechanism of seepage erosion around the shield of tunnels using a CFD-DEM approach. They considered three types of sands, including dense, medium sand, and loose silty sand. They modeled the simulations with different confining pressures, axial pressure, and hydraulic pressures. For all simulations gap-graded, grain size distribution was considered. They showed that the migration of fine particles between the large particles increased by increasing axial pressures and hydraulic pressures.

Wang et al. (2019) tried to define the relationship between the drag coefficient and Reynolds number for irregular particles. By performing several laboratory experiments on the settling of calcareous sand particles in water and water-glycerin, they proposed a new drag relationship, which links C_D to a particle shape factor.

Kanitz and Grabe (2019) investigated the influence of different drag force models on suffusion potential in gap-graded soils. They used four different drag models, including Di Felice, Gidaspow, Schiller-Neumann, and Koch-Hill drag models, to compare the efficiency and the amounts of particle loss in each model. This study showed that the choice of drag model has a substantial effect on the suffusion modeling.

2.7.3. *Particle Equations of Motion*

The conservation equation of momentum for a particle can be written in the Lagrangian framework. The change in momentum is balanced by surface and body forces that act on the particle.

The following equation defines the conservation of linear momentum for material or DEM particle of mass m_p:

$$m_p \frac{dV_p}{dt} = F_s + F_b \tag{2-24}$$

where V_p indicates the instantaneous particle velocity, F_s is the resultant of the forces that act on the surface of the particle, and F_b is the resultant of the body forces. These forces, in turn, are decomposed into:

$$F_s = F_d + F_P + F_{vm} \tag{2-25}$$

and

$$F_b = F_g + F_{MRF} + F_u + F_c + F_{Co} \tag{2-26}$$

where:

F_d drag force, F_P pressure gradient force, F_{vm} virtual mass force, F_g gravity force, F_u the user-defined body force, F_c contact force (DEM modeling only), F_{Co} Coulomb force

The pressure gradient force is as defined as:

$$F_p = -V_p \nabla p_{static} \tag{2-27}$$

where V_p is the volume of the particle and ∇p_{static} is the gradient of the static pressure in the continuous phase.

The resultant of the surface forces F_s denotes the momentum transfer from the continuous phase to the particle. When using the two-way coupling modeling approach, F_s is accumulated over all the parcels and applied in the continuous phase momentum equation.

In DEM modeling, the contact force F_c represents inter-particle and particle-boundary interaction. This force is accumulated over the contacts that a particle has, and it is applied as a body force:

$$F_c = \sum_{contacts} F_{cm} \tag{2-28}$$

where F_{cm} is a contact force model. Simcenter STAR-CCM+ provides several contact force models that describe the contact force F_{cm}. Additionally, DEM particles have orientations, and therefore their angular momentum must also be conserved:

$$I_p \frac{d\omega_p}{dt} = M_b + M_c \tag{2-29}$$

where:

I_p particle moment of inertia, which is described by a second-order tensor, ω_p particle angular velocity, M_b drag torque that is, the moment that acts on the particle due to rotational drag, M_c the total moment from contact forces, both from rolling resistance models (M_{cm}) and any other contact forces ($r_c \times F_{cm}$)

$$M_c = \sum_{contacts}(r_c \times F_{cm} + M_{cm}) \tag{2-30}$$

where:

r_c position vector from the particle center of gravity to the contact point, M_{cm} position vector from the particle center of gravity to the contact point

2.7.4. Drag Force

The drag force in Equation 2-25 is defined as:

$$F_d = \frac{1}{2} C_d \rho A_p |V_s| V_s \qquad \text{2-31}$$

Where C_d is the drag coefficient of the particle, ρ density of the continuous phase, $V_s = V - V_p$ the particle slip velocity with V being the instantaneous velocity of the continuous phase, A_p the projected area of the particle

Equation 2-31 can also be written as:

$$F_d = m_p V_S / \tau_v \qquad \text{2-32}$$

where τ_v is the momentum relaxation time-scale:

$$\tau_v = \frac{2m_p}{C_d \rho A_p |V_S|} \qquad \text{2-33}$$

The drag coefficient C_d in Equation 2-31 is a function of the small-scale flow features around the individual particles.

These features are impractical to resolve spatially, and so the usual practice is to obtain the drag coefficient from correlations, typically derived from experiments or theoretical studies. These correlations depend on the nature of the dispersed phase. Droplets, bubbles, and solid particles have different correlations. The shape of the particle, the presence of inter-phase mass and energy transfer, and so on, affect these correlations.

Simcenter STAR-CCM+ provides the different drag force models; between them, the following drag force is applied in this research: Schiller-Naumann, Di Felice drag models.

Schiller-Naumann Drag Coefficient Method

The Schiller-Naumann correlation (Schiller and Naumann 1933) is suitable for spherical solid particles, liquid droplets, and small-diameter bubbles. It is formulated as:

$$C_d = \begin{cases} \frac{24}{Re_p}\left(1 + 0.15 Re_p^{0.687}\right) & Re_p \leq 10^3 \\ 0.44 & Re_p > 10^3 \end{cases} \qquad 2\text{-}34$$

where Re_p is the particle Reynolds number that is defined as:

$$Re_p \equiv \frac{\rho |V_s| D_p}{\mu} \qquad 2\text{-}35$$

where D_p is the particle diameter, and μ is the dynamic viscosity. This correlation is available only when the continuous phase is viscous.

Di Felice Drag Coefficient Method

This drag method introduces an additional term in the fluid drag force expression (Equation 2-31) to account for the presence of other particles around a particle. The Di Felice drag coefficient is given as:

$$C_d = (0.63 + \frac{4.80}{\sqrt{\epsilon_i Re_p}})^2 \epsilon^{2-\zeta} \qquad 2\text{-}36$$

where Re_p defines the particle Reynolds Number, ϵ_i is the void fraction around a particle, and:

$$\zeta = 3.7 - 0.65 exp\left[-0.5\left(1.5 - log\left[\epsilon Re_p\right]\right)^2\right] \qquad 2\text{-}37$$

The term $\epsilon^{2-\zeta}$ accounts for the effect of enhanced drag on a particle due to the presence of other particles around it.

2.7.5. Two-Way Coupling Model

For Lagrangian and DEM simulations, the two-way coupling model allows the particle phase to exchange mass, momentum, and energy with the continuous phase.

Without the Two-Way Coupling model, the default "one-way coupling" means that the continuous phase influences the particles through drag in the momentum equation and heat transfer in the energy equation. However, there is no reverse effect. With the Two-Way Coupling model, the reverse effect is accounted for, and Lagrangian source terms appear in continuous phase equations. Typically, this effect becomes more critical at higher particle loadings (Crowe et al. 1998).

2.7.6. Two-Way Coupling with the Continuous Phase

In Simcenter STAR-CCM+, the interactions between the dispersed and continuous phases can be modeled as one-way coupling or two-way coupling. The coupling refers to the way that momentum, heat, and mass are exchanged between the phases.

Only the continuous phase influences the dispersed phase with one-way coupling, but not in the reverse direction. With two-way coupling, the dispersed phase's effects on the continuous phase, such as displacement, interphase momentum, mass, and heat transfer, are taken into account.

The displacement of the continuous phase by the dispersed phase is accounted for through the volume fraction. The volume fraction of a Lagrangian phase is the fraction of the local cell volume that phase occupies. It is calculated for both discrete material particles and DEM particles.

The volume fraction $\emptyset_c$ of all Lagrangian phases for which the two-way coupling is active is accumulated. This volume is seen as a void by the continuous phase: the continuous phase volume decreases by this volume fraction. The available volume fraction for the continuous phase (corresponding to the void fraction) η is defined as the ratio of the volume occupied by all continuous fluid phases to the total cell volume, as given by $\eta = \frac{\sum_i V_i^F}{V}$. The volume fraction of the Lagrangian phase is related to the available volume fraction for the continuous phase as:

$$\emptyset_c = 1 - \eta \qquad \text{2-38}$$

In practice, $\emptyset_c$ is under-relaxed to promote stability:

$$\emptyset_c = \alpha(\sum \phi) + (1 - \alpha)\phi_{c,old} \qquad \text{2-39}$$

where α is an under-relaxation factor of the two-way coupling solver and $\sum \phi$ is the sum of the volume fractions of the relevant Lagrangian phases. The value of $\emptyset_c$ which is contributed to the continuous phase void fraction is limited to min($\emptyset_c, \emptyset_{c,max}$), again to promote stability.

When integrated over a cell, the Lagrangian dispersed phase equations yield the changes in the momentum, mass, and energy of each particle between its entry and exit. The sum of these changes for all particles crossing the volume provides the net momentum, mass, and energy exchanged with the continuous phase. These net exchanges enter the continuous phase equations as source terms. The source terms are not computed for massless particles as these particles do not influence the continuous phase.

Momentum Transfer

The rate of momentum transfer to a single particle from the continuous phase is $F_s + \dot{m}_p V_p$, where F_s is the force acting on the surface of the particle, defined in Equation 2-25 and $\dot{m}_p$ is the rate of mass transfer to the particle.

In unsteady simulations, the rate of momentum transfer from all particles in a cell c to the continuous phase is:

$$S_V = -\frac{1}{\Delta t}\sum(\int_t^{t+\Delta t}\int_{V_c}\delta(r-r_\pi)\,n_\pi(F_s + \dot{m}_p\,V_p)\ \mathrm{dV\ dt} \tag{2-40}$$

where the volume integral is over the cell; the Dirac delta function filters out parcels that are not in the cell. The summation is over all parcels for which two-way coupling is active. The discrete form of Equation 2-40 is:

$$S_V = -\frac{1}{\Delta t}\sum_\pi\sum_{\delta t_p} n_\pi(F_s + \dot{m}_p\,V_p)\,\delta t_p \tag{2-41}$$

where the second summation is over all δt_p for which parcel π is in cell c.

Mass Transfer

The rate of mass transfer to a single particle from the continuous phase is $\dot{m}_p$.

In unsteady simulations, the rate of mass transfer from all particles in a cell c to the continuous phase is

$$S_m = -\frac{1}{\Delta t}\sum_\pi(\int_t^{t+\Delta t}\int_{V_c}\delta(r-r_\pi)n_\pi\,\dot{m}_p\,)\ \mathrm{dV\ dt}) \tag{2-42}$$

where the volume integral is over the cell; the Dirac delta function filters out parcels that are not in the cell. The summation is over all parcels for which two-way coupling is active. The discrete form of Equation 2-42 is

$$S_m = -\frac{1}{\Delta t}\sum_\pi\sum_{\delta t_p} n_\pi\,\dot{m}_p\,\delta t_p \tag{2-43}$$

where the second summation is over all δt_p for which parcel π is in cell c.

Energy Transfer

The rate of total energy transfer to a single particle from the continuous phase is

$$Q_t + F_S . V_P + \frac{1}{2}\dot{m}_p V_p^2 + \dot{m}_p h \qquad 2\text{-}44$$

where Q_t is the surface heat transfer, F_S is the surface force that is defined in Equation 2-25, $\dot{m}_p$ the rate of mass transfer to the particle and h the enthalpy of transferred material.

In unsteady simulations, the rate of energy transfer from all particles in a cell c to the continuous phase is

$$S_m = -\frac{1}{\Delta t}\sum_\pi(\int_t^{t+\Delta t}\int_{V_c} \delta(r - r_\pi)n_\pi \, (Q_t + F_S . V_P + \frac{1}{2}\dot{m}_p V_p^2 + \dot{m}_p h) \text{ dV dt}) \qquad 2\text{-}45$$

where the volume integral is over the cell; the Dirac delta function filters out parcels that are not in the cell. The summation is over all parcels for which two-way coupling is active. The discrete form of Equation 2-45 is

$$S_m = -\sum_\pi \sum_{\delta t_p} \dot{n}_\pi(Q_t + F_S . V_P + \frac{1}{2}\dot{m}_p V_p^2 + \dot{m}_p h) \, \delta t_p \qquad 2\text{-}46$$

where the second summation is over all δt_p for which parcel π is in cell c.

2.7.7. Contact Force

Contact force formulation in DEM is typically a variant of the spring-dashpot model. The spring generates repulsive force pushing particles apart, and the dashpot represents viscous damping and allows simulation of collision types other than perfectly elastic.

The forces at the point of contact are modeled as a pair of spring-dashpot oscillators. A parallel linear spring-dashpot model represents the normal force and, a parallel linear spring-dashpot in series with a slider represents the tangential direction of force with respect to the contact plane normal vector. In both, the spring accounts for the elastic part of the response, and the dashpot accounts for energy dissipation during a collision (Figure 2-17).

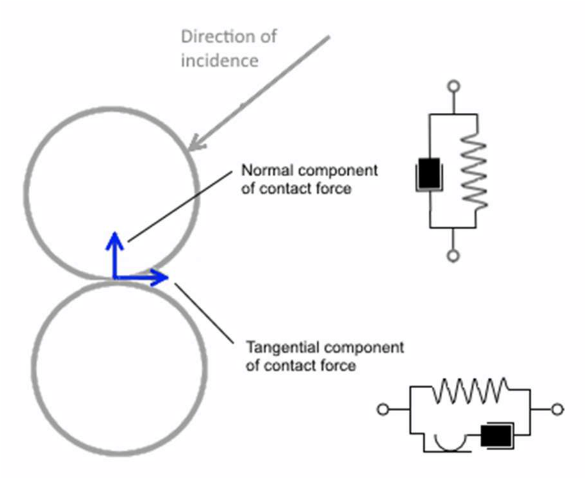

Figure 2-17. Spring-dashpot contact model

Simcenter STAR-CCM+ provides three contact models: Hertz Mindlin, Linear Spring, and Walton Braun. In this research, Hertz Mindlin is used to modeling the contact between the particles.

Hertz-Mindlin Contact Model

The Hertz-Mindlin contact model is a variant of the non-linear spring-dashpot contact model based on the Hertz-Mindlin contact theory (Johnson, 1987 and Di Renzo et al. 2004). The forces between two spheres, A and B, are described by the following set of equations:

$$\boldsymbol{F}_{contact}=F_n\mathrm{n}+F_t\mathrm{t} \qquad 2\text{-}47$$

Where F_n and F_t are the magnitudes of the normal and tangential components, respectively.

The normal direction is defined by the following:

Normal force:

$$F_n = -K_n d_n - N_n dv_n \tag{2-48}$$

Normal spring stiffness:

$$K_n = \frac{4}{3} E_{eq}\sqrt{d_n R_{eq}} \tag{2-49}$$

Normal damping:

$$N_n = \sqrt{(5K_n M_{eq})}\, N_{n\,damp} \tag{2-50}$$

where $N_{n\,damp}$ is the normal damping coefficient as given in Equation 2-54.

The tangential direction is defined by the following:

The tangential force is defined by $-K_t d_t - N_t v_t$ if $K_t d_t < |K_n d_n| C_{fs}$, where C_{fs} is a static friction coefficient. Otherwise:

$$F_t = \frac{|K_n d_n| C_{fs} d_t}{|d_t|} \tag{2-51}$$

Tangential spring stiffness:

$$K_t = 8\, G_{eq}\sqrt{d_t R_{eq}} \tag{2-52}$$

Tangential damping:

$$N_t = \sqrt{(5K_t M_{eq})}\, N_{t\,damp} \tag{2-53}$$

Where $N_{t\,damp}$ is the tangential damping coefficient as given in Equation 2-55.

$$N_{n\,damp} = \frac{-\ln\,(C_{n\,rest})}{\sqrt{\ln\,(C_{n\,rest})^2 + \pi^2}} \tag{2-54}$$

$$N_{t\,damp} = \frac{-\mathrm{l}\ \ (C_{t\,rest})}{\sqrt{\ln\,(C_{t\,rest})^2 + \pi^2}} \tag{2-55}$$

Here, $C_{n\,rest}$ and $C_{t\,rest}$ are the normal and tangential coefficients of restitution, model parameters set by the user. If $C_{n\,rest} = 0$, then $N_{n\,damp} = 1$, and if $C_{t\,rest} = 0$, then $N_{t\,damp} = 1$.

The equivalent radius is defined as:

$$R_{eq} = \frac{1}{\frac{1}{R_A}+\frac{1}{R_B}} \qquad 2\text{-}56$$

The equivalent particle mass is:

$$M_{eq} = \frac{1}{\frac{1}{M_A}+\frac{1}{M_B}} \qquad 2\text{-}57$$

The equivalent Young's modulus is expressed as:

$$E_{eq} = \frac{1}{\frac{1-v_A^2}{E_A}+\frac{1-v_B^2}{E_B}} \qquad 2\text{-}58$$

The equivalent shear modulus is:

$$G_{eq} = \frac{1}{\frac{2(2-v_A)(1+v_A)}{E_A}+\frac{2(2-v_B)(1+v_B)}{E_B}} \qquad 2\text{-}59$$

where:

M_A and M_B are masses of sphere A and sphere B, d_n and d_t are overlaps in the normal and tangential directions at the contact point, R_A and R_B are the radii of the spheres, E_A and E_B are the Young's modulus of the spheres, v_A and v_B are the Poisson's ratios, v_n and v_t are the normal and tangential velocity components of the relative sphere surface velocity at the contact point.

For particle-wall collisions, the formulas stay the same, but the wall radius and mass are assumed to be $R_{wall} = \infty$ and $M_{wall} = \infty$, so the equivalent radius is reduced to $R_{eq} = R_{particle}$ and equivalent mass to $M_{wall} = M_{particle}$.

Di Renzo et al. (2004) proposed several formulations for a detailed treatment of tangential micro-slip and tangential force computation. Simcenter STAR-CCM+ uses Tsuji's formulation, where the tangential force is assumed to be non-linear, but an analytical expression replaces the detailed micro-slip tracking. The resulting code is computationally efficient while still matching experimental data.

Linear Cohesion

Generally, to model the linear cohesion behavior in DEM, two models are used. Johnson-Kendall-Roberts model (JKR) and Derjaguin-Muller-Toporov (DMT) model. Both models consist of two components, a deformation according to the Hertz model and an adhesion component due to the surface energy. The JKR model contact force is defined by the following equation assuming a single asperity in contact with a flat surface in contact:

$$F_{JKR} = \frac{4Ea^3}{3R} - \sqrt{8\pi a^3 \Delta\gamma E} \qquad 2\text{-}60$$

Where a is the contact radius, R is the particle radius, E is a composite elastic modulus of two particles in contact defined as $E = \left(\frac{1-v_1^2}{E_1} + \frac{1-v_2^2}{E_2}\right)^{-1}$, with $E_1\ and\ E_2$ as the Young moduli of particles and $v_1\ and\ v_2$ Poisson's ratio of the particles in contact and $\Delta\gamma$ is the

The corresponding deformation which adhesion force acts on explained by the following equation:

$$\delta_{JKR} = \frac{a^2}{R} - \frac{2}{3}\sqrt{\frac{\pi a \Delta\gamma}{E}} \qquad 2\text{-}61$$

The contact force for the DMT model explained by the following model:

$$F_{DMT} = \frac{4Ea^3}{3R} - 2\pi R\Delta\gamma \qquad 2\text{-}62$$

And the corresponding deformation would be:

$$\delta_{DMT} = \frac{a^2}{R} \qquad 2\text{-}63$$

Where a is the contact radius, R is the particle radius, E is a composite elastic modulus of two particles in contact defined as $E = \left(\frac{1-v_1^2}{E_1} + \frac{1-v_2^2}{E_2}\right)^{-1}$, with E_1 *and* E_2 as the Young moduli of particles and v_1 *and* v_2 Poisson's ratio of the particles in contact.

Rolling Resistance

The following rolling resistance methods apply to DEM particles:

Force Proportional Method, Constant Torque Method, and Displacement Damping Method.

The force-proportional method is considered in this research. In Hertz-Mindlin contact models, together with the Rolling Resistance model, the Rolling Resistance model applies a rolling friction coefficient to the contact models.

Force Proportional Method only supplies a coefficient of rolling resistance, μ_r, also called the coefficient of rolling friction. It can take on any positive real value. The default value is 0.001.

$$F_r = \mu_r F_n \qquad 2\text{-}64$$

where:

F_r is the rolling resistance force.

μ_r is the coefficient of rolling friction, also called the coefficient of rolling resistance.

F_n is the magnitude of the contact force.

3. NUMERICAL SIMULATION OF EROSION TESTS

In this chapter, the CFD simulation of erosion tests has been investigated. In the first section, shear stress magnitudes in conventional erosion tests, including the Erosion Function Apparatus (EFA), Hole Erosion Test (HET), Jet Erosion Test (JET) and, Borehole Erosion Test have been compared with the results from the moody chart. This section is the result of Dr. H. C. Chen simulations on the mentioned tests with non-erodible boundaries as a part of the NCHRP research report 915. In the second section, the research has been extended to create the eroded shape of the soil boundary due to erosion. This task has been done by mesh morphing technique in STAR-CCM+ software and utilizing an erosion function resulting from EFA.

3.1. Comparison of Shear Stress Magnitudes in Some Erosion Tests by Numerical Simulation on Non-Erodible Soils

This section of the dissertation focuses on shear stress magnitudes in conventional erosion tests, including the Erosion Function Apparatus (EFA), Hole Erosion Test (HET), Jet Erosion Test (JET) and, Borehole Erosion Test. For the CFD simulation in non-erodible soils, the CHEN4D code is used to simulate these erosion tests. The finite analytic technique has been implemented to solve Reynolds-Averaged Navier-Stokes (RANS) equations in the general curvilinear coordinate system. The results indicate that the shear stress values increase with increasing velocity and soil roughness in all tests. For the EFA test with 1 m/s velocity, the shear stress can reach 8 Pa on the upstream side of the sample. At a velocity of 6m/s, the shear stress on the upstream side of the sample can reach 70 Pa. In the HET, for a typical velocity of 2.5 m/s, the shear stress value starts at 30 Pa at the inlet of the hole and decreases to a constant value of 25 Pa right after the inlet. For the JET with a nozzle velocity of 4 m/s, the shear stress can reach 85 Pa and decreases away from the center down to 2 Pa. In the BET, with an average velocity of 4.52 m/s and with a 2.5 cm gap between the tip of the rod and the bottom of the borehole, the shear stress at the bottom of the hole can reach 120 Pa and decreases to near zero at the edge of the hole. For the borehole sides, the shear stress starts around 110 Pa at the bottom of the rods and finally reaches 7 Pa after two borehole diameter of flow length up from the bottom of the rods.

3.1.1. Introduction

The Erosion Function Apparatus (EFA) test, Hole Erosion Test (HET), Jet Erosion Test (JET), and Borehole Erosion Test (BET) seem to be among the most common erosion tests. Each test method has its drawbacks and advantages and aims to quantify the erodibility of soil by different test procedures. In all these tests, shear stress plays an essential role in quantifying the action of the flow on the soil boundary. These erosion tests aim to give the erosion function, which is the relationship between the erosion rate versus mean velocity or shear stress. By using Computational Fluid Dynamics (CFD), a better understanding of the magnitude and distribution of the shear stresses on the soil could be achieved.

In this section, the CFD method is applied through the use of the CHEN4D code. CHEN4D (Computational Hydraulic ENgineering in 4 Dimensions) was developed by H.C. Chen [Chen & Chen (1984)]. CHEN4D uses the finite-analytic method, which incorporates the analytic solution of the differential equation in its linearized form and the respective small subdomain. The Reynolds-Averaged Navier-Stokes equations are solved in the general curvilinear coordinate system. The accuracy of the CHEN4D code has been proved in different publications [Chen & Chen (1982), Chen & Chen (1984)].

The Erosion Function Apparatus (EFA) test was designed at Texas A&M University by Briaud in 1991 to measure the erodibility of soils and rocks [Briaud et al., 1999, 2001a, 2001b]. The EFA can accommodate the samples directly from ASTM standard thin wall steel tubes. The output of the test is the erosion rate vs. velocity curve and the erosion rate vs. shear stress curve. The critical velocity and critical shear stress are the velocity and the shear stress at which the soil starts to erode. The erosion function is the erosion rate versus shear stress (or velocity) curve and can be utilized to estimate the final amount of erosion for a hydraulic structure. The soil erodibility category can also be specified from the prepared chart (Briaud et al., 2019). The shear stress is obtained from the following equation.

$$\tau = \frac{1}{8} f \rho v^2 \qquad 3\text{-}1$$

Where τ refers to the shear stress (pa), ρ is the density of water, v is the flow velocity (m/s), and f is the friction factor obtained from the Moody chart (Figure 3-1).

The Hole Erosion Test (HET), can be attributed to Robin Fell in Australia [Wan and Fell, 2002; Wahl et al., 2009; Benahmed and Bonelli, 2012]. The soil specimen for this test can be prepared in a compaction mold; a 6 mm hole is drilled at the center of the sample, and water is circulated through that hole. The erosion rate in kg/s/m2 is quantified as the rate of mass removal per unit area, which is connected to the rate of change in the diameter of the hole.

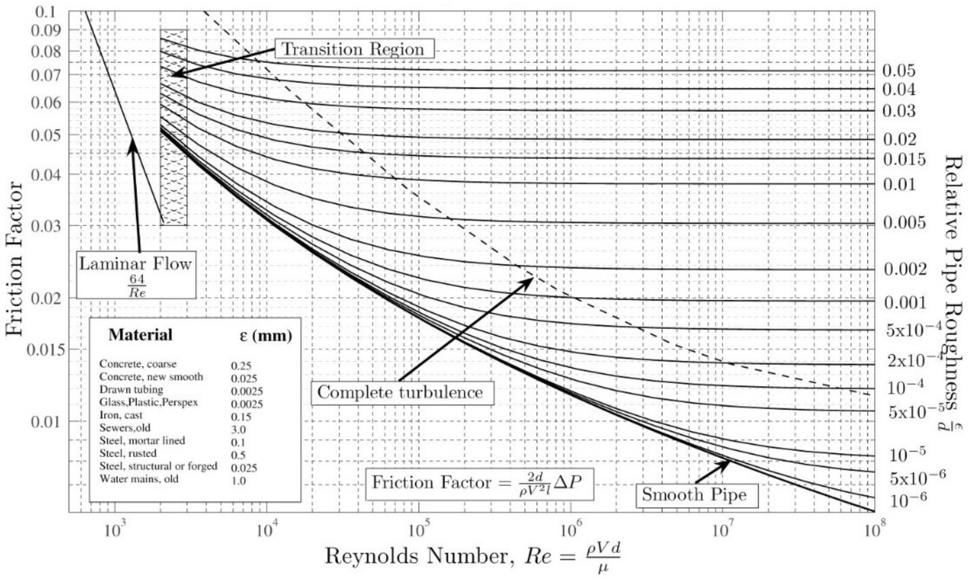

Figure 3-1. Moody diagram (reprinted from Moody, 1944)

The Jet Erosion Test can be attributed to Hansen at the USDA-ARS [Hanson, 1990]. The JET test was later modified by Hanson and Hunt (2007), and the CFD simulations presented here are based on the modified JET. As in the HET case, the soil specimen can be prepared in a compaction mold, and the surface of the sample is exposed to a jet with a diameter of 6.4 mm and placed 33 mm above the sample surface. The depth of the crater created on the sample surface can be plotted against the time of jetting, and the slope of that line is called the erosion rate. Hanson and Cook defined the critical shear stress for the JET test as the stress at which the depth of the crater does not progress anymore [Hanson and Cook, 2004].

The Borehole Erosion Test was developed at Texas A&M University by Briaud [Briaud et al. 2016]. The erosion test is conducted in the field inside a borehole. A borehole is drilled and can be 100 mm in diameter and 10 m in depth. With a mechanical borehole caliper, the profile of the initial diameter of the hole can be measured. Water is circulated downward through the center of the rods and then upward in the annulus between the rods and the borehole wall; after 10 to 15 min of water flow, the flow is stopped, and the diameter of the hole is measured again to record the increase in radius due to the water flow; this process can be repeated several times. The erosion rate is calculated as the increase in the borehole radius at a specific depth divided by the flow time; a soil erodibility profile is obtained with depth.

3.1.2. EFA Simulation

Figure 3-2-a to c presents the results of shear stress distribution on the bottom surface and the top surface of the EFA for fluid velocities of 1 m/s, 3 m/s, and 6 m/s, respectively. The EFA channel has a width of 10.16 cm and a height of 5.08 cm. The soil sample was modeled as a circle with a diameter of 7.62 cm. In the simulations, the roughness is ε/D which ε is the roughness height, and D depends on the erosion test; for example, in the case of EFA, D is the hydraulic diameter. The roughness of the soil surface is 5% for all the cases, and the channel height is used as the characteristic length instead of the channel hydraulic diameter (Dh = 6.77 cm). The top and bottom surface of the channel are assumed to be smooth except where the soil surface exists. The circle shows the soil sample.

For the smooth surface, with a velocity of 1 m/s, the shear stress on the sample is constant and equal to 3 Pa. The shear stress increases from 3 Pa to 20 Pa, when the velocity increases from 1 m/s to 3 m/s. Finally, by increasing the velocity from 3 m/s to 6 m/s, the shear stress rises to 70 Pa.

For the case with 5% of soil roughness (ε/D), with a velocity of 1 m/s, the shear stress on the sample surface is higher at the upstream side of the sample (8 Pa) than at the downstream face of the sample (6 Pa). By increasing the velocity from 1 m/s to 3 m/s, the upstream shear stress rises to 70 Pa, and the downstream shear stress increases to 55 Pa. By increasing the velocity from 3 m/s to 6 m/s, the shear stress increases to 180 Pa at the upstream side and 150 Pa at the downstream side. The difference in shear stress between the upstream and the downstream of the sample increases when the velocity increases (2 Pa, 15 Pa, and 30 Pa), but the percentage increase decrease with the velocity (25%, 21%, and 17%).

In the EFA test, the shear stress can be calculated by using the Moody chart. By considering ρ_w=1000 kg/m3, D = 0.0677 m, and $\mu_w = 1.027 \times 10^{-3}$ kg/m/s the Reynolds number can be calculated as 49464, 148393 and 296786 for a velocity of 1 m/s, 3 m/s and 6 m/s respectively. For a roughness (ε/D) equal to 5%, these Reynolds numbers correspond to friction factors equal to 0.072, for all cases. Shear stress values can be calculated from Equation 1 as 9, 81, and 324 Pa, respectively. Compared to the CFD shear stress values, the Moody chart gives higher shear stress values. The Moody chart values are 29%, 30%, and 96% higher than the average CFD values for 1, 3, and 6 m/s, respectively.

For the smooth case, the friction factors are equal to 0.021, 0.017, and 0.015, respectively. Shear stress values can be calculated from Equation 1 as 2.6, 19, and 67 Pa. For the smooth case, the Moody chart's values are about the same and comparable to the values of the CFD simulations

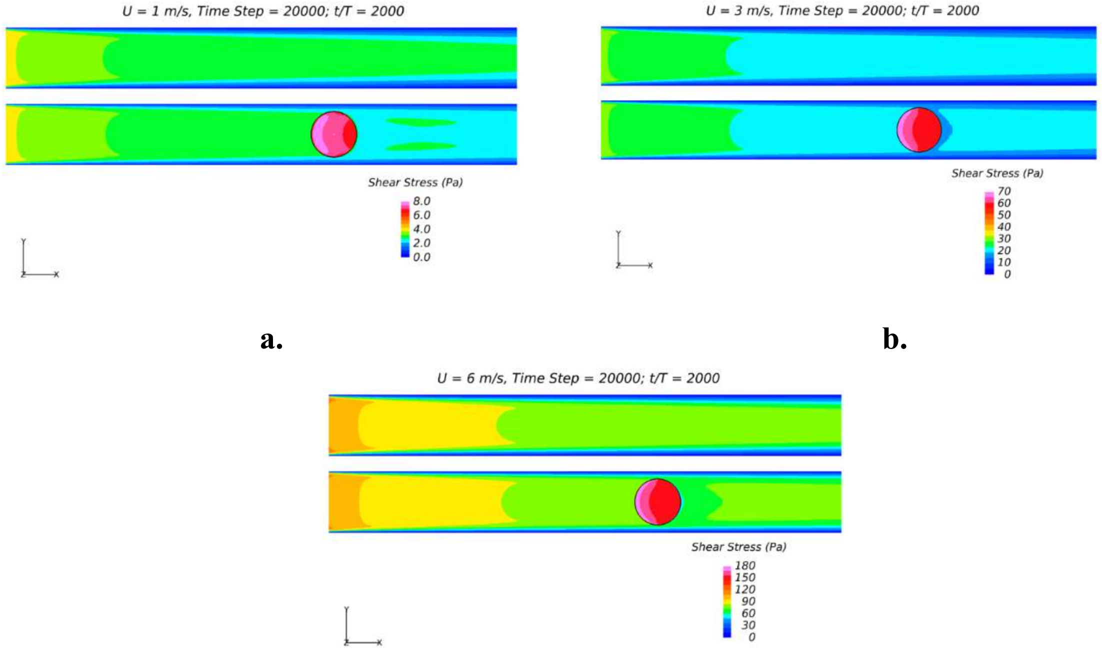

a. **b.**

c.

Figure 3-2. Shear stress distribution on the top surface (smooth), the bottom surface (smooth), and soil sample (with 5% roughness (ε/D)) for the U = 1 m/s, 3m/s and 6 m/s

3.1.3. HET Simulation

CFD simulations were also performed for the HET with a smooth and 5% surface roughness (ε/D). The model consists of two flow chambers with the soil specimen between the two chambers; the soil sample has a diameter of 10.16 cm and a length of 11.64 cm. The hole diameter in the soil sample was 6 mm. The soil was assumed to be nonerodible. Figure 3-3 shows the flow velocity distribution for an inlet velocity of 1 m/s at the entry of the 6 mm hole. The blue and the colored regions represent the fluid, while the two white regions represent the soil sample. The simulations were performed with a velocity of 2.5 m/s for the smooth case and for the case with 5% of soil roughness (ε/D). Figure 3-4 shows the time-averaged shear stress distribution along the hole in the sample from the inlet to the outlet. The shear stress right at the inlet is high as the fluid flow is constricted into the 6 mm diameter hole. The existence of negative shear stresses is due to a small recirculation region where the flow impinges into the hole.

After a small flow distance in the hole, the shear stress reaches the values of 15 Pa and 30 Pa for the smooth case and the 5% roughness (ε/D) case, respectively. The shear stress for the smooth case stays constant at 15 Pa while it decreases to 25 Pa at the hole exit for the rough case.

These results can be compared to the results of the shear stress calculated from the Moody chart. Considering the flow velocity of 2.5 m/s, a hole diameter of 6 mm, the fluid density of 1000 kg/m3, and dynamic viscosity of 1.027×10^{-3} kg/m/s, the Reynolds number can be calculated as 14606. For the smooth case with Re = 14606, the value of the friction factor is 0.028. The equation gives a value of 22 Pa for the shear stress, which is 46% higher than the simulation. For the case with 5% roughness (ε/D) and Re = 14606, the friction factor is 0.073, and the Moody Chart gives 57 Pa for the shear stress, which is about 107% higher than the values of 25 to 30 Pa (mean: 27.5) for the simulation.

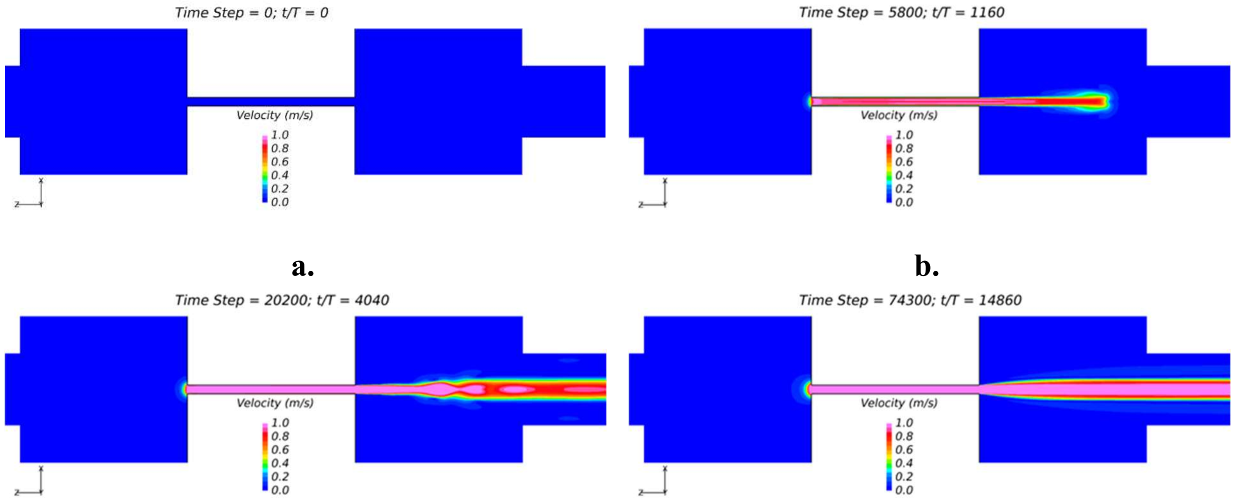

a. b.

c. d.

Figure 3-3. Velocity evolution for the smooth case

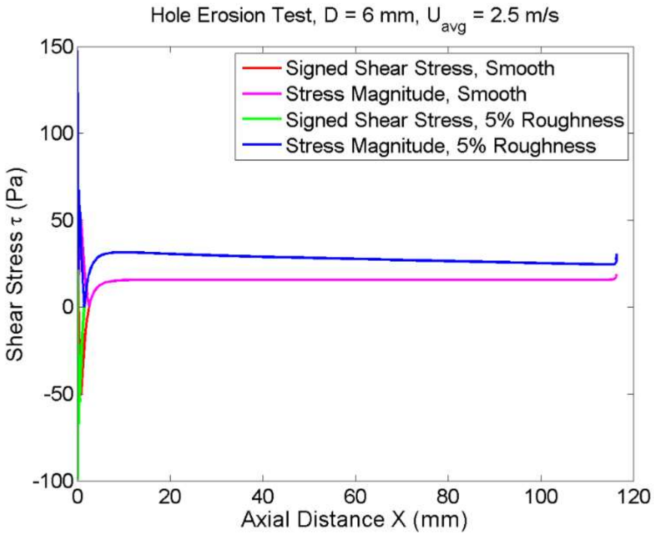

Figure 3-4. Shear stress distribution through the drilled hole along the length of the sample for both smooth and 5% of roughness (ε/D), considering an average velocity of 2.5 m/s in the hole

3.1.4. JET Simulation

In this section, the CFD simulation results of the JET test are presented for an average nozzle velocity equal to 4 m/s. The CFD model consists of a fluid chamber with a height of 30.48 cm and a diameter of 30.48 cm; it is in blue in Fig. 4. The soil specimen in the center has a 10.16 cm diameter and a height of 11.64 cm; it is in white in Fig. 4. The top middle pipe diameter is 5 cm; this pipe extends down to the nozzle, which has a diameter of 6.4 mm. Similarly to the other two simulations, the soil is assumed to be nonerodable, and the output is the distribution of velocity and shear stress on the sample surface. Simulations were done for the smooth case, possibly more representative of a clay surface and a case with a 5% roughness (ε/D) possibly more representative of a sand or gravel surface. Figure 3-5 shows the distribution and evolution of the velocity from the tip of the nozzle to the surface of the sample.

The results of shear stress for the two cases are presented in Figure 3-6. In both cases, the shear stress at the point of impingement is zero. The maximum shear stress for the smooth case occurs from 2 to 6 mm from the center of the sample with a value of 51 Pa (the first maximum near the impingement point because of recirculation of fluid is disregarded), and the shear stress approaches 2.5 Pa at the edge of the sample. For the case with 5% roughness (ε/D), the shear stress starts with a magnitude of zero at the center and reaches a magnitude of 85 Pa at a distance equal to 9 mm from the center. This value decreases to a magnitude of 3 Pa at the edge of the sample.

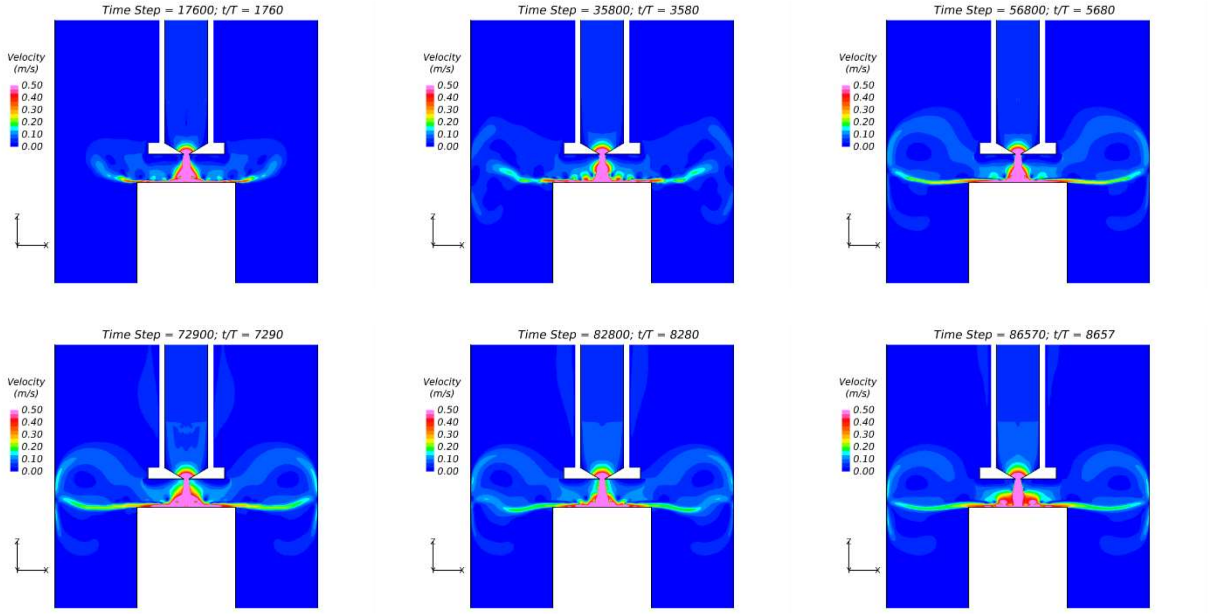

Figure 3-5. Velocity results of submerged jet evolution in different time steps for the rough surface (starting from top left to bottom right)

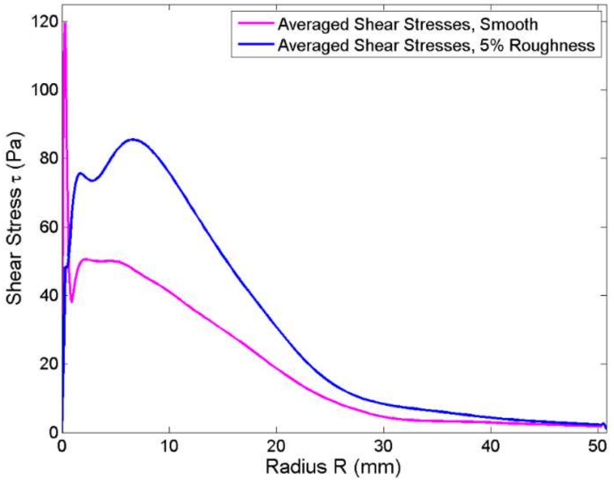

Figure 3-6. Time-averaged shear stress distribution for smooth and with 5% roughness (ε/D) surfaces.

3.1.5. BET Simulation

A similar CFD simulation was done for the BET with the CHEN4D code. The borehole diameter was set to be 100 mm, and the rods inside diameter 40 mm with a wall thickness of 15 mm. The boundaries of the borehole were assumed to be nonerodible, and the distribution of velocity and shear stress were obtained for two different flow rates (1.45×10^{-3} m^3/s and 5.68×10^{-3} m^3/s). Figure 3-7 shows the distribution of velocity with a 25 mm gap between the orifice (bottom of the rods) and the bottom surface of the borehole. The blue region and the colored regions show the fluid (water), and the two thick white regions show the walls of the rods while the surrounding environment starting from the outer boundary represents the soil.

Figure 3-8 presents the shear stress distribution on the bottom surface of the borehole for a flow rate of 5.68×10^{-3} m3/s and three different gaps between the tip of the rod and the bottom of the borehole. As can be seen, by increasing the distance between the rod and the bottom of the borehole, the peak shear stress decreases, and the maximum shear stress moves closer to the center of the borehole. For the 150 mm gap, the shear stress starts from 12.5 Pa at the impingement point and reaches a peak of 76.5 Pa at 21.5 mm from the center. For the 75 mm gap, the shear stress is zero at the center and reaches a maximum of 96 Pa at a 25 mm distance from the borehole center. For the 25 mm gap, the shear stress at the impingement point is 2.7 Pa and increases to a peak of 119 Pa at a 27 mm distance from the center.

Figure 3-9 presents the shear stress distribution for the side of the borehole for the three gap cases and with 5.68×10^{-3} m3/s flow rate. The same trends are observed with different peaks at different distances from the bottom of the borehole. The shear stress reaches a maximum value at different distances from the bottom of the borehole. For the 150 mm gap, the maximum shear stress happens 24 mm above the bottom with a magnitude of 87 Pa. For the 75 mm gap, the shear stress reaches its peak value 25 mm above the bottom with the value of 155 Pa, and for the 25 mm gap, the shear stress starts reaches a maximum of 111 Pa 17 mm above the bottom of the borehole. The peak for the 75 mm gap is larger than the other two cases. In all cases and for the 5.68×10^{-3} m3/s flow value, the shear stresses approach a steady-state value of 7 Pa at a distance of 0.3 m above the bottom of the rods.

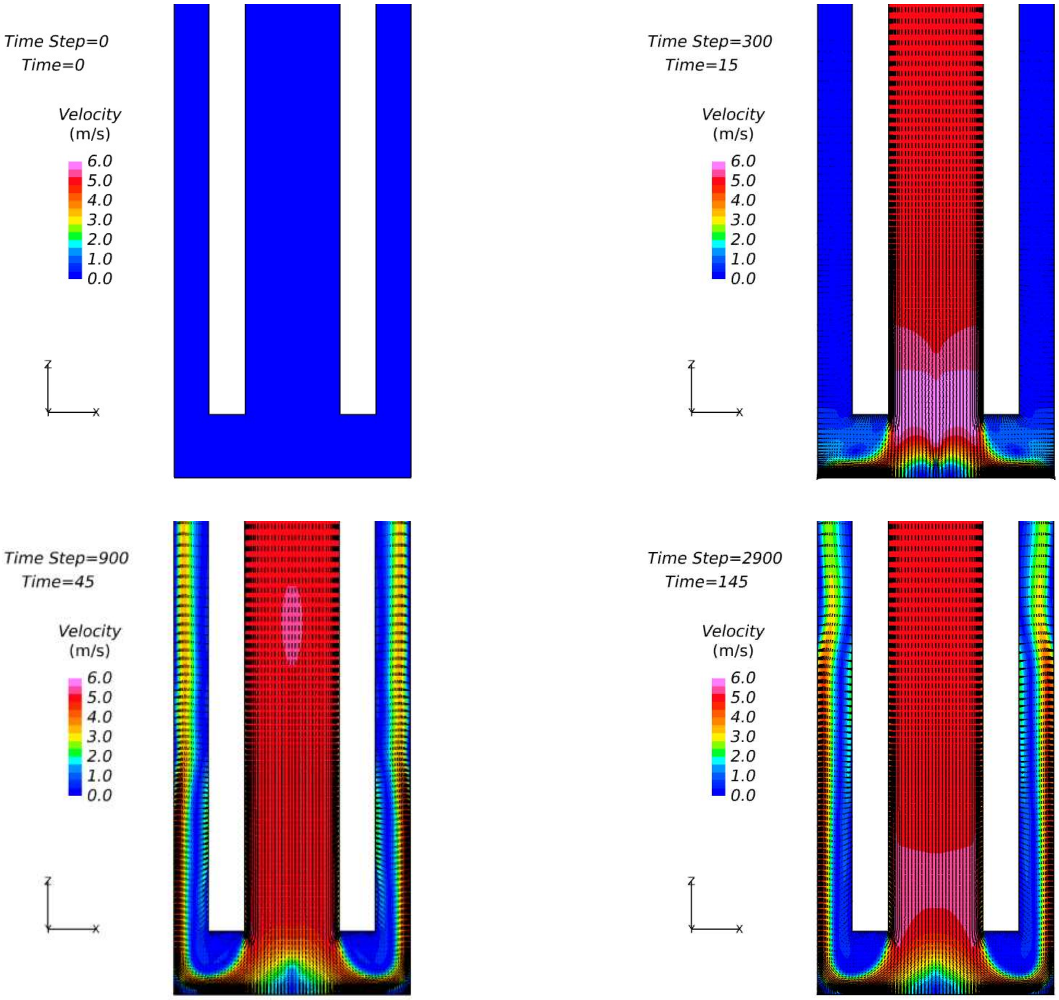

Figure 3-7. Evolution of flow velocity in BET test at different steps considering the rough surface and 2.54 cm gap between the tip of the rod and the bottom of the borehole

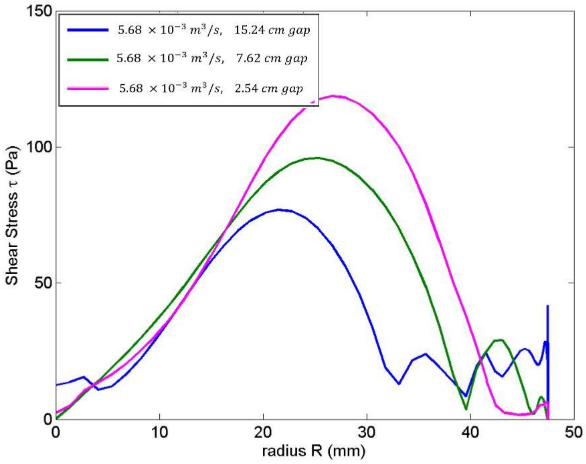

Figure 3-8. Shear stress distributions at the bottom of the borehole for three different gaps between the tip of the rod and the bottom of the borehole, when flow rate is $\mathbf{5.68 \times 10^{-3}\, m^3/s}$

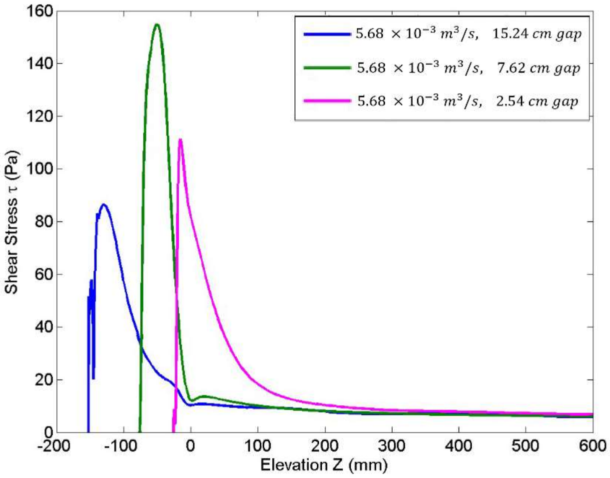

Figure 3-9. Shear stress distributions at the sidewall of the borehole for three different gaps between the tip of the rod and the bottom of the borehole, when flow rate is $\mathbf{5.68 \times 10^{-3}\, m^3/s}$

3.1.6. Conclusions

Four common erosion tests were numerically simulated. The soil was non-erodible; therefore, the simulations correspond to the initial stage of the tests. Table 3-1 summarizes the comparison of shear stress ranges for the erosion tests. Overall, the shear stresses are in the range of 0 to 200 Pa. The shear stress is reasonably constant in the EFA, in the HET, and the BET along the borehole wall starting at 0.3 m above the bottom of the rods. The shear stresses vary dramatically along the soil surface in the JET and the BET at the bottom of the borehole. For those two tests, the shear stress is near zero at the center of the soil surface reaches a peak at some small distance from the center, and decreases beyond that. This significant variation makes the theoretical interpretation of those two tests difficult, yet they are valuable as index erosion tests. The shear stresses evaluated based on the Moody chart give consistently higher values than those obtained by numerical simulations.

Table 3-1. Comparison of shear stress ranges in EFA, HET, JET, and BET resulting from CFD simulation

Test			U(ave) (m/s)	Surface condition	CHEN4D		Moody Chart
					Min. Shear Stress (Pa)	Max. Shear Stress (Pa)	
EFA			1	Smooth	3	3	2.6
				Rough	6	8	9
			3	Smooth	20	20	19
				Rough	55	70	81
			6	Smooth	70	70	67
				Rough	150	180	324
HET			2.5	Smooth	15	30	22
				Rough	25	30	57
JET			3	Smooth	2.5	51	-
				Rough	3	85	-
BET	SIDE	Gap (mm)	4.5	Rough	12.5	76.5	-
		150					
		75			0.5	96	-
		25			2.7	119	-
	BOTTOM	150			0	87	-
		75			0	155	-
		25			0	111	-

3.2. Comparison of laboratory test results and numerical simulation equipped with mech morphing technique

As discussed in chapter 2, the numerical simulation of erosion can be performed with CFD empowered by dynamic mesh techniques. The term "Mesh Morphing," which means a change of mesh based on a difference in the boundary, is common in the CFD literature and can be used instead of the dynamic mesh technique to prevent misunderstanding of the method. This technique has been utilized in CD-adapco's Star Computational Continuum Mechanics (Star CCM+) to model the JET, HET, and BET tests.

CFD-Mesh Morphing has been utilized to model the JET, HET, and BET and compare the laboratory test results. The laboratory tests have been done on the same sample. To use the same sample in the numerical simulation, an EFA test has been done on the sample, and the resulted erosion function (The relationship between the erosion rate and the shear stress (or velocity)) used as an input to apply as a constative model of erosion on the soil boundaries.

Figure 3-10, Schematically shows how this method is implementing in STAR-CCM+. After constructing the required geometry with the proper mesh shape and size, the fluid domain is ready. In this case, the soil boundaries are erodible and should move based on the magnitude of shear stress. As explained in Chapter 2, this movement should be perpendicular to the interface to prevent the wrong results and mesh corruption. The relationship between the shear stress and the erosion rate, called erosion function, should be written as a field function. At the first step, after reaching the equilibrium, the correct magnitude of shear stress defines the magnitude of erosion rate. Then nodes on the soil boundary move based on erosion rate magnitude. Since the geometry of the model change for the next step, the new magnitude of shear stress should be recalculated, and the new value of erosion rate should be calculated. This process can be repeated to the end of the numerical simulation.

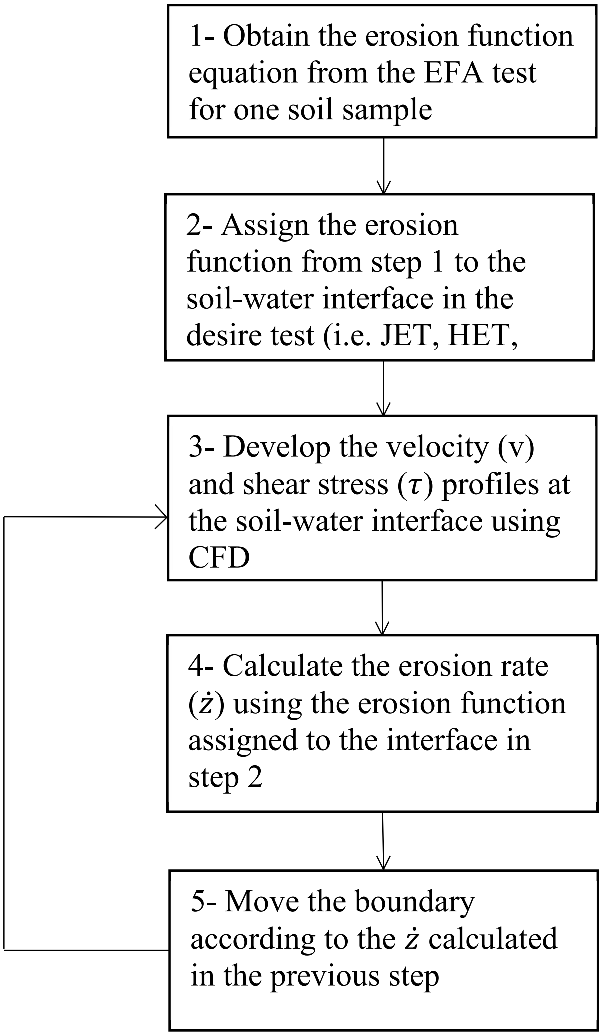

Figure 3-10. The process of CFD-Mesh Morphing framework to simulate results of the HET, the JET, and the BET and compare with the laboratory tests

The CFD-Mesh Morphing framework based on the procedure summarized in Figure 3-10 is performed for the three common erosion tests. The erosion function resulted from the EFA test has been utilized on the soil sample surface in the JET to perform the simulation and observe the progress of erosion during the test. This method has also been utilized for on the hole surfaces of HET to track the erosion progress during the test. For the borehole erosion test, the erosion function acts on the bottom and the borehole side. In the following, the details of numerical simulation considered for the JET, HET, and the BET in the software (Star CCM+) is presented.

3.2.1. Geometry, Mesh, Soil-Water Interface, and wall treatment

For all the three erosion tests (JET, HET, and BET), two-dimensional axisymmetric models were created. The mesh used in these models is quadrilateral. The detailed information on the mesh used for each erosion test is presented in Table 3-2. Also, Figure 3-11, Figure 3-12, and Figure 3-13 show the axisymmetric models created for the JET, the HET, and the BET, respectively. It should be noted that the dimensions used for the models are in accordance with the dimension of these testing devices in the Erosion Laboratory at Texas A&M University.

Table 3-2. Detailed information on the created mesh for each erosion test

Erosion Test	Type of Mesh	Number of Cells	Number of Faces	Number of Vertices
JET	Quadrilateral	8809	17501	9115
HET	Quadrilateral	22918	45151	23673
BET	Quadrilateral	31765	62244	33054

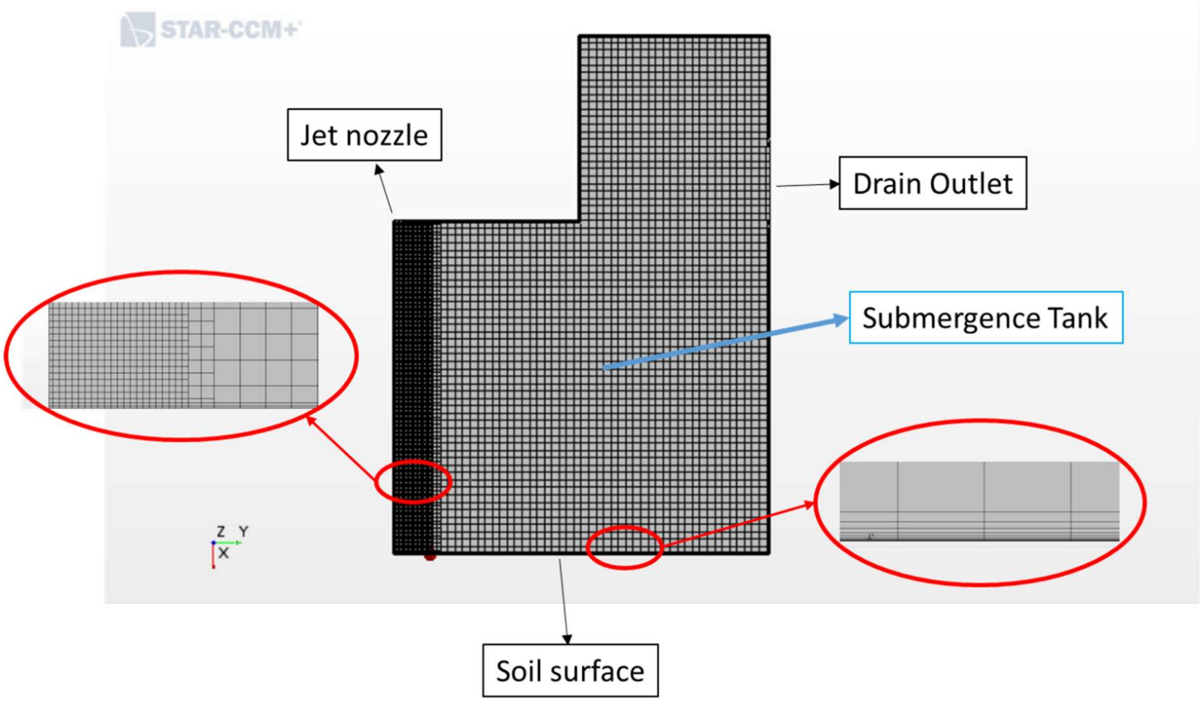

Figure 3-11. The axisymmetric model for the JET

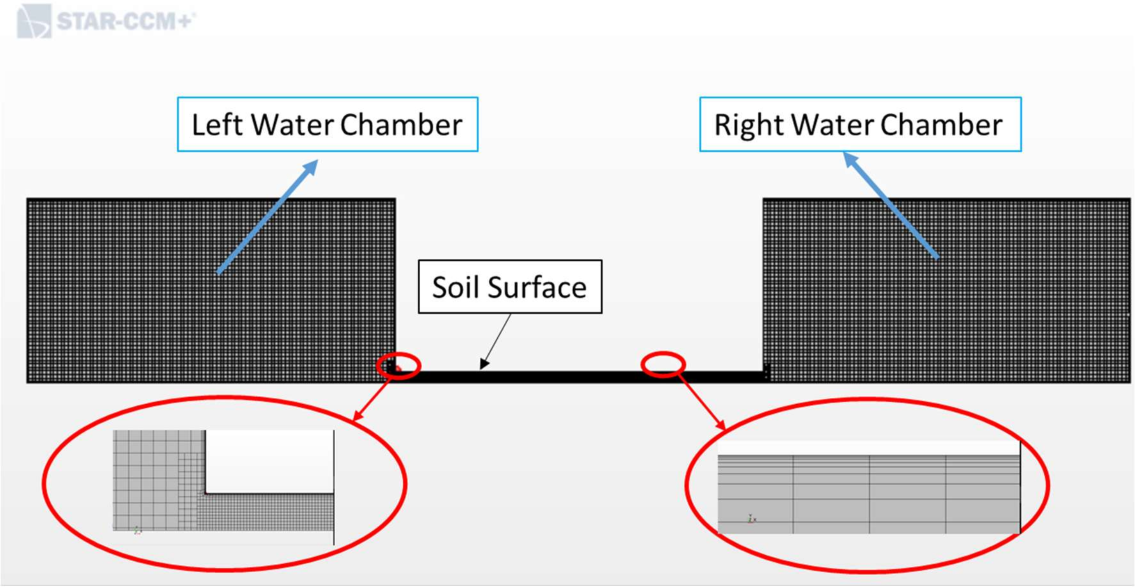

Figure 3-12. The axisymmetric model for the HET

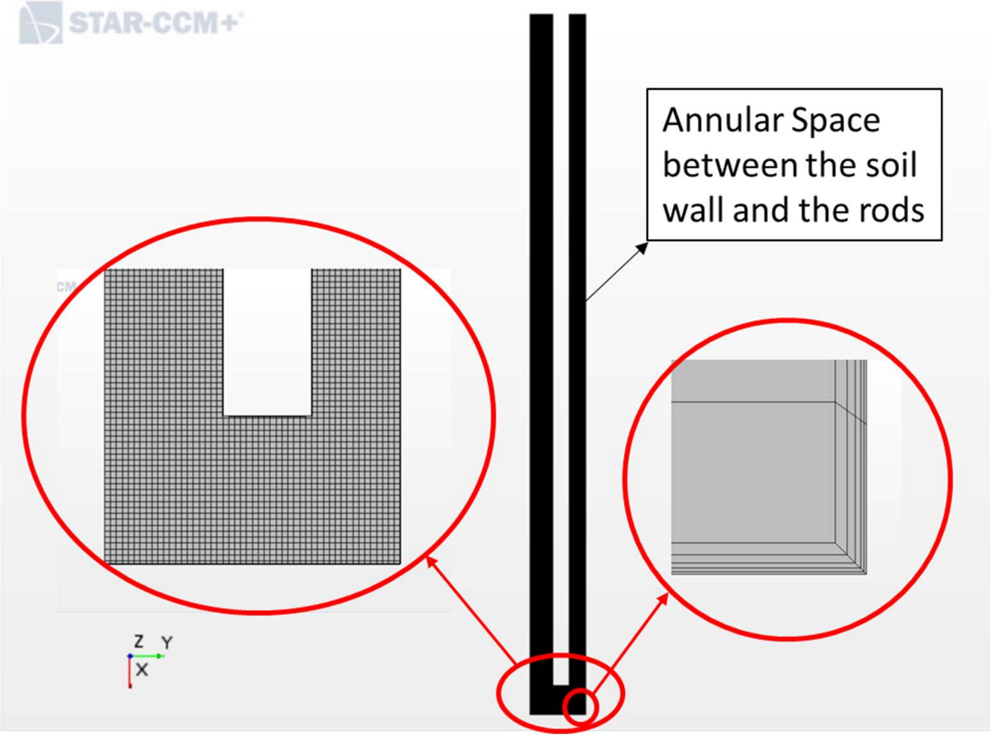

Figure 3-13. The axisymmetric model for the BET

One of the essential laws in fluid dynamics is the law of the "wall". This law states that in turbulent flow, the mean velocity at a specific point and the logarithm of the distance between that point and the fluid region boundary (or the "wall") are proportional. The effect of this law is very significant, especially for those parts of the flow that are closer than 20% of the flow height to the wall. The general formulation of the law of the wall (Eq. 58) solves for the average velocity parallel to the wall in turbulent flows (high Reynold's numbers).

$$u^{+} = \frac{1}{\kappa} \ln y^{+} + C^{+} \tag{3-2}$$

Where u^+ is a dimensionless velocity parameter and equals u (average velocity parallel to the wall) divided by the u_T (friction velocity); y^+ refers to the dimension-less wall coordinate and is obtained using Eq. 59. The parameters κ and C^+ are two constants that are equal to 0.41 and 0.5, respectively, for a smooth wall, according to Schlichting and Gersten (2000).

$$y^+ = \frac{y \times u_T}{\nu} \qquad 3\text{-}3$$

Where ν is the local kinematic viscosity of the fluid; u_T is mentioned earlier is the friction velocity at the closest fluid region boundary, and y is the distance of the point to the nearest wall. y^+ is one of the essential parameters in defining the law of the wall and conducting the fluid mechanics numerical simulations. For this study, the value of y^+ is designed to be less than 1 to achieve minimal cell distance between the wall and the point of flow ($y < 10^{-6}\ m$).

3.2.2. Model Development

Numerical simulations were performed for the JET, HET, and BET, as explained in the previous sections (Figure 3-10). The results of comparisons between the EFA Test with other erosion tests are presented separately in the following sections.

3.2.2.1. EFA's Erosion Function on the JET

As discussed in Section 6.2.1, the erosion rate can be written as a function of shear stress. To compare the EFA test results with the JET results, a procedure, as described in Figure 3-10, was followed for four different samples (2 sand, one silt, and one clay). The names of these samples are Sand #1 & Sand #2 (sand samples), FHWA Sample 2 (silt sample), and B-1 (4'-6') Beaumont (clay sample).

As presented in Figure 3-10, the first step was to obtain the relationship between the erosion rate ($\dot{z}$) and the shear stress for each sample in the EFA. This relationship, also called the erosion function, is obtained after testing each of the four samples in the EFA, and then assigned to the soil-water interface in the JET simulation, which is defined in the form of a moving boundary. Once the shear stress is developed on the soil-water interface, the erosion rate at the boundary is calculated using the assigned erosion function, and the boundary moves accordingly. This process repeats itself, and the boundary keeps moving until the developed shear stress on the interface becomes equal or less than the critical shear stress for the tested soil.

The Roughness Height (RH) is defined in Star CCM+ To distinguish between smooth clay and rough sand surface. RH is the roughness height of the soil particles (equivalent to Ɛ defined in the Moody diagram shown in Figure 3-1). In this study, for each simulation whether the sample is clay, silt, or sand, four RH values were considered: 1) RH = 0 mm or smooth surface, 2) RH = 0.5 mm, 3) RH = 1 mm, and 4) RH = 3 mm.

Figure 3-14 shows the erosion function obtained from the EFA test on the Sand #1 sample. Figure 3-15 shows the results of the numerical simulations for the sample Sand #1 when the EF is used at the soil-water interface in the JET model. It is shown that the observed JET results (black circles) are slightly over-estimated through Star CCM+ when their erosion function obtained from the EFA is assigned to the soil-water interface. This over-estimation is less pronounced when the roughness height is close to 0 mm (smooth surface). The actual average roughness height ($D_{50}/2$) for SE-1 is about 0.14 mm. Therefore, smooth surface results would be a relatively reasonable assumption.

Figure 3-16 shows an example of the numerical simulations in four different time steps for the Sand #1 sample. In this example, the soil-water interface is defined as a moving boundary. Also, the velocity profile of the flow is shown for each time step. Velocity for this example ranges between 0 to 3.2 m/s. The highest amount of velocity is, of course, at the jet nozzle, and when the water reaches the soil surface, its velocity becomes less. This process continues until the shear stress-induced on the boundary (soil-water interface) becomes less than the measured critical shear stress from the EFA's erosion function.

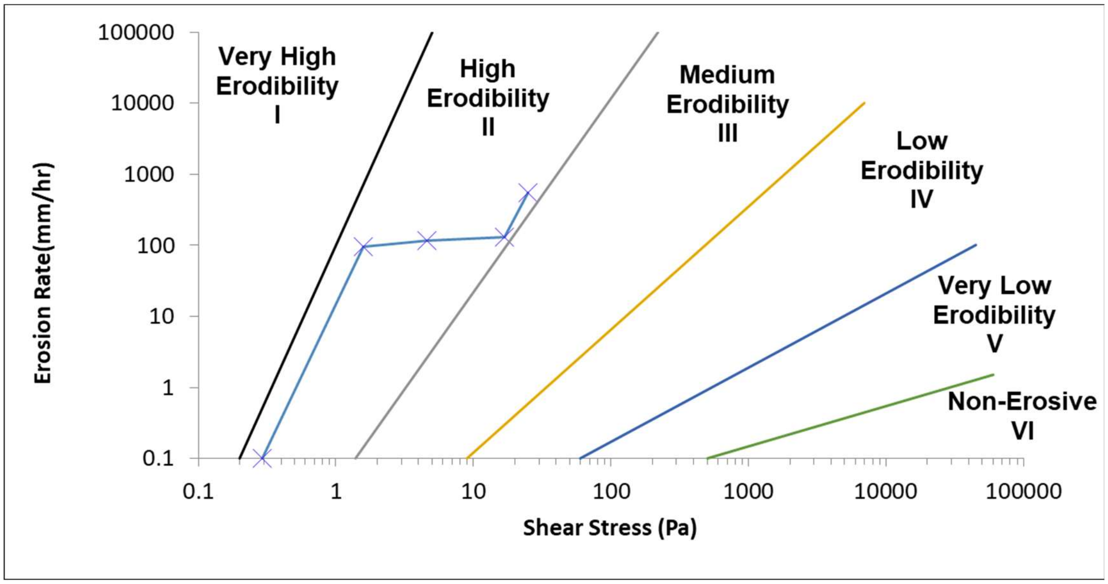

Figure 3-14. Erosion function (erosion rate vs. shear stress) of sand #1 used in the CFD

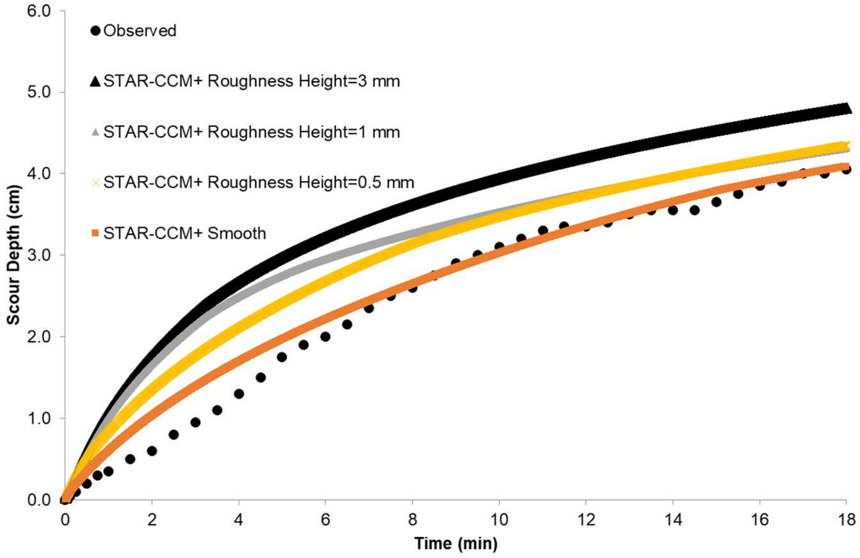

Figure 3-15. The scour depth versus time for observed JET & simulated JET for Sand #1

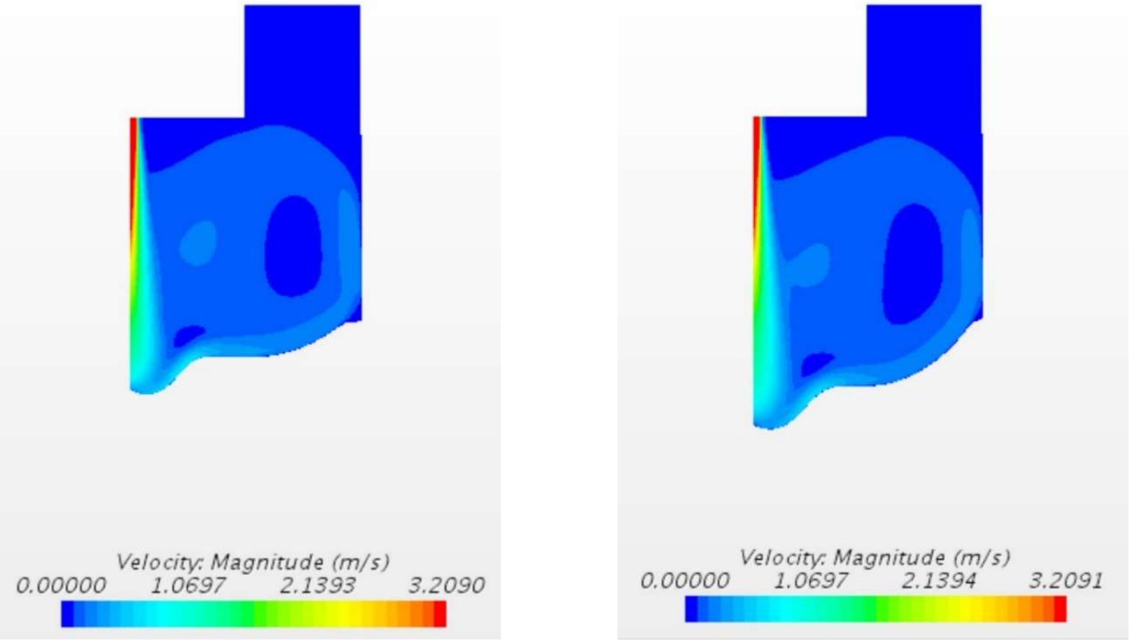

Time = 4.5 min

Time = 9 min

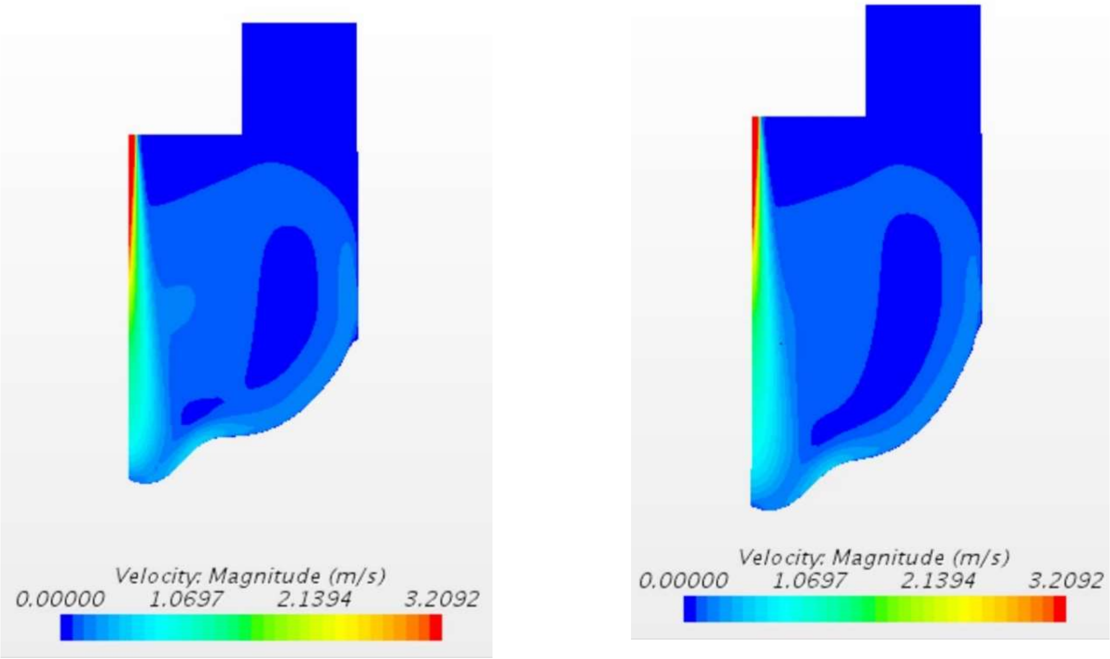

Time = 13.5 min

Time = 18 min

Figure 3-16. An example of the moving boundary for Sand #1 with RH = 0.5 mm.

Figure 3-17 shows the erosion function obtained from the EFA test on the Sand #2 sample. Figure 3-18 shows the results of the numerical simulations for the sample Sand #2 when the erosion function is used at the soil-water interface in the JET model. It is shown that the observed JET results (black circles) are slightly under-estimated through Star CCM+ when their erosion function obtained from the EFA is assigned to the soil-water interface. This under-estimation is more pronounced when the roughness height is close to 0 mm (smooth surface). The actual average roughness height ($D_{50}/2$) for SE-2 is about 0.122 mm. At the end of the 40 minutes JET, the observed scour hole was 2.2 cm, while the Star CCM+ simulations (using the EFA erosion function assigned to the soil-water interface) resulted in an almost 1.4 cm scour hole in the smooth surface case. Figure 3-18 also shows that in higher roughness heights (near 3 mm), the numerical simulations results tend to be closer to the observation for the sample SE-2.

Figure 3-19 shows the erosion function obtained from the EFA test on the B-1 (4'-6’) sample. Figure 3-20 shows the results of the numerical simulations for the sample B-1 (4'-6’) when the erosion function is used at the soil-water interface in the JET model. It is shown that the observed JET results (black circles) are slightly over-estimated through Star CCM+ when their erosion function obtained from the EFA is assigned to the soil-water interface. This over-estimation is more pronounced when the roughness height is higher. The actual average roughness height ($D_{50}/2$) for B-1 (4'-6’) is about 0.0024 mm. At the end of the 40 minutes JET, the observed scour hole was 0.62 cm, while the Star CCM+ simulations (using the EFA erosion function assigned to the soil-water interface) resulted in an almost 1.0 cm scour hole in the smooth surface case.

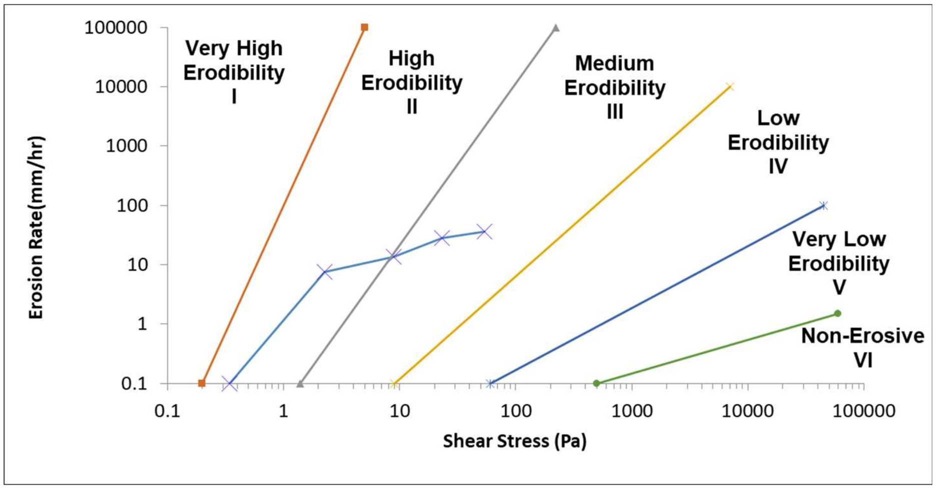

Figure 3-17. Erosion function (erosion rate vs. shear stress) of sand #2 used in the CFD

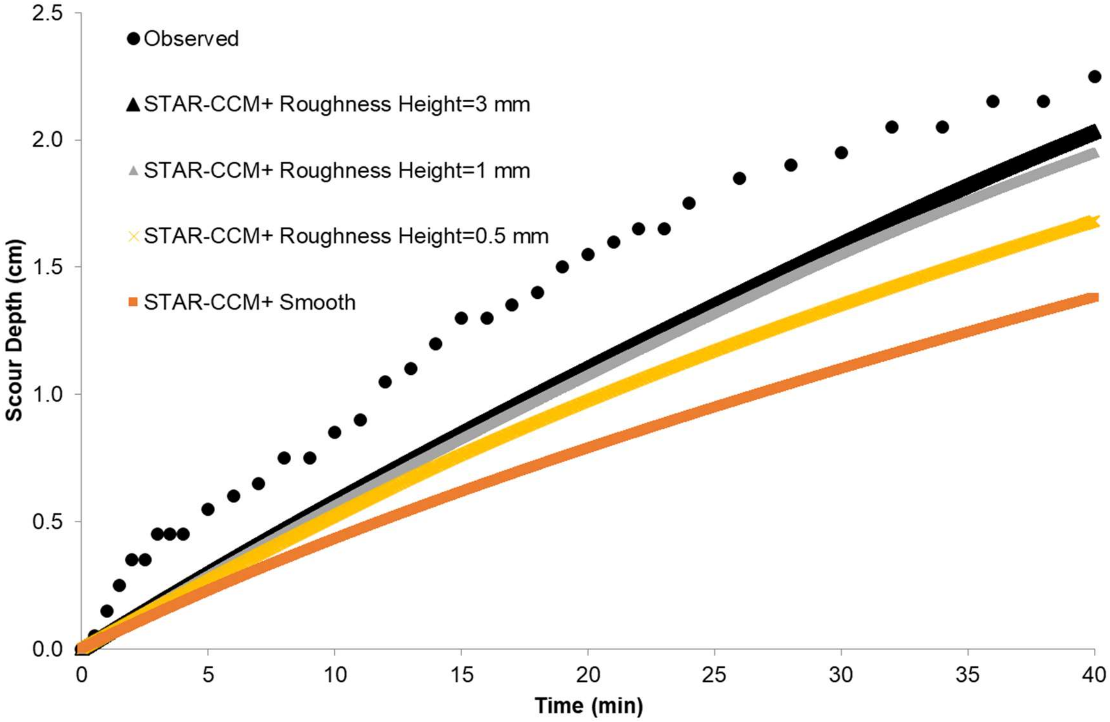

Figure 3-18. The scour depth versus time for observed JET & simulated JET for Sand #2

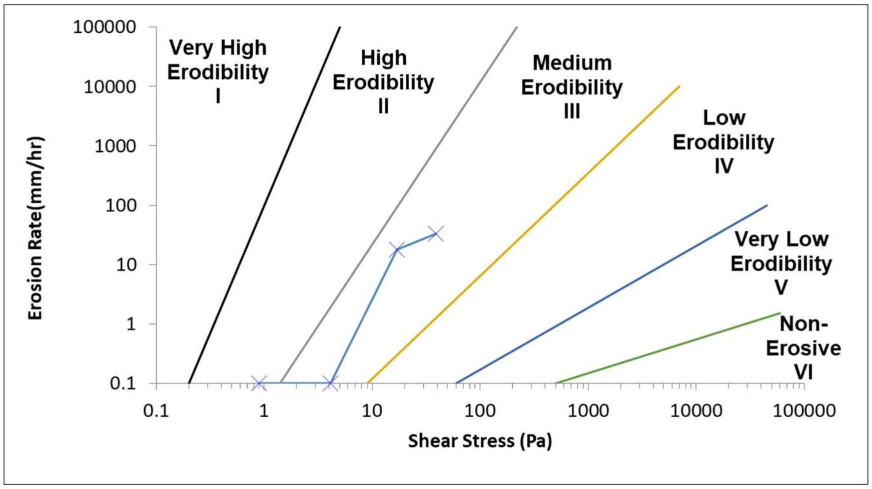

Figure 3-19. Erosion function of B-1 (4'-6') sample used in the CFD

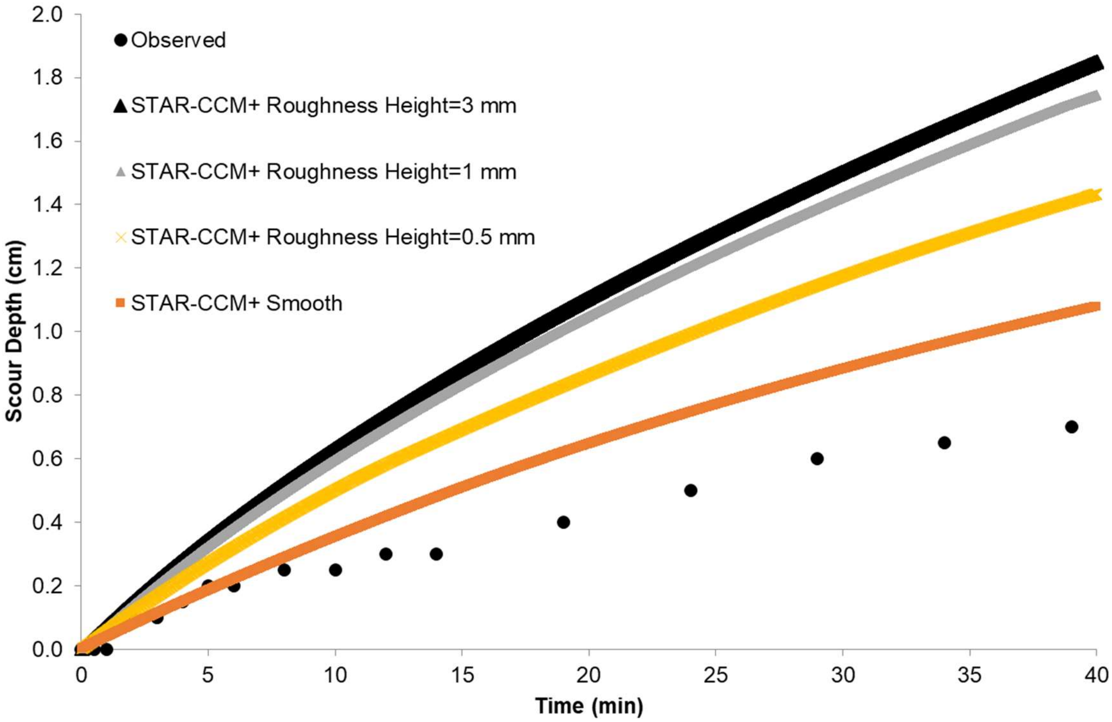

Figure 3-20. The scour depth versus time for observed JET & simulated JET for B-1 (4'-6') sample

Figure 3-21 shows the erosion function obtained from the EFA test on sample 2. Figure 3-22 shows the results of the numerical simulations for FHWA Sample 2 when the erosion function obtained from the EFA test on the same sample is used at the soil-water interface in the JET model. It is shown that the observed JET results (black circles) are slightly under-estimated through Star CCM+ when their erosion function obtained from the EFA is assigned to the soil-water interface. This under-estimation is less observed when the roughness height is higher. The actual average roughness height ($D_{50}/2$) for FHWA Sample 2 is about 0.0031 mm. At the end of the 40 minutes JET, the observed scour hole was 1.6 cm, while the Star CCM+ simulations (using the EFA erosion function assigned to the soil-water interface) resulted in an almost 0.8 cm scour hole in the case of smooth surface.

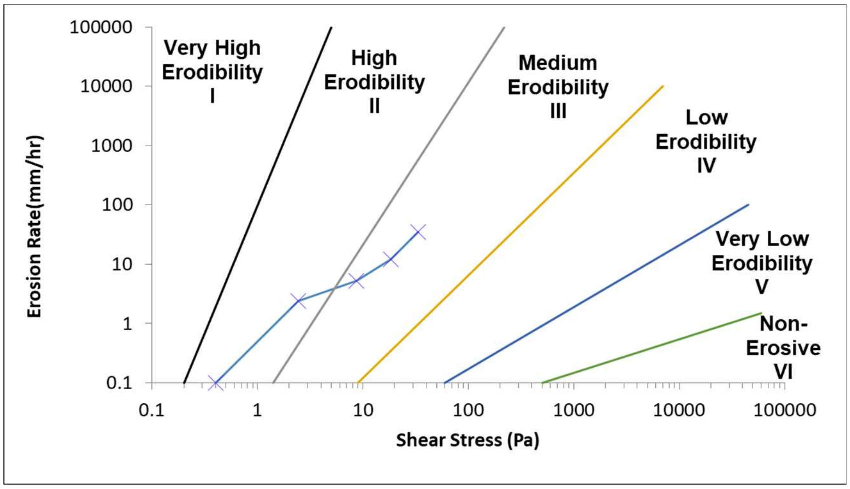

Figure 3-21. Erosion function (erosion rate vs. shear stress) of FHWA Sample 2 used in the CFD

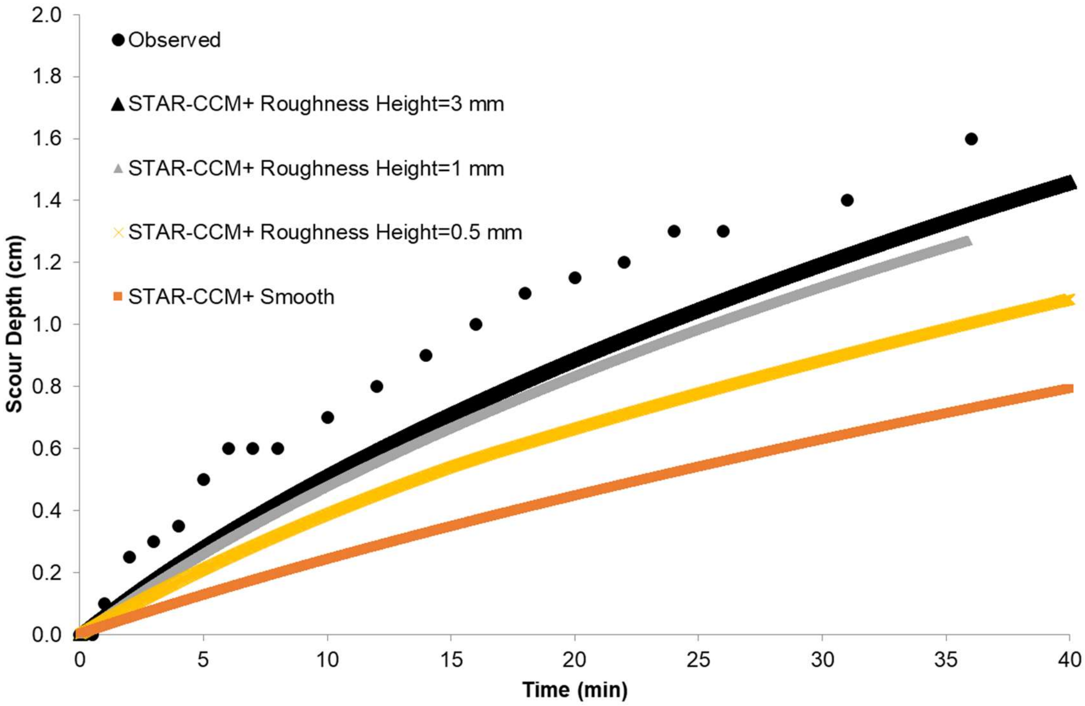

Figure 3-22. The scour depth versus time for observed JET & simulated JET for FHWA Sample 2

3.2.2.2. EFA's Erosion Function on the HET

As outlined in Figure 3-10, a similar approach was taken to compare the results of the EFA with the HET on the same soil samples. The erosion process for two different samples (1 silt and one clayey sand) was simulated using Star CCM+ after assigning the EFA erosion function to the soil-water interface in the HET model. The names of these samples are SH-1 (sand samples) and Teton Sample (silt sample). The results of the numerical simulations were compared with the observations of the hole diameter enlargement during the HET for the same samples. Similar to the case of EFA-JET comparison, four different roughness heights (RH) were considered: smooth, 0.5 mm, 1 mm, and 3 mm for each simulation.

Figure 3-23 shows the erosion function obtained from the EFA test on the sample SH-1. Figure 3-24 shows the results of the numerical simulations for SH-1 when the erosion function is used at the soil-water interface in the HET model. It is shown that the observed average hole diameter evolution during the HET would lie between the results of the Star CCM+ numerical simulations for the cases of smooth to 0.5 mm RH surface. The actual average roughness height ($D_{50}/2$) for SH-1 is about 0.1 mm. At the end of the 1500 seconds (25 minutes) HET, the average diameter of the initial hole has become around 13 mm. The Star CCM+ simulations (using the EFA erosion function assigned to the soil-water interface) also resulted in almost an average 13 mm hole diameter in the case of 0.5 mm roughness height. It is worth mentioning that at the beginning of the test, where the longitudinal hole wall is smoother, the observed evolution of hole diameter tends to be more matching with the results of numerical simulations for the case of a smooth surface.

Figure 3-25 shows an example of the numerical simulations in three different time steps for SH-1. In this example, the soil-water interface is defined as a moving boundary. Also, the velocity profile of the flow is shown for each time step. Velocity for this example ranges between 0 to 3.75 m/s.

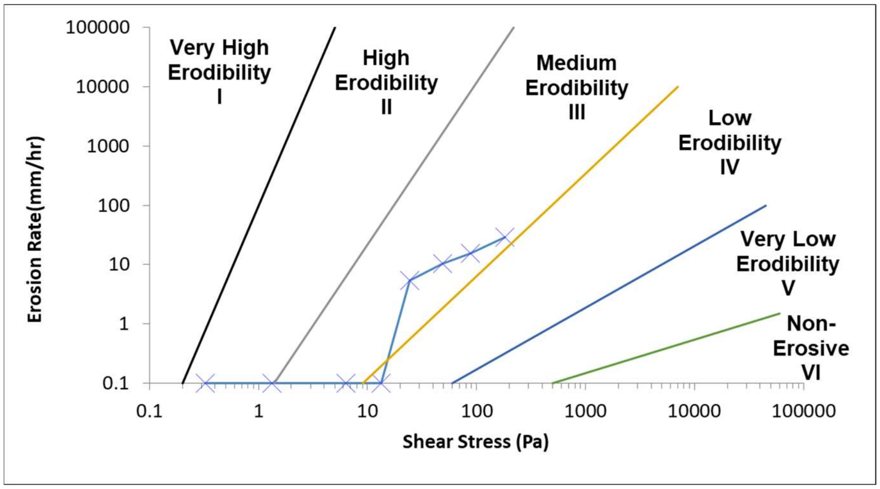

Figure 3-23. Erosion function (erosion rate vs. shear stress) of SH-1 used in the CFD

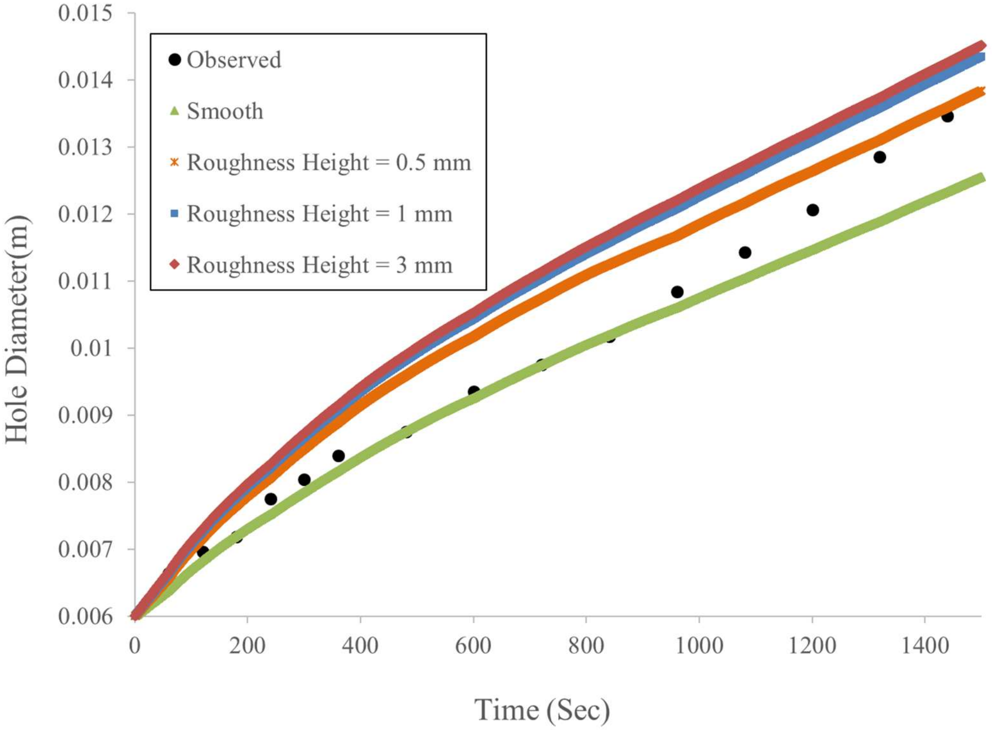

Figure 3-24. The average hole diameter versus time for observed HET & simulated HET for SH-1

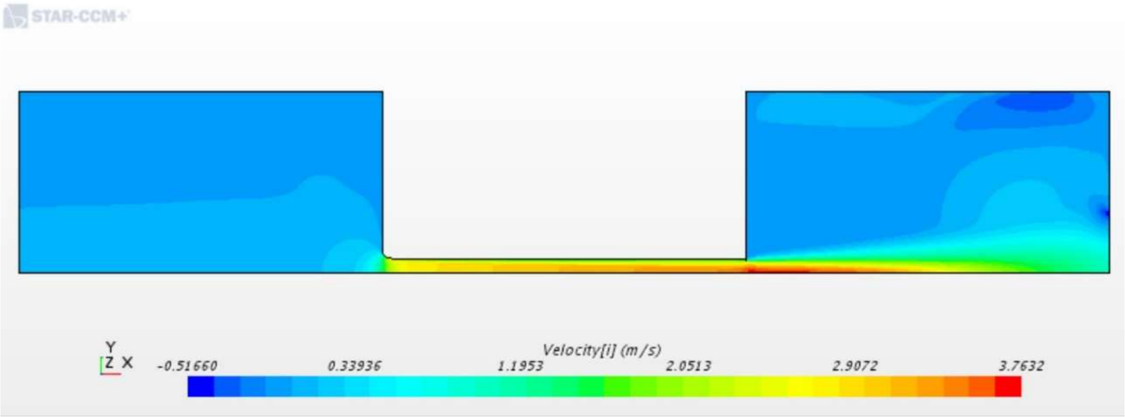

Time = 350 sec

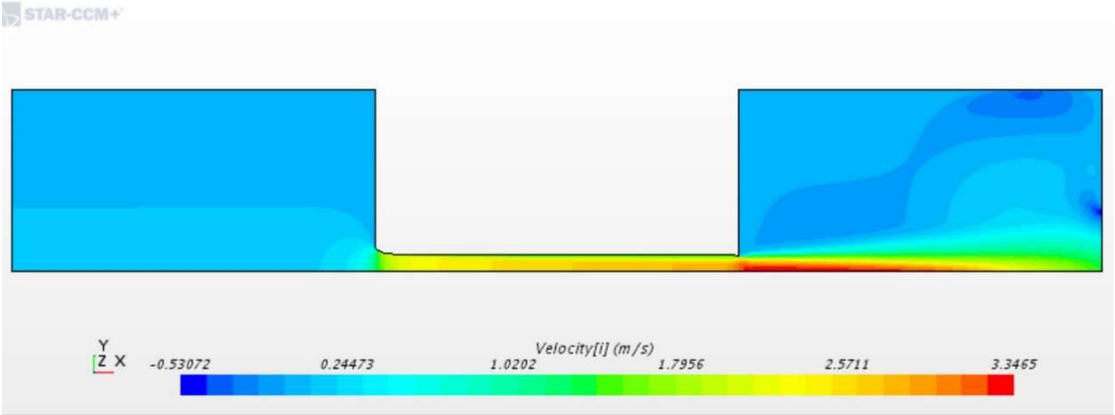

Time = 700 sec

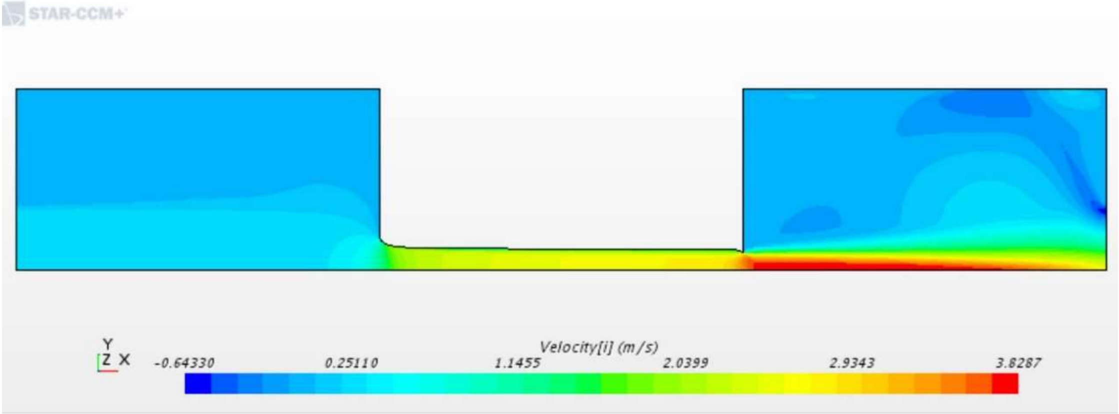

Time = 1400 sec

Figure 3-25. An example of the moving boundary for SH-1 with RH = 0.5 mm

3.2.2.3. EFA's Erosion Function on the BET

As outlined in Figure 3-10, a similar approach was taken to compare the EFA results with the BET on the same soil samples. The erosion process for one clay sample (CBH3) was simulated using Star CCM+ after assigning the EFA erosion function to the soil-water interface in the BET model. The results of the numerical simulations were compared with the observations of the borehole diameter enlargement at depth 8 to 10 ft during the BET for the same samples. Three different roughness heights (RH) were considered: smooth, 0.5 mm, 1 mm for each simulation.

Figure 3-26 shows the erosion function obtained from the EFA test on the sample CBH3. Figure 3-27 shows the results of the numerical simulations for CBH3 when the erosion function is used at the soil-water interface. It was observed that change in the RH did not make a noticeable difference in the diameter enlargement profile. Therefore, only one line represents the scour profile in the three cases. Also, it must be noted that in the numerical simulations, the initial borehole profile had to be considered as a straight vertical line (dashed line in Figure 3-27). In contrast, in reality, the borehole profile was very irregular in comparison. The difference between the initial borehole profiles in the numerical simulations and the actual BET field measurement resulted in different scour profiles after 20 minutes of the test; however, both results confirmed two frequent observations: 1) The maximum scour happens close to the bottom of the borehole (z = 9.8 ft), and 2) the maximum diameter enlargement is close to 2 cm.

Figure 3-28 shows an example of the numerical simulations in three different time steps for SH-1. In this example, the soil-water interface is defined as a moving boundary. Also, the velocity profile of the flow is shown for each time step. Velocity for this example ranges between 0 to 3.75 m/s.

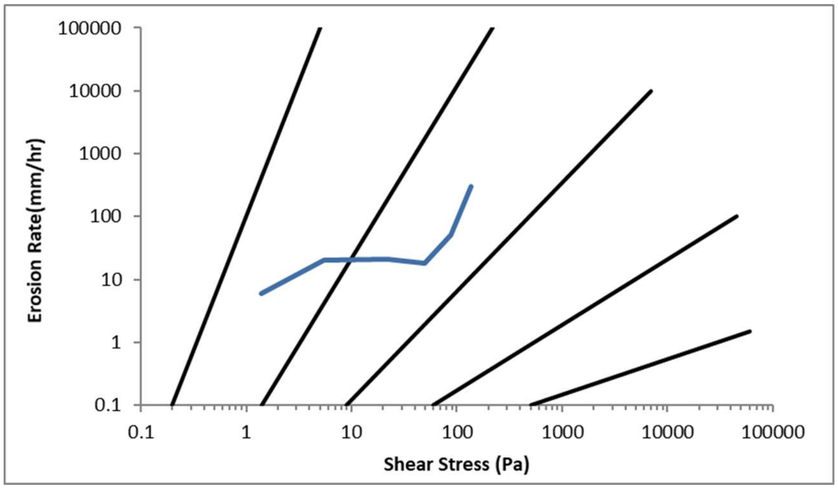

Figure 3-26. Erosion Function used as input for numerical simulation of BET

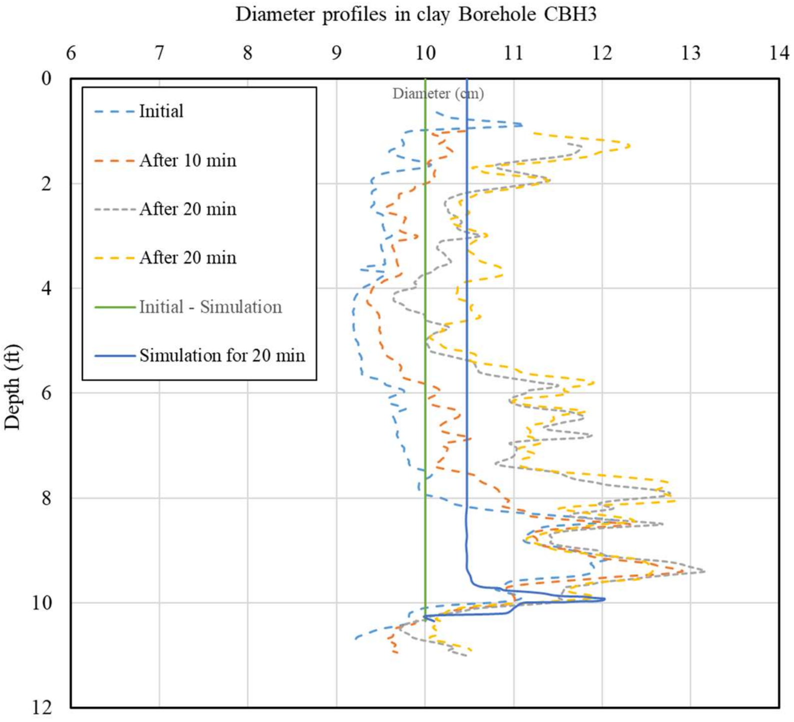

Figure 3-27. Results of the BET numerical simulation after 20 minutes using the EFA's erosion function

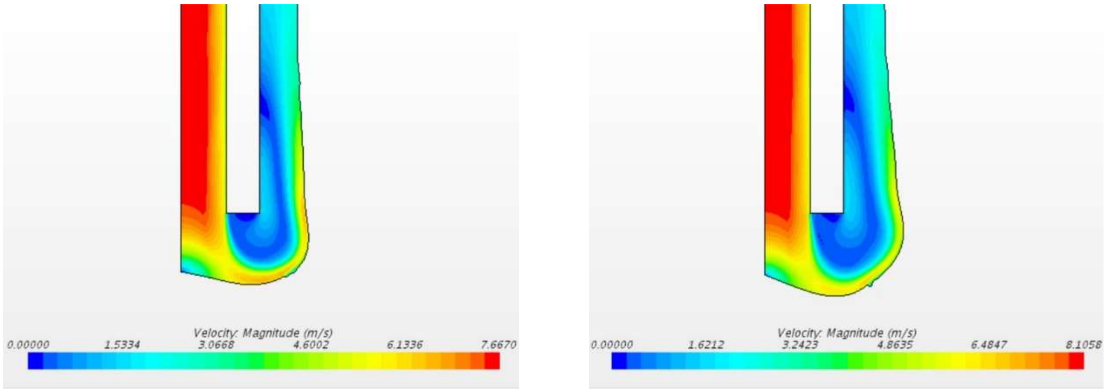

Time = 5 min Time = 10 min

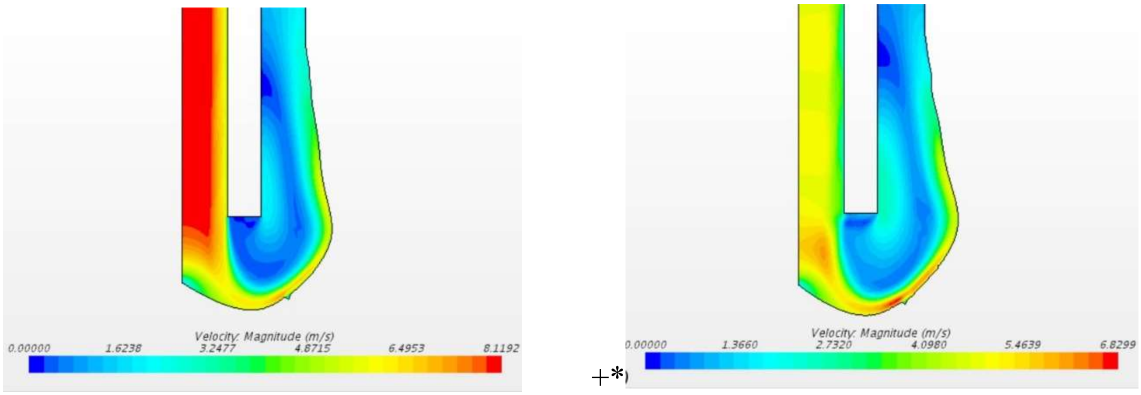

Time = 15 min Time = 20 min

Figure 3-28 An example of the moving boundary for the Riverside Sample with RH = 0.5 mm

3.3. Evolution of Shear Stress in JET, HET, and BET

The evolution of shear stress during the test defines the behavior and progress of erosion in the tests mentioned above. A CFD simulation considering mesh morphing technique has been done on JET, HET, and BET, to compare the evolution of shear stress with increasing erosion. For the erosion function, the same erosion function for a medium erodible soil has been considered as an input to the CFD simulation (Figure 3-29). All tests have been simulated for 10 minutes, and for each minute, the distribution of shear stress on the soil boundary has been graphed.

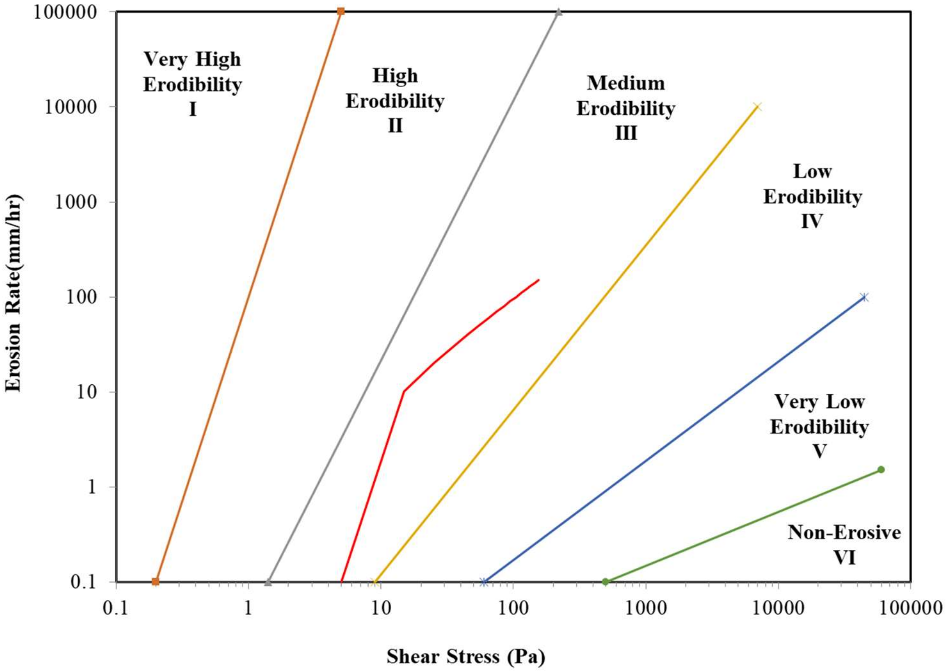

Figure 3-29 The erosion function used on the soil boundary to study the evolution of shear stress during the test

3.3.1. *Evolution of Shear Stress in JET*

Figure 3-30 illustrates the evolution of shear stress along with the radius of the sample for a nozzle velocity of 3.2 m/s, soil roughness height of 3 mm, and the above-mentioned erosion function. By increasing the time, the maximum shear stress decreases, and for the last minutes of the test, the peak of the curve is no longer available. The peak shear stress value of 56.1 Pa at the first minute of the tests decreases to the amount of 35.6 at the last minute of the test. It means that the maximum erosion rate for this test (with the current erosion function) decreases from 51.1

mm/hour to 30.6 mm/hour. For all times, similar to the non-erodible boundary case, shear stress starts with a value, then reaches its peak and finally decreases to near zero at the edge of the sample.

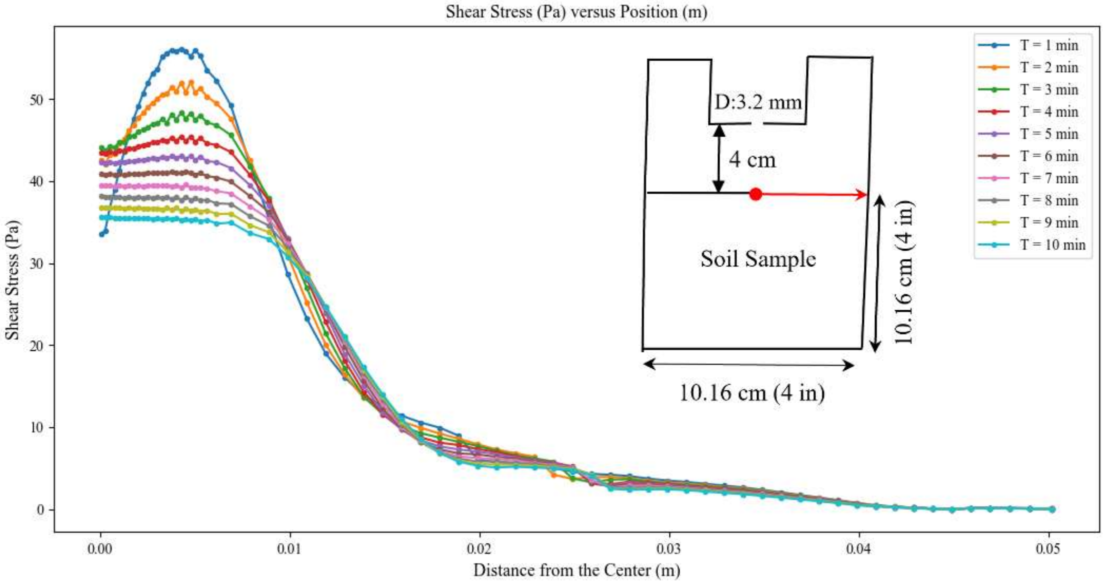

Figure 3-30 The erosion function used on the soil boundary to study the evolution of shear stress during the test

3.3.2. Evolution of Shear Stress in HET

Figure 3-31 indicates the evolution of shear stress during the test for the hole erosion test for an inlet velocity of 2.5 m/s, a roughness height of 3 mm, and the above-mentioned erosion function. The distribution od the shear stress along with soil interface is similar to the nob-erodible case. Shear stress starts from a maximum value, then decreases to a constant value. For the first minute of the test, the maximum amount is 71.1 Pa, and the constant value is 38 Pa. for the last minute of the simulation, the pea value is 14.2 Pa and decreases to the constant magnitude of 10.2 Pa.

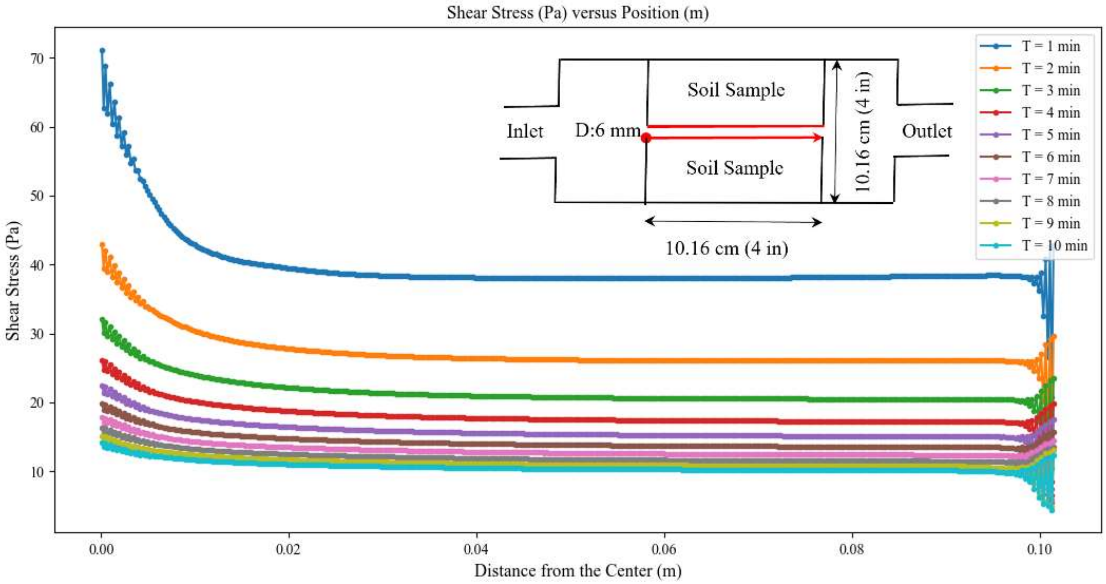

Figure 3-31 The erosion function used on the soil boundary to study the evolution of shear stress during the test

3.3.3. Evolution of Shear Stress in BET

Figure 3-32 shows the shear stress distribution along the borehole bottom radius for a flow rate of 5.68×10^{-3} m^3/s, a gap of 25 mm between the orifice and the bottom of the borehole and roughness height of 3 mm for the bottom and side of the borehole. For every minute of the test simulation, shear stress starts from a value near zero at the center of the hole, then reaches its maximum and decreases to near zero at the edge of the borehole. For the first minute of the test, the maximum value is 108 and decreases to 3.6 Pa at the edge of the borehole. Since the first minute is similar to the static case, the value is the same as the value calculated with CHEN4D (Section 3.1.5) as 111 Pa. For the last minutes of the test, the peak shear stress decreases to 60 Pa (if we disregard the fluctuations at the edge of the borehole). it means that erosion rate decreases from 103 mm/hour to 55 mm/hour ($ER_{max@t=10\ min} / ER_{max@t=1\ min} = 0.53$).

Figure 3-33 presents the shear stress distribution during the test side of the borehole for a flow rate of 5.68×10^{-3} m^3/s, a gap of 25 mm between the orifice and the bottom of the borehole and roughness height of 3 mm for the bottom and side of the borehole. The same trend as the bottom of the borehole can be observed here. Shear stress starts near zero at the end of the borehole and reaches its maximum at the point where the flow jet hit the side of the borehole and, after several fluctuations, continues to decrease to a constant value. The peak shear stress at the first minute of the test is 99.6 Pa and decreases to 59.4 Pa at the end of numerical simulation (10 minutes). It corresponds to a decrease in erosion rate from 94.6 mm/hour to 54.4 mm/ hour ($ER_{max@t=10\ min} / ER_{max@t=1\ min} = 0.58$).

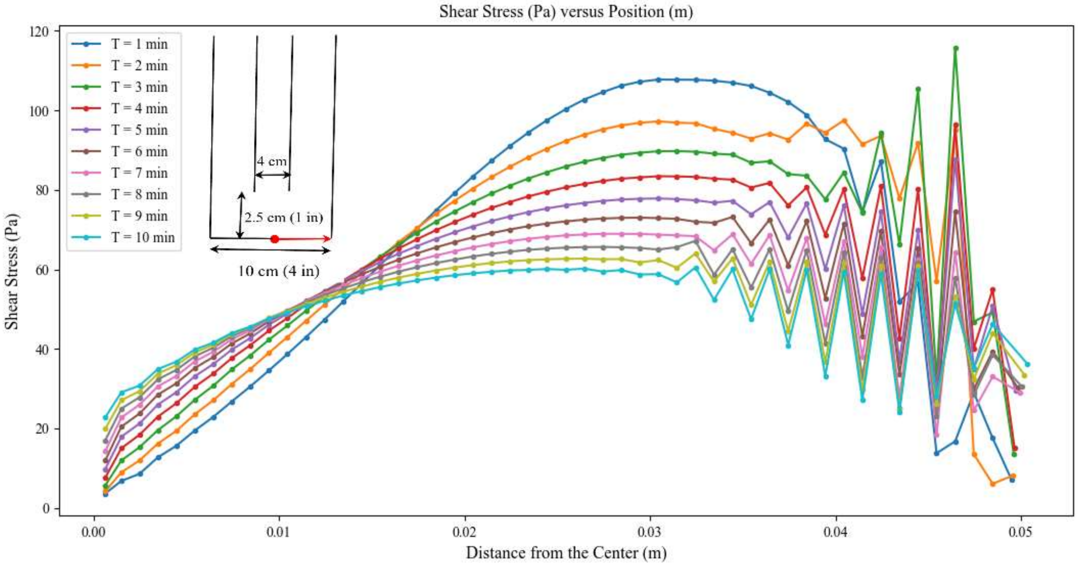

Figure 3-32 The erosion function used on the soil boundary to study the evolution of shear stress during the test

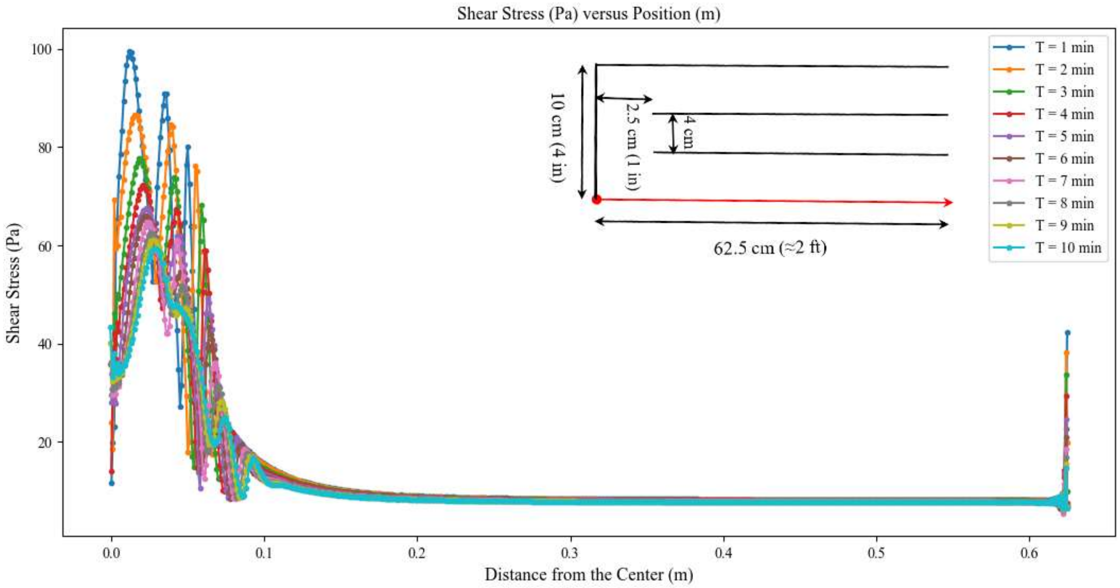

Figure 3-33 The erosion function used on the soil boundary to study the evolution of shear stress during the test

3.3.4. Conclusion

The final aim of this section was to compare the results of numerical simulation of JET, HET, and BET with the experimental results. The erosion function resulted from the EFA test applied as a constitutive law of erosion on the soil fluid interface in a CFD framework with mesh morphing to observe the progression of the erosion. By this comparison, the efficiency of the CFD method with mesh morphing to capture the results of these tests with an input erosion function was presented. In the following, a summary of the results is presented.

Table 3-3 summarizes the numerical simulation results, as discussed in Section 6.2 of this report. The findings show that the erosion function obtained from the EFA test for each sample can be reasonably used to produce a similar "scour versus time" plot to what the JET, the HET, and the BET experiments would result. However, the variety of interpretation techniques that are used for each test to obtain the shear stress in the soil-water interface leads to different erosion functions. Therefore, one must be aware of the interpretation techniques that each test uses to obtain the erosion function (erosion rate versus shear stress). It is also worth noting that for the case of the HET results, the scour values refer to the average diameter of the drilled hole in the center of the sample.

Finally, by using an erosion function for the three tests, the evolution of shear stress in the JET, HET, and BET during the test was investigated. For all tests, the peak shear tests were decreased with time.

Table 3-3. Summary of the numerical simulation results

	Sample Name	Roughness	Final observed scour (mm)	Final Calculated Scour using the EFA Erosion Function (mm)				Figure
				RH = 0 mm	RH = 0.5 mm	RH = 1 mm	RH = 3 mm	
JET	Sand #1	0.14	40	40.8	43.5	43.1	48	Figure 3-15
	Sand #2	0.122	23	13.8	16.8	20	20.3	Figure 3-18
	B-1 (4-6)	0.0024	7	10.8	14.3	17.5	18.5	Figure 3-20
	FHWA S2	0.0031	17	8	10.8	12.8	14.6	Figure 3-22
HET	SH-1	0.1	13.4	12.5	13.5	14	14.2	Figure 3-24
BET	CBH3	0.00038	20[1]	20.31	20.35	20.40	-	Figure 3-27

[1] The scour values shown for the BET are the maximum diameter enlargements in 8'-10’ depth of the borehole

4. COMPARISON OF CFD-DEM SIMULATION RESULTS WITH VIDEO ANALYSIS

In the first section of this chapter, a typical benchmark example in chemical engineering, fluidized bed, which was tested in the laboratory (Buijteen et al. 2011), is studied by the CFD-DEM technique. This example is an excellent benchmark to examine the validity of the CFD-DEM model, especially in terms of drag force accuracy.

In the second section, the CFD-DEM method has been utilized to simulate six Erosion Function Apparatus (EFA) tests on samples with different sizes and roughnesses. Erosion functions (EF) derived from the laboratory tests on five samples are compared with the erosion functions extracted from the CFD-DEM simulations. The results prove the efficiency of the CFD-DEM process in providing erosion functions in sand and gravel particles, which can save energy and time. These results can be a complementary section to the first section in terms of accuracy and validation of the numerical technique.

Finally, in the last section, the results of numerical simulations of these five tests can be utilized to study the efficiency of the CFD-DEM technique in capturing velocity and accelerations at the start of the motion (incipient motion) in gravel particles. These samples are tested in the soil erosion laboratory (TAMU-SEL) before, and the velocities and accelerations have been determined by video analysis. A comparison of video analysis results with CFD-DEM can capture more insight into the incipient motion of sand and gravel particles.

4.1. CFD-DEM model Validation

Van Buijtenen et al. (2011) tested a pseudo-2D single-sprout fluidized bed. The particle image velocimetry (PIV) and positron emission particle tracking (PEPT) were used to study the motion of glass particles with a diameter of 3 mm. Figure 4-1 illustrates the dimensions of the single-sprout fluidized model and setup used by the researchers to PIV and PEPT on the glass particles. Pressurized air enters the domain from the bottom with two different velocities. In the two 70 mm side inlets, the air enters the area with a speed of 2.1 m/s, while from the 5 mm center inlet, enter with a velocity of 43.5 m/s.

Table 4-1presents the input parameters for the CFD-DEM model. The dimensions of the model are similar to Figure 4-1.a, and the simulation has been done for 20 s. Figure 4-2 indicates the particle velocity, particle velocity contours, pressure inside the fluidized bed, and volume fraction of lagrangian phase (glass particles) in three different time steps during the simulation (t=0.05 s, 0.5 s and 5 s). Particle Reynolds number ($\rho V_p D_p/\mu$) has range from near zero values to more than 10000, which proves a mixture of laminar and turbulent behavior in the fluidized bed.

Figure 4-3.a Shows the variation of vertical particle velocity at the elevation of 0.05 m. The velocity of particles at the center is more than 0.25 m/s (the zone with the inlet velocity of 43.5 m/s), while in the region which inlet velocity is 2.1 m/s, the velocity of particles is lower than 0. Figure 4-3.b illustrates the time-average vertical particle velocity and its comparison with particle image velocimetry (PIV) and positron emission particle tracking (PEPT) methods performed by Van Buijtenen et al. (2011). Good agreement can be observed between the CFD-DEM simulation and experimental results.

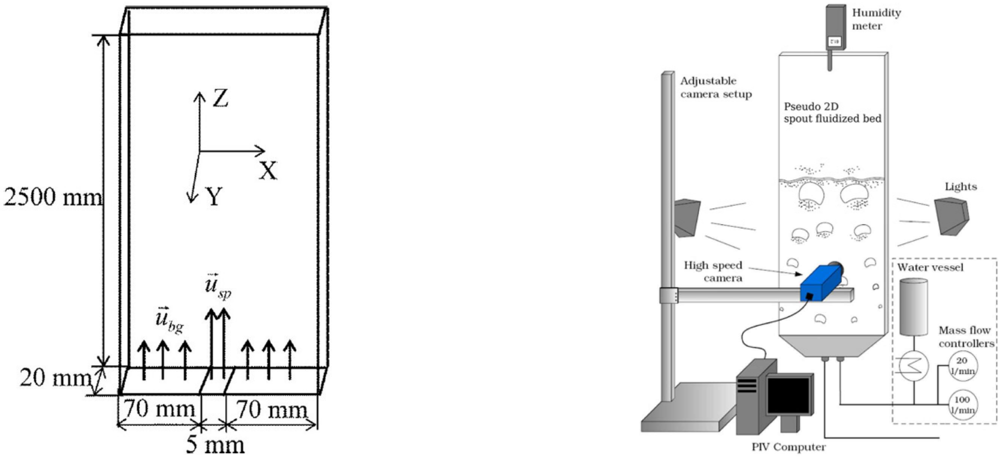

a) b)

Figure 4-1.a) Schematic overview of the single-spot fluidized bed with dimensions in mm and b) the setup to capture the movement and velocities of glass particles

Table 4-1. Input parameters for the particles and fluid domain

Parameter	Particles	Walls
Density (kg/m^3)	2505	2700
Modulus of Elasticity (Pa)	5×10^7	5.5×10^7
Poisson Ratio	0.2	0.4
Friction Coefficient	0.5	0.5
Normal Restitution Coefficient	0.6	0.6
Tangential Restitution Coefficient	0.6	0.6
Coefficient of Rolling Resistance	0.01	-
Computational parameters		
DEM time step	1.14×10^{-5}	
CFD time step	1×10^{-3}	
CFD mesh size (mm)	$5 \times 5 \times 5$	
CFD turbulence model	$k - \varepsilon$ Turbulence	
Drag Force Model	Di Felice	

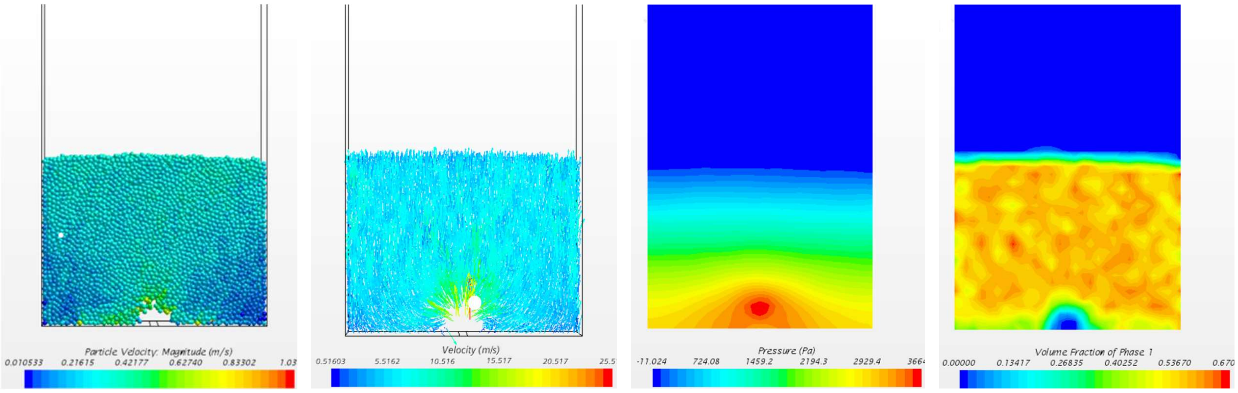

T = 0.05 S

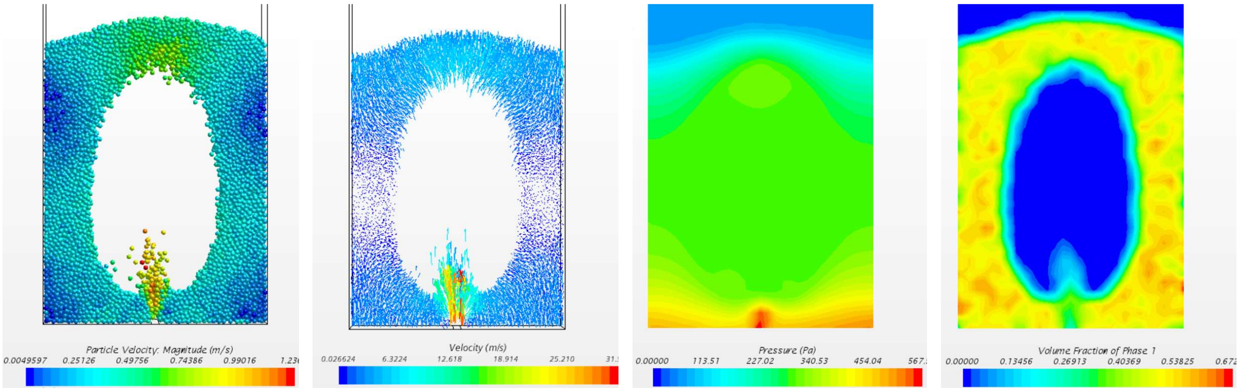

T = 0.5 S

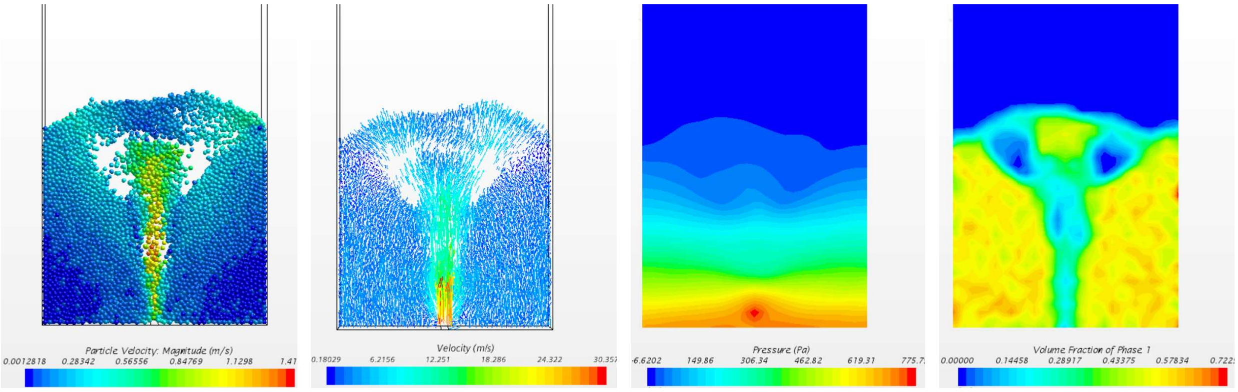

T = 5 S

Figure 4-2. Particle velocity, velocity contours, pressure in the region, and volume fraction of glass particles for different step times.

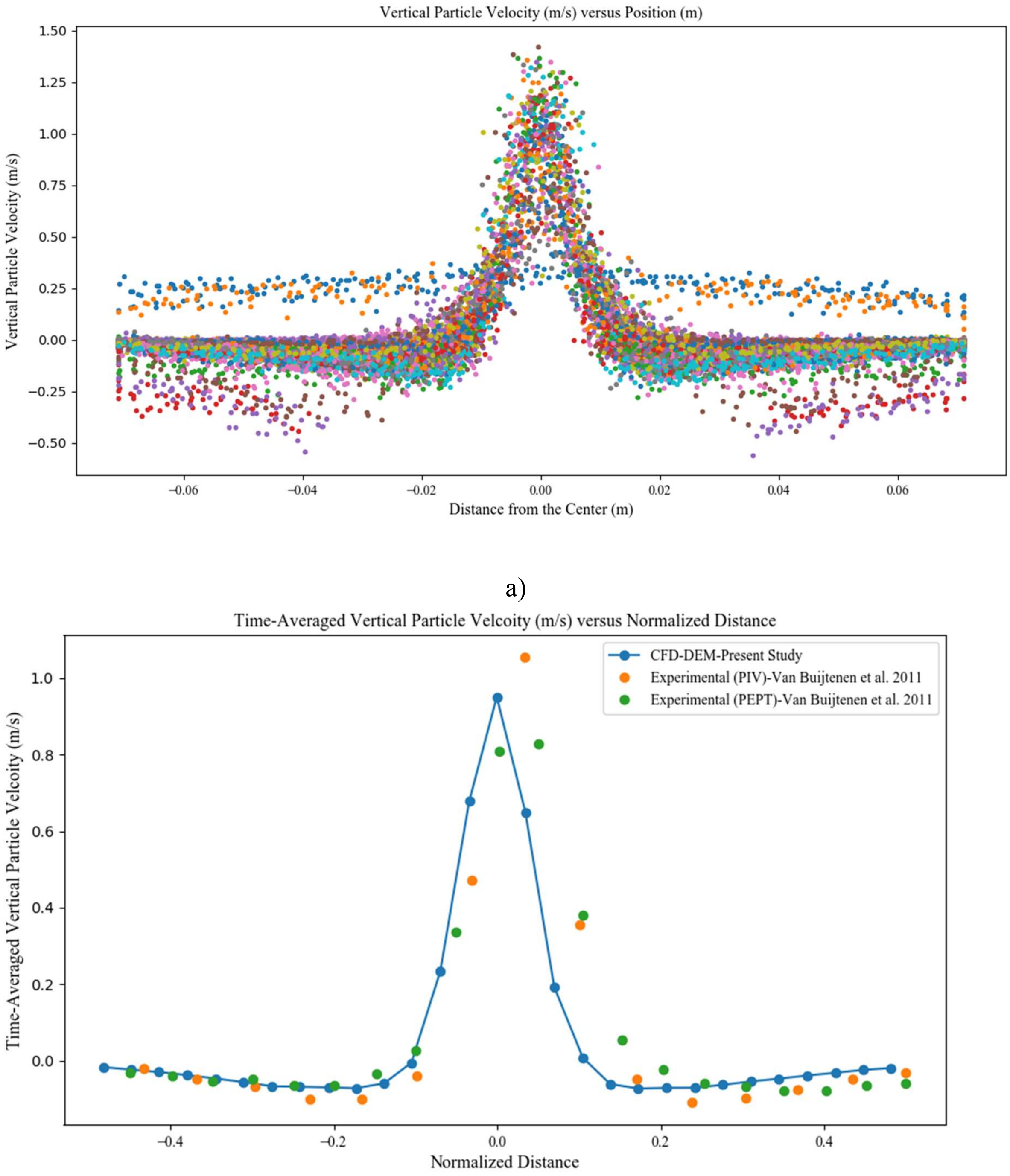

a)

b)

Figure 4-3.a) Verticle velocity of particles at the elevation of 0.05 m b) Time-averaged vertical particle velocity for the particles at the elevation of 0.05 m.

4.2. Comparison of erosion function extracted from laboratory test and erosion function resulted from numerical simulation

In the background knowledge (Chapter 2), several research with innovative apparatus and methods to measure the hydrodynamic forces on particles in incipient motion are presented. Still, a comprehensive study to do an experimental and numerical study for the incipient motion of particles is needed. In the following section, the final erosion function extracted from the EFA tests has been compared to the erosion function obtained from the numerical simulation. These results can serve as a benchmark to prove the efficiency of the CFD-DEM technique in evaluating erosion function from the numerical simulation.

4.2.1. Laboratory EFA test

In previous research in Briaud's erosion research group (Zhang (2018)), the behavior of different samples with EFA tests was studied in the soil erosion laboratory (SEL). Figure 4-4 shows photos of the surface of all five samples in the EFA before testing. G1, G2, and GB are natural gravel samples, while TB and SB are artificial samples. TB is composed of uniformly distributed 5 mm diameter "Polytetrafluoroethylene (PTFE)" or Teflon spheres. The friction at the contact surface between the particles is expected to be close to zero for TB. SB is composed of uniformly distributed 5 mm sand-coated PTFE spheres. The friction at the contact surface between the particles and the water is expected to be high for SB compared to almost zero for TB. The three samples GB, TB, and SB, have about the same mean particle size, with the only difference being their specific gravity (G_s) and friction characteristics (Table 4-2). The movement of the soil particles is recorded by a camera for further video analysis.

All five samples were tested in the Erosion Function Apparatus, and the results in the format of erosion rate vs. mean-depth velocity are shown in Figure 4-5. GB, TB, and SB are in the high erodibility category, while G1 and G2 are in the medium erodibility category when the water velocity is low. As the velocity becomes higher, finally, G1 and G2 switch to the high erodibility category.

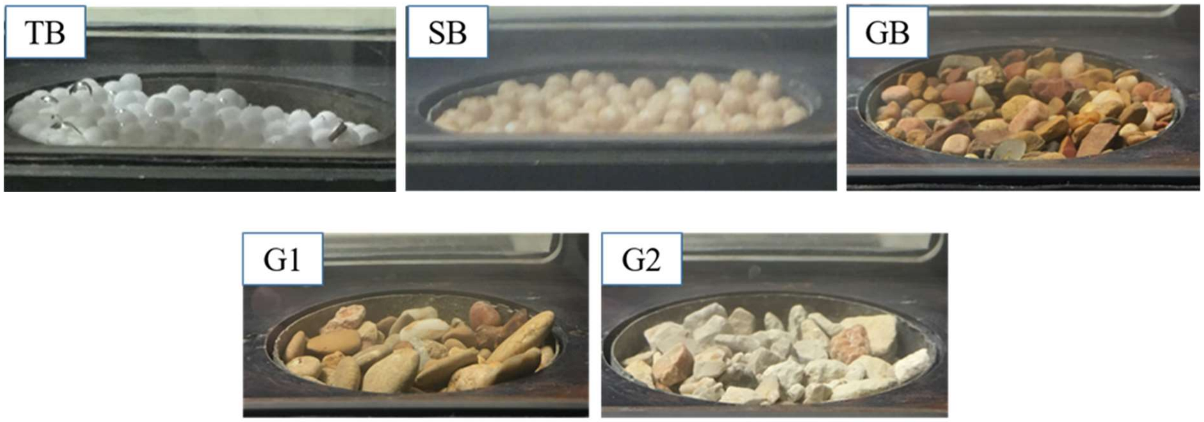

Figure 4-4. Five samples tested with EFA (reprinted from Zhang 2018)

Table 4-2. Parameters of five coarse-grained sample intended to be tested by Erosion Function Apparatus (EFA) (reprinted from Zhang 2018)

Sample name	Sample symbol	US	D_{50} mm	C_c	C_u	G_s
Gravel 1	G1	GP	11	0.93	2.17	2.3
Gravel 2	G2	GP w/ sand	6	1.23	2.41	2.2
Teflon balls	TB	GP	5	1	1	2.16
Sand coated Teflon balls	SB	GP	5	1	1	2.16
Gravel 3	GB	GP	5	1	1	2.3

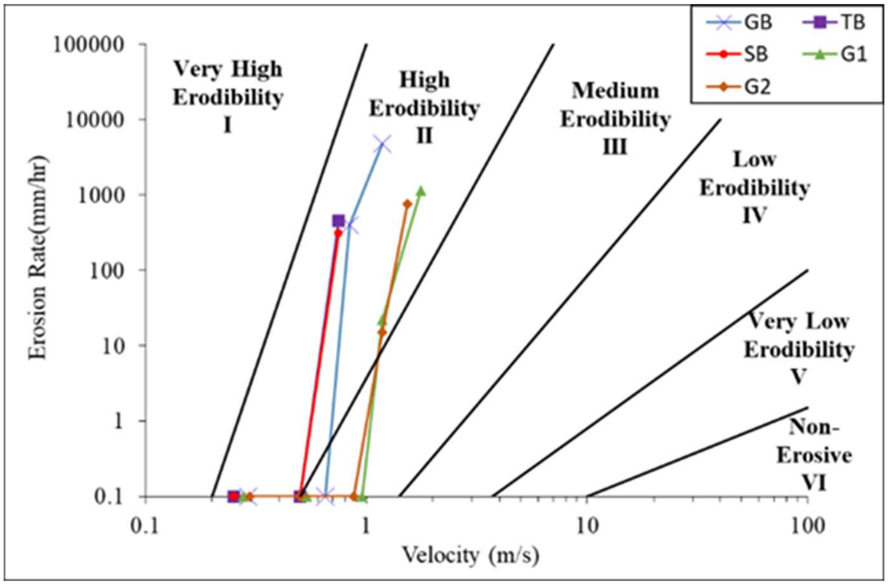

Figure 4-5. Results of five EFA tests on the samples (reprinted from Zhang, 2018)

4.2.2. CFD-DEM Simulation of EFA

The over-mentioned samples are reconstructed in CFD-DEM models to compare the EFA test results with the result of the numerical simulation. Figure 4-6 shows the typical geometry of the CFD-DEM model, which is considered based on the real dimensions of the EFA test. The flow comes into the channel from the inlet with the intended velocity and exit from the outlet. The flow modeled in CFD with the $k - \varepsilon$ model, which is explained in Chapter 2. Table 4-3 introduces the parameters used to model the particles and the fluid in a CFD-DEM framework. The CFD time step is considered as 1×10^{-3}. This value is chosen as the maximum time step for the simulation without affecting the results. The CFD mesh size is selected based on the diameter of the sample grains. The CFD mesh size should be selected larger than the maximum particle size to ensure the accuracy of the drag force in the CFD-DEM. Otherwise, the simulation may diverge or terminate. The "Smooth Large Particles" can be utilized to improve the accuracy of the solution when the mesh size is smaller than the particle sizes. Still, this option is relevant only if the 2-way coupling has been implemented. Even with the use of smooth large particles option, simulation accuracy is lower than when the mesh size is larger than the particles.

For this reason, all the meshes in this simulation are chosen larger than the particle size (Table 4-3). For the interaction of the fluid and particles, the 2-way coupling has been implemented. In all the simulations, Schiller-Naumann and Deflice darg models are considered for the drag force, which is explained in Chapter 2. The density of particles is the same as the real values, but to save the computational cost, the modulus of elasticity of the simulated particles is lower than their real values. As explained in Chapter 2, the DEM time step is inversely proportional to the modulus of elasticity. Thus, the modulus of elasticity is considered as the minimum amount that does not change the results. Chend et al. (2012) showed that the smaller value of modulus of elasticity slightly changes the response of a particulate media. Table 4-4 presents the parameters that other researchers used in their CFD-DEM simulation for different applications.

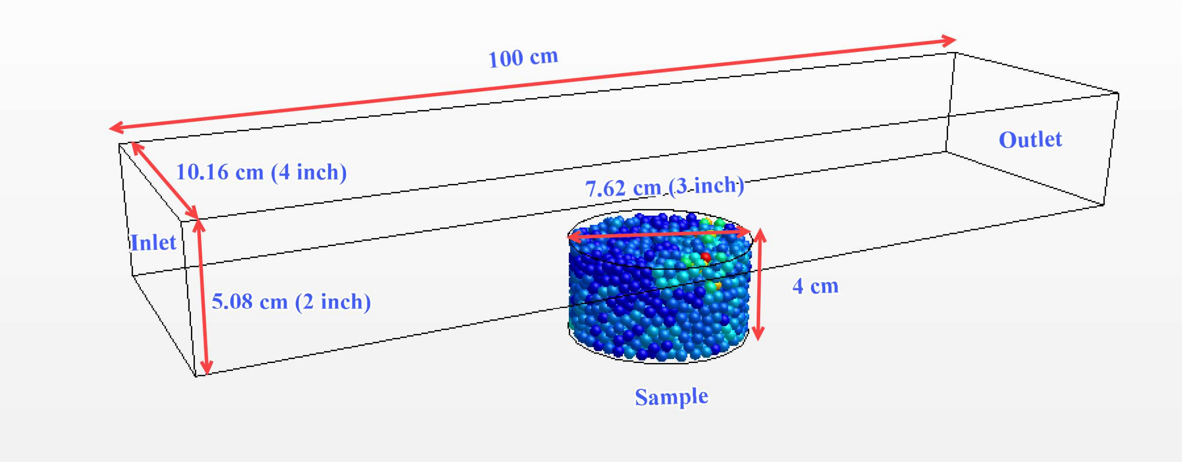

Figure 4-6. Typical geometry of the numerical simulation of the EFA test

Hertz-Mindlin model has been utilized for the interaction model between the particles. This model is also explained in the background knowledge. The values of static friction angle and coefficient of rolling resistance of the particles are chosen based on their repose angles. The static friction coefficient can be simply considered as the tangent of the angle of repose.

Wensrich and Katerfeld (2012) studied the relationship between the angle of repose, sliding friction, and coefficient of rolling resistance for particles with a diameter range between 4.6 mm to 5.2 mm. Figure 4-7 shows their results, which are used in this research to choose sliding friction and rolling resistance coefficient for different particle shapes.

Chen et al. 2018 studied the coefficient of restitution for gravel particles with various sizes by experiment. They defined the COR has a range from 0.407 to 0.559 for gravel particles. For the gravel samples in this study, the coefficient of restitution is considered as 0.5. For the Teflon balls, the COR is near one and larger than 1, but considering this fact that COR underwater is smaller than the dry mediums (Joseph 2003), the COR of 0.5 has been considered for the Teflon balls.

Figure 4-8 shows five numerical models constructed for simulation of Teflon Balls (TB), Sand-coated Bals (SB), Gravel Balls (GB), Gravel 1 (G1), and Gravel 2 (G2). The diameter of the TB, SB, and GB are constant with a diameter of 5 mm. For the G1 and G2 samples, the gradation curve is considered for the samples with parameters as Table 4-2.

Table 4-3. Physical properties of particles and fluid for five numerical EFA samples

Parameter	TB	SB	GB	G1	G2
Density (kg/m^3)	2200	2200	2650	2650	2650
Modulus of Elasticity (Pa)	1×10^7	1×10^7	1×10^7	1×10^7	1×10^7
Poisson Ratio	0.45	0.45	0.3	0.3	0.3
Friction Coefficient	0.05	0.2	0.3	0.5	0.4
Normal Restitution Coefficient	0.5	0.5	0.5	0.5	0.5
Tangential Restitution Coefficient	0.5	0.5	0.5	0.5	0.5
Coefficient of Rolling Resistance	0.01	0.02	0.2	0.4	0.3
Computational parameters					
DEM time step	3.9×10^{-5}	3.9×10^{-5}	3.9×10^{-5}	7×10^{-5}	2.7×10^{-5}
CFD time step	1×10^{-3}	1×10^{-3}	1×10^{-3}	1×10^{-3}	1×10^{-3}
CFD mesh size (mm)	$10 \times 10 \times 10$	$10 \times 10 \times 10$	$10 \times 10 \times 10$	$20 \times 20 \times 20$	$15 \times 15 \times 15$
CFD turbulence model	$\mathrm{k}-\varepsilon$	$\mathrm{k}-\varepsilon$	$\mathrm{k}-\varepsilon$	$\mathrm{k}-\varepsilon$	$\mathrm{k}-\varepsilon$
Drag Force Model	Schiller -Naumann	Schiller -Naumann	Schiller -Naumann	Schiller -Naumann	Schiller -Naumann

Table 4-4. Physical properties used by different researchers to simulate different CFD-DEM applications

Reference	Application	Diameter (mm)	Young's Modulus (Pa)	Poisson's ratio	Friction coefficient	DEM Timestep (s)	CFD Timestep (s)
El Shamy et al. 2010	Lateral spreading	4.8-7.2	6.67×10^9	0.15	0.7	1.75×10^{-6}	3.5×10^{-6}
Belheine et al. 2009	Drianed triaxial test	43-175	1×10^8	0.3-0.35	0.7		
Zhou et al. 2011	Erosion	0.15-0.35	1×10^7	0.3	0.4	1×10^{-6}	
Zhou and Ooi 2009	Pressure distribution	2	1×10^7	0.3	0.3 (sliding) 0.3 (rolling)		
Zhou et al. 2010	Fluidization	4	1×10^7	0.3	0.4 (sliding) 0.04 (rolling)	1.75×10^{-7}	
Zhou et al. 1999	Sandpile formation	6 10	1×10^6	0.3	0.4 (P-P) 0.7 (P-W)	4×10^{-6} 1.5×10^{-5}	
El Shamy and Zeghal 2007	Liquefaction	0.6-1.4	1×10^6	0.31	0.5	2×10^{-6}	2×10^{-3}
Zhao and Shan 2013	Sandpile formation in water	2 (1-3)	70×10^9	0.3	0.7 (sliding) 0.1 (rolling)	5×10^{-7}	5×10^{-4}
Chand et al	Rotating drum	1.4-2.8	2×10^6	0.45	0.5	1×10^{-5}	

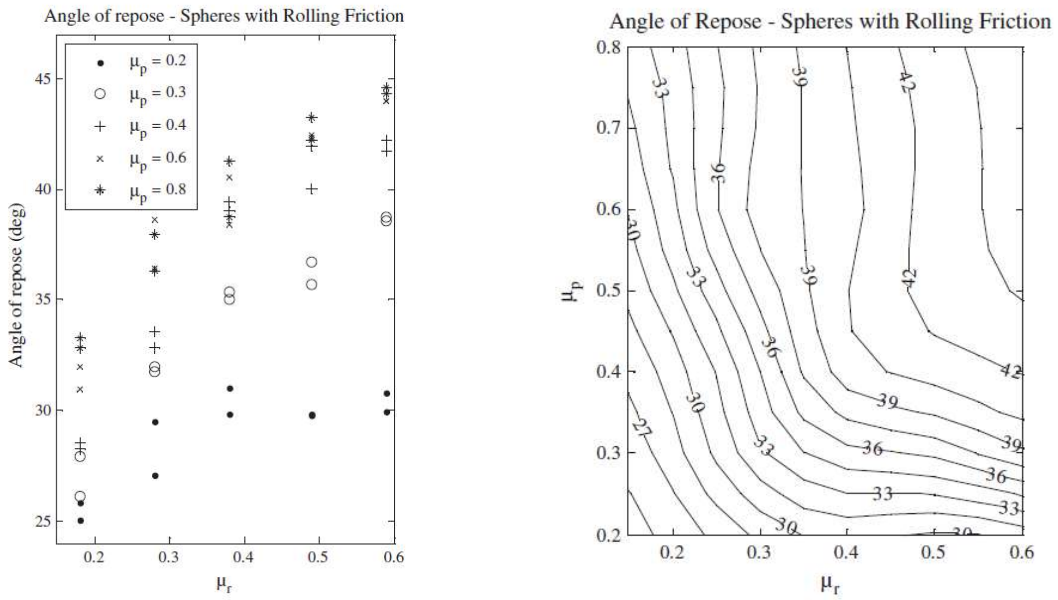

Figure 4-7. The relationship between the angle of repose, sliding friction coefficient and coefficient of rolling resistance (reprinted from Wensrich and Katerfeld (2012))

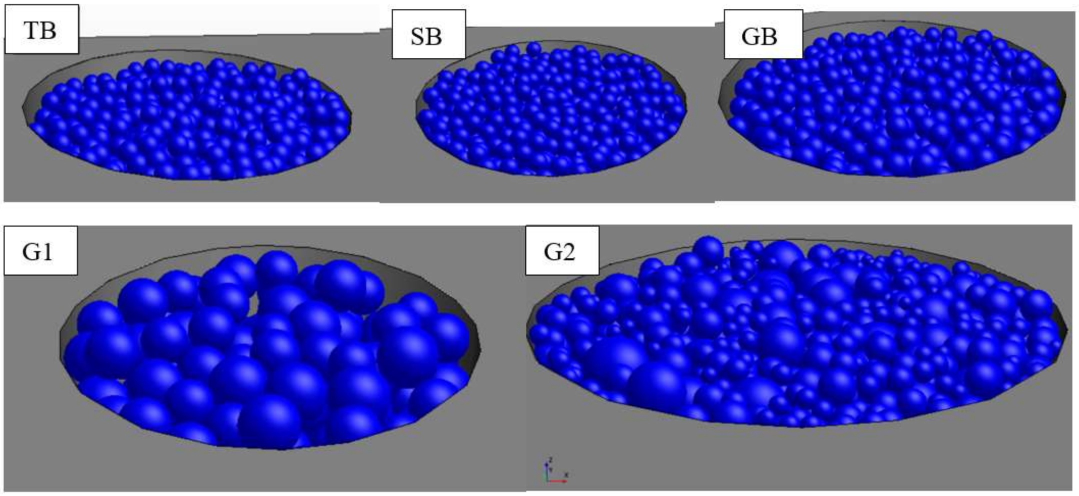

(b)

Figure 4-8. Five numerical models constructed for simulation of Teflon Balls (TB), Sand-coated Bals (SB), Gravel Balls (GB), Gravel 1 (G1) and Gravel 2 (G2)

4.2.3. Determining Erosion Function from numerical simulation

In the laboratory EFA test, the flow velocity can be controlled, and the specimen can be pushed up during the test. The magnitude of pushing can be measured manually or by the computer connected to the apparatus. The time step for the velocity is 10 minutes or the time in which 10 mm of erosion happens, whichever is smaller. The output data are velocity and erosion rate. The roughness of the sample surface was recorded during the test by visual inspection. The friction factor can be calculated from the velocity and roughness of the surface and based on the moody chart. Finally, based on Equation 3-1 ($\tau = \frac{1}{8} f \rho v^2$), shear stress can be calculated.

For the CFD-DEM simulation, first, the geometry of the EFA is constructed. After, the sample preparation is performed as the first step for the simulation. As summarized in Table 4-3, the DEM time step is in the order of 10^{-5}, it means to simulate each second of the test, around 10^5 increments are needed. Another limitation of the simulation is the movement of the sample. To prevent change in the specimen porosity due to movement, the sample specimen is stationary; instead, the simulation has been done separately for each velocity. It means each erosion function is the result of several CFD-DEM simulations. A sample preparation step and several simulations depend on the number of required steps for the velocity. After running each step, the mass loss is converted to mm/hour. The shear stress is calculated with separate CFD simulation.

4.2.4. Numerical simulation of Teflon balls (TB)

Figure 4-9 shows the comparison of erosion functions (erosion rate vs. velocity) derived from the laboratory simulation of the Teflon balls sample (TB) and its corresponding CFD-DEM simulation. The critical velocity for both cases is 0.5 m/s. Both erosion functions lied on the high erodibility zone of erosion categories.

Figure 4-10 illustrates the comparison of the erosion functions but in terms of erosion rate vs. shear stress. The critical shear stress for the CFD-DEM is 2.2 Pa, while in the case of the laboratory simulation, the value is 2. Good agreement can be observed between the overall trend of the EF curve from the numerical simulation and the laboratory test.

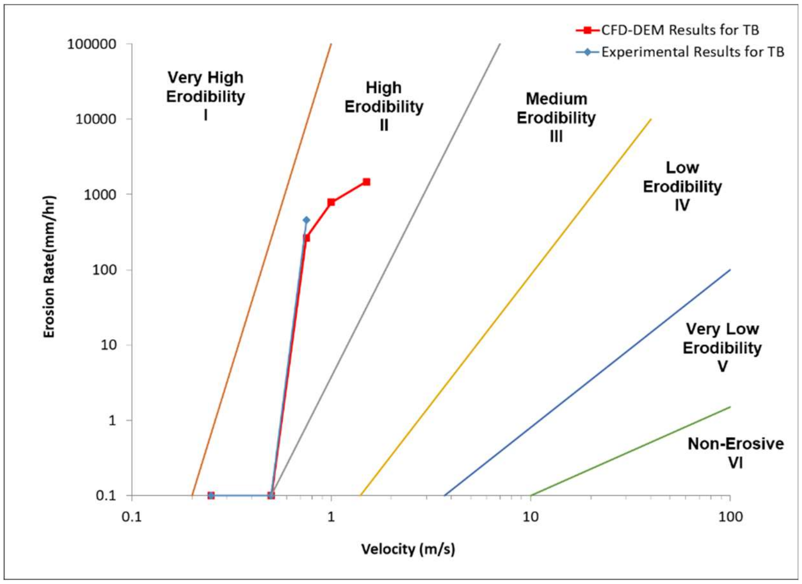

Figure 4-9. comparison of EF curve (erosion rate vs. velocity) derived from the laboratory simulation and CFD-DEM simulation of the TB

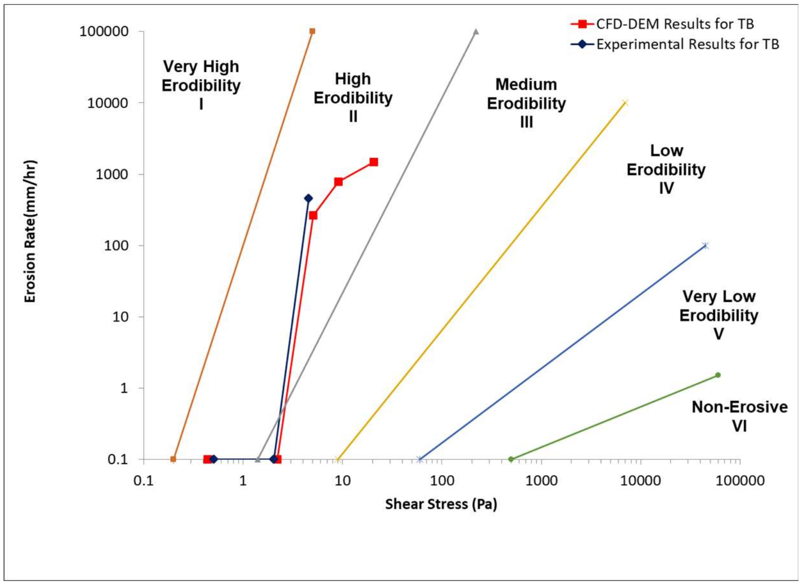

Figure 4-10. Comparison of EF curve (erosion rate vs. shear stress) derived from the laboratory simulation and CFD-DEM simulation of the TB

4.2.5. Numerical simulation of sand-coated Teflon balls (SB)

Figure 4-11 indicates the erosion function derived from the numerical simulation for the sand-coated balls (SB). In this case, the sample is the same as the TB, but to simulate the friction between the particles, the friction coefficient is considered as 0.2. the shape of sand-coated balls still is perfectly rounded. For this reason, the rolling resistance coefficient is still near zero (0.02 compared to 0.01 for the TB). But this particle surface roughness does not affect the overall value of surface roughness ($D_{50}/2$), and the experimental and numerical results for the SB is similar to TB.

The same trend can be observed in the comparison of erosion rate vs. shear stress (Figure 4-12).

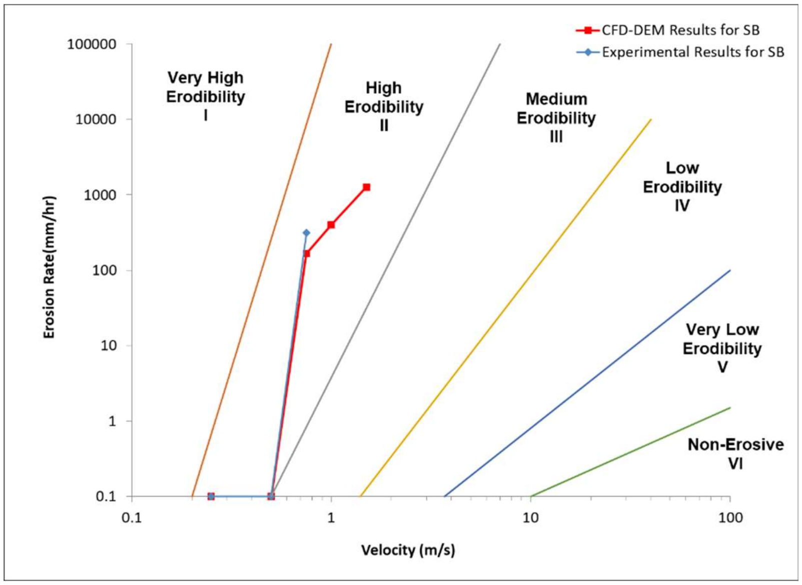

Figure 4-11. Comparison of EF curve (erosion rate vs. velocity) derived from the laboratory simulation and CFD-DEM simulation of the SB

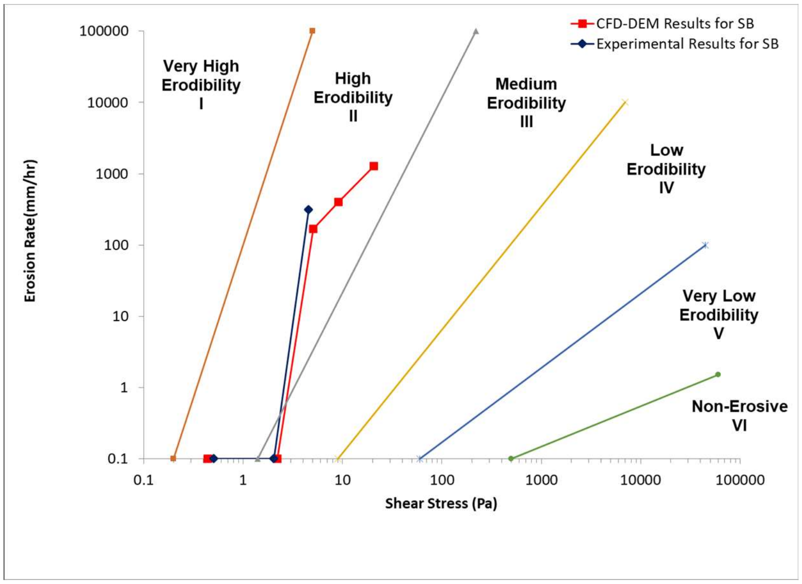

Figure 4-12. Comparison of EF curve (erosion rate vs. shear stress) derived from the laboratory simulation and CFD-DEM simulation of the SB

4.2.6. Numerical simulation of gravel balls (GB)

For the GB sample, the size (D_{50}) roughness height ($D_{50}/2$) is still the same as the TB and SB, but due to the increase of specific gravity (G_s), both critical velocity and critical shear stress are increased. Figure 4-13 presents the results for the experimental and numerical modelings. The critical velocity is 0.75 m/s, although the values of EF curves in high values of erosion rate do not perfectly match. Still, a good agreement can be observed between the results.

Critical shear stress for the GB sample is 4.6, which shows an increase compared to both TB and SB samples (Figure 4-14).

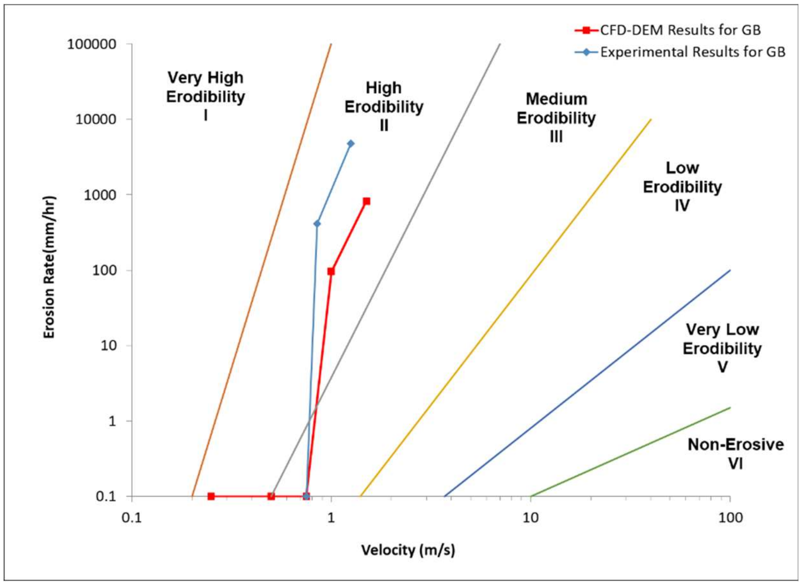

Figure 4-13. comparison of EF curve (erosion rate vs. velocity) derived from the laboratory simulation and CFD-DEM simulation of the GB

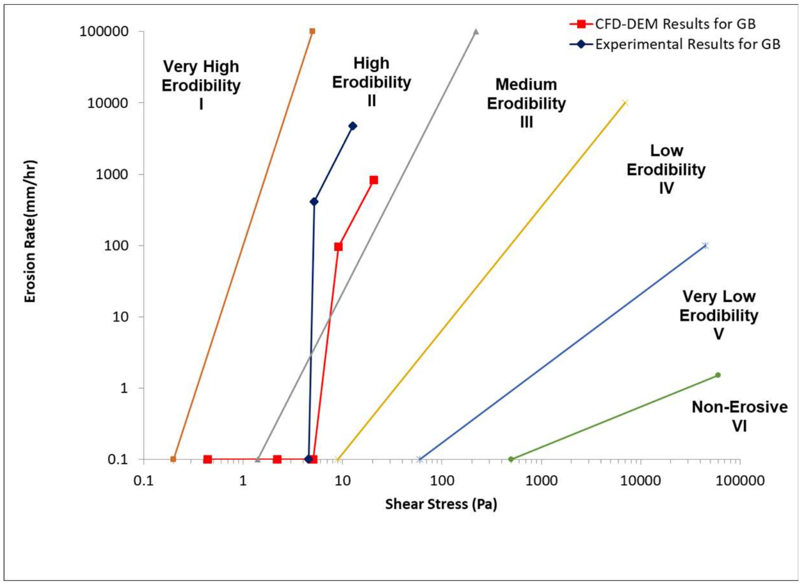

Figure 4-14. Comparison of EF curve (erosion rate vs. shear stress) derived from the laboratory simulation and CFD-DEM simulation of the GB

4.2.7. Numerical simulation of gravel (G2)

Figure 4-15 presents the erosion rate vs. velocity for the G2 sample. In the case of G2, the average size of particles increases to 6 mm compared to TB, SB, and GB. The critical velocity of the G1 sample is 0.9 m/s, and the overall matching of the curve to the experimental results is acceptable.

The critical shear stress for the G1 sample is 9.5 Pa for the numerical results and 9.1 for the experimental results. The overall slope of the EF curve is the same in both cases (Figure 4-16).

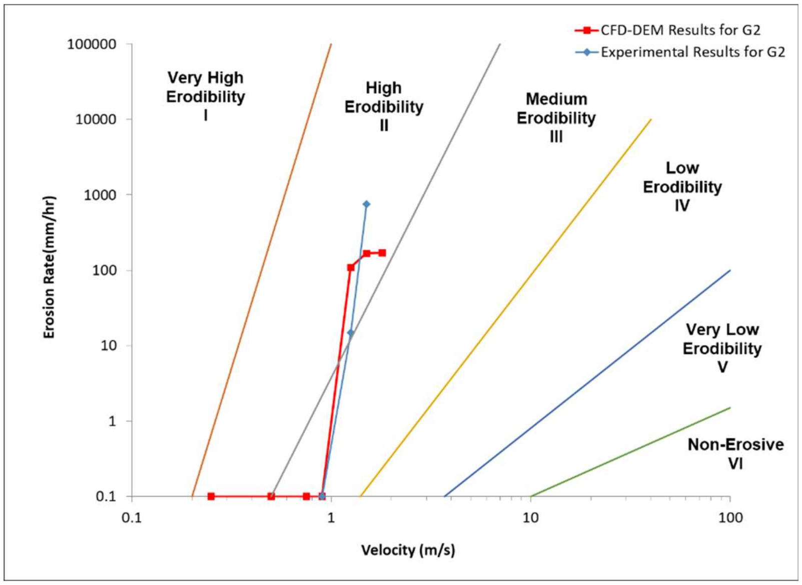

Figure 4-15. comparison of EF curve (erosion rate vs. velocity) derived from the laboratory simulation and CFD-DEM simulation of the G2

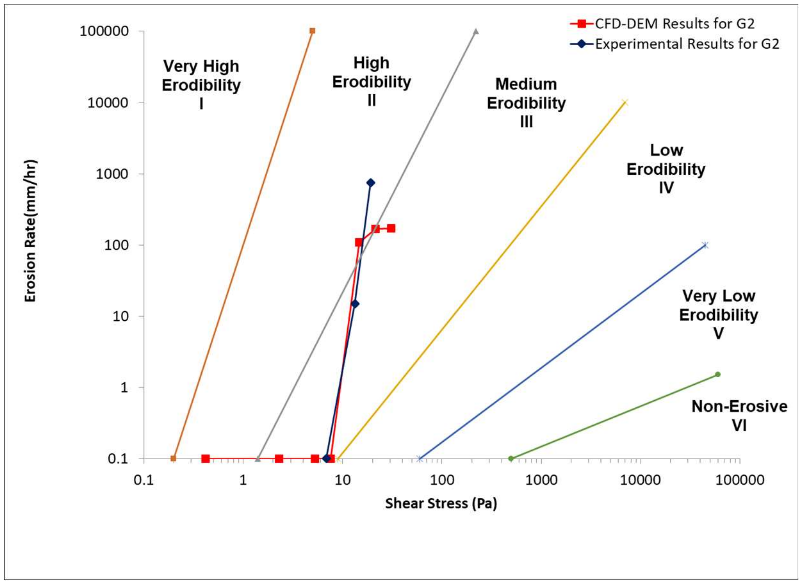

Figure 4-16. Comparison of EF curve (erosion rate vs. shear stress) derived from the laboratory simulation and CFD-DEM simulation of the G2

4.2.8. Numerical simulation of gravel (G1)

For the G1 gravel sample, D_{50} of particles is maximum between the samples by the value of 11 mm. Figure 4-17 displays both results of the numerical simulation and experimental modeling. In this case, the specific gravity, particle size, and particle surface roughness are increased. The critical velocity is 1 m/s for both experimental tests and numerical simulation.

Figure 4-18 shows a value of 10 Pa for the critical shear stress. The critical shear stress is expected to be more than 10 Pa compared to the G2 sample, but, in high values of roughness height, the friction factor is constant, and the shear stress for the same velocity (0.9 m/s and 1 m/s) is similar (9.5 Pa vs. 10 Pa).

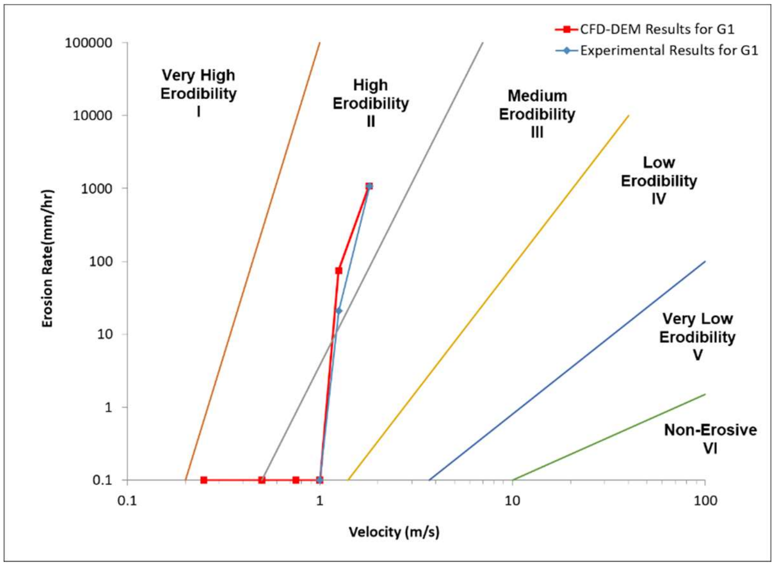

Figure 4-17. comparison of EF curve (erosion rate vs. velocity) derived from the laboratory simulation and CFD-DEM simulation of the G1

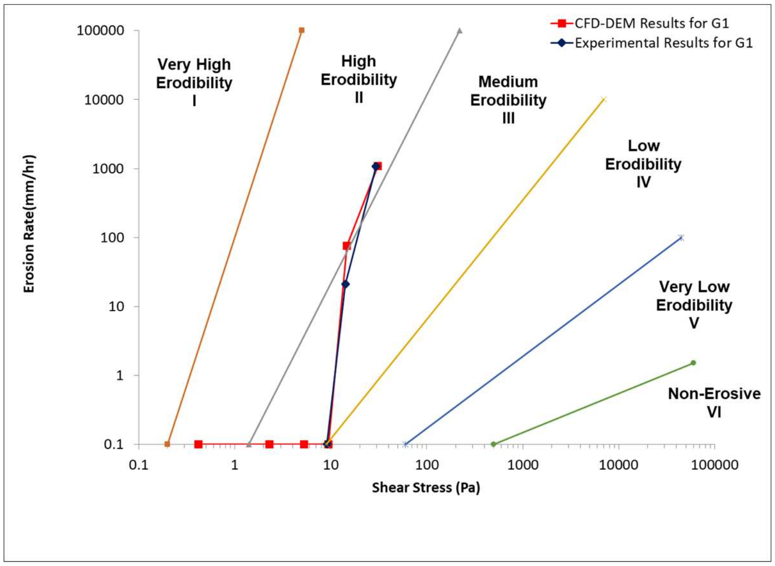

Figure 4-18. Comparison of EF curve (erosion rate vs. shear stress) derived from the laboratory simulation and CFD-DEM simulation of the G1

4.2.9. Comparison of the results to the current relationships for the critical velocity and critical shear stress

To summarize the results of numerical simulation in one chart and compare them simultaneously with the current relationships, the critical velocity and the critical shear stress are plotted along with the data from other researchers. The original curves are presented by Briaud (Briaud, 2013). Figure 4-19 indicates good agreement between the numerical simulation results and the data from Shields, Casey, US.WES, Gilbert, and white (reported by Vanoni (1975)).

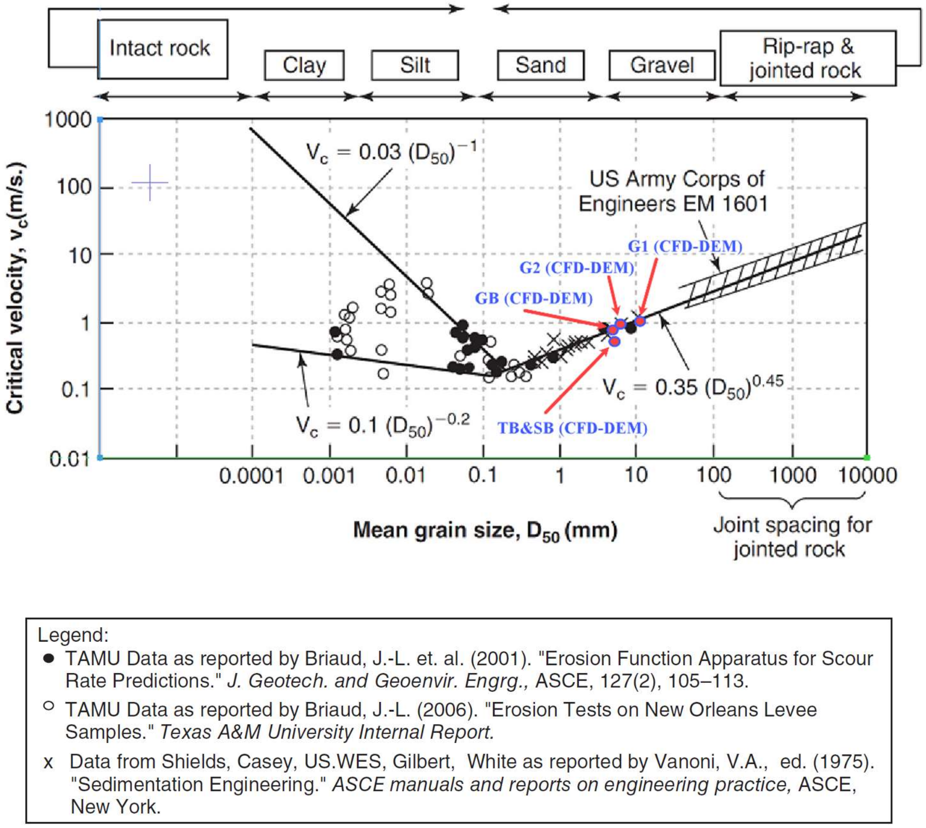

Legend:

- ● TAMU Data as reported by Briaud, J.-L. et. al. (2001). "Erosion Function Apparatus for Scour Rate Predictions." *J. Geotech. and Geoenvir. Engrg.,* ASCE, 127(2), 105–113.
- ○ TAMU Data as reported by Briaud, J.-L. (2006). "Erosion Tests on New Orleans Levee Samples." *Texas A&M University Internal Report.*
- x Data from Shields, Casey, US.WES, Gilbert, White as reported by Vanoni, V.A., ed. (1975). "Sedimentation Engineering." *ASCE manuals and reports on engineering practice,* ASCE, New York.

Figure 4-19. Critical velocity for the simulated samples and their comparison to current relationships

The same good match can be observed for the critical shear stress results in Figure 4-20. The results conform to the data from Shields, Casey, US.WES, Gilbert, and white (reported by Vanoni (1975)).

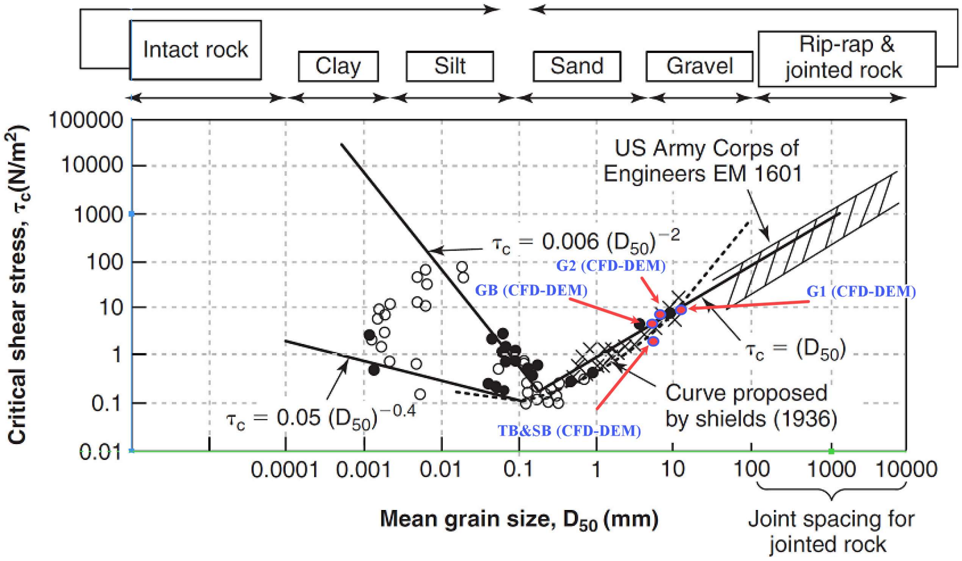

Legend:

- ● TAMU Data as reported by Briaud, J.-L. et. al. (2001). "Erosion Function Apparatus for Scour Rate Predictions." *J. Geotech. and Geoenvir. Engrg.,* ASCE, 127(2), 105–113.
- ○ TAMU Data as reported by Briaud, J.-L. (2006). "Erosion Tests on New Orleans Levee Samples." *Texas A&M University Internal Report.*
- x Data from Shields, Casey, US.WES, Gilbert, White as reported by Vanoni, V.A., ed. (1975). "Sedimentation Engineering." *ASCE manuals and reports on engineering practice,* ASCE, New York.

Figure 4-20. Critical shear stress for the simulated samples and their comparison to current relationships

4.3. Comparison of velocities and accelerations from laboratory tests and numerical simulations

This section focuses on comparing velocity and accelerations calculated from the video analysis of the EFA tests mentioned in the above and numerical simulation (CFD-DEM). These simulations can give more insight into the micromechanics of the incipient motion of coarse-grained particles (sand and gravel). Before presenting the final results, an introduction to the incipient motion of particles can give more insight on the definition of the problem, assumptions, essential parameters involved in the process, and unknowns that shall be sought.

4.3.1. Incipient motion of the particles

Figure 4-21 schematically presents the forces involved in the incipient motion of the particles. As formerly explained in the background knowledge, these forces can be categorized as resistance against motion or stimulant to the movement. Other forces can also play a role in which their presence depends on the regime of the flow (laminar or turbulent), the shape of particles (sand or clay), and chemical ingredients of the fluid and eroded material. The samples are gravel, and the water is taped water, so the forces shown here can be representative enough to describe the initiation of motion. By considering that the out of plane component of fluid force is zero, the fluid force can be divided into the horizontal component (drag force) and the vertical component (lift force) (Figure 4-21). These forces are the macro result of several micro effects. The viscous flow which creates shear stress on the surface of the particle and pressure changes around the particle. These effects depend on the flow regime, and their summation can be emerged in both drag and lift forces. When the flow is laminar, the viscous effects are more influential on the top surface of the particles, and the motion can be more influenced by the drag force (Figure 4-22-a). With a high Reynolds number, the flow separation happens, and pressure forces outweigh the viscous effects. In this case, also, both drag force and lift force are responsible for the incipient motion of the particles (Figure 4-22-b). Generally, the position of the particles is also important. Assuming that sliding is not the case when the moment of the fluid force around the front contact point (toe) is higher than the resisting moment, the movement starts. Before reaching this point, there are fluctuations in the drag force and the lift force. It could be attributed to the fluctuations of the velocity and large eddies just outside of the near-boundary layer of the flow. Former experimental measurements show fluctuations in the values of both drag and lift forces (Coleman and Ellis, 1976; Shafii, Zhang, and Briaud (2018)).

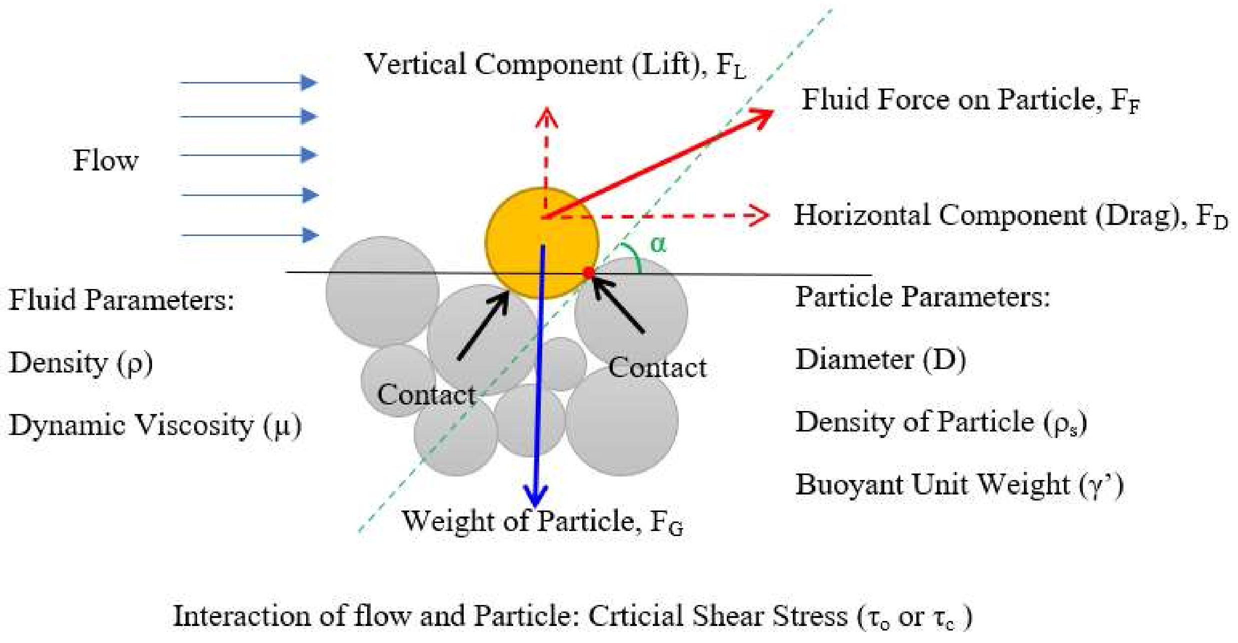

Figure 4-21. A simplified schematic diagram of forces, involved in the incipient motion of particles (adapted from Southard (2006))

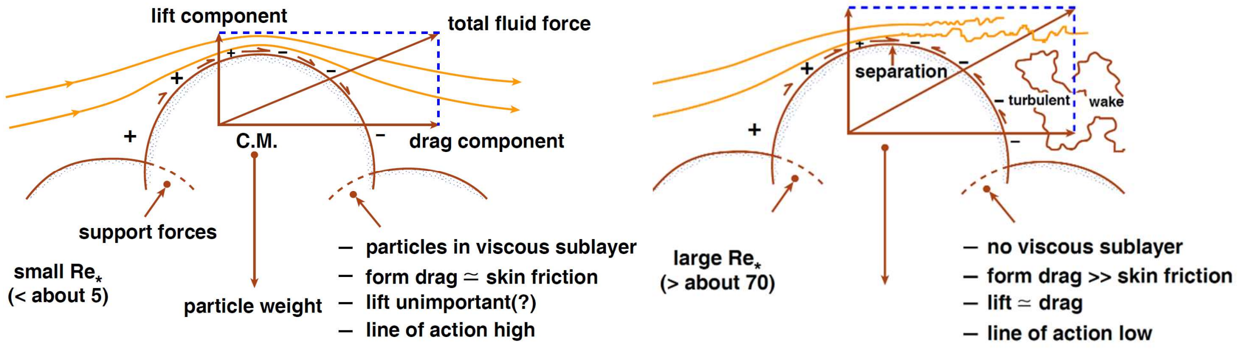

(a) (b)

Figure 4-22. The effect of flow regime on the viscous sublayer and the pressure changes around the particle; a) Laminar flow b) Turbulent flow (reprinted from Southard (2006))

Solving the equilibrium at the start of motion or pursuing dimensional analysis with the essential parameters explained in Figure 4-21, leads to the following equation (Southard (2006)):

$$\frac{\tau_c}{\gamma' D} = f\left(\frac{\rho u_* D}{\mu}\right) \qquad 4\text{-}1$$

Where $u_* = \sqrt{\frac{\tau_c}{\rho}}$ is the critical velocity and, the $\frac{\rho u_* D}{\mu}$ is called boundary Reynolds number.

In this equation, the only horizontal component of the fluid force (drag) is considered. The relationship mentioned above is the base of the Shield curve. Figure 4-23 presents the Shields curve along with the results from the CFD-DEM simulation of samples.

The above description explained the problem and the parameter involved in the problem, but still, several questions remained unanswered. The contribution of lift force (vertical component of the fluid force) in the incipient motion of the particle needs to be more studied, the values of vertical and horizontal accelerations at the start of the movement needs to be investigated and, the difference between average shear stress and local shear stress on a particle needs to be reviewed.

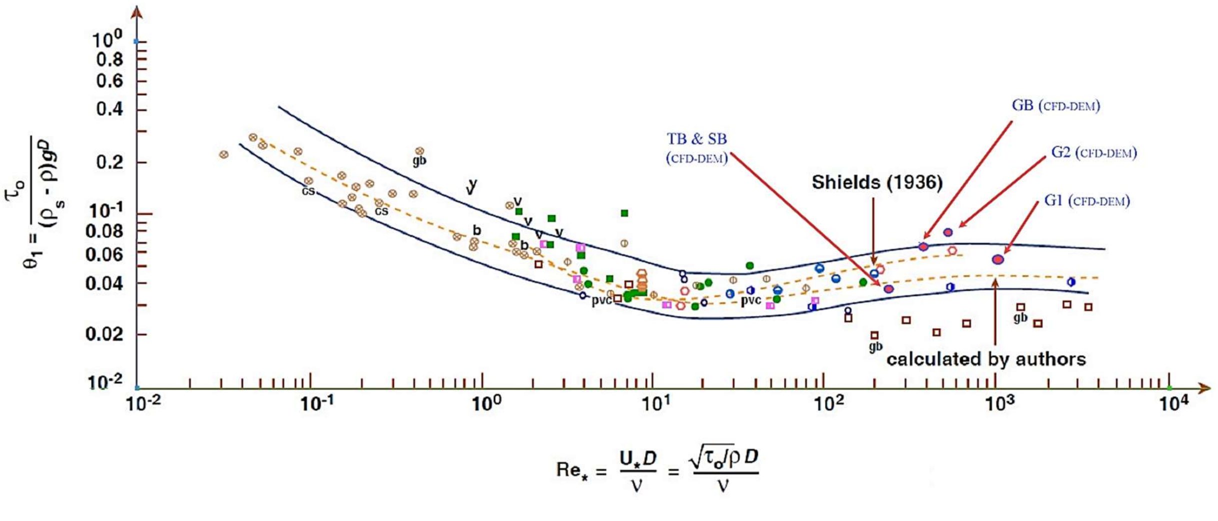

Figure 4-23. Comparison of the results with the Shields curve (proposed by Miller at al., 1977)

4.3.2. Video analysis of EFA tests

The video analysis of the EFA tests was done by Tracker (Zhang, 2018). Tracker is a free video analysis and modeling tool built on the Open Source Physics (OSP) Java framework (Tracker, 2018). The algorithm Tracker uses to calculate velocity and acceleration is based on the Finite Difference Method. The corrected time, velocity, and acceleration in both the horizontal (x) and vertical (y) directions are generated using the following algorithm (Equations 4-2 to 4-4):

$$r = (x^2 + y^2)^{0.5} \tag{4-2}$$

$$v_i = \frac{x_{i+1} - x_{i-1}}{2\Delta t} \tag{4-3}$$

$$a_i = \frac{2x_{i+2} - x_{i+1} - 2x_i - x_{i-1} + 2x_{i-2}}{7\Delta t^2} \tag{4-4}$$

Where r refers to the resultant displacement of the particle, v_i is the velocity of the particle, and a_i the acceleration of the particle. From the acceleration values, the drag force and the normal force on the particle were calculated by multiplying the acceleration by the mass of the particle. The shear stress and the normal stress were then obtained by dividing the force by the area. The calculations of forces and stresses are detailed in the next section. The average magnitude of a time history (displacement, velocity, or acceleration) is calculated with the method used by Zhang (2018). The average magnitude of the time history is the distance between the positive average and negative average of the time history from the start of motion to the departure time. The positive average is the average of the values above the average line, and the negative average is the average of values under the average line (Figure 4-24).

In the CFD-DEM analysis, the velocities from the software can be calculated. The accelerations are calculated from the velocities. The same method is used for determining the average magnitudes of velocities and accelerations. Figure 4-24 to Figure 4-28 presents the time history of the horizontal and vertical components of velocities and accelerations for one particle of each sample. The region considered for the calculation of average is highlighted with a yellow color. The departure time is determined with the visual inspection of the particle in the software, which in most cases conforms with the horizontal velocity of 0.1 m/s for the particles (if the particle reaches to this velocity and also the acceleration is high enough for the movement to continue).

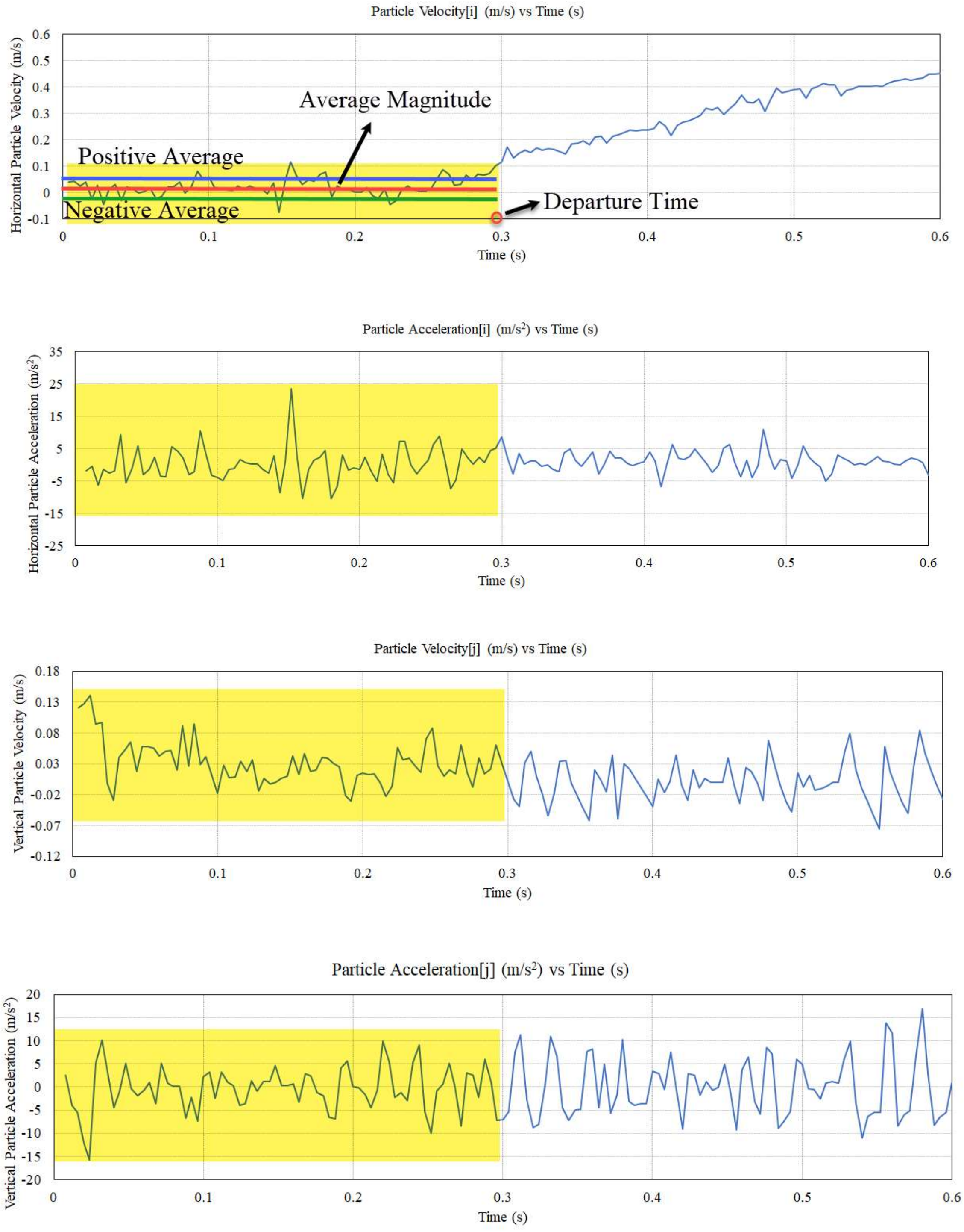

Figure 4-24. Horizontal and vertical velocities and acceleration for a particle of teflon ball (TB) sample

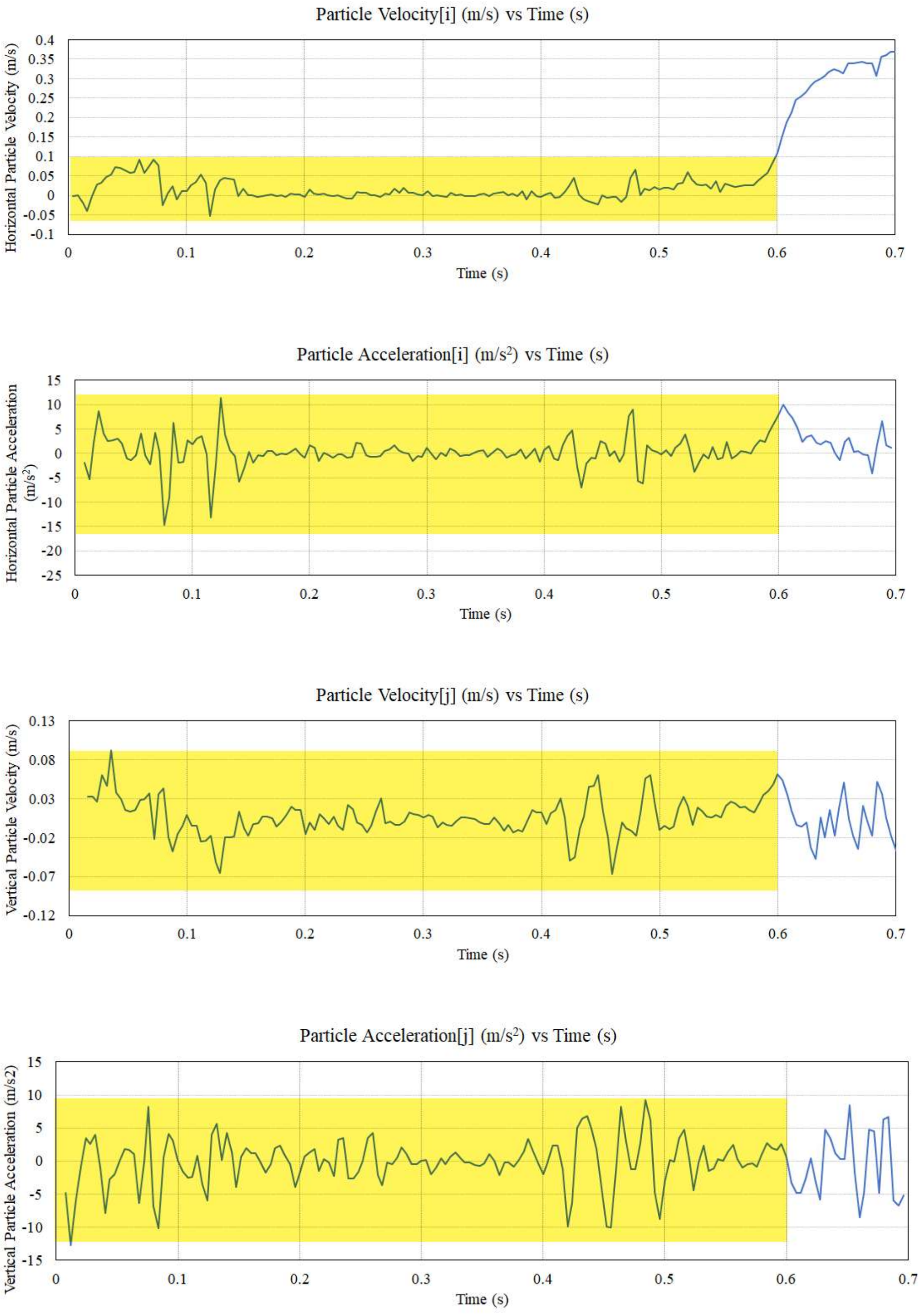

Figure 4-25. Horizontal and vertical velocities and acceleration for a particle of sand-coated Teflon ball (SB) sample

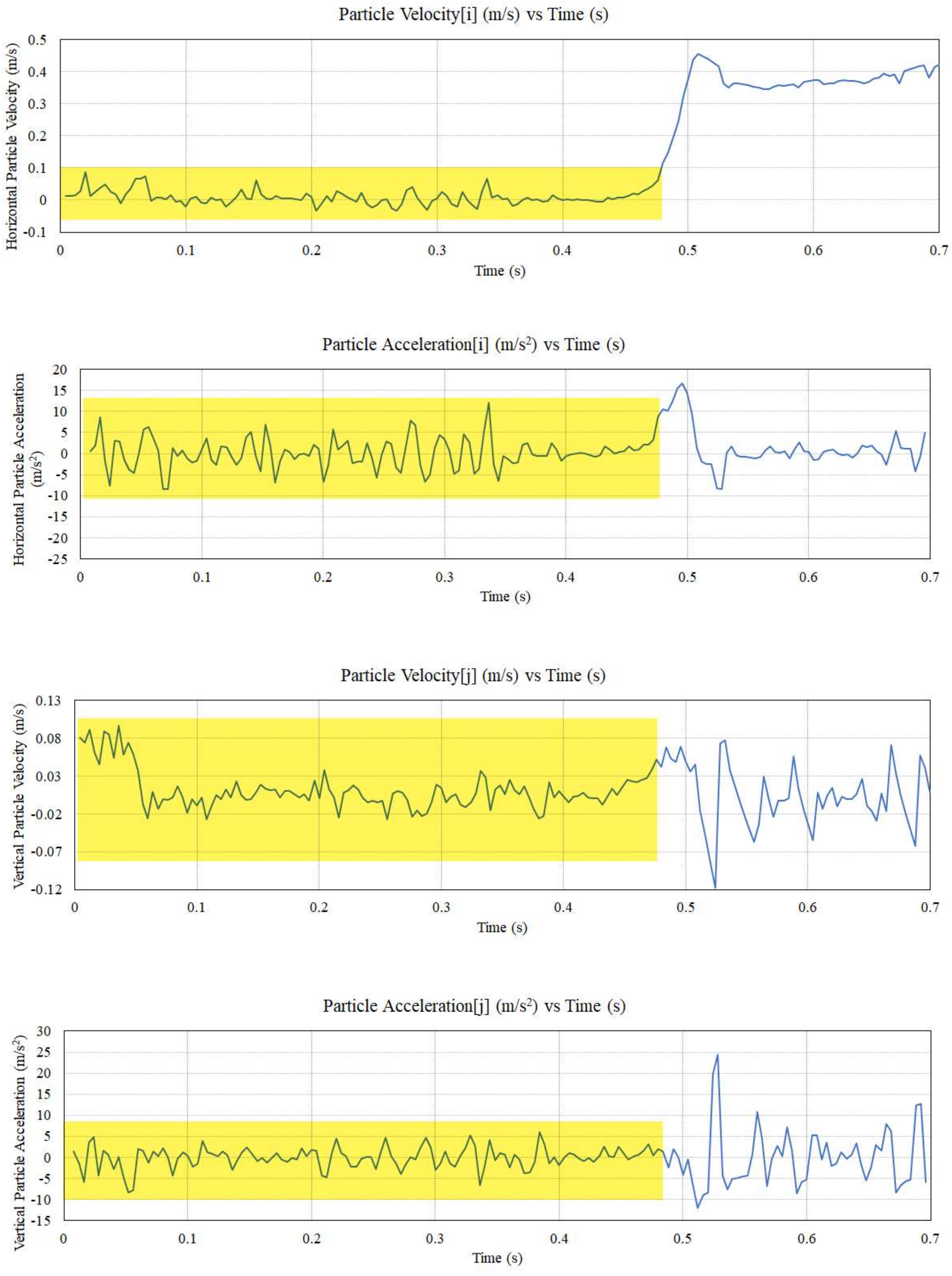

Figure 4-26. Horizontal and vertical velocities and acceleration for a particle of gravel ball (GB) sample

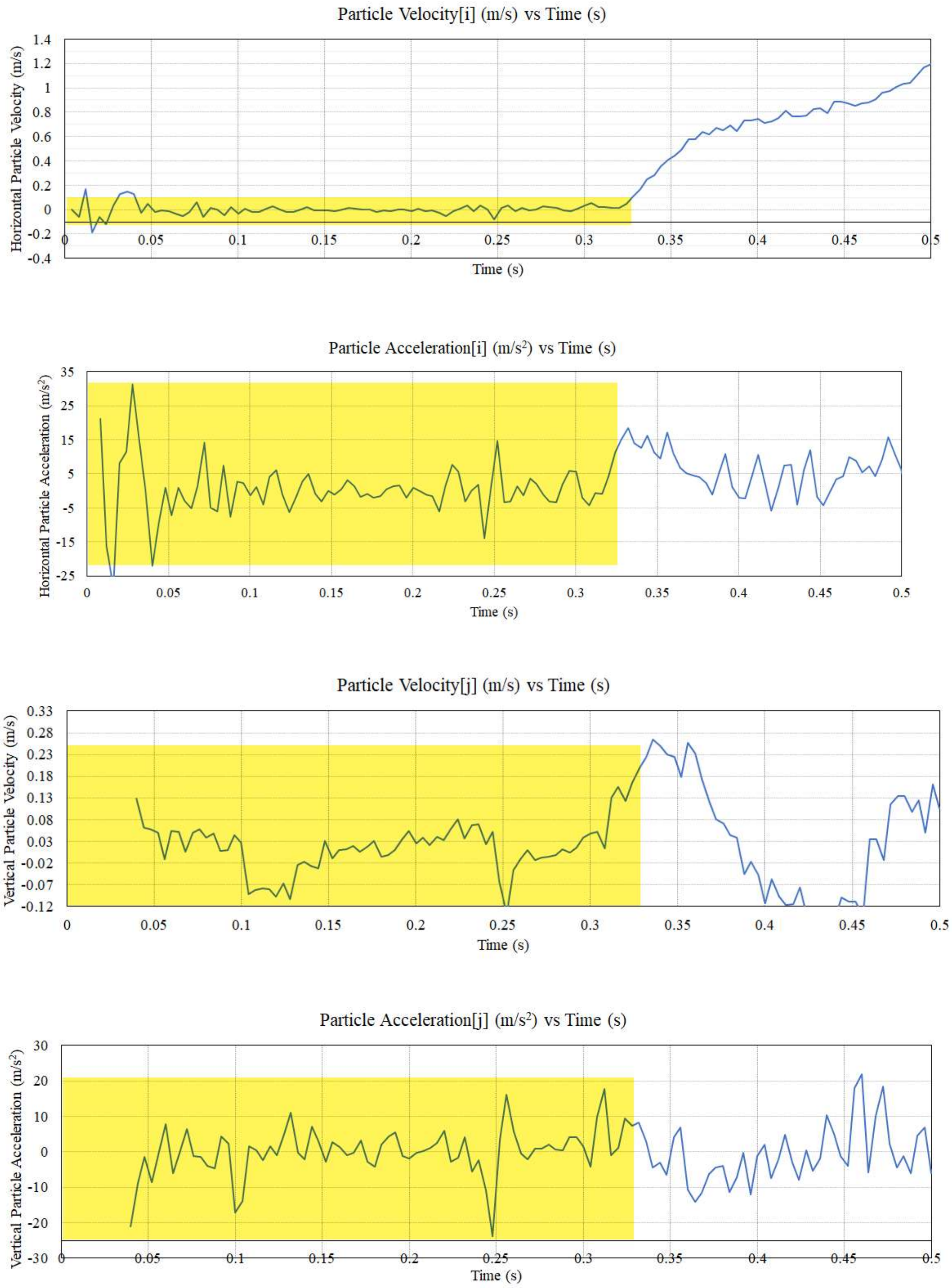

Figure 4-27. Horizontal and vertical velocities and acceleration for a particle of gravel 1 (G1) sample

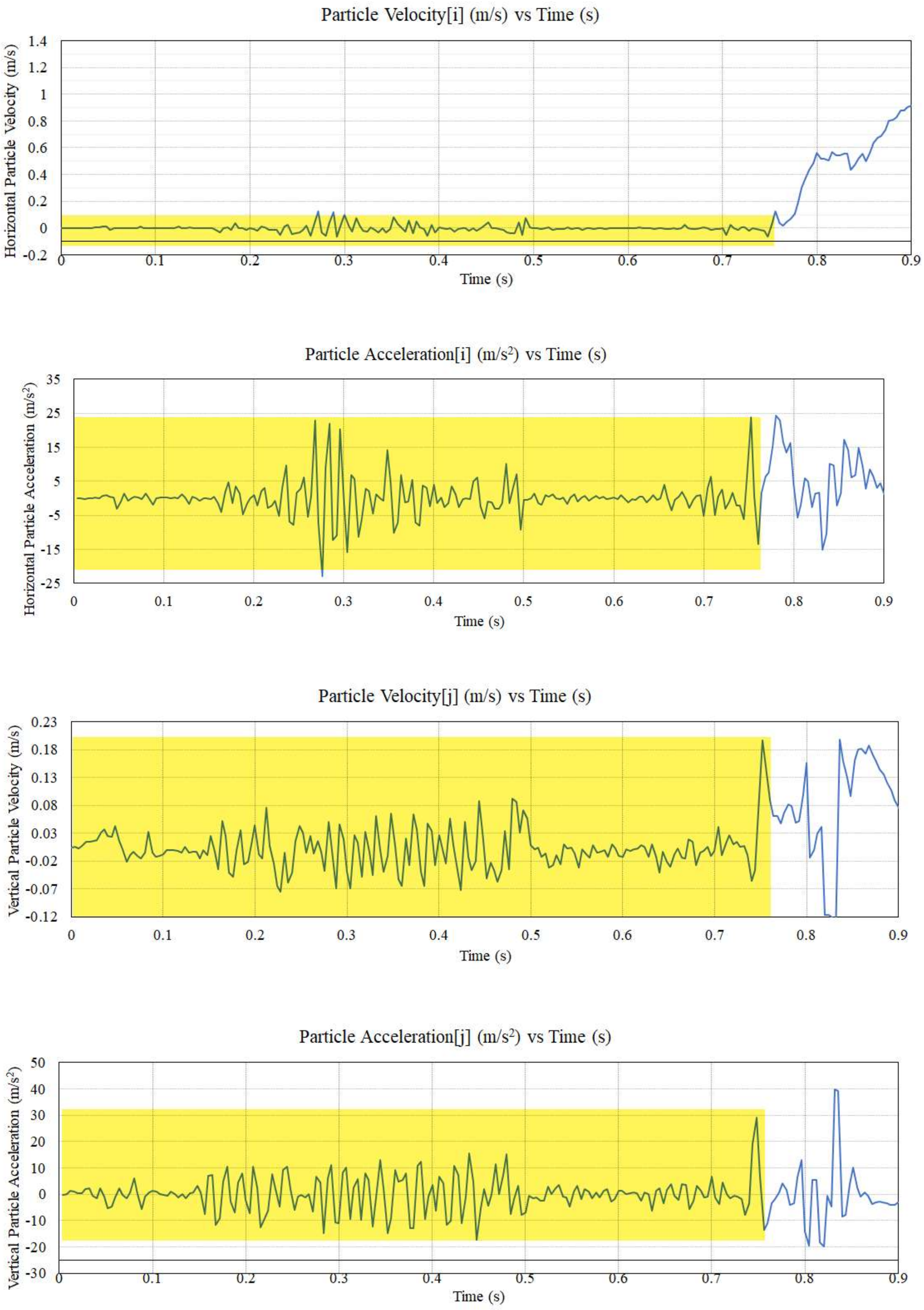

Figure 4-28. Horizontal and vertical velocities and acceleration for a particle of gravel 2 (G2) sample

Figure 4-29 indicates the final average horizontal and vertical velocities derived from the video analysis of experimental samples (Zhang, 2018). All the average values of velocities are smaller than 0.1 m/s. for the samples with an average size of 5 mm, the horizontal component is larger than the vertical component (TB, SB, and GB), while for the larger particles (G1 and G2), the values of both components are similar.

Figure 4-30 displays the horizontal and vertical velocities resulted in numerical simulation. Similar to the video analysis results, the average velocity values are proportional to the D_{50} of the particles. For the numerical results, except for G1 particles, all other velocities are smaller than 0.1 m/s.

Figure 4-31 shows the final average horizontal and vertical accelerations from video analysis of EFA tests on each sample (G1, G2, TB, SB, and TB). The average horizontal accelerations for all samples are higher than g. for TB, SB, and GB, the horizontal accelerations are higher than the vertical accelerations. At the same time, for the G1 and G2 cases, both components are similar.

Figure 4-32 presents the final average horizontal and vertical accelerations for the numerical simulation of the EFA test on the same samples. With the numerical simulation, the overall average accelerations (horizontal and vertical) are lower than the video analysis calculations. It should be noted that in the experimental analysis, the vibration f pump can cause more fluctuations, and the amplitudes of accelerations are higher. In both cases, for the smaller size of particles (TB, SB, and GB), horizontal components can play a significant role in the start of motion, while for larger particles (G1 and G2), the effect of vertical component (lift) can balance the effect of horizontal component.

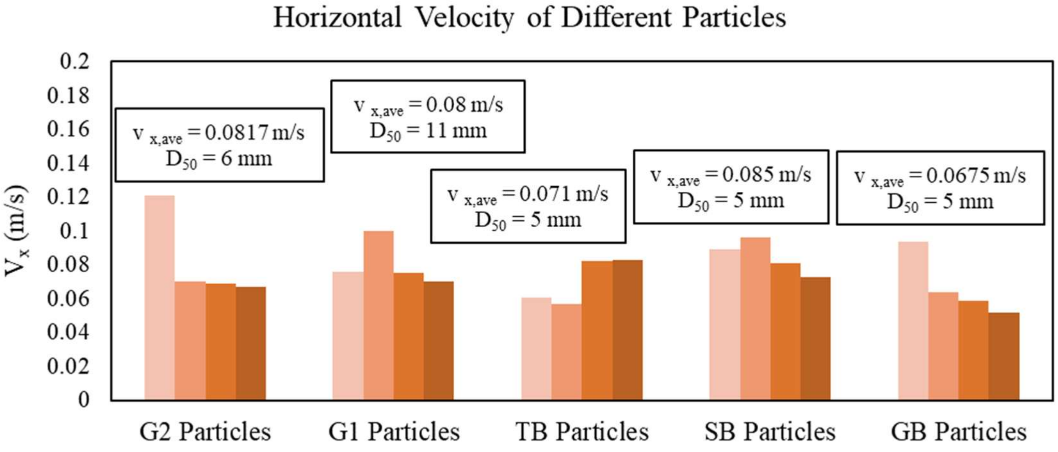

(a)

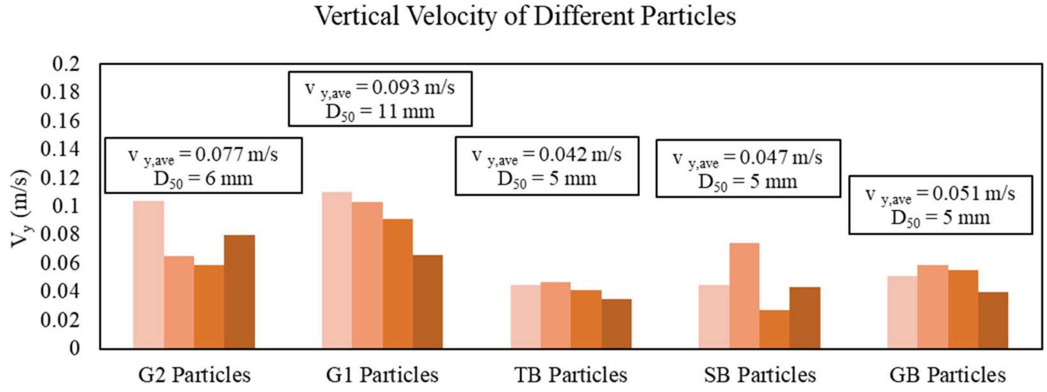

(b)

Figure 4-29. Average horizontal and vertical velocities resulted from video analysis of different samples

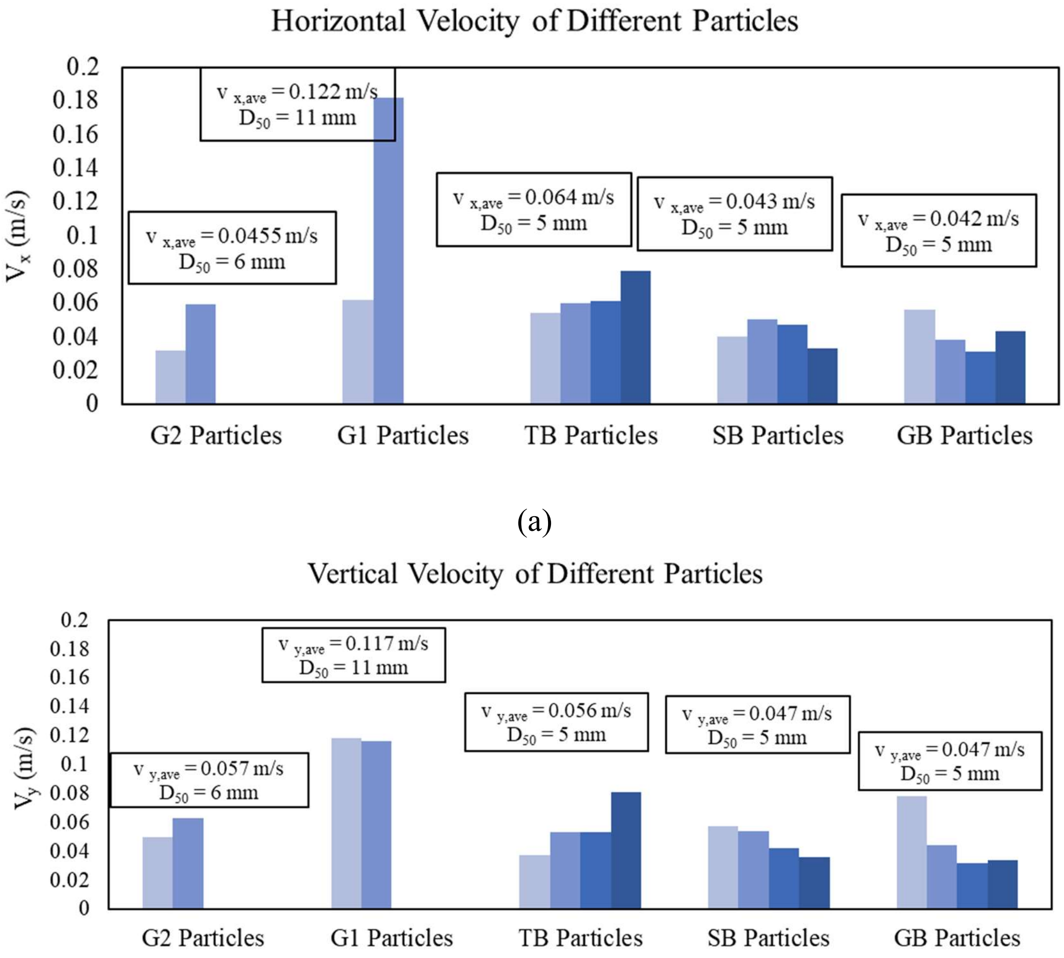

(a)

(b)

Figure 4-30. Average horizontal and vertical velocities resulted from CFD-DEM simulation of different samples

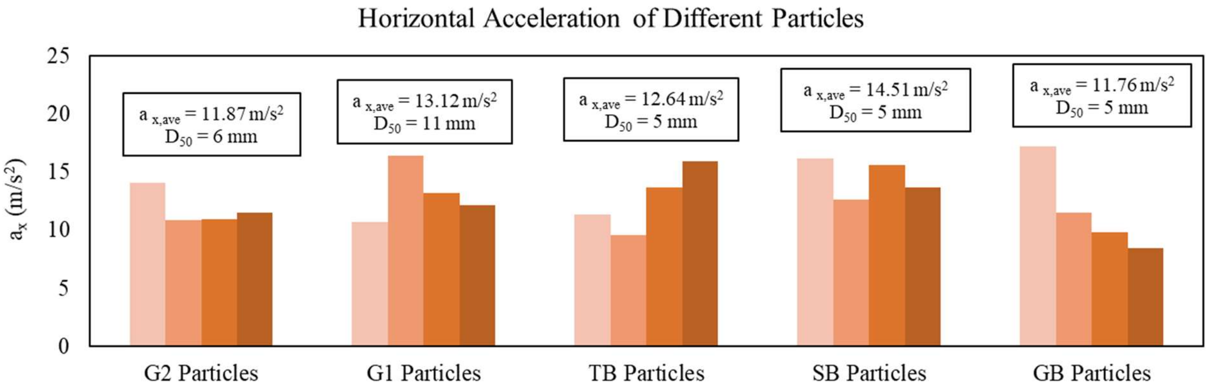

(a)

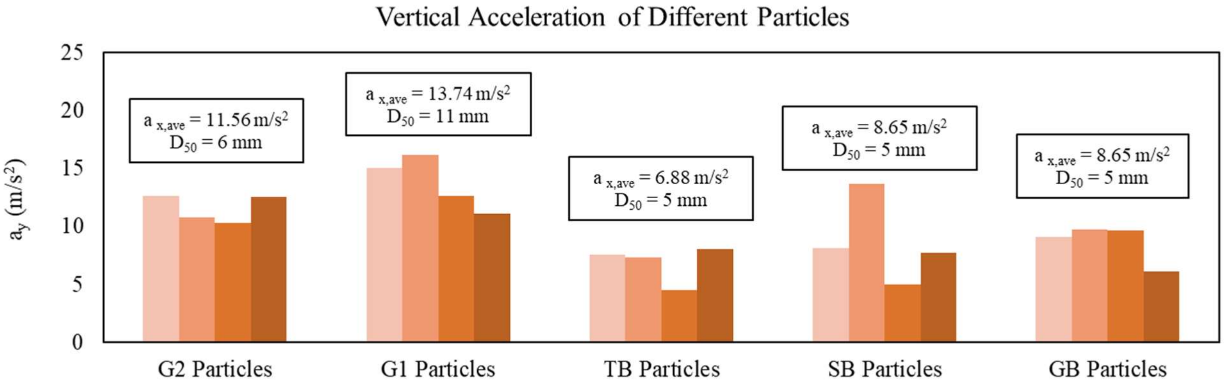

(b)

Figure 4-31. Average horizontal and vertical accelerations resulted from video analysis of different samples

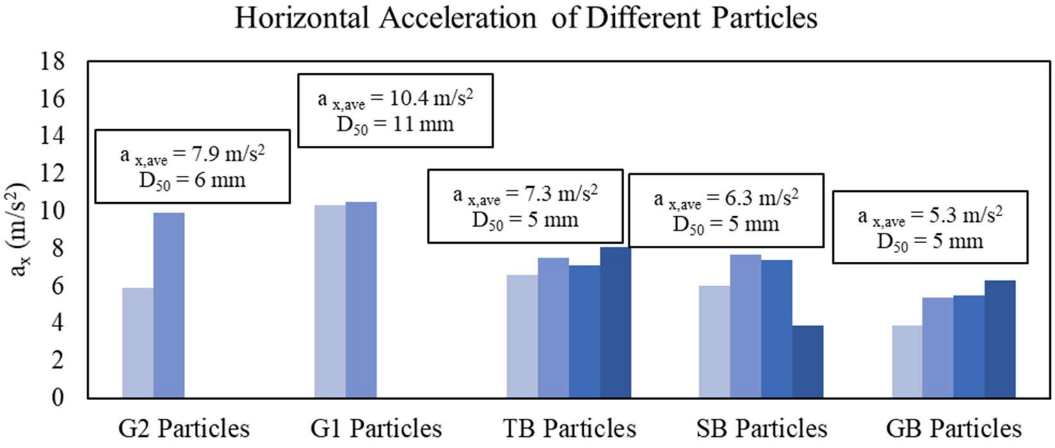

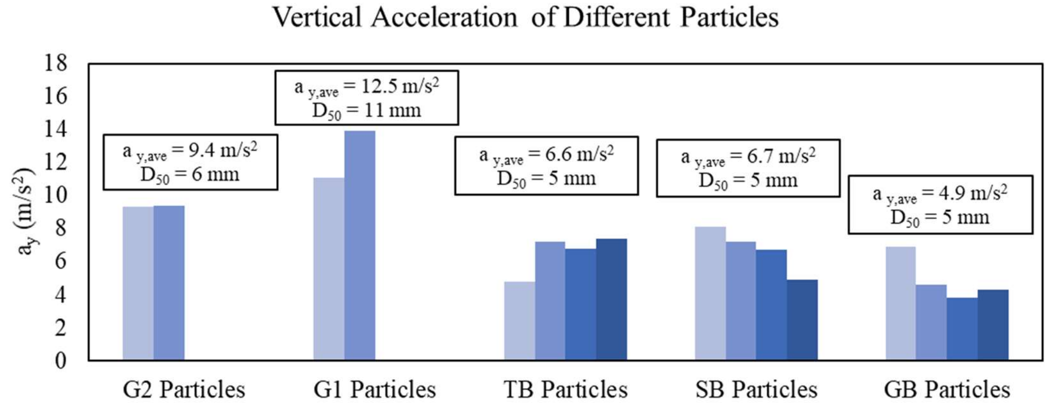

Figure 4-32. Average horizontal and vertical accelerations resulted from CFD-DEM simulation of different samples

4.3.3. Contributions of horizontal and vertical components of fluid force at the start of motion

Figure 4-33 shows the drag force against the lift force. Both drag and lift forces are normalized with water density (ρ), flow velocity (v), and the average size of particles (D_{50}) as $F_{Drag}/\rho\ v^2 D_{50}^2$ and $F_{Lift}/\rho\ v^2 D_{50}^2$ respectively. The effect of the horizontal component of fluid force (shear stress) is predominant. However, for several particles, the effect of the vertical component of fluid force (normal stress) can not be denied. It can be inferred from the position of particles that the contribution of each component in the start of motion depends on the initial position of the particle inside other particles and the particle size. If the particle stocked inside other particles, the start of motion can be triggered when the driving moment is higher than the resisting moment. When the pivot point in which the particle can rotate around it is shallow, the horizontal component (drag) has a significant contribution. When the pivot point is deep, the horizontal stress is not large enough to start the motion, and the role of the vertical component is more highlighted. The particle needs to move upward, and after that, the fluid force can be enabled to start the motion.

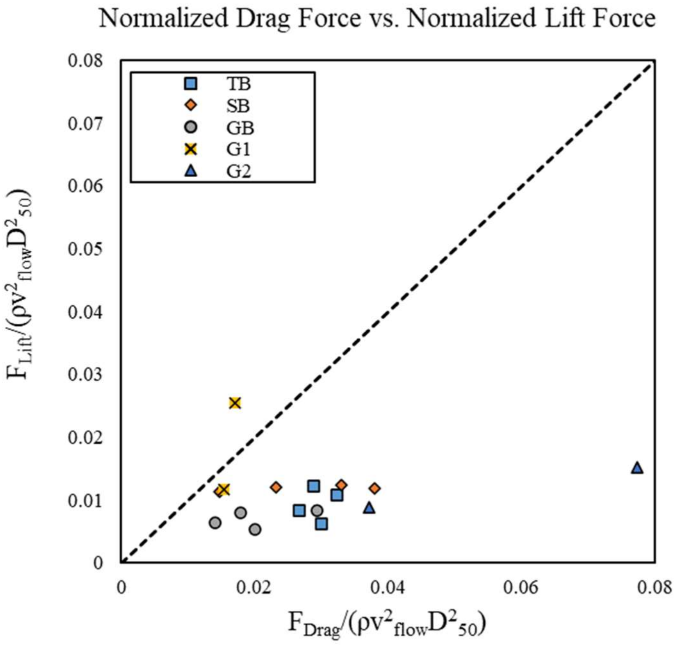

Figure 4-33. Comparison of drag force and lift force contributions in the incipient motion of different particles

4.3.4. Comparison of shear stress calculated from the moody chart and the fluid forces

Figure 4-34 presents the shear stress calculated from the moody chart, compared to the shear stress calculated in the CFD software, assuming an interface with a roughness height of $D_{50}/2$ instead of the sample. The former method utilizes Equation 3-1 ($\tau = \frac{1}{8} f \rho v^2$) to calculate shear stress. This equation is calculated for a circular shape and from the equilibrium of pressure forces and viscous forces. More importantly, it is assumed that the shear stress is uniformly distributed on the surface. The CFD method uses the $k - \varepsilon$ method to calculate the shear stress, and since an interface with a roughness of $D_{50}/2$ has been assumed instead of the soil sample, the values of shear stress are similar to the values calculated from the moody chart.

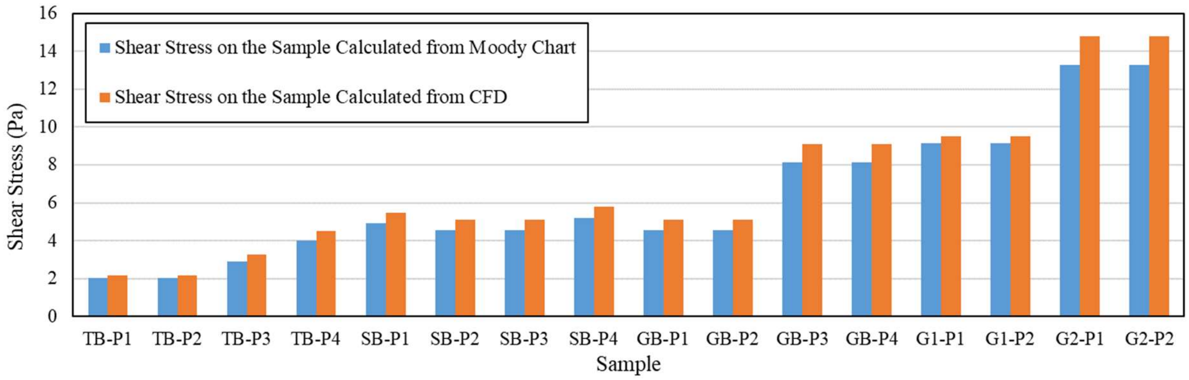

Figure 4-34. Comparison of shear stress calculated from the Moody chart and CFD

Figure 4-35 shows the shear stress on the particle, which is calculated from the drag force divided by the area of the particle area (projected area). These values are higher than the values calculated from the moody chart and the CFD method. This result is reasonable since the local shear stress is calculated for one particle and not for the whole surface (average shear stress). The drag forces for the particles on the surface have different values, and their values differ with time; this is why particles start to move from particular areas at different times based on their position and their exposure to the viscous and pressure forces. It means that the boundary shear stress is not exactly the value that causes the start of motion. Still, the local shear stress, which is variant with time and is more significant than boundary shear stress, is responsible for starting the motion of particles. Although, since average shear stress represents the average of drag forces on the bed particles, it can be a good descriptor for the threshold of the movement (Southard (2006)).

Figure 4-35, also indicated all the shear stress together. Although for large particle sizes, the difference between shear stress is high, for other samples, values are closer to each other. Obviously, this value is near the moody chart, and CFD shear stresses for the smaller size of particles, but by increasing the size, due to more voids and significant change in the sample surface, the difference tends to be increased.

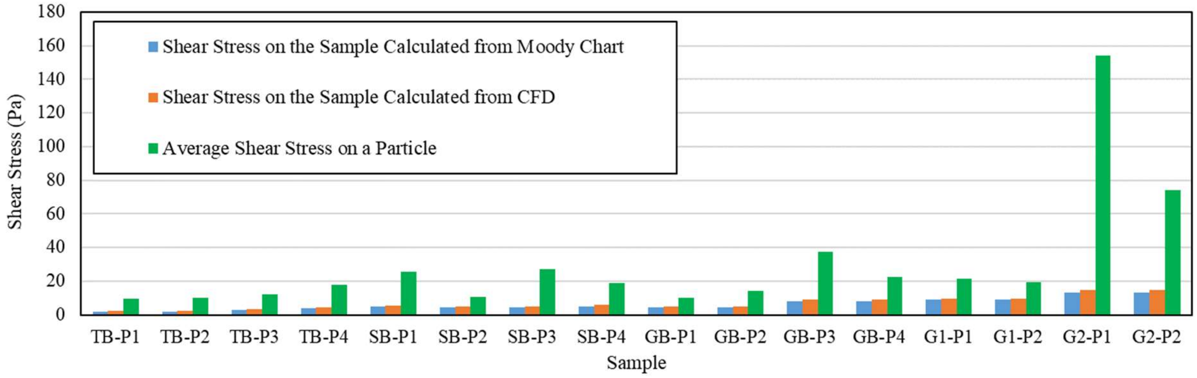

Figure 4-35. Comparison of shear stress calculated from the Moody chart, CFD, and average shear stress on the sample calculated from average shear stress on one particle

4.4. Conclusion

In this chapter, by utilizing a validation example, the ability of CFD-DEM in capturing the velocity, accelerations, and drag forces was demonstrated. By modeling the Erosion Function Apparatus (EFA), erosion functions resulted from experimental modeling and the CFD-DEM method, was compared. The accordance of the results was excellent. By tracking the velocities and acceleration of the results in CFD-DEM, their values were compared with the corresponding experimental results using video analysis. A good agreement was observed between the numerical and experimental results. More importantly, critical velocities and critical shear stresses were perfectly fitted to the results from former researchers.

Accelerations calculated from the numerical simulation were applied to study the contributions of horizontal and vertical components of fluid force in the incipient motion of the particles. Results indicated that in small particles, the horizontal component plays the primary rule, while, in large gravel particles, the contribution of the vertical component also highlighted its rule.

Finally, the shear stress calculated form the moody chart and CFD (by considering a plane with a roughness of $D_{50}/2$ instead of the sample) and local shear stress on the particles by CFD-DEM method was investigated. The local shear stress in the gravel particles is larger than the average shear stress calculated from the moody chart, and CFD method, and this difference can be magnified in the larger particles.

5. NUMERICAL SIMULATION OF EROSION USING CFD-DEM TECHNIQUE AND APPLICATIONS

In this chapter, a more in-depth CFD-DEM analysis of erosion is presented. In the first section, by constructing a numerical EFA test simulation, the effect of several parameters on the erosion function is investigated. These parameters are the diameter of particles, the density of particles, dry density of the sample, static friction factor, rolling friction factor, cohesion between particles, and abrasion of suspended particles on the sample particles.

In the presence of infilling, the scour depth, which is measured after a storm, may not represent the maximum scour depth. It highlighted the importance of infilling and the necessity to study it more. The second section covers the CFD-DEM modeling of infilling, including the essential parameters which can affect its magnitude. Parameters such as the depth of the scour hole, the scour hole slope, dry density of bed, friction between particles, and cohesion are considered.

Internal erosion can be initiated by concentrated leak erosion, backward erosion, soil contact erosion, or suffusion (Fell and Fry 2007). It is responsible for numerous failures in hydraulic structures and needs to be more studied. In hydraulic geotechnical structures such as dams and levees, soil with different gradation curves can be in contact, for example, at the boundary of the core material and filter or filter and shell. The effect of seepage flow inside the soil can migrate the small particles through the voids between the large ones. This phenomenon is called soil contact erosion. In the core and filter materials, the migration of small particles through the large ones by the effect of fluid flow, which is called suffusion, can increase the hydraulic gradient and change the shear stress in the core and shell materials. In the third section, the numerical modeling of these two types of internal erosion is studied. By the CFD-DEM modeling of these two phenomena, several geometric criteria used in the design of common hydraulic structures is investigated. The adequacy of the Terzaghi (1939) criterion in soil contact erosion is explored. For suffusion, Istomenia (1957), Kezdi (1969), Kenney and Lau (1985), Burenokova (1993), Li and Fennin's (2008) criteria are examined with several CFD-DEM models.

5.1. Erosion Function Apparatus (EFA)

Erosion function (EF) is considered as the constitutive law of soil in erosion. Erosion function can be explained in terms of erosion rate vs. velocity or erosion rate vs. shear stress. Since the erodibility of the soil is tied to the soil properties, understanding the sensitivity of soil erosion function to the physical parameters can help to know the essential parameters in the erosion process. Briaud et al. (2019) studied the relationship between soil erodibility and soil properties and published their results as an NCHRP report (research report 915). The relationship between the erodibility and soil properties depends on the type of soil. The properties that affect the erodibility and erosion function are different in coarse-grained soils and fine-grained soils. The number of correlation parameters affecting the soil erodibility increased by decreasing the size of particles from sand to clay. In coarse-grained soils, the mean grain size is the essential parameter. For the fine-grained soils, due to the presence of clay minerals, a large number of parameters affect the erodibility, which is very complex to be modeled with numerical simulation. As explained by Briaud, and former researchers (Shields 1935, Vanoni (1975)), critical shear stress in pascal is approximately equal to the mean grain size of particles in mm. Critical velocity also can be correlated with the mean grain size of particles with acceptable accuracy.

In Chapter 3, the validation of the CFD-DEM model is performed with a validation model (fluidized bed). More importantly, five real EFA tests were constructed with CFD-DEM, and their results were compared to the experimental results, which proved the accuracy of the framework. In the following numerical simulations, the effect of several parameters on critical shear velocity and critical shear stress, velocity-based erosion function slope, shear stress based erosion function slope, and overall shape and curvature of the erosion function is studied. Size of particles, dry density of sample (void ratio and porosity), friction between particles, rolling resistance of particles, dry density of the sample, and cohesion between the particles are parameters that their effects on EF are probed. Finally, the effect of abrasion of suspended particles on the bed particles in EF is also investigated with several models.

5.1.1. CFD-DEM model of EFA

The numerical model utilized to do the sensitivity analysis is similar to the model used in Chapter 4. The exact geometry of the EFA is constructed. Fluid flow enters the circuit from the right side (inlet) and exit from the left side of the circuit (outlet). Figure 5-1 displays the geometry of the model, including mesh configuration. The number of DEM particles and the number of CFD meshes depends on the size of particles. In the modeling, only 4 cm of the DEM sample is simulated to save the computational cost. The sample was kept stationary during the simulation. Each point of erosion function is the result of one simulation with a specific velocity. Table 5-1 summarizes the properties of the numerical model.

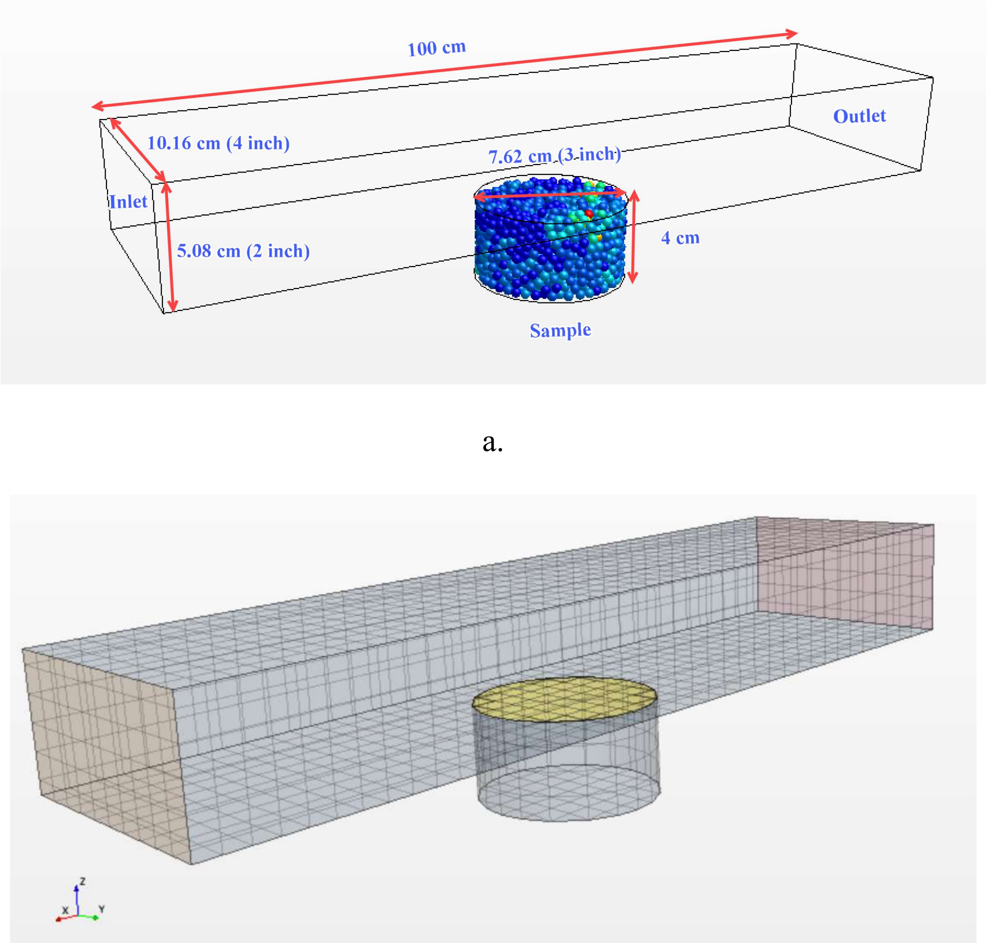

a.

b.

Figure 5-1 a) Geometry of the EFA b) Typical mesh configuration for the model

Table 5-1. Physical and computational properties for the particulate and fluid media

Parameter	Particles	Walls
Density (kg/m^3)	2650	7850
Modulus of Elasticity (Pa)	1×10^7	1×10^{11}
Poisson Ratio	0.3	0.3
Friction Coefficient	0.5	0.5
Normal Restitution Coefficient	0.5	0.5
Tangential Restitution Coefficient	0.5	0.5
Coefficient of Rolling Resistance	0.1	
Computational parameters		
DEM time step	1.14×10^{-5}	
CFD time step	1×10^{-3}	
CFD mesh size (mm)	$5 \times 5 \times 5$	
CFD turbulence model	$\mathrm{k} - \varepsilon$ Turbulence	
Drag Force Model	Schiller-Naumann	

5.1.2. Effect of particle diameter

Figure 5-2 shows the change of erosion function for three different particle diameters. The distinct difference between erosion functions is clear. With the increase of the diameter of particles, the erosion function curve shifts toward the right. Critical velocity values are 0.25 m/s, 0.4 m/s and 0.75 m/s for 1 mm, 2mm and 5 mm of diameter respectively. Although, by increasing the value of erosion rate, the slope of the erosion function for each case decreases, the slopes of the curves for all cases are approximately similar. In terms of erosion category, it changes from high erodibility for 1 mm and 2 mm particle sizes to near medium erodibility for 5 mm particle size.

Figure 5-3 presents these data along with other measurements published in the literature (Briaud, 2013). Current results are specified with blue and red colors on the chart. The critical velocity data conform to these data.

Figure 5-4 displays the erosion functions in terms of shear stress vs. erosion rate. The same trend for the effect of particle size can be observed in shear stress based erosion functions. Critical shear stress values are 0.3 Pa, 0.9 P a, and 5.1 Pa for 1 mm, 2mm, and 5 mm of diameter, respectively. Figure 5-5 shows the data from tests as a function of mean grain size published in the literature (Briaud, 2013). Current results are specified with blue and red colors on the chart. These data perfectly fitted to the curve proposed by shields in 1936.

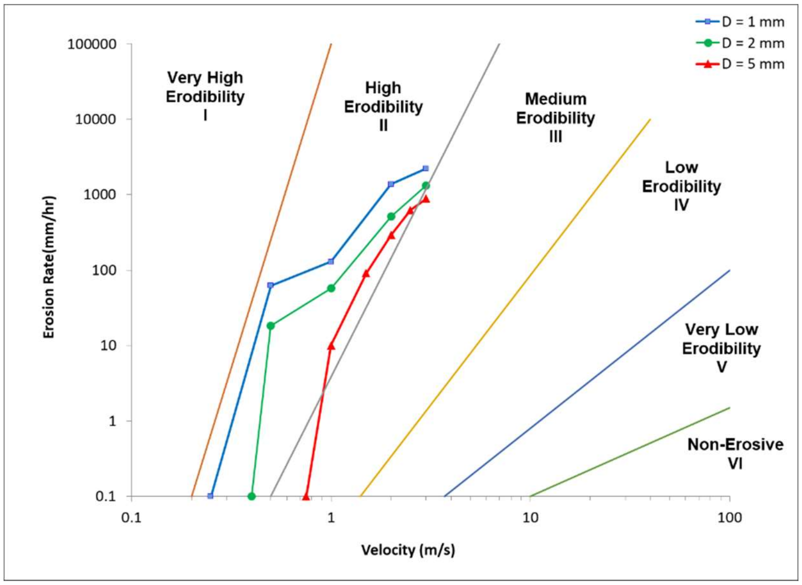

Figure 5-2. Erosion rate vs. velocity for different sand particle sizes

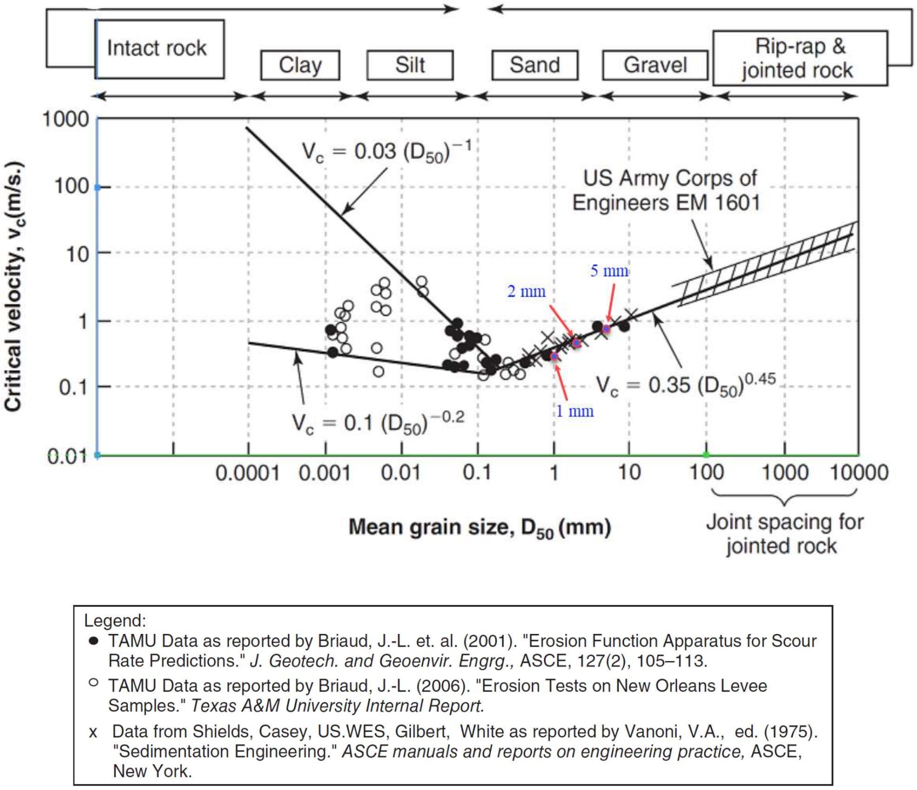

Legend:

- ● TAMU Data as reported by Briaud, J.-L. et. al. (2001). "Erosion Function Apparatus for Scour Rate Predictions." *J. Geotech. and Geoenvir. Engrg.,* ASCE, 127(2), 105–113.
- ○ TAMU Data as reported by Briaud, J.-L. (2006). "Erosion Tests on New Orleans Levee Samples." *Texas A&M University Internal Report.*
- x Data from Shields, Casey, US.WES, Gilbert, White as reported by Vanoni, V.A., ed. (1975). "Sedimentation Engineering." *ASCE manuals and reports on engineering practice,* ASCE, New York.

Figure 5-3. Critical velocity as a function of mean grain size

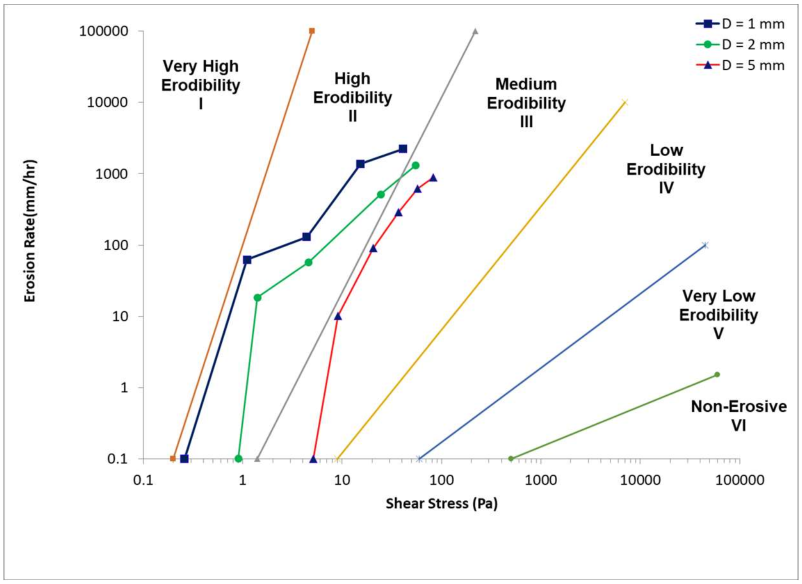

Figure 5-4. Erosion rate vs. shear stress for different sand particle sizes

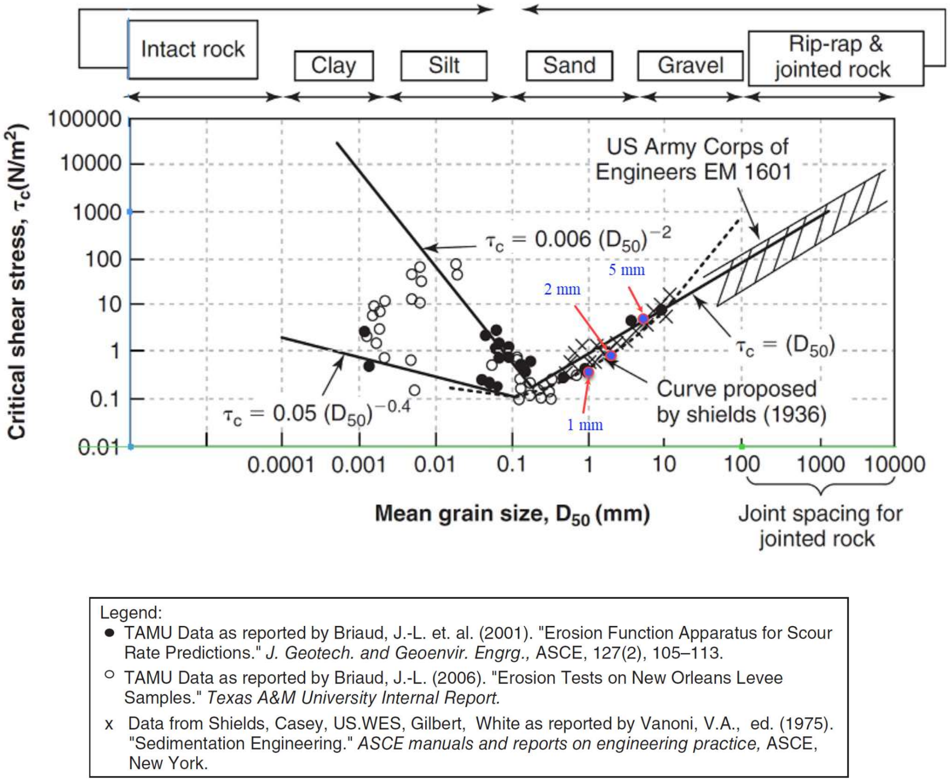

Figure 5-5. Critical shear stress as a function of mean grain size

5.1.3. Effect of static friction coefficient

The static friction coefficient is a physical parameter that can stand for the friction and angularity between the particles. A sample with a mean grain size of 5 mm has been simulated to investigate the effect of friction between the particles on erosion function. The rolling resistance for all cases is considered as 0.1 to differentiate the effect of friction coefficient from the rolling resistance. Figure 5-6 and Figure 5-7 show the velocity vs. erosion rate and shear stress vs. erosion rate graphs. Both critical velocity and critical shear stress are affected by the friction between the particles. Although the slope of erosion functions is close to each other, their values are distinctive.

A more angular sample with high friction coefficient between particles can be classified as medium erodibility, while a sample with smooth particles can be classified as high erodibility.

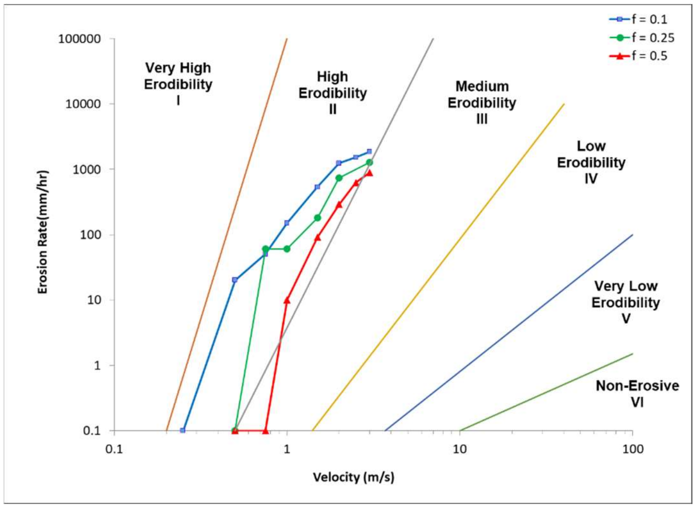

Figure 5-6. Erosion rate vs. velocity for different friction coefficients between particles

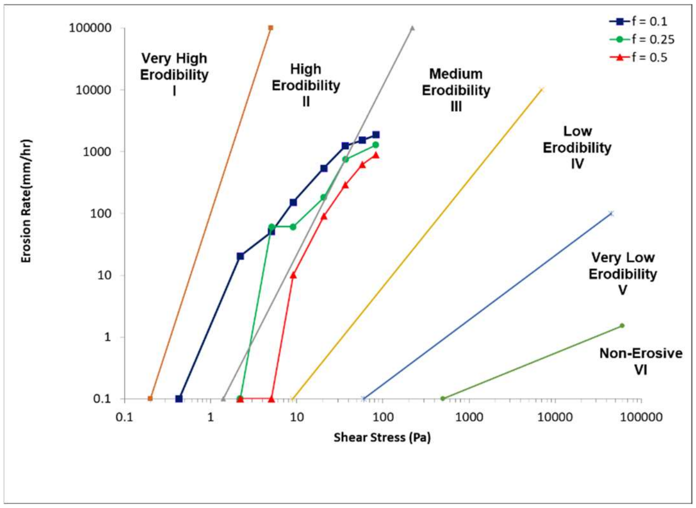

Figure 5-7. Erosion rate versus shear stress for different friction coefficients between particles

5.1.4. Effect of rolling resistance coefficient

Modeling the shape of particles in DEM is computationally expensive; instead of rolling resistance can be used as an alternate way to see the effect of shape (Wensrich and Katerfeld (2012)). As explained in the background knowledge, the coefficient of rolling resistance defines as the factor of resisting torque against the rolling. When rolling resistance is zero, the particle does not have any resistance against the driving moment. In contrast, a particle with a high rolling resistance value shows a substantial resisting torque against rolling. The friction coefficient is kept as 0.5 to differentiate the effect of rolling resistance from the friction coefficient. Figure 5-10 and Figure 5-11 indicate velocity vs. erosion rate and shear stress vs. erosion rate for samples with different coefficient of rolling resistance. In each case, by increasing the velocity, the shape of the curve is inclined to the horizontal axis, which is compatible with the experimental testing. More importantly, it shows that the shape of the erosion function is always concave downward in a log-log plot. Both of critical shear velocity and critical shear stress increase by increasing the resistance of the parties towards rolling. When the rolling resistance is zero (spherical shape), the erosion rate is much higher than the cases with lower values of the rolling resistance coefficient.

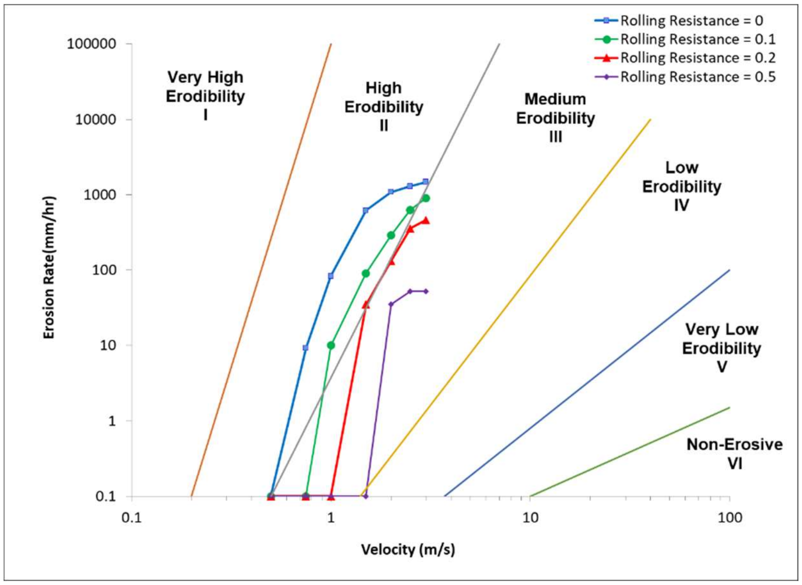

Figure 5-8. Erosion rate vs. velocity for different values of rolling resistance coefficient between particles

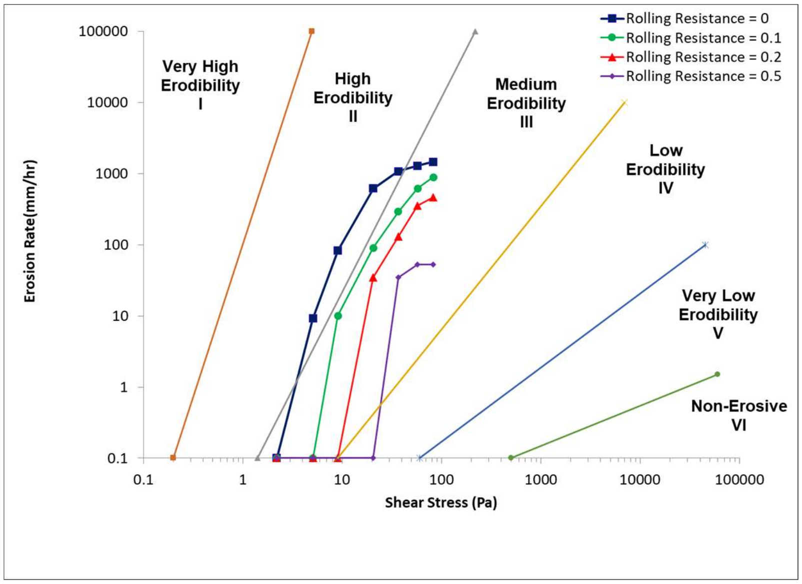

Figure 5-9. Erosion rate vs. shear stress for different values of rolling resistance coefficient between particles

5.1.5. *Effect of dry sample density*

Figure 5-10 and Figure 5-11 show the effect of dry density on the velocity-based and shear stress based erosion functions. The dry density does not affect the erosion function at a low erosion rate. The difference becomes distinctive in high erosion rates (more than 100 mm/hr). Although the difference is distinguishable in high erosion rates (more than 100 mm/hr), it is minimal compared to the effect of other parameters. A looser sample can be more affected by the velocity and boundary shear stress than a dense sample. This can be attributed to lower interlocking between the particles. In this way, the pressure fluctuations around the particles are higher, and the exposed surfaces of the particles are more significant. Simultaneously, the particles have enough space and can be rotated easily by a driving moment.

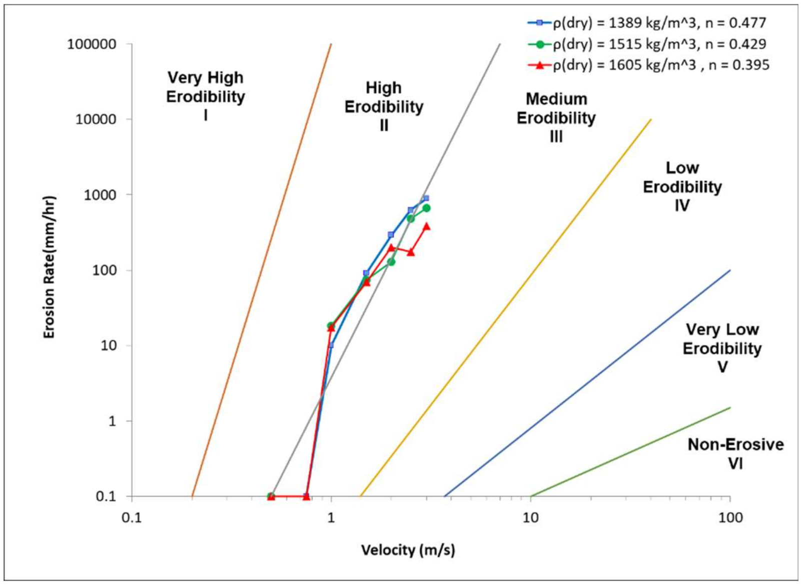

Figure 5-10. Erosion rate vs. velocity for samples with different dry densities

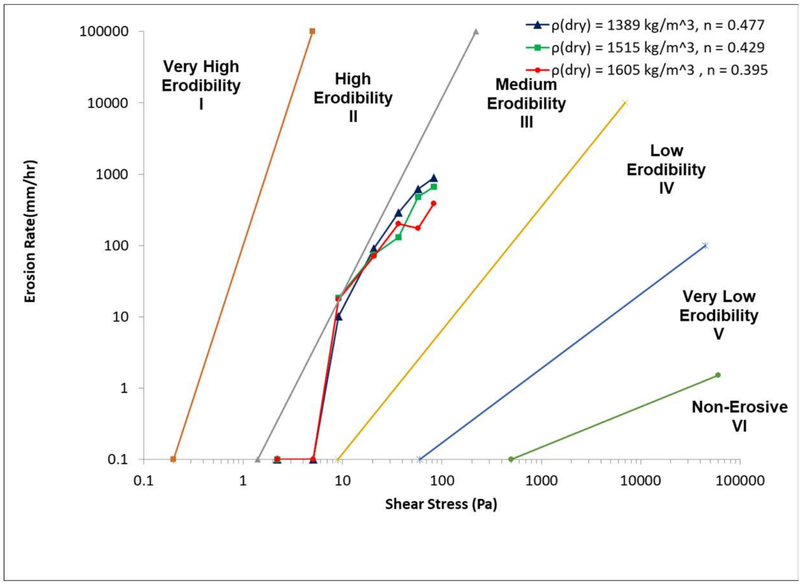

Figure 5-11. Erosion rate vs. shear stress for samples with different dry densities

5.1.6. Effect of cohesion between particles

Understanding the behavior of cohesive materials in erosion is complicated. Although the effect of cohesion on the increase of soil resistance against erosion is apparent, its mechanism needs to be more speculated. Numerous factors affect the behavior of clay particles, and considering the size of clay particles, their modeling to investigate the effect of cohesion is very computationally expensive. For this reason, two sand samples with different mean grain sizes are simulated to investigate the effect of cohesion on the behavior of samples against erosion.

In DEM, the bond between the particles can be simulated by linear cohesion between the particles and parallel bonds. In the former, the bond allows the particles to rotate with respect to each other. While in the latter, the bond does not allow the rotation. The linear cohesion model is used in this section to model the cohesion. As explained in the background knowledge, the work of cohesion is the parameter that should be defined between the particles to observe the effect of cohesion. Cohesion is connected to the work of cohesion by the following cohesion:

$$2w\pi a = c' \pi R^2 \; \& \; a = \frac{R}{4} (a, radius\ of\ surface\ in\ contact) \implies c' = w/(2R) \qquad 5\text{-}1$$

where w is the adhesion between particles in N/m, a is the radius of the surface, which can be considered as a fraction of particle radius (Here a assumed as $\frac{R}{4}$ and R, is particle radius), and c' is the cohesion between the particles.

Figure 5-12 and Figure 5-13 show the velocity-based and shear stress based erosion functions for samples with different cohesions on the erosion categories chart. By increasing the cohesion from 0 to 5 kPa, the critical velocity increases from 0.75 m/s to 4 m/s. In the same trend, critical shear stress increases from 5.1 Pa to 147.3 Pa. The initial erosion rate in shear stress based erosion function (erosion modulus) is higher than the erosion modulus in erosion rates more than 10 to 20 mm/hr. The overall shape of the erosion functions is concave downward, the same as the erosion functions observed in the experimental modeling. In terms of erosion categories, erosion function with high to medium erodibility in the case of zero cohesion shifts to erosion category of low erodibility in cases with higher cohesion.

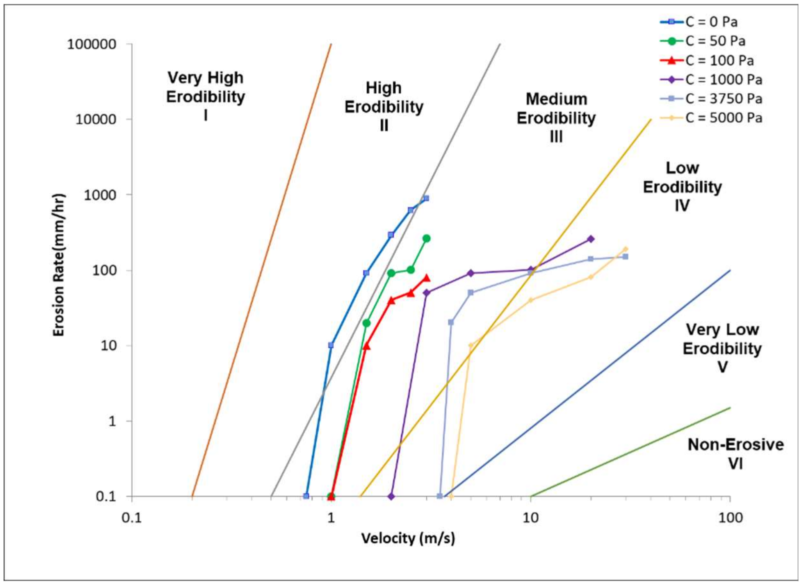

Figure 5-12. Erosion rate vs. velocity for samples with a mean grain size of 5 mm and different cohesion values

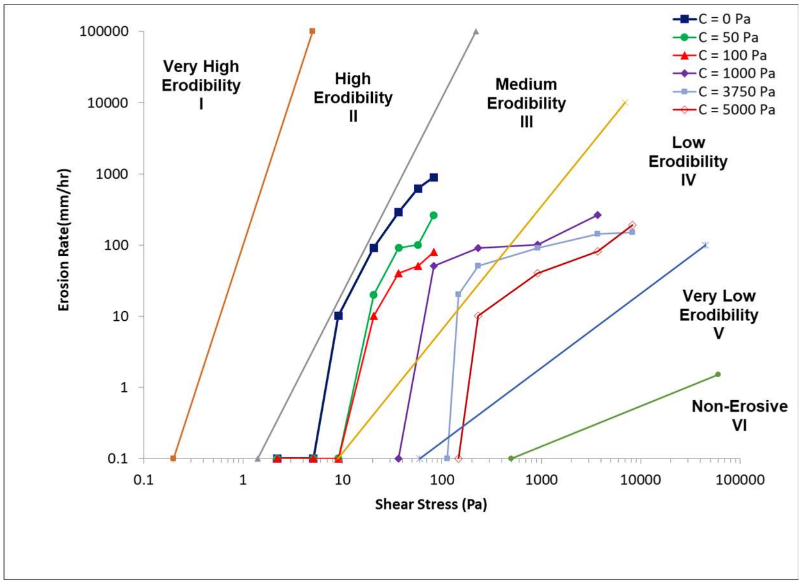

Figure 5-13. Erosion rate vs. shear stress for samples with a mean grain size of 5 mm and different cohesion values

Figure 5-14 displays the relationship between the critical velocity and cohesion for the samples with a mean grain size of 5 mm and different cohesion values. A quadratic curve can define the relationship between the critical velocity and cohesion. Critical velocity increases by increasing the value of cohesion, although its rate decreases with cohesion. Figure 5-15 indicates the relationship between the critical shear stress and cohesion for the samples with a mean grain size of 5 mm and different cohesion values. The relationship between the critical shear stress and cohesion is linear for this sample.

There are many equations in the literature which explains the values of critical velocity and critical shear stress. These equations are empirical and mostly suited for clays. The mean grain size of the particles is an essential parameter in the values of critical shear stress and critical velocity. Critical shear stress in Pascal is approximately equal to the mean grain size of particles in mm (Figure 5-5). Mean grain size is also the primary parameter in the empirical equations of critical shear stress (Figure 5-3).

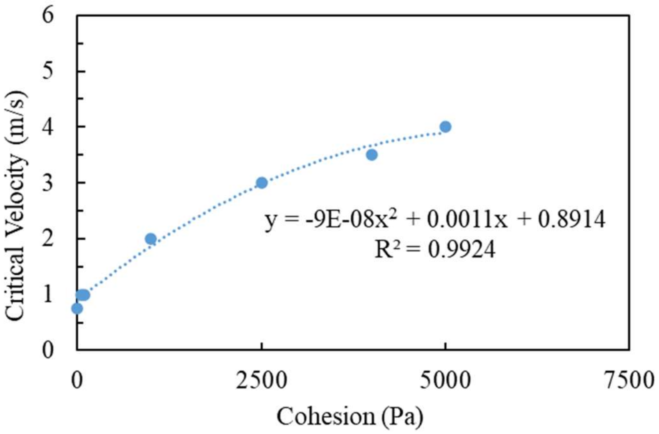

Figure 5-14. The relationship between the critical velocity and cohesion for the samples with a mean grain size of 5 mm and different cohesion values

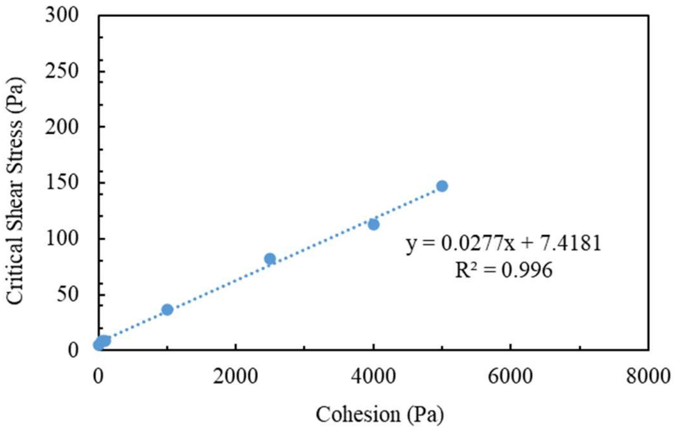

Figure 5-15. The relationship between the critical shear stress and cohesion for the samples with a mean grain size of 5 mm and different cohesion values

Figure 5-16 and Figure 5-17 illustrate the erosion rate vs. velocity and erosion rate vs. shear stress for samples with a mean grain size of 3 mm and different cohesions. In terms of critical velocity, critical shear stress, and overall shape of the erosion function, the same trend can be observed for the sample with 3 mm particles. By increasing the cohesion from zero to 3.3 kPa, critical velocities increase from 0.25 m/s to 6 m/s. The values of shear stresses increase from 0.43 Pa to 260.3, by increasing the cohesion from 0 to 3.3 kPa. The cohesion remarkably affects the resistance of the soil sample against erosion. On the erosion category chart, the position of the curve shifts to the right. The erodibility decreases from the high erodibility (II) category to medium (III) and low (IV) erodibility categories.

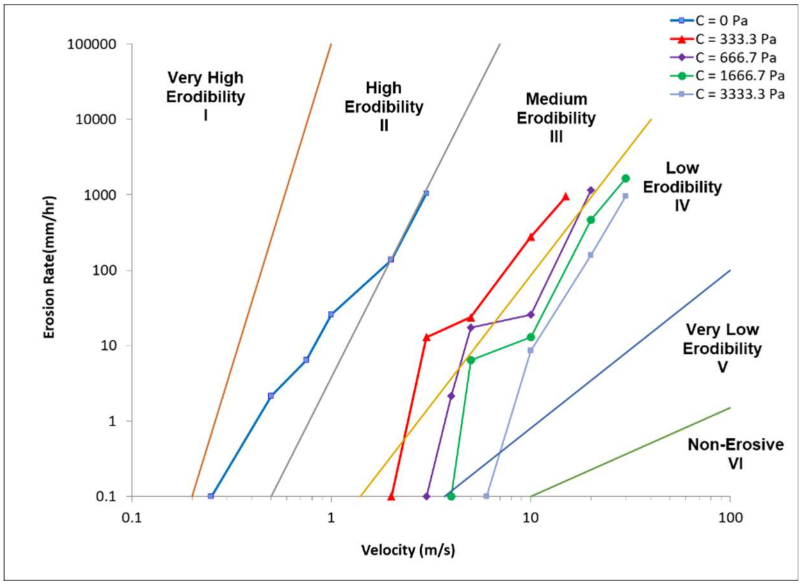

Figure 5-16. Erosion rate vs. velocity for samples with different dry densities for a sample with a mean grain size of 3 mm

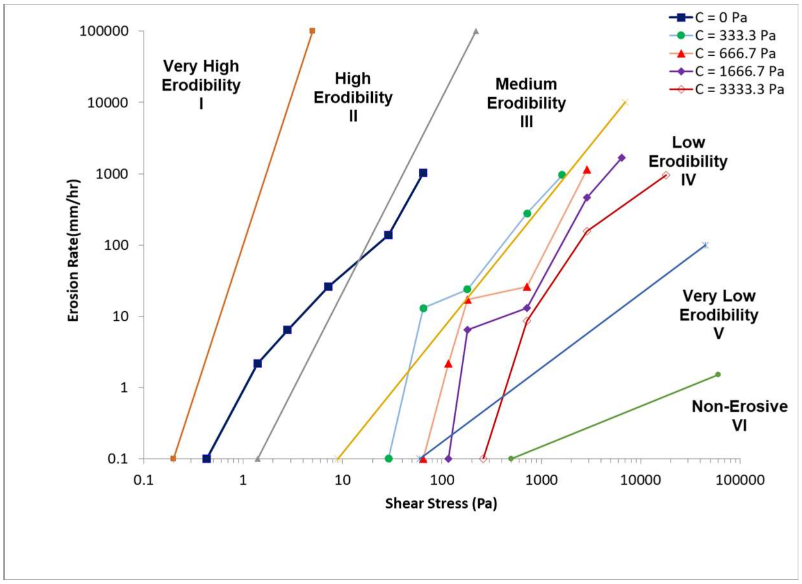

Figure 5-17. Erosion rate vs. shear stress for samples with different dry densities for a sample with a mean grain size of 3 mm

Figure 5-18 shows the critical shear stress vs. cohesion of the two samples with a mean grain size of 5 mm and 3 mm. The relationship between the critical shear stress and cohesion is linear for both cases. The value of cohesion is dependent on the particle size. To compare both cases, the sample's cohesion with 3 mm particles scaled by 2.78 ($(5/3)^2$). This factor incorporates the effect of more contact points in 3 mm particles than 5 mm particles. The effect of cohesion on the critical shear stress outweighs any other contributing factors to increasing critical shear stress. Another interesting observation is that a small amount of work of cohesion between the particles (micro parameter, w (N/m)) and small value of cohesion (macro parameter, c (Pa)) can increase the resistance of the soil against erosion.

The big question here would be why the value of cohesion is so smaller than critical shear stress (for example, in this linear relationship, cohesion is approximately 37 times of critical shear stress)? The answer could be related to the nature of these two parameters; cohesion is a macro parameter, while critical shear stress is a micro parameter. Although the final cohesion of a sample results from small micro adhesions between particles, its emergence depends on the action of sample particles together, and this mobilization increases the final value of cohesion. Critical shear stress is the required shear stress to detach one particle from the surface, which depends on the interaction between particles and micro adhesion forces between particles, which are significantly smaller than cohesion.

Figure 5-20 illustrates the critical velocity vs. cohesion of the two samples with a mean grain size of 5 mm and 3 mm. In both cases, the relationship between the critical velocity and cohesion is quadratic. The critical shear stresses of these points are also illustrated in Figure 5-19. Since our modes are restricted to sand and gravel particles, the diameter of 0.002 mm is considered for the data to be located in the clay zone (with cohesion) of the curve. The increase in critical shear stress due to an increase of cohesion is noticeable in Figure 5-19. Figure 5-21 displays the critical velocity vs. particle size chart data, considering the size of 0.002 mm instead of 3 mm and 5 mm. The position of the new data located above the data on the chart. The distinct increase of critical velocity with the increase of cohesion is specific.

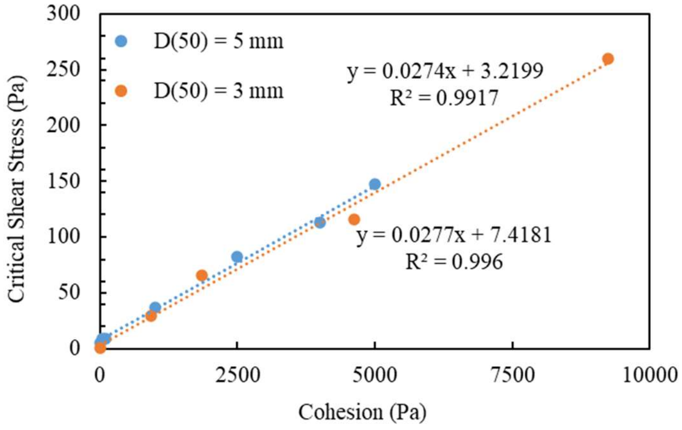

Figure 5-18. The relationship between the critical velocity of the sample and its cohesion for a sample with a mean grain size of 3 mm

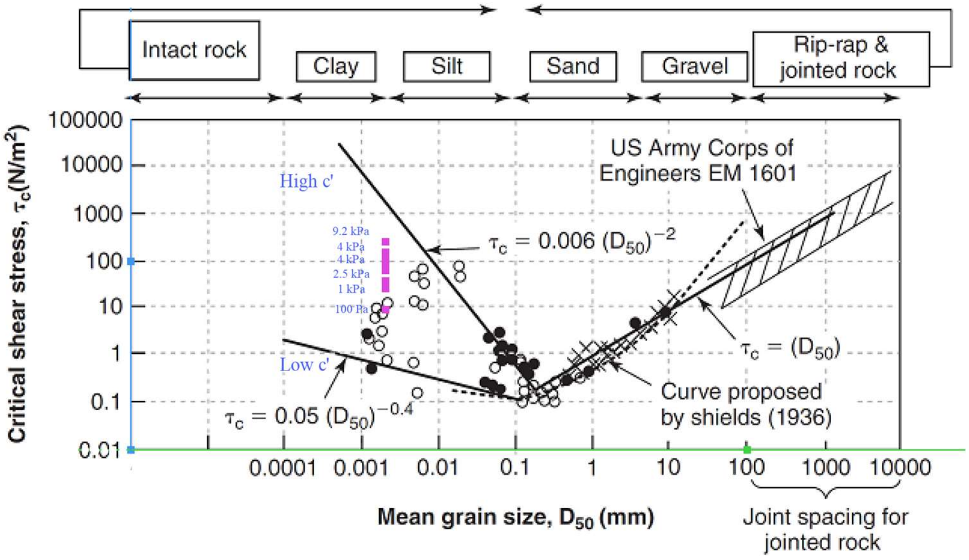

Legend:

- ● TAMU Data as reported by Briaud, J.-L. et. al. (2001). "Erosion Function Apparatus for Scour Rate Predictions." *J. Geotech. and Geoenvir. Engrg.*, ASCE, 127(2), 105–113.
- ○ TAMU Data as reported by Briaud, J.-L. (2006). "Erosion Tests on New Orleans Levee Samples." *Texas A&M University Internal Report.*
- x Data from Shields, Casey, US.WES, Gilbert, White as reported by Vanoni, V.A., ed. (1975). "Sedimentation Engineering." *ASCE manuals and reports on engineering practice,* ASCE, New York.

Figure 5-19. Critical shear stress as a function of mean grain size

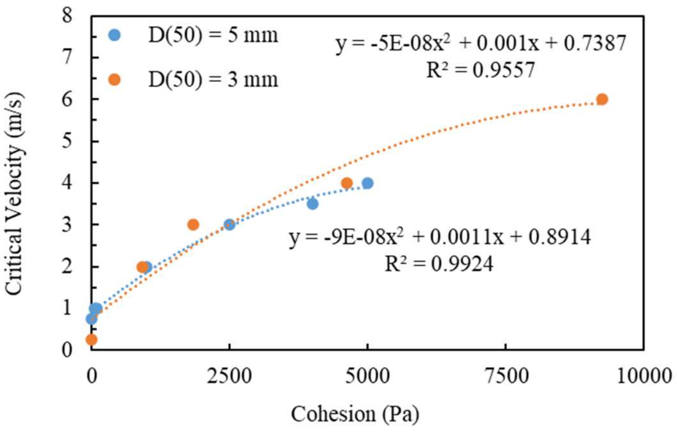

Figure 5-20. The relationship between the critical velocity of the sample and its cohesion for a sample with a mean grain size of 3 mm

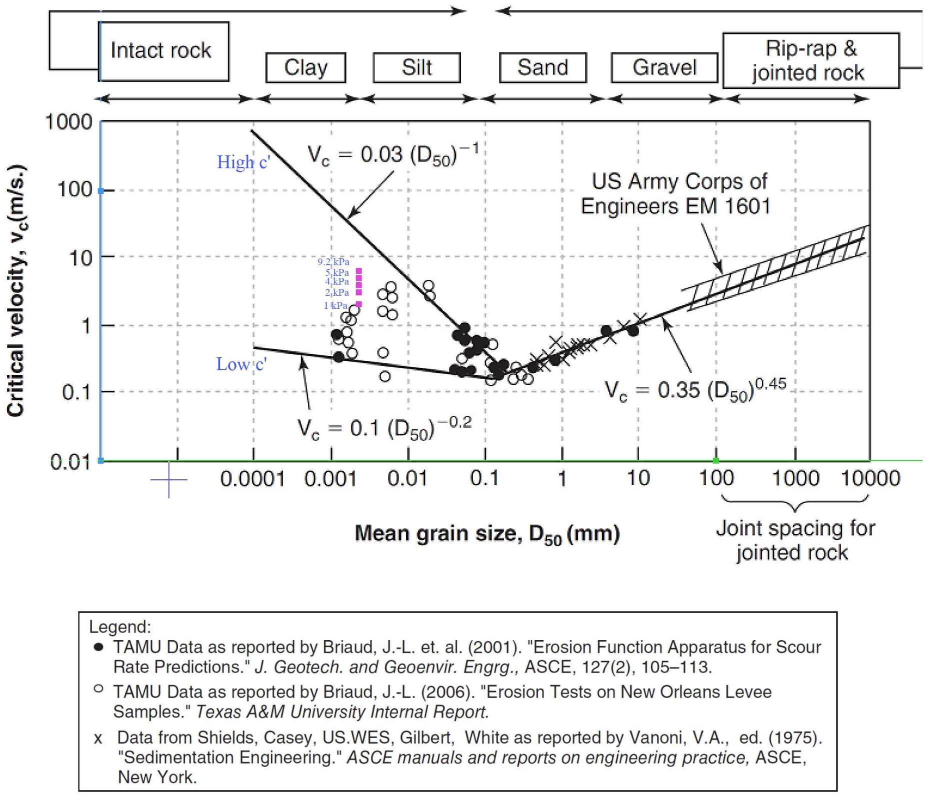

Figure 5-21. Critical velocity as a function of mean grain size

5.1.7. Effect of suspended particles abrasion on the Erosion Function

The following numerical setup has been considered to investigate the effect of suspended particles abrasion on the erosion rate of particles at the sample. Suspended particles come to the flow channel from the inlet (upstream) with a special mass flow rate. Other characteristics of the model are the same as the model, which was previously utilized to run the numerical models and derive the erosion functions. Two particle mass concentrations in the fluid have been considered with three different sizes to differentiate the effect of different sizes of suspended particles. For the sample, three particle sizes have been modeled. Table 1 indicates the input parameters for the particles and the fluid domain.

Table 5-2. Input parameters for the particles and fluid domain

Parameter	Particles	Walls
Density (kg/m^3)	2650	7850
Modulus of Elasticity (Pa)	1×10^{7}	1×10^{11}
Poisson Ratio	0.3	0.3
Friction Coefficient	0.5	0.5
Normal Restitution Coefficient	0.5	0.5
Tangential Restitution Coefficient	0.5	0.5
Coefficient of Rolling Resistance	0.1	
Computational parameters		
DEM time step	$8.91 \times 10^{-6}(1\ mm)$ $1.78 \times 10^{-5}(2\ mm)$ $4.46 \times 10^{-5}(5\ mm)$	
CFD time step	1×10^{-3}	
CFD mesh size (mm)	$10 \times 10 \times 10$	
CFD turbulence model	$\mathrm{k} - \varepsilon$ Turbulence	
Drag Force Model	Schiller-Naumann	

Case 1. Diameter of sample particles = 1 mm, Diameter of suspended particles = 1 mm

Figure 5-22 and Figure 5-23 present the velocity-based and shear stress-based erosion functions for the sample, respectively. The overall difference between the erosion functions is low. In low (0.5 m/s) and high velocities (3m/s), there is no difference between the results, while in average velocities (1m/s and 2 m/s), a small difference can be observed. This can be connected to the velocity of suspended particles and the location in which particles hit the sample. Figure 5-24 shows the configuration of suspended particles towards sample particles. It can be observed that in low velocities due to low energy of particles, the impact between the suspended particles and sample particles is minimum, and the particles do not have an abrasion effect on the sample.

Instead, they infilled near the sample particles. In high velocities, particles have high kinetic energy, and again their contact to sample particles is low. In average velocities, suspended particles can contact sample particles, and abrasion can show its effect. Figure 5-25 shows the same configurations for a concentration of 3 g/lit. It is clear that due to the lower concentration of particles in the fluid, their abrasion effect on the sample particles is lower than the case with 5 g/lit of particle concentration in the fluid.

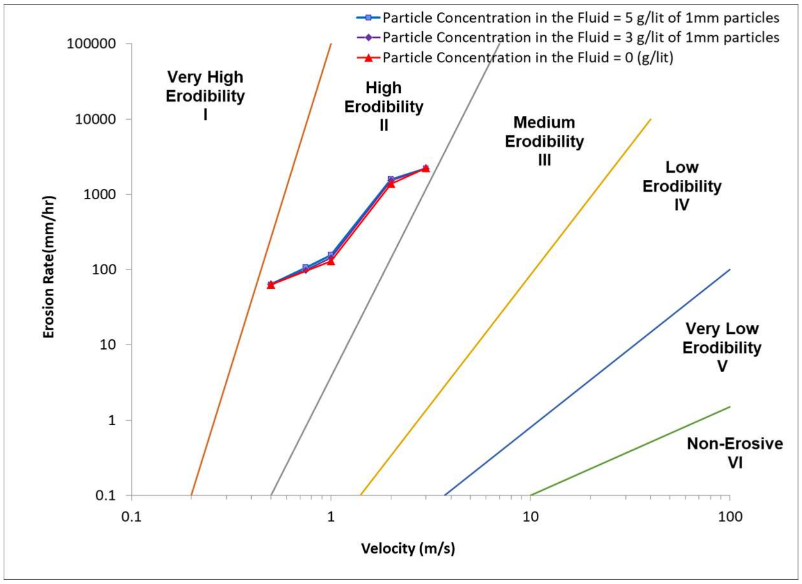

Figure 5-22. Comparison of velocity-based erosion function for a sample with a particle size of 1 mm and three different concentrations of 1 mm particles in the fluid

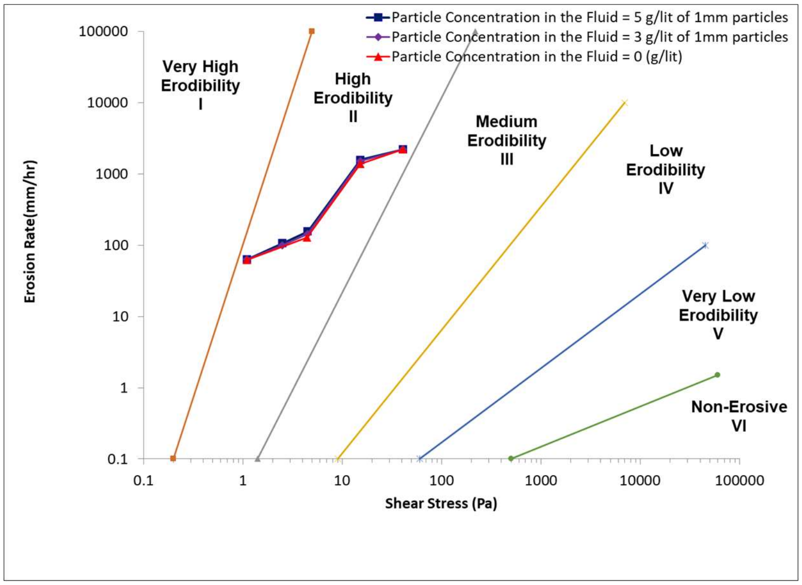

Figure 5-23. Comparison of shear stress based erosion function for a sample with a particle size of 1 mm and three different concentrations of 1 mm particles in the fluid

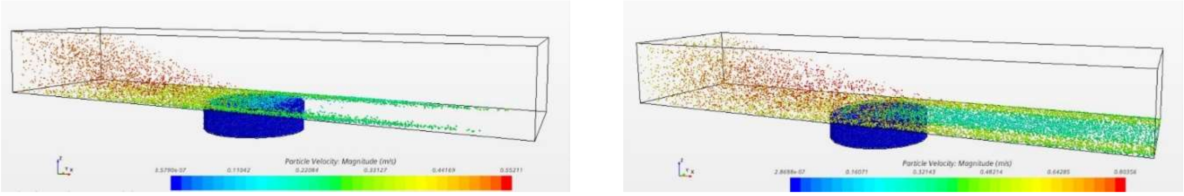

a) V= 0.5 m/s & Particle concentration in the flow = 5 g/lit

b) V= 0.75 m/s & Particle concentration in the flow = 5 g/lit

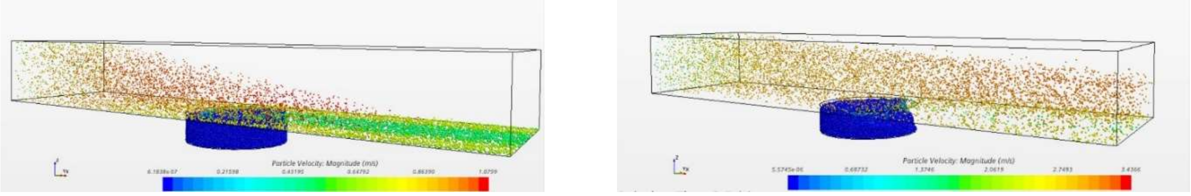

c) V= 1 m/s & Particle concentration in the flow = 5 g/lit

d) V= 3 m/s & Particle concentration in the flow = 5 g/lit

Figure 5-24. EFA models for the sample with 1 mm particle size, different inlet flow velocities, and a particle mass concentration of 5 g/lit in the flow

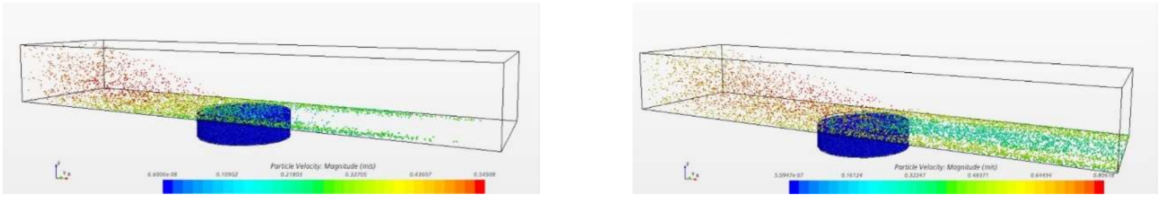

a) V= 0.5 m/s & Particle concentration in the flow = 3 g/lit

b) V= 0.75 m/s & Particle concentration in the flow = 3 g/lit

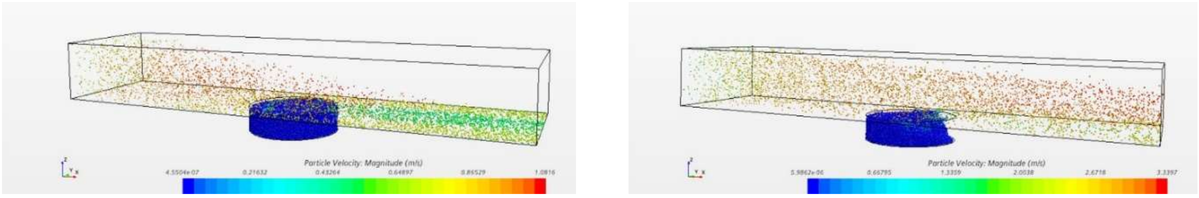

c) V= 1 m/s & Particle concentration in the flow = 3 g/lit

d) V= 3 m/s & Particle concentration in the flow = 3 g/lit

Figure 5-25. EFA models for the sample with 1 mm particle size, different inlet flow velocities, and a particle mass concentration of 3 g/lit in the flow

Case 2. Diameter of sample particles = 2 mm, Diameter of suspended particles = 2 mm

Figure 5-26 and Figure 5-27 shows the velocity vs. erosion rate and velocity vs. erosion rate for a sample with 2 mm particles and three different particle concentrations in the fluid. In this case, the overall difference between the samples is noticeable. Although in 0.5 m/s and 3 m/s velocities, the values of erosion rate are the same, on velocities between these two values, due to higher impact between suspended particles and the surface of the sample, the difference is distinct.

The kinetic energy of suspended particles to move the settled particles is higher in 2 mm particles than 1 mm particles, and this explains the higher difference in this case compared to the sample with 1 mm particles. Figure 5-28 and Figure 5-29 demonstrate the configuration of suspended particles towards settled particles in different velocities for 5 g/lit and 3 g/lit of mass concentrations, respectively. In both cases, the contact in cases with velocities between 0.5 m/s and 3 m/s are higher. More importantly, the proper angle of impact in velocities between 05 m/s and 3 m/s velocities can increase the effect of abrasion on the sample surface.

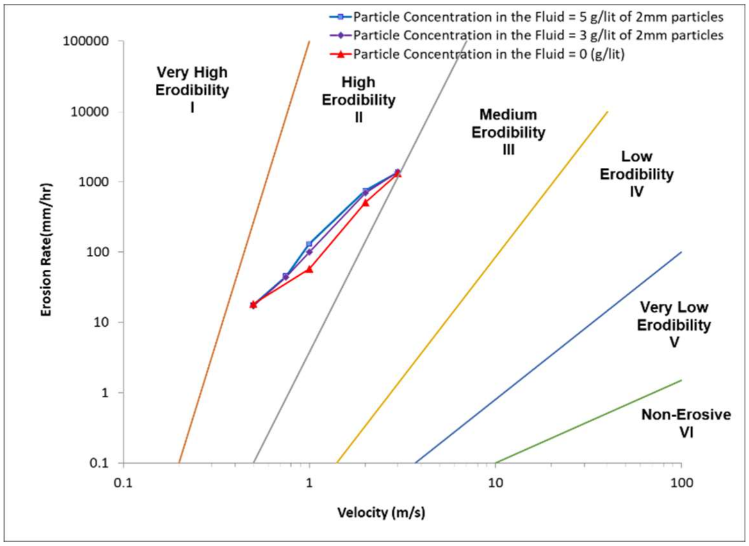

Figure 5-26. Comparison of velocity-based erosion function for a sample with a particle size of 2 mm and three different concentrations of 2 mm particles in the fluid

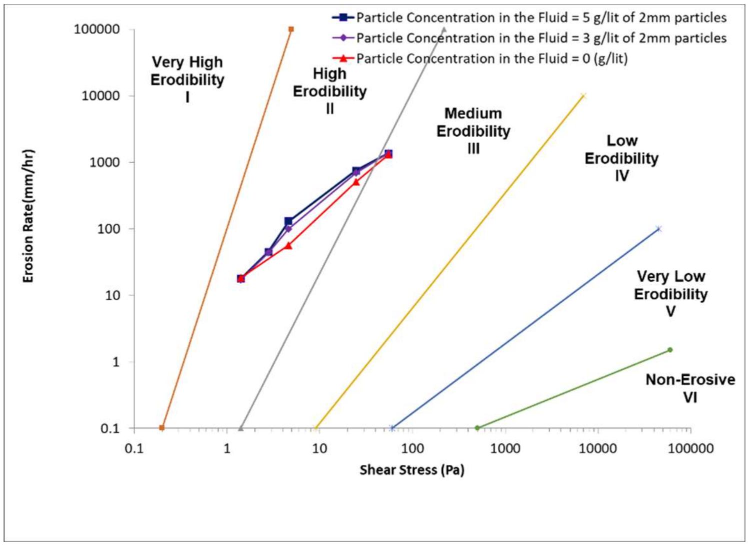

Figure 5-27. Comparison of shear stress based erosion function for a sample with a particle size of 2 mm and three different concentrations of 2 mm particles in the fluid

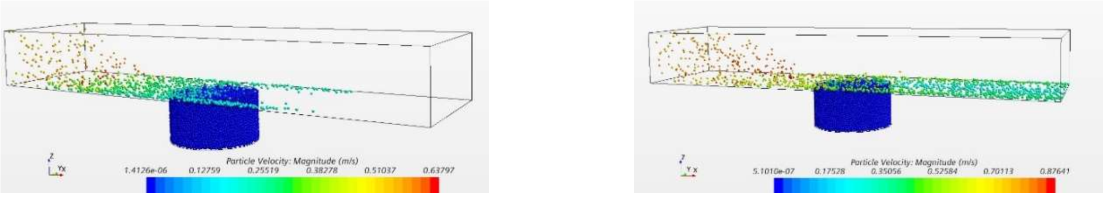

a) V= 0.5 m/s & Particle concentration in the flow = 5 g/lit

b) V= 0.75 m/s & Particle concentration in the flow = 5 g/lit

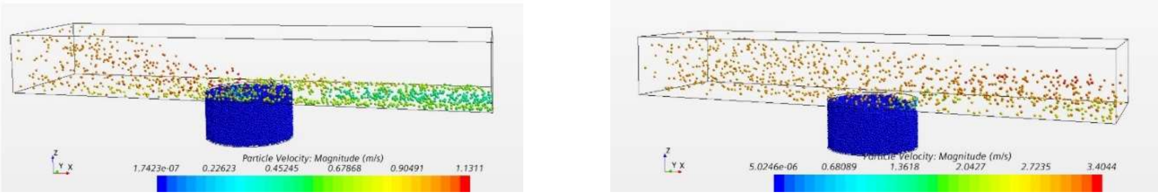

c) V= 1 m/s & Particle concentration in the flow = 5 g/lit

d) V= 3 m/s & Particle concentration in the flow = 5 g/lit

Figure 5-28. EFA models for 2 mm particles size with different inlet flow velocities and particle mass concentration of 5 g/lit in the flow

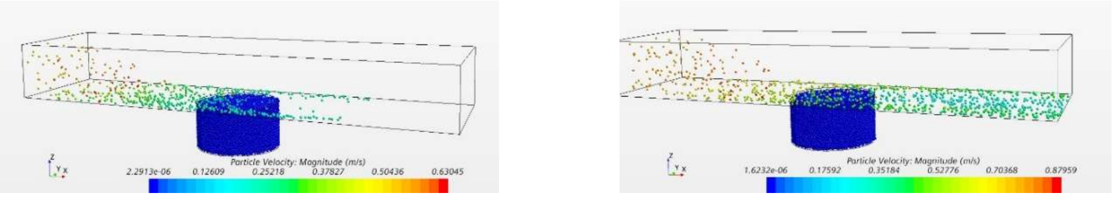

a) V= 0.5 m/s & Particle concentration in the flow = 3 g/lit

b) V= 0.75 m/s & Particle concentration in the flow = 3 g/lit

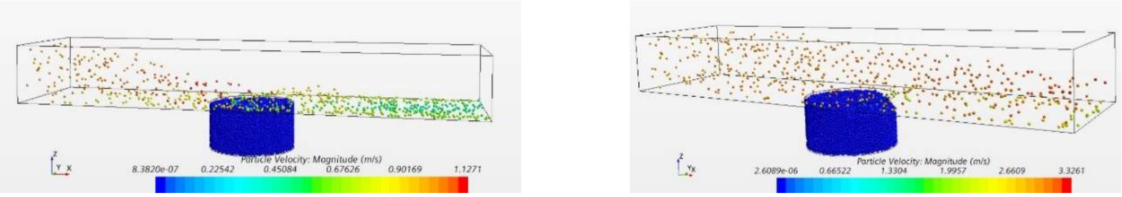

c) V= 1 m/s & Particle concentration in the flow = 3 g/lit

d) V= 3 m/s & Particle concentration in the flow = 3 g/lit

Figure 5-29. EFA models for 2 mm particles size with different inlet flow velocities and particle mass concentration of 3 g/lit in the flow

Case 3. Diameter of sample particles = 5 mm, Diameter of suspended particles = 5 mm

Figure 5-30 and Figure 5-31 indicate erosion rate in mm/hour versus velocity and erosion rate vs. shear stress on the chart classified by erosion categories. In 0.75 m/s and 3 m/s velocities, the values of erosion rates are close, while in velocities between these two ranges, the difference becomes highlighted. The difference in erosion rates for particles mass concentration of 3 g/lit and 5 g/lit is lower than the case with 2 mm particles.

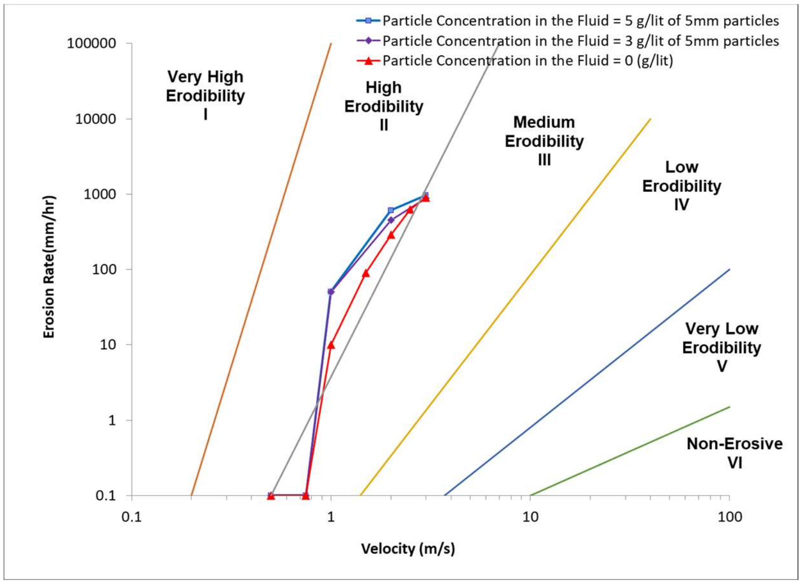

Figure 5-30. Comparison of velocity-based erosion function for two samples with a particle size of 5 mm and two different concentration of 5 mm particles in the fluid

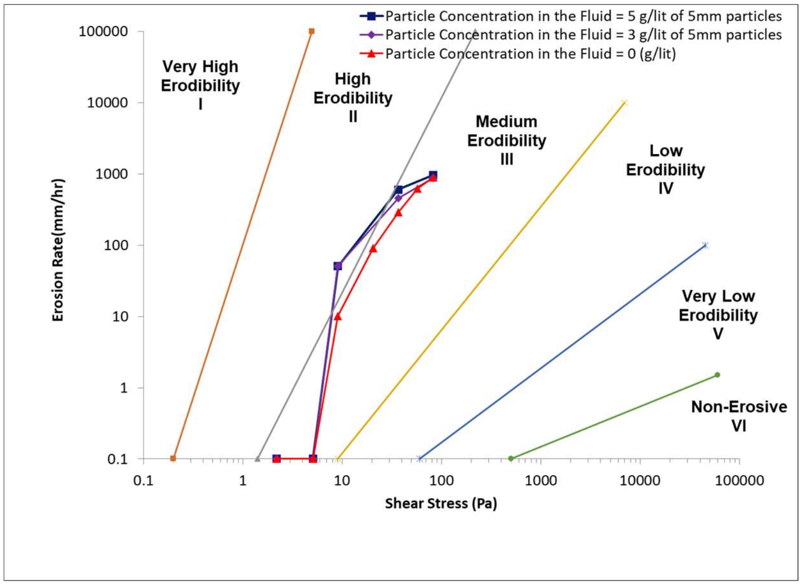

Figure 5-31. Comparison of shear stress based erosion function for two samples with a particle size of 5 mm and two different concentration of 5 mm particles in the fluid

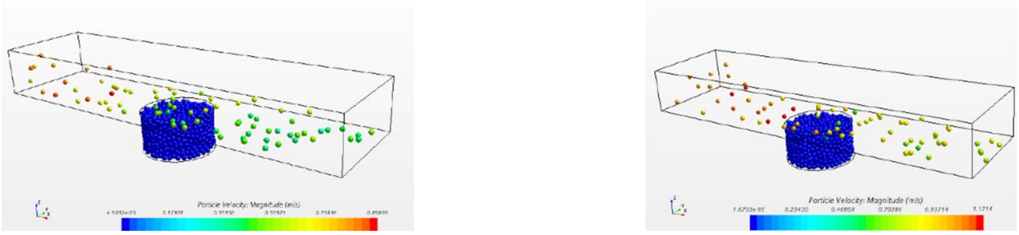

a) V= 0.75 m/s & Particle concentration = 5 g/lit

b) V= 1 m/s & Particle concentration = 5 g/lit

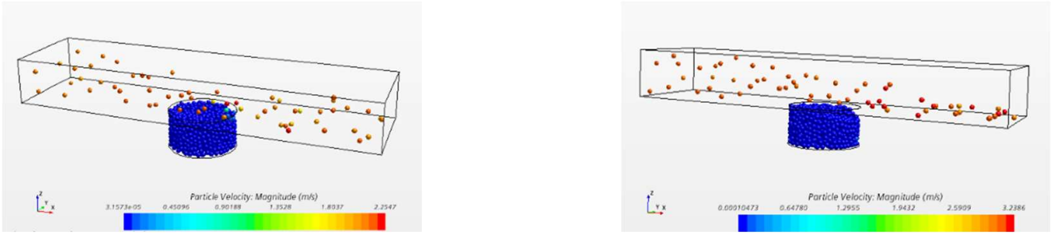

c) V= 2 m/s & Particle concentration = 5 g/lit

d) V= 3 m/s & Particle concentration = 5 g/lit

Figure 5-32. EFA models for 5 mm particles size with different inlet flow velocities and particle mass concentration of 5 g/lit in the flow

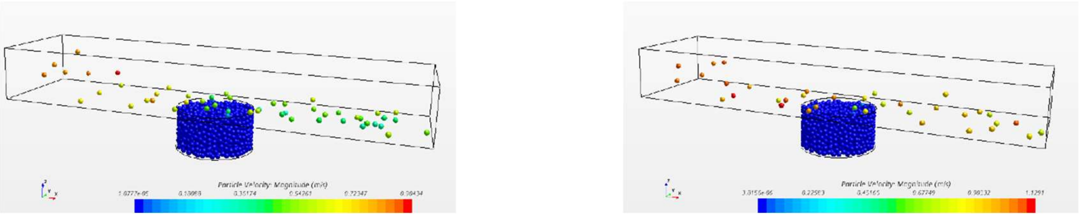

a) V= 0.75 m/s & Particle concentration = 3 g/lit b) V= 1 m/s & Particle concentration = 3 g/lit

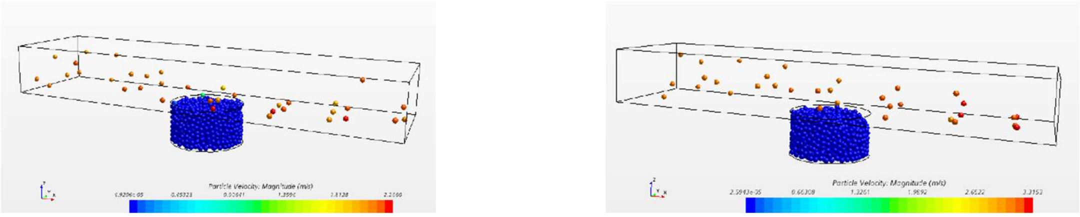

c) V= 2 m/s & Particle concentration = 3 g/lit d) V= 3 m/s & Particle concentration = 3 g/lit

Figure 5-33. EFA models for 5 mm particles size with different inlet flow velocities and particle mass concentration of 3 g/lit in the flow

Case 4. The diameter of sample particles = 5 mm, the diameter of suspended particles = 1mm, 2 mm and 5 mm

For the last case to study the effect of abrasion of suspended particles on the sample surface, the effect of different sizes of particles (1 mm, 2 mm, and 5 mm) on a sample with 5 mm particles is investigated. Figure 5-34 and Figure 5-35 shows the velocity-based and shear-stress based erosion functions for the three case along with a case without particle mass concentration in the fluid. The results showed the effect of abrasion of suspended particles on the erosion function, especially when the size of suspended particles and settled particles are the same.

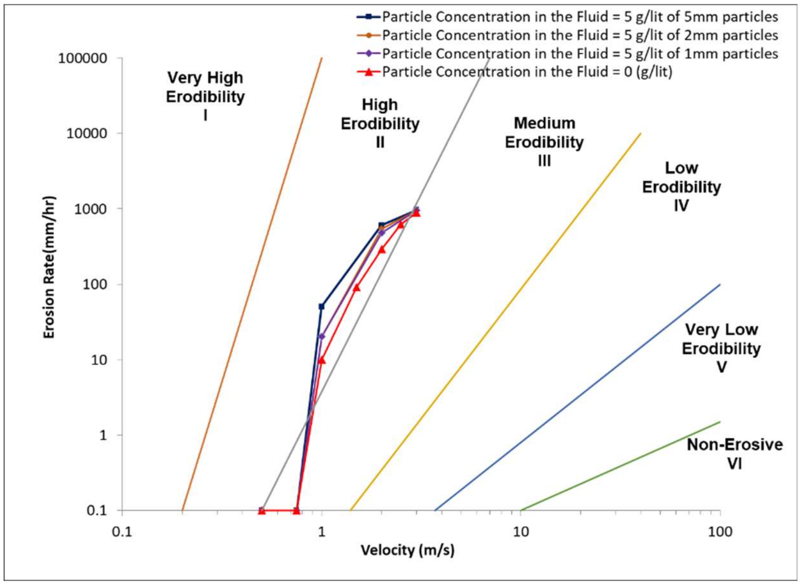

Figure 5-34. Comparison of velocity-based erosion function for two samples with a particle size of 5 mm and a different size of particles in the fluid with a concentration of 5 g/lit

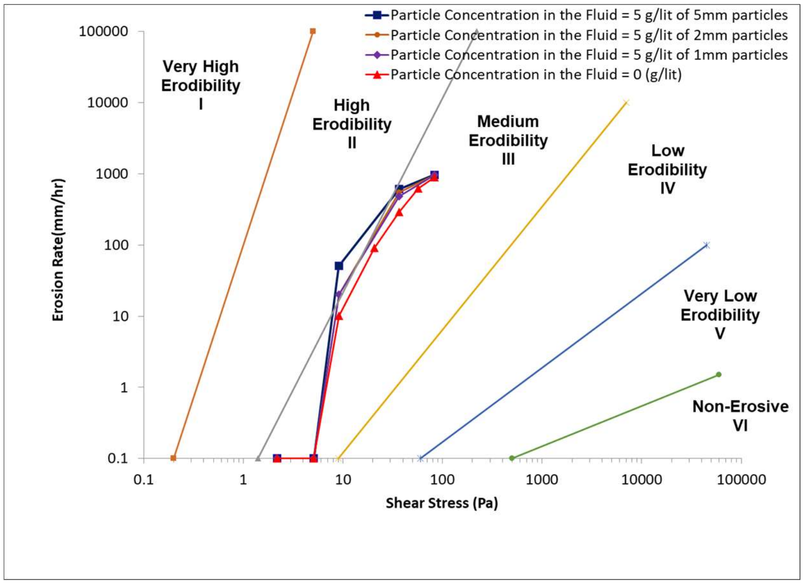

Figure 5-35. Comparison of shear stress based erosion function for two samples with a particle size of 5 mm and a different size of particles in the fluid with a concentration of 5 g/lit

5.2.Infilling Modeling

A better understanding of the scouring infilling process and its contributing factors is essential in the successful prediction of scour depth. The published work and ongoing research on the infilling process are limited. This limited research emphasizes the necessity to investigate this process with the CFD-DEM method numerically.

In this research, the infilling process is simulated to study several contributing parameters, including the size of particles, the depth of the hole, the slope of the scour hole, the friction coefficient and rolling resistance coefficient between the particles, porosity of the bed, and cohesion between the particles.

The model was constructed with an inlet, an outlet, and a prefabricated scour hole to simulate the infilling process. A bed of particle with a depth of is considered before the scour hole. Figure 5-36.a demonstrates the simulated model. The resulted particles mass scaled by 30 to simulate a channel with 3 m of width. The scaled channel is illustrated in Figure 5-1.b.

Figure 5-37 displays the hydrograph utilized in the simulation to calculate the mass of infilling.

. The hydrograph starts from 2 m/s and decreases to 0.5 m/s in 12 hours after the peak flood velocity. The process for calculating the mass of infilling is as following:

1. Simulating with each velocity in the hydrograph and calculate the erosion rate at the end of each velocity step.
2. Calculating the mass entered the scour hole for the time for the simulation.
3. Scaling the geometry to have the real dimensions of the scour hole.
4. Scaling the simulated mass rate to have the real mass of infilling.
5. Calculating the percent of infilling by dividing the volume of infilling to the volume of the scour hole.

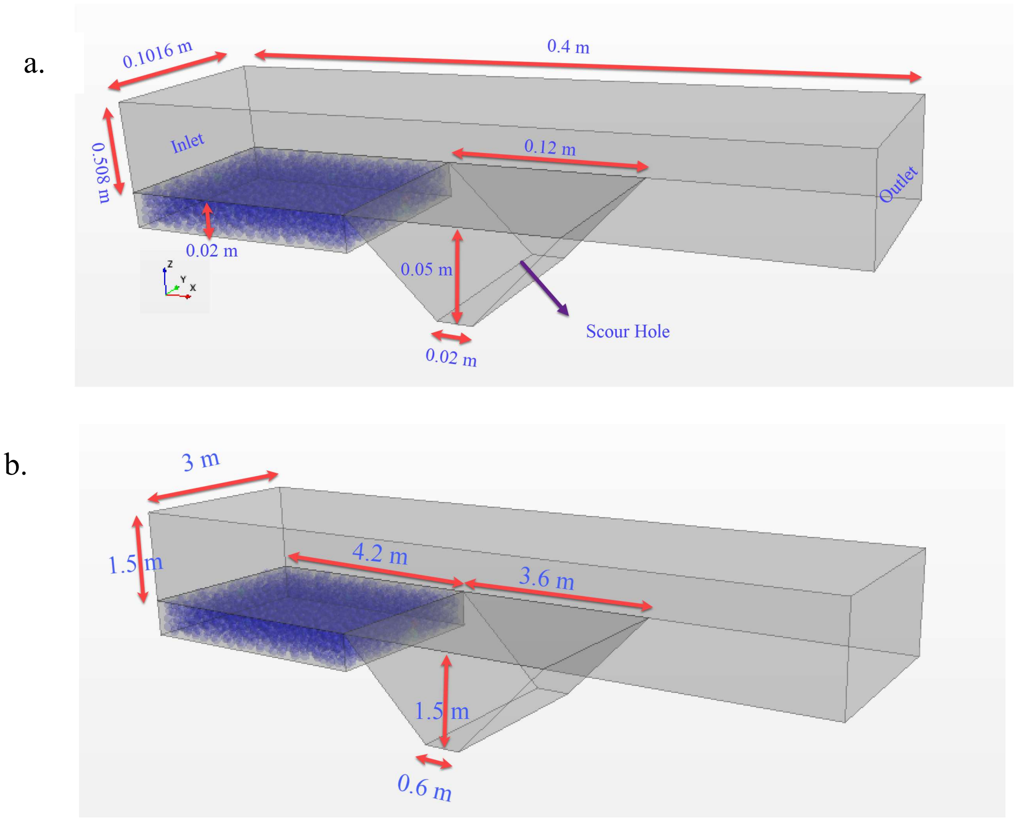

Figure 5-36. The model setup for the CFD-DEM modeling of erosion

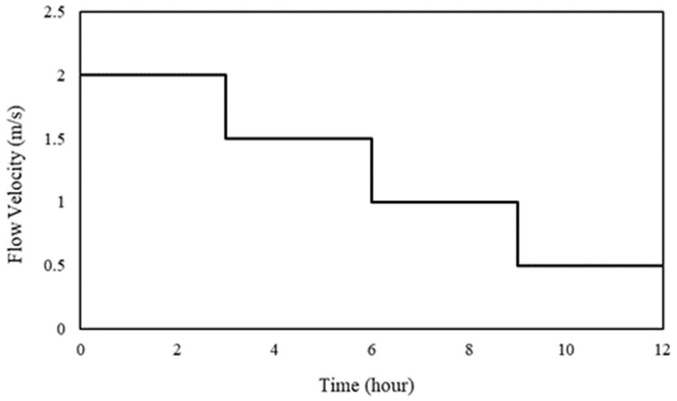

Figure 5-37. Hydrograph considered for infilling modeling

5.2.1. The magnitude of infilling with the diameter

Figure 5-38 shows the variation of infilling with the size of particles for two different porosities. Both mass of infilling and percent of infilling decreases with the increase of the diameter of particles.

In section 5.1.2, the effect of particle size on erosion function was investigated. Critical shear stress and critical velocity increase with particle diameter (Figure 5-3 and Figure 5-5). This increase leads to the lower mass of infilling to the scour hole. Since the volume of the scour hole keeps constant, the percent of infilling also decreases.

Models are simulated with two different porosities. In both cases, a similar trend can be observed. Although, due to the denser configuration of particles in the bed, by decreasing the porosity of the particles at the bed, the mass of infilling values decreases. Denser particles increase the resistance against erosion and decrease the mass of infilling.

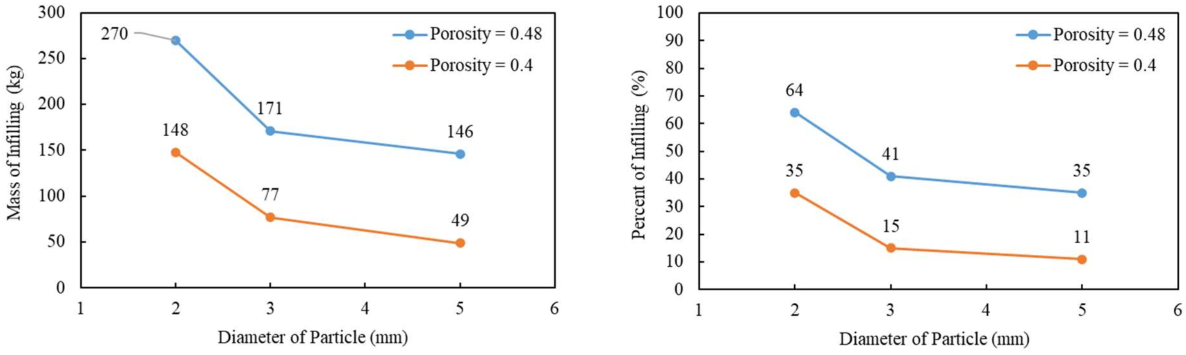

a. b.

Figure 5-38. Variation of infilling with the size of particles a) Mass of infilling vs. particle size b) Percent of infilling volume to the volume of scour hole vs. particle size

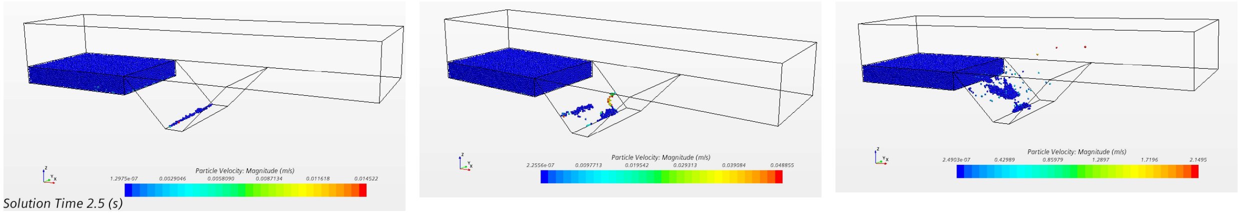

a. V=0.5 m/s , D=1 mm b. V=1 m/s , D=1 mm c. V=2 m/s , D=1 mm

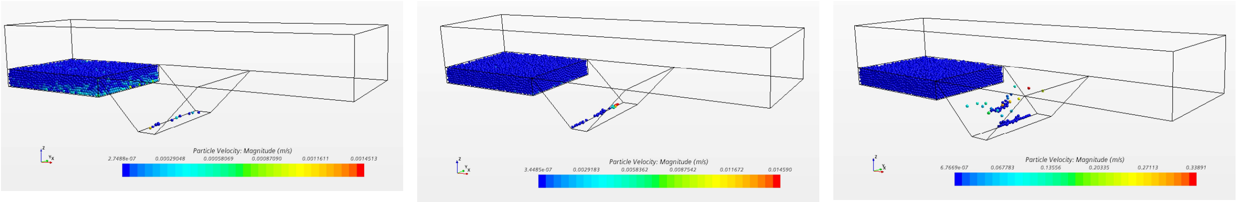

d. V=0.5 m/s , D=2 mm e. V=1 m/s , D=2 mm f. V=2 m/s , D=2 mm

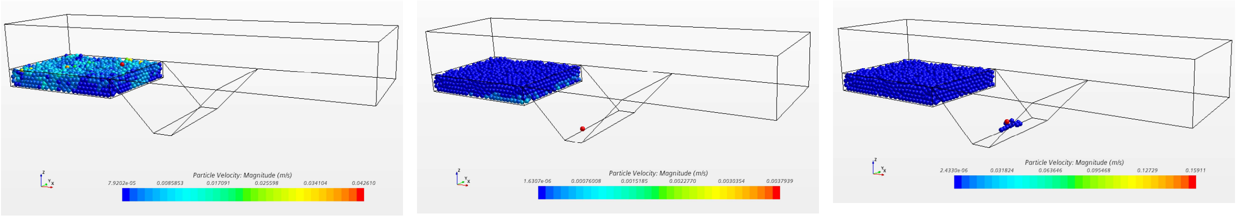

g. V=0.5 m/s , D=5 mm h. V=1 m/s , D=5 mm i. V=2 m/s , D=5 mm

Figure 5-39. Infilling after 1 s of flow with three different velocities and three different particle sizes

5.2.2. The magnitude of infilling with the depth and slope of the scour hole

Figure 5-40 and Figure 5-41 indicate the variation of infilling with the depth of the scour hole and its slope, respectively. In the case of a shallow scour hole (1 m depth), the particles can not stand at the bottom of the scour hole and move with the flow motion as soon as they reach the bottom of the hole. While in case of enough depth of scour hole, the particles can stay in the scour hole, and the infilling process can happen. The variation of the mass of infilling for the depth of the hole higher than 2 m is approximately constant. By increasing the depth of the hole, the volume of the scour hole increases, resulting in a decrease of infilling percent.

The same trend can be observed with the slope. In 10 degrees slope, the scour hole is shallow, and fluid velocity distribution can emerge in the hole, which results in a small value of shear stress at the bottom of the scour hole enough to move the particles (Figure 5-42 and Figure 5-43). This distribution of velocity and shear stress give the particles the ability to pass the scour hole. In steeper scour holes (deeper hole), the distribution of velocity around the bottom of the hole is small, and shear stress on the bottom is almost zero (Figure 5-42 and Figure 5-43). This leads to the infilling of particles at the bottom of the hole. But the mass of infilling for slope more than 20 degrees is the same while the percent of infilling decreases with an increase of slope (due to an increase of the volume of scour hole by increasing the depth and slope).

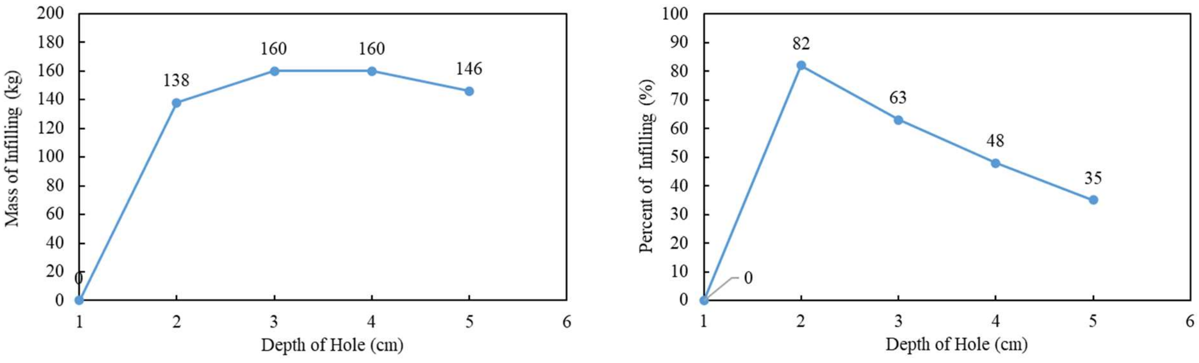

a. b.

Figure 5-40. Variation of infilling with the depth of the scour hole a) Mass of infilling vs. depth of scour hole b) Percent of infilling volume to the volume of scour hole vs. depth of scour hole

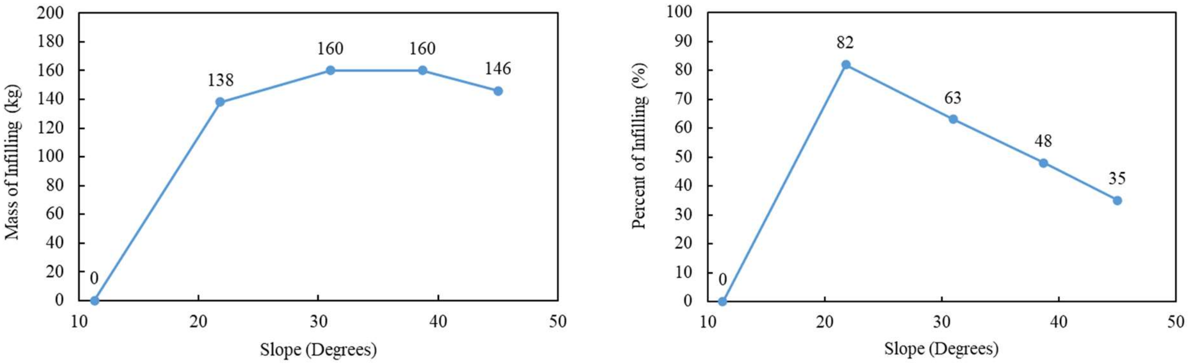

a. **b.**

Figure 5-41. Variation of infilling with the slope of the scour hole a) Mass of infilling vs. slope of scour hole b) Percent of infilling volume to the volume of scour hole vs. slope of scour hole

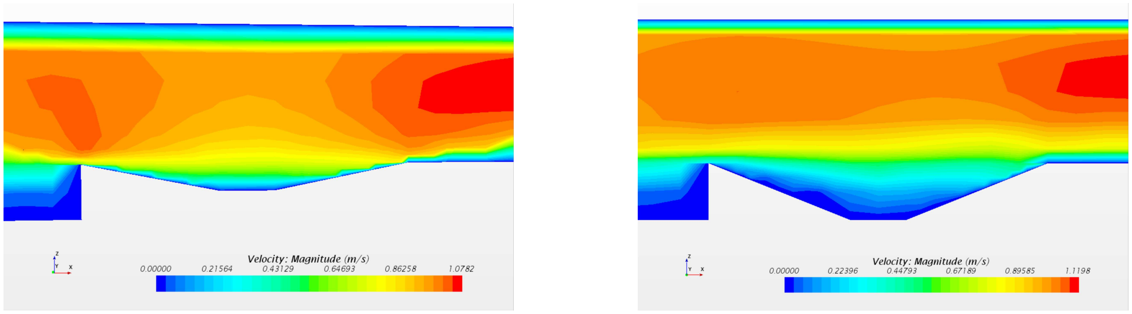

a) V = 1 m/s, H = 1cm

b) V = 1 m/s, H = 2cm

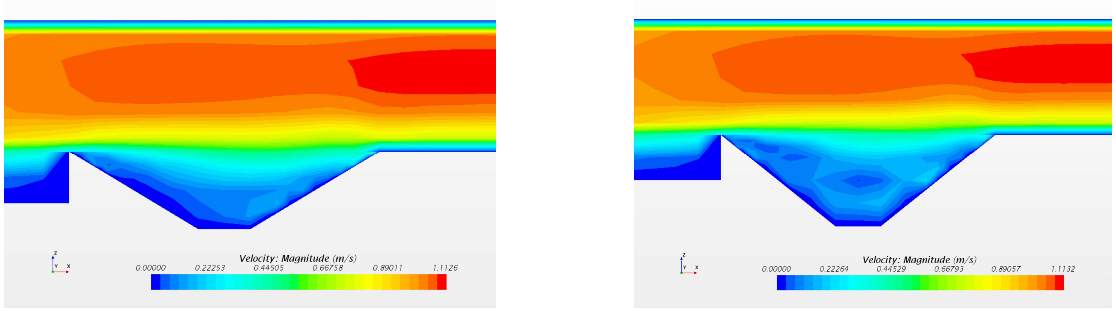

c) V = 1 m/s, H = 3cm

d) V = 1 m/s, H = 4cm

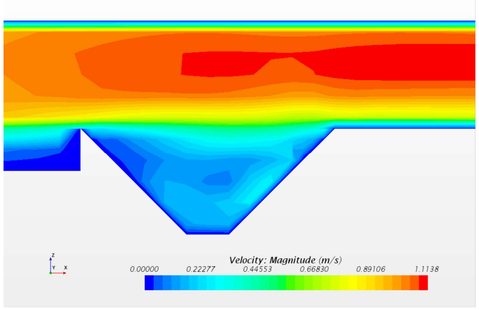

e) V = 1 m/s, H = 5cm

Figure 5-42. Velocity distribution in the scour hole for a flow velocity of 1 m/s

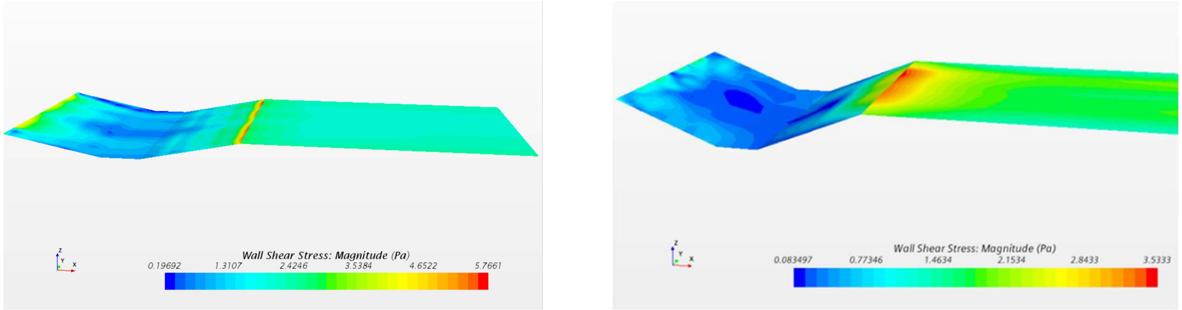

a) V = 1 m/s, H = 1cm b) V = 1 m/s, H = 2cm

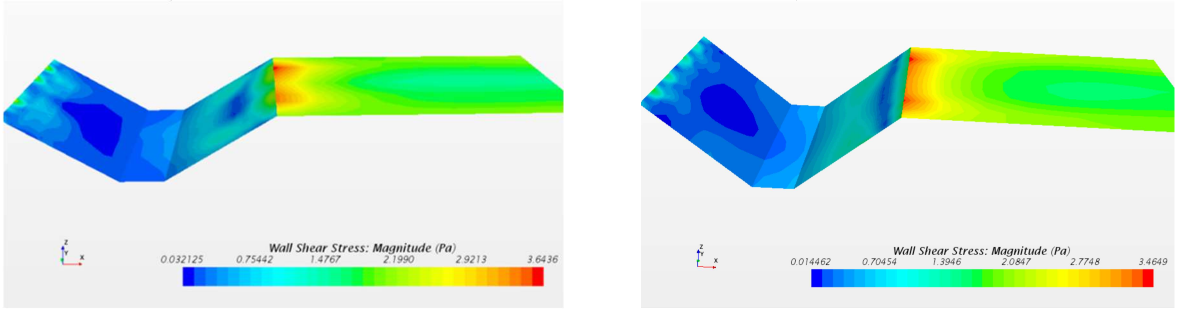

c) V = 1 m/s, H = 3cm d) V = 1 m/s, H = 4cm

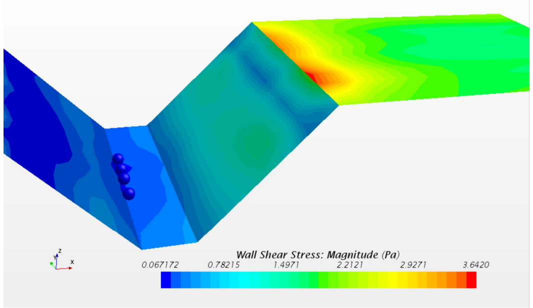

e) V = 1 m/s, H = 5cm

Figure 5-43. Shear Stress distribution in the scour hole for a flow velocity of 1 m/s

5.2.3. The magnitude of infilling with the coefficient of rolling resistance

Increasing the rolling resistance hardens the motion of particles and increase the critical velocity and critical shear stress (Figure 5-8 and Figure 5-9). Higher critical velocity and shear stress lead to lower mass loss from the upstream bed and more mass of infilling in the scour hole. Since the volume of the scour hole stays constant, the percent of infilling also decreases.

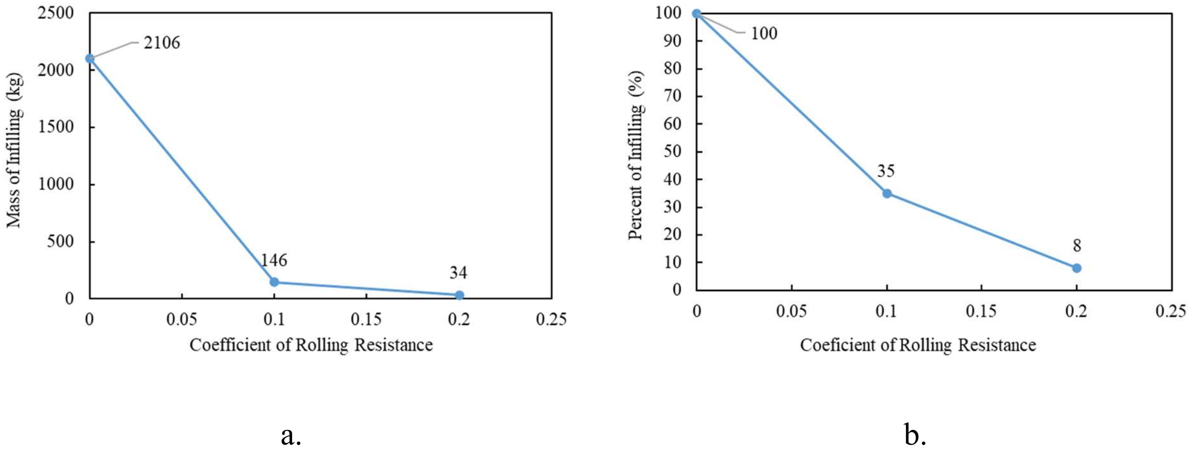

Figure 5-44. Variation of infilling with the coefficient of rolling resistance a) Mass of infilling vs. coefficient of rolling resistance b) Percent of infilling volume to the volume of scour hole vs. coefficient of rolling resistance

5.2.4. The magnitude of infilling with the friction coefficient

Figure 5-45 plots the variation of mass and percent of infilling with friction coefficient. There is a noticeable decrease in the values with increasing the coefficient friction. The increase of friction coefficient improves the interlocking of particles between each other and increases critical velocity and critical shear stresses (Section 5.1.3, Figure 5-6 and Figure 5-7). This leads to lower values of mass and percent of infilling.

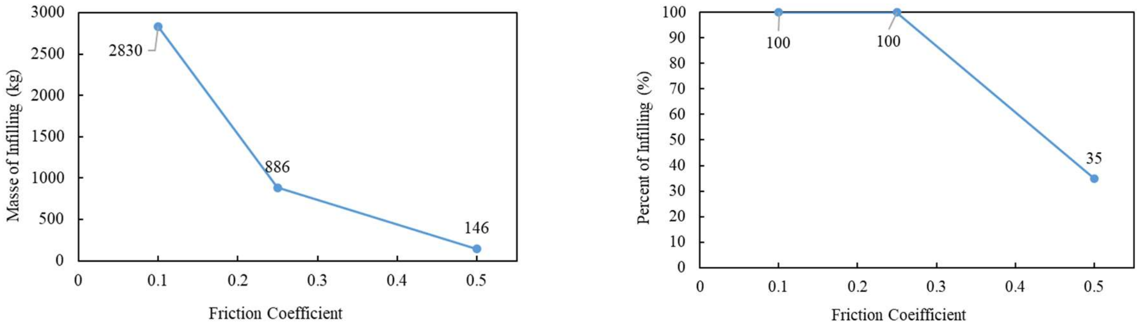

a. **b.**

Figure 5-45. Variation of infilling with the friction coefficient between particles a) Mass of infilling vs. friction coefficient b) Percent of infilling volume to the volume of scour hole vs. friction coefficient.

5.2.5. The magnitude of infilling with the porosity

Figure 5-46 presents the effect of porosity on the mass of infilling (kg) and percent of infilling. An increase of porosity decreases the interaction between the particles and facilitates the start of motion, which leads to the increase of mass of infilling and its percent.

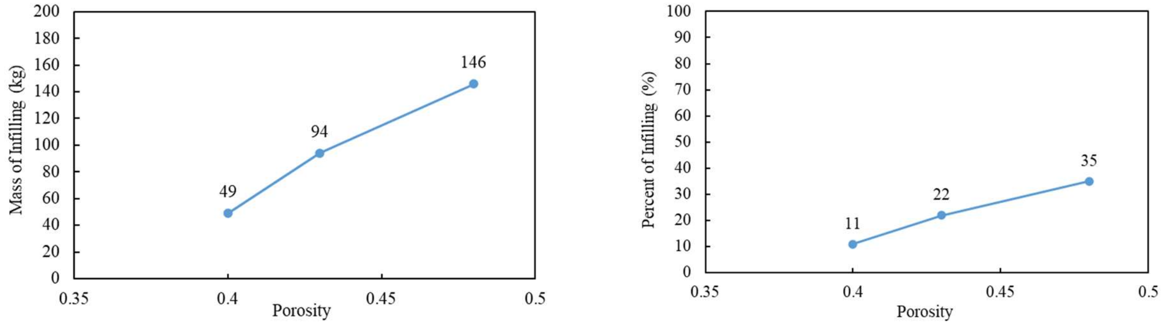

a. b.

Figure 5-46. Variation of infilling with the porosity of bed particles a) Mass of infilling vs. porosity b) Percent of infilling volume to the volume of scour hole vs. porosity

5.2.6. The magnitude of infilling with the cohesion

As explained in section 5.2.6, the particles' cohesion notably affects both critical velocity and critical shear stress (Figure 5-18 and Figure 5-20). Figure 5-47 plots the mass of infilling and percent of infilling vs. cohesion, respectively. A substantial decrease in the mass and percent of infilling with even a low erosion value increase is apparent. The value of cohesion in the plot is calculated from Equation 5-1.

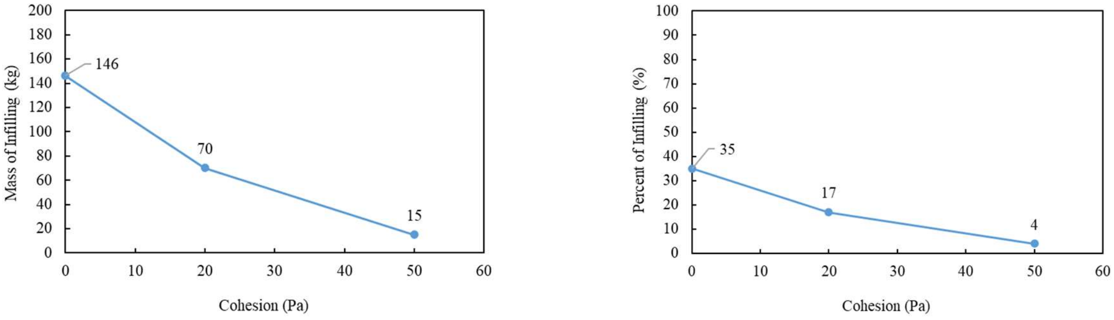

a. **b.**

Figure 5-47. Variation of infilling with the cohesion between particles a) Mass of infilling vs. cohesion b) Percent of infilling volume to the volume of scour hole vs. cohesion

5.3.CFD-DEM Modeling of Two Types of Internal Instability; Contact Erosion and Suffusion

In an internally stable soil, the coarse grain particles of the soil can prevent the movement of fine particles due to seepage forces. If the coarse grain particles allow the fine particles to migrate through the pores inside the soil fabric, soil can be considered internally unstable (Fell and Fry, 2007). As explained in the literature review, internal erosion can be initiated by suffusion, soil contact erosion, concentrated leak erosion, or backward erosion. In suffusion, constant loss of fine particles from the soil skeleton increases the volumetric strain and permeability of the soil and decreases in the shear strength (Kuwano et al. 2020).

In this section, the CFD-DEM modeling of contact erosion and suffusion is pursued. Before introducing the modeling details and their results, the validation of the model has been done. In the model validation, the utilized drag force model is verified with different drag model tests found in the literature. Finally, the model validation is examined by the numerical simulation of quicksand condition.

As mentioned in the introduction of this chapter, The last section investigates the usual criteria in the internal stability (contact erosion and suffusion) of soils with the CFD-DEM technique.

5.3.1. Model Validation

In the CFD-DEM method, the energy required to move the particles calculated from fluid characteristics and by a drag force model. There are different drag force models than can be used in the CFD-DEM framework. In chapter 3, Schiller-Nauman and di Felice were used in the simulations. The description of both models was presented in background knowledge. Both models, successfully utilized by different researchers in their CFD-DEM modelings (Tao and Tao 2017). These two drag force models are similar; the only difference is that the Di Felice drag model introduces an additional term to consider the presence of other particles around a particle (STAR-CCM+ Manual).

Figure 5-48 shows the constructed model to compute the magnitude of the drag force in the CFD-DEM model. This model was formerly used by Abdelhamid and Elshamy (2016) to verify their LBM-DEM model. The model is a simple channel with an inlet and outlet and a spherical particle with a 1 mm diameter in the center. The fluid density is 1000 kg/m^3, and the dynamic viscosity, μ 0.04 Pa.s. The fluid velocity is chosen with different values, and each step drag force is calculated.

Figure 5-49 compares the results with the results of experimental testing found in the literature (Allen 1900, Arnold 1911, Leibster 1927) along with the results of numerical simulations (Jenson 1959, Dennis and Walker 1971, Ihme et al. 1972, Abdelhamid and El Shamy, 2016) and empirical formulations (Brauer 1973, White 1974). Current CFD results show a good agreement with the previous test, numerical simulations, and empirical formulations. The Di Felice drag model shows a higher drag coefficient compared to Schiller Naumann's results.

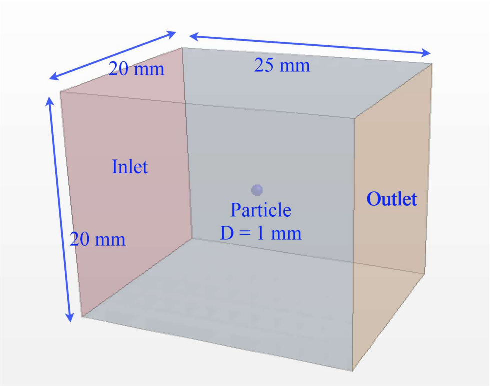

Figure 5-48. CFD-DEM simulation model to check the magnitude of drag force in different velocities

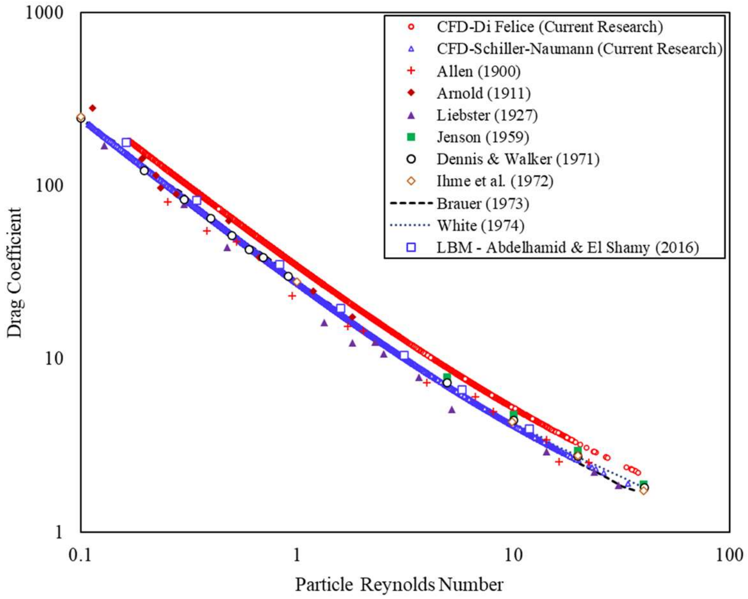

Figure 5-49. Drag force comparison between computed drag force from experiments, numerical simulations, and empirical formulations

A numerical model is constructed to check the condition of particles in quicksand and boiling conditions and to complete the validation (Figure 5-50.a). Table 1 displays the parameters of the model. Grain size distribution for the sample ranges from 4.8 mm to 7.2 mm with a mean of 6 mm and a standard deviation of 0.4 mm. The sample is a cylinder with 5 cm of diameter and 11.8 cm of length. Figure 5-50.b Shows the pressure exerted at the bottom of the sample during the simulation. The pressure at the top of the sample is zero, and this pressure difference creates an upward flow regime and a hydraulic gradient from 0 to 1.4 along the sample length.

Figure 5-51.a presents the pressure increases vs. time at the bottom of the sample and the corresponding value of the hydraulic gradient throughout the sample. Figure 5-51.b shows the coordination number variation for the top layer of the sample simulated with the LBM-DEM method (Abdelhamid and El Shamy (2016)). In DEM, the coordination number is the average value of contacts per particle. Degradation of the coordination number starts near t=1 s. In this time, the hydraulic gradient value is 0.8 and on the verge of rising to reach one, equivalent to boiling condition at the top layer of the sample. In this condition, contacts between the particles get weaker and weaker, which is evident in the coordination number plotted in the figure.

Figure 5-51.c indicates the coordination number plot resulted from the CFD-DEM technique in this research. The same trend can be observed with the results of CFD-DEM simulation. With both Di-Felice and Schiller-Naumann drag models, the same degradation in the coordination number happens before t=1 s, which is equal to a hydraulic gradient of 0.8 and on the verge to reach 1, which is equivalent to the boiling condition in the sample.

Table 5-3. Parameters of quicksand validation model

Parameter	Magnitude
Number of Particles	1079
Density (kg/m^3)	2650
Modulus of Elasticity (Pa)	1×10^7
Poisson Ratio	0.3
Friction Coefficient	0.5
Normal Restitution Coefficient	0.2
Tangential Restitution Coefficient	0.2
Coefficient of Rolling Resistance	0.1
Computational parameters	
DEM time step	4.27×10^{-5}
CFD time step	1×10^{-3}
CFD mesh size (mm)	$10 \times 10 \times 10$
Drag Force Model	Di Felice Schiller - Naumann
CFD flow model	Laminar

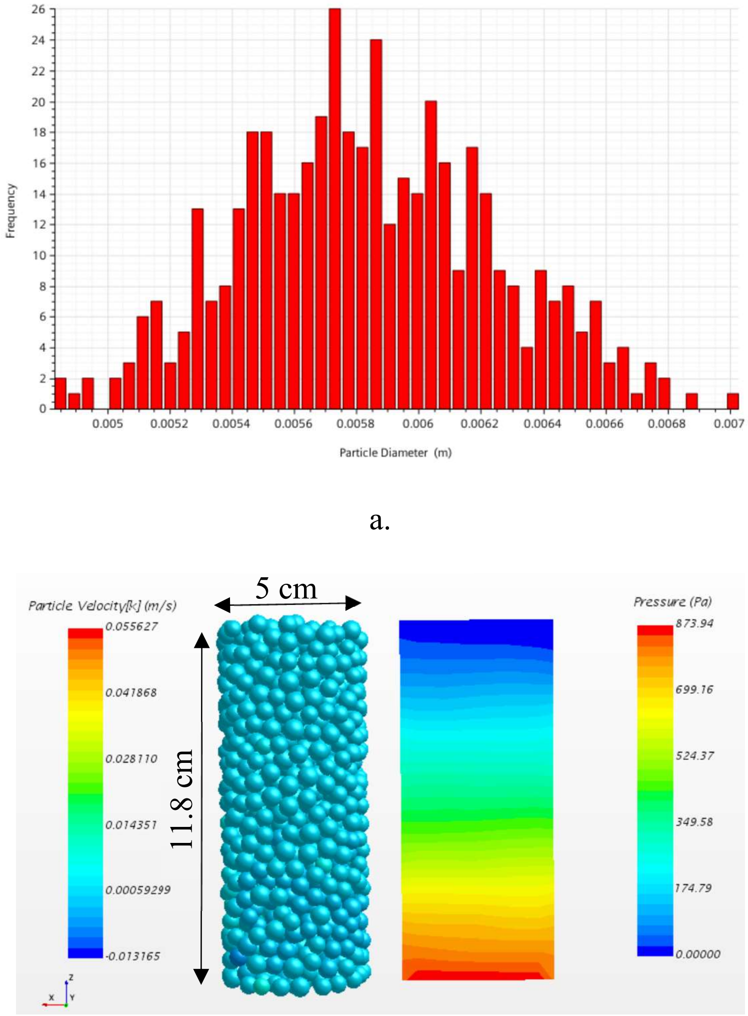

b.

Figure 5-50. a) The grain size distribution of the numerical sample for the validation model b) The simulated sample and pressure distribution along with the sample

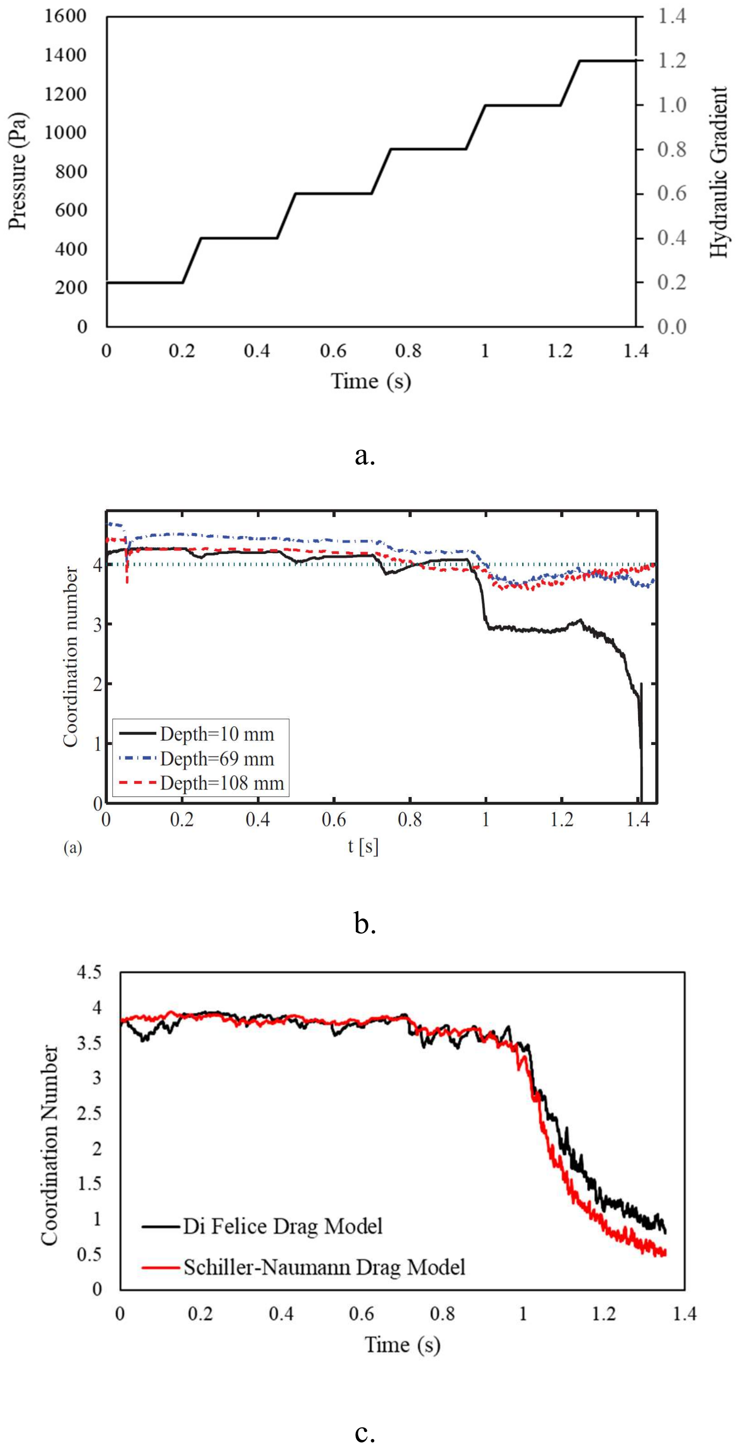

Figure 5-51. a) Pressure and hydraulic gradient variation with time b)Time history of coordination number during the increase of pressure and hydraulic gradient for LBM-DEM method (Abdelhamid and El Shamy 2016) c) Time history of coordination number during the increase of pressure and hydraulic gradient for CFD-DEM method

5.3.2. Terzaghi filter criterion

Terzaghi proposed a criterion for soil retention for the first time during his consulting work for Giovanni Rodio in 1932 (Fannin 2008). He designed a filter with five layers for the Bou-Hanifa dam in Algeria and finally proposed his findings in the 2nd International Congress on Large Dams at Washington in 1936 (Fannin 2008). His criteria cover two parts, providing retention capacity of the filter and enough permeability in the filter. For the above criterion, the D_{15} (Diameter of the 15% of mass passing) of the filter should be smaller than the fourth times of D_{85} (Diameter of the 85% of mass passing) of the base soil. In the latter criterion, the D_{15} of filter should be more significant than the fourth times of D_{15} of the base soil. This criterion is well established in the literature and the standard manuals (United States Army Corps of Engineers, USACE (1953), and later validated by several researchers and they also provided their criteria (e.g., Vaughan and Soares 1982; Sherard et al. 1984a, b; Sherard and Dunnigan 1989; Honjo and Veneziano 1989; Indraratna et al. 1996).

Table 5-4 summarizes the parameters utilized to model the particles, the interaction between them, drag force models, and other physical parameters. Figure 5-52 presents the typical shape of the sample with the dimensions. The sample is a cylinder with 5 cm of diameter and 11.8 cm of length. Figure 5-53 presents the models utilized to simulate the contact erosion process. The sample, cross-section of the sample, and pressure distribution along with the sample, are presented in four different gap ratios. The fine fraction particles are 5 mm, while the coarse fraction particles increased each time (15 mm, 20 mm, 25 mm) to create a range of D_c/D_f. For the 5 mm and 20 mm case, two different porosities are simulated. Figure 5-54 presents the pressure applied at the top of the specimen to model contact erosion (downward flow). Pressure starts from zero to 10000 Pa in 0.5 s and keeps constant for 1 sec. This pressure is equivalent to:

$$i = \frac{P}{\rho g L} \tag{5-2}$$

where P is the pressure at the top of the sample in Pa, ρ is the density of the fluid (water) in kg/m^3, g is the gravity acceleration in (m/s^2), and L is the length of the sample in m. for P = 10000 Pa. The sample's length is 0.2 m, the hydraulic gradient is about 5.1, which is enough to move the small particles.

Table 5-4. Parameters of CFD-DEM simulation of contact erosion

Parameter	Magnitude
Number of Particles	17450 to 18489
Density (kg/m^3)	2650
Modulus of Elasticity (Pa)	1×10^7
Poisson Ratio	0.3
Friction Coefficient	0.5
Normal Restitution Coefficient	0.2
Tangential Restitution Coefficient	0.2
Coefficient of Rolling Resistance	0.1
Computational parameters	
DEM time step	4.46×10^{-5} $(5\ mm)$ 1.33×10^{-4} $(15\ mm)$ 1.78×10^{-4} $(20\ mm)$ 2.23×10^{-4} $(25\ mm)$
CFD time step	1×10^{-3}
CFD mesh size (mm)	*depends on the model*
Drag Force Model	Di Felice
CFD flow model	Laminar

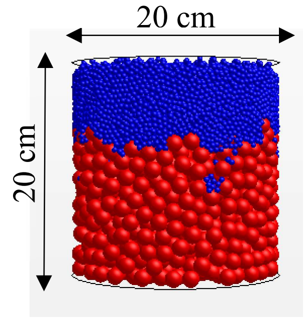

Figure 5-52. The dimensions of the simulated models

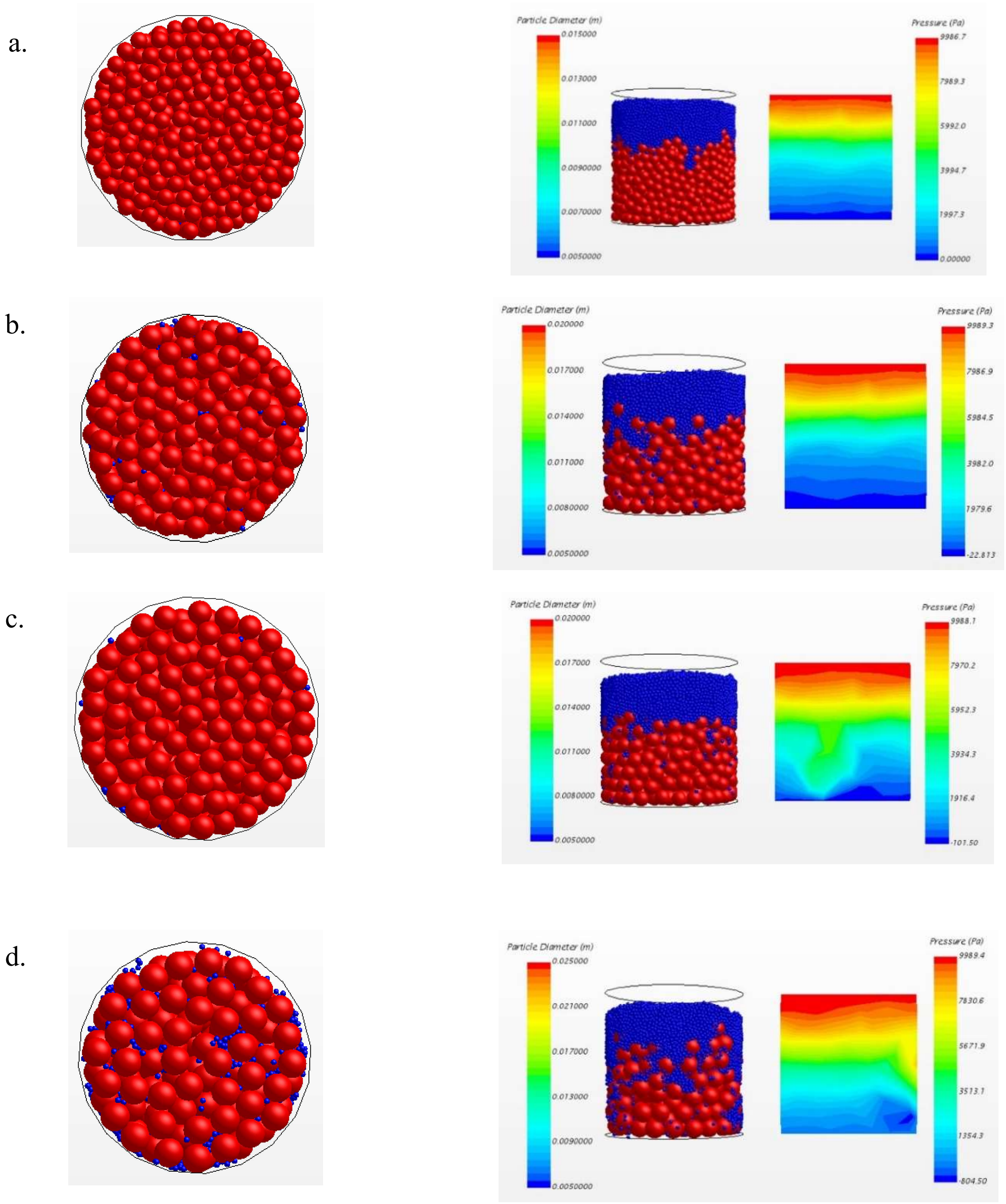

Figure 5-53. CFD-DEM models to investigate Terzaghi filter criterion; a) 5 mm and 15 mm, b) 5 mm and 20 mm-n=0.44, c) 5 mm and 20 mm-n=0.4, and d) 5 mm and 25 mm

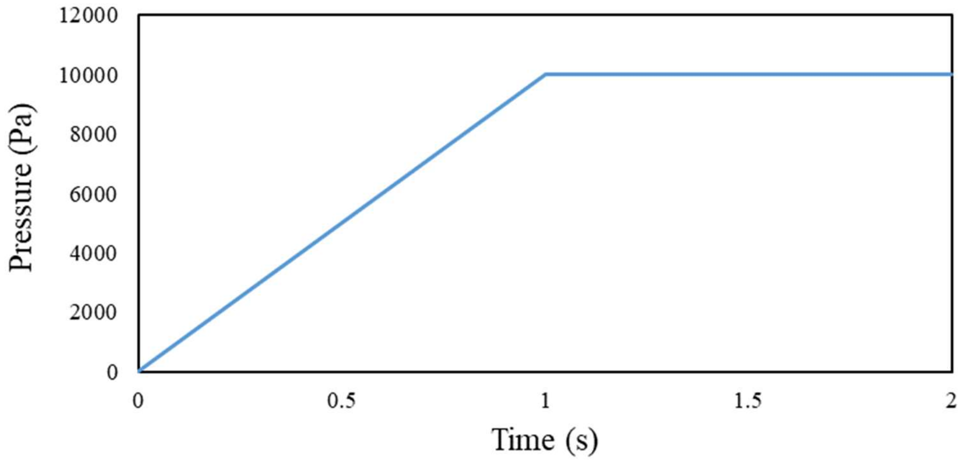

Figure 5-54. The pressure applied at the top surface of the sample

Figure 5-55 indicates the normalized mass loss to the mass of 5 mm particles during the simulation time, and Figure 5-56 shows their final values. If we consider the values smaller than 1% as negligible, the number 4 can act as a boundary for deciding the possibility of contact erosion in the proposed samples. Although in the sample 5mm & 20 mm with n=0.4, the final value is lower than 1%, by increasing the porosity to 0.44, it goes beyond 1%. While case 5mm & 15 mm with the D_c/D_f ratio of 3 can be considered a stable case in contact erosion, case 5 mm & 25 mm with the D_c/D_f of 5 shows a substantial erosion.

In Figure 5-53, the cross-section of the bottom of the sample at the end of the simulation is also presented. In the first case ($D_c/D_f = 3$), no 5 mm can be observed, while for the last case ($D_c/D_f = 5$) the presence of 5 mm particles is clear. In the case of $D_c/D_f = 3$ and n=0.4, several particles can migrate through the boundaries of the sample. In contrast, in the case of $D_c/D_f = 3$ and n=0.44, due to the looser matrix of particles, the migration of 5 mm particles through the voids between the particles (center part of the sample) can also be observed.

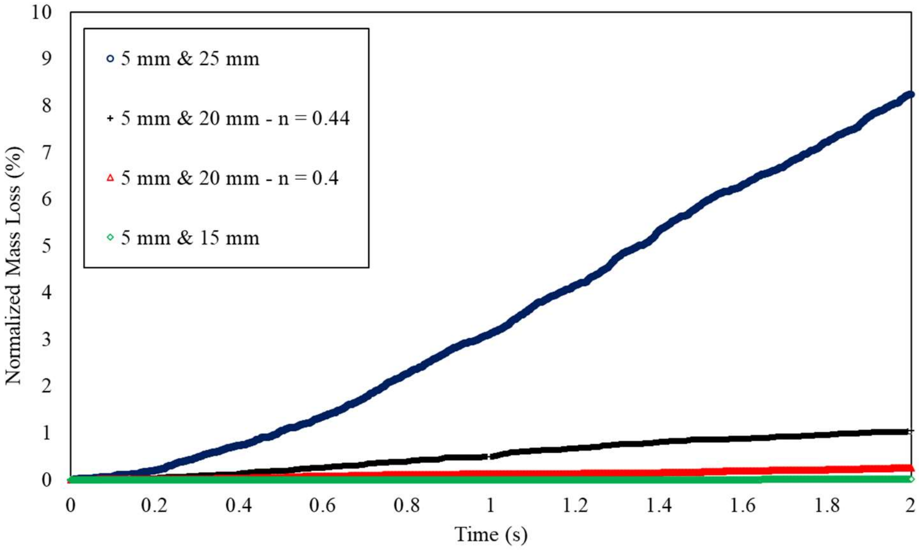

Figure 5-55. Normalized mass loss (%) (mass loss to the mass of 5 mm particles) for four samples considered to check Terzaghi criterion

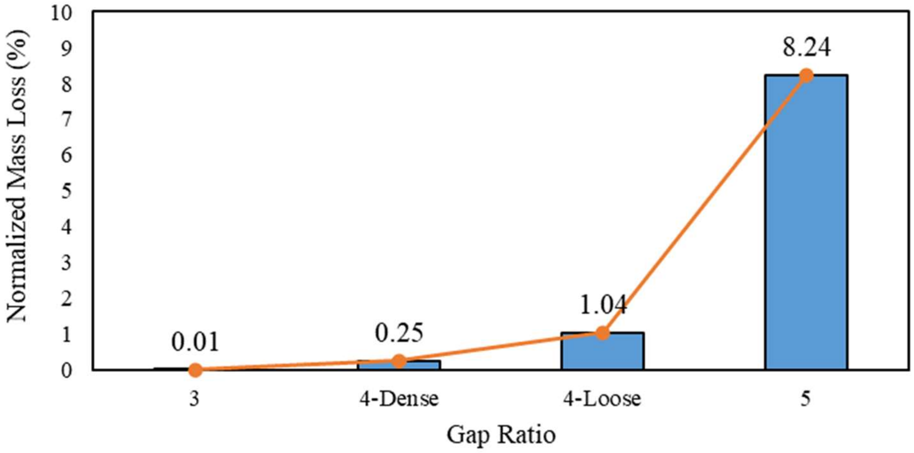

Figure 5-56. The final value of the normalized mass loss (mass loss to the mass of 5 mm particles) at the end of simulations

Gradation of particles and the self-filtering effect of the particles can affect the magnitude of erosion. More importantly, the broader distribution of particles helps to decrease the value of erosion. More samples with gradation curves were simulated to investigate the Terzaghi criterion more deeply to investigate this effect. The properties of these grain size distributions are summarized in Table 5-5. Same profile pressure and a downward flow have been utilized to simulate the model.

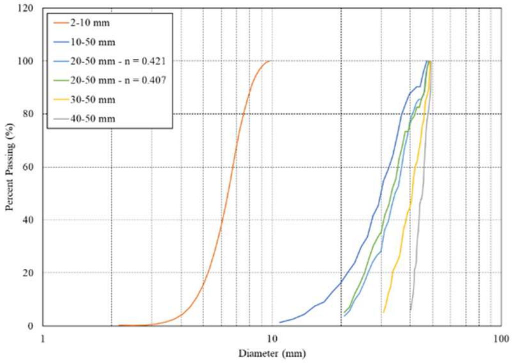

Figure 5-57. The grain size distribution of the samples simulated to investigate the Terzaghi criterion in contact erosion

Table 5-5. Properties of grain size distributions considered to investigate contact erosion and Terzaghi filter criterion

Sample	Min. (mm)	Max. (mm)	Mean (mm)	SD (mm)	C_u	C_c	D_{15} (mm)	D_{85} (mm)
2-10 mm	2.16	9.75	5.96	2.33	1.46	1.04	4.98	7.77
10-50 mm	10.79	47.32	29.05	11.20	1.88	1.08	19.37	38.67
20-50 mm n = 0.421	20.61	48.17	34.39	8.45	1.60	1.07	24.85	43.22
20-50 mm n = 0.407	20.62	48.61	34.62	8.58	1.57	0.96	23.88	44.70
30-50 mm	30.59	48.98	39.79	5.64	1.34	0.99	32.94	46.79
40-50 mm	40.32	49.49	44.90	2.81	1.12	0.98	41.51	48.59

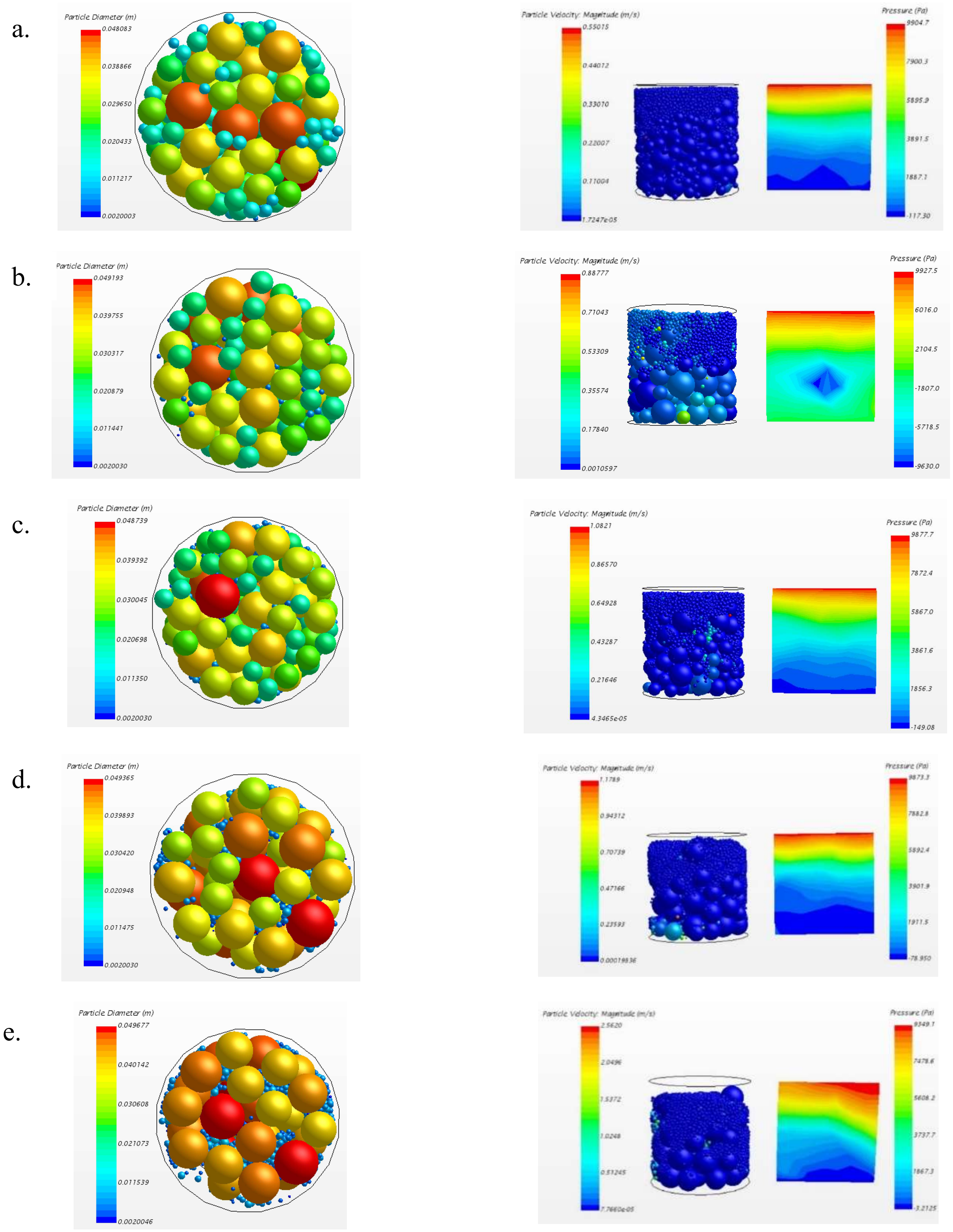

Figure 5-58. CFD-DEM models to investigate contact erosion and Terzaghi filter criterion; a) 2-10 mm and 10-50 mm, b) 2-10 mm and 20-50 mm-n = 0.407, c) 2-10 mm and 20-50 mm-n = 0.421, d) 2-10 mm and 30-50 mm and e) 2-10 mm and 40-50 mm

Figure 5-59 displays the normalized mass loss to the mass f 2-10 mm particles (%) during the time (s), and Figure 5-60 shows their final values if values more than 1% as unstable and under 1% as stable, only the first sample (2-10 mm & 10-50 mm) can be considered as stable. In the case of samples with a grain size distribution, even samples with $D_{15coarse}/D_{85fine}$ smaller than four shows instability, although for the case with n = 0.407, the mass loss is very low, still it is more than 1%. It can also be observed from Figure 5-54 that the value of erosion for the cases with $D_{15coarse}/D_{85fine}$ lower than 4 (2-10 mm & 10-50 mm and 2-10 mm & 20-50 mm – n = 0.407 and 2-10 mm & 20-50 mm – n = 0.421 the normalized mass curve (%) is not progressive and its rate of increase tends to be about zero with time. While for the cases with $D_{15coarse}/D_{85fine}$ lower than four, the rate is decreased but still is substantial with time. Although for samples b and c in Figure 5-58, the final value of the mass loss is higher than 1%, considering the constant rate after t = 1 s can be considered as stable compared to the two unstable cases of d and e in Figure 5-58.

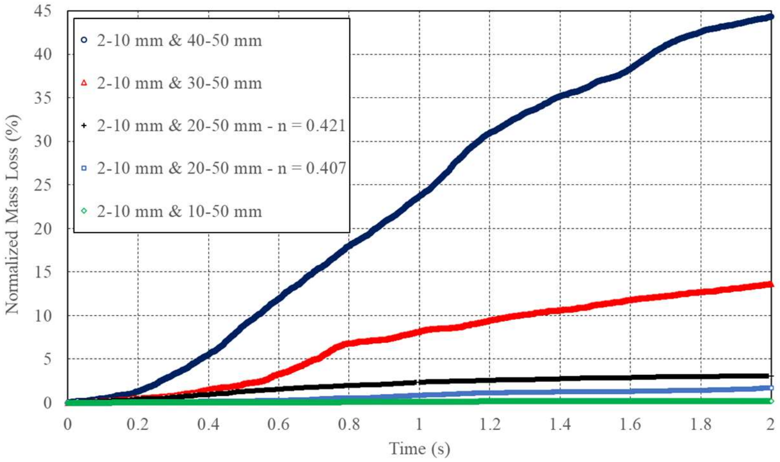

Figure 5-59. Normalized mass loss (%) (mass loss to the mass of 2-10 mm particles) for five samples considered to check Terzaghi criterion

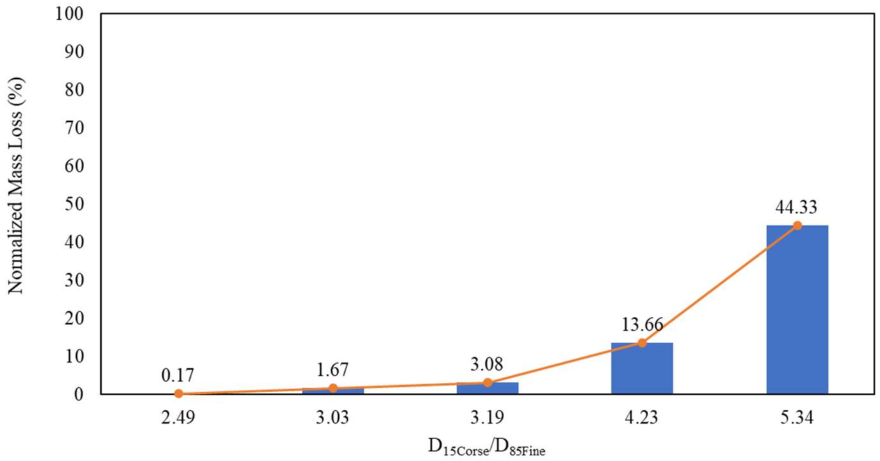

Figure 5-60. The final value of the normalized mass loss (mass loss to the mass of 2-10 mm particles) at the end of simulations

Both the categories mentioned above of CFD-DEM simulations, including constant diameter samples and samples with grain size distributions, validate the efficiency of the Terzaghi filter design criterion.

5.3.3. Investigation of common criteria for internal erosion

In this part with 12 cases of mixed samples (fine and coarse parts), has been investigated to investigate another form of internal erosion, which is suffusion. The same soil parameters, interaction properties, and drag force models as the contact erosion case have been considered in suffusion CFD-DEM simulations (Table 5-4). The dimensions of the model are These twelve samples are classified into three groups. In the first group, the fine content is smaller than 17%, and their porosities are in the range of 0.398 to 0.414 (Figure 5-62). The second group has a fine fraction lower than 15% with porosities between 0.325 to 0.344 (Figure 5-63), and the third group samples have fine content between 18 % to 20.4% and porosities between 0.386 to 0.366 (Figure 5-64).

Table 5-7 summarizes the common criteria utilized in standards to investigate the vulnerability of different samples of granular soils to the suffusion. All of these criteria focus on geometric properties of the grain size distribution of the particles. The result of the simulated samples is tested with each criterion and compared.

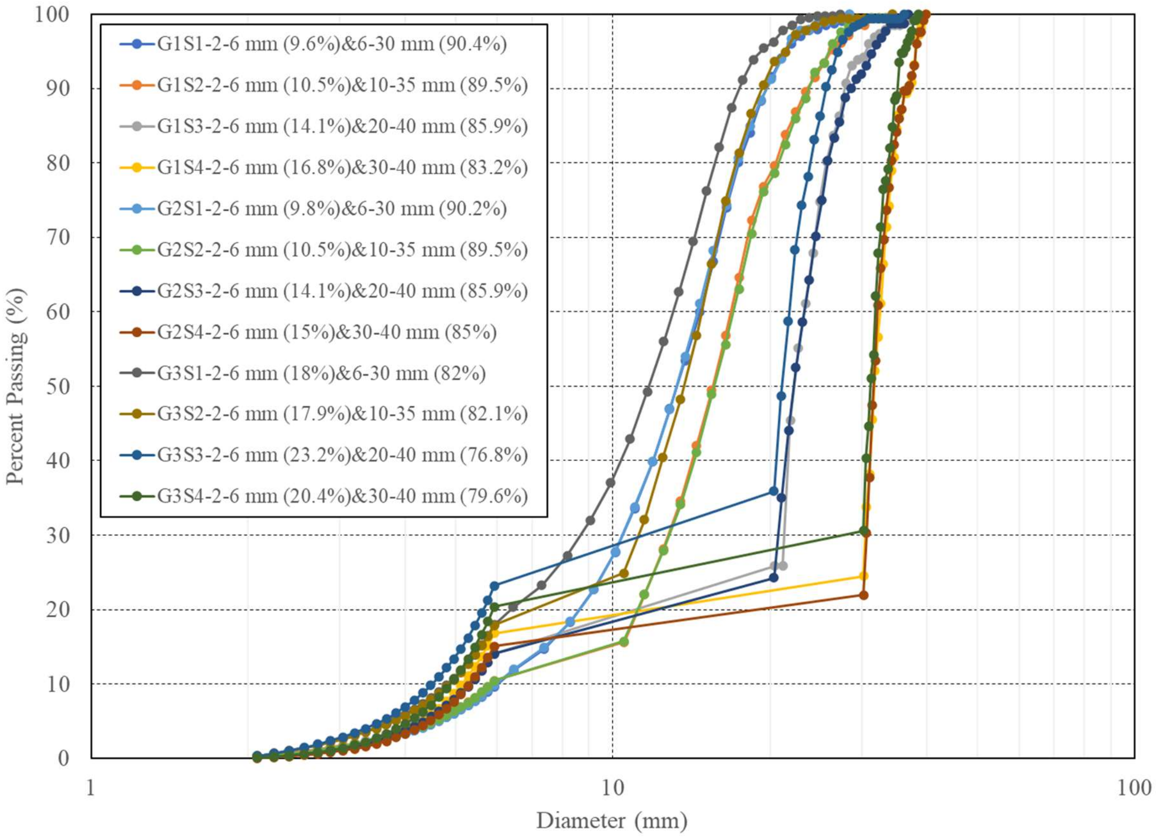

Figure 5-61. Grain size distributions of twelve samples simulated to investigate the suffusion phenomenon

Table 5-6. Properties of grain size distributions simulated to investigate the suffusion phenomenon

Sample Designation	Fine Fraction (%)	Coarse Fraction (%)	Porosity	Min.D (mm)	Max.D (mm)	D_{10} (mm)	D_{15} (mm)	D_{30} (mm)	D_{50} (mm)	D_{60} (mm)	D_{85} (mm)
G1S1	9.60	90.40	0.398	2.08	28.35	6.01	7.45	10.46	13.27	14.67	18.53
G1S2	10.50	89.50	0.403	2.08	34.28	5.83	9.93	12.77	15.53	16.85	21.80
G1S3	14.10	85.90	0.403	2.08	38.55	5.35	5.35	20.70	22.23	22.85	20.43
G1S4	16.80	83.20	0.414	2.08	39.80	5.14	5.74	30.44	31.67	32.50	35.09
G2S1	9.80	90.20	0.325	2.08	28.35	5.96	7.39	10.45	13.25	14.52	18.34
G2S2	10.50	89.50	0.328	2.08	34.28	5.88	6.95	12.73	15.72	17.09	22.01
G2S3	14.10	85.90	0.327	2.08	36.80	5.33	7.25	20.71	22.20	23.25	27.05
G2S4	15.00	85.00	0.344	2.08	39.80	5.31	5.91	30.60	31.58	32.16	35.19
G3S1	18.00	82.00	0.386	2.08	27.28	4.82	5.57	8.68	11.74	13.04	16.47
G3S2	17.90	82.10	0.388	2.08	34.28	4.87	5.58	11.20	13.67	14.79	18.12
G3S3	23.20	76.80	0.372	2.08	38.45	4.51	5.15	13.62	21.09	21.75	24.70
G3S4	20.40	79.60	0.396	2.08	38.45	4.88	5.44	28.74	31.17	31.82	34.34

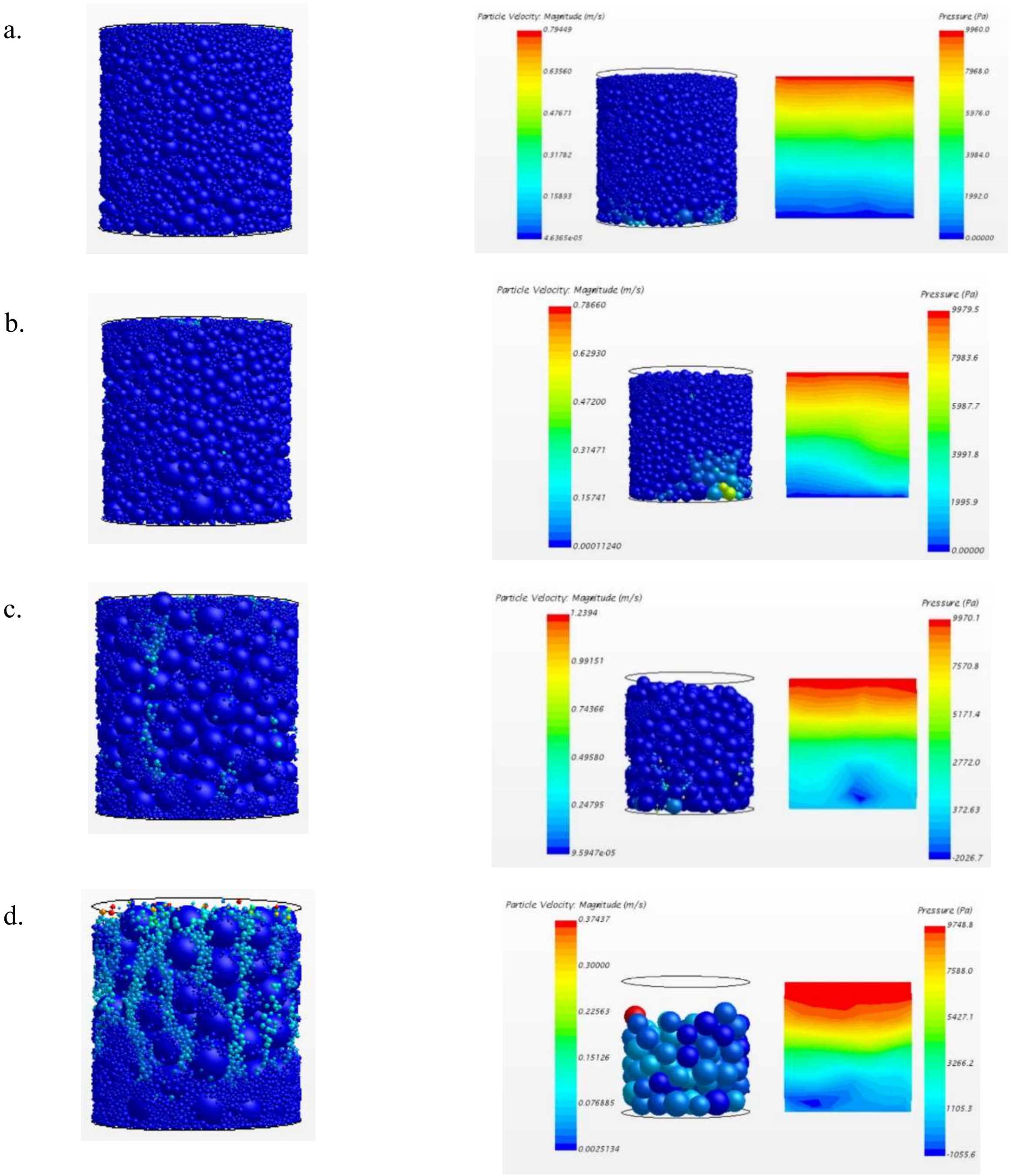

Figure 5-62. The first group of simulations a) 2-6 mm & 6-30 mm with a fine content of 9.6% and the porosity of 0.398 b) 2-6 mm & 10-35 mm with a fine content of 10.5% and the porosity of 0.403 c) 2-6 mm & 20-40 mm with a fine content of 14.1% and the porosity of 0. 403 d) 2-6 mm & 30-40 mm with a fine content of 16.8% and the porosity of 0.414

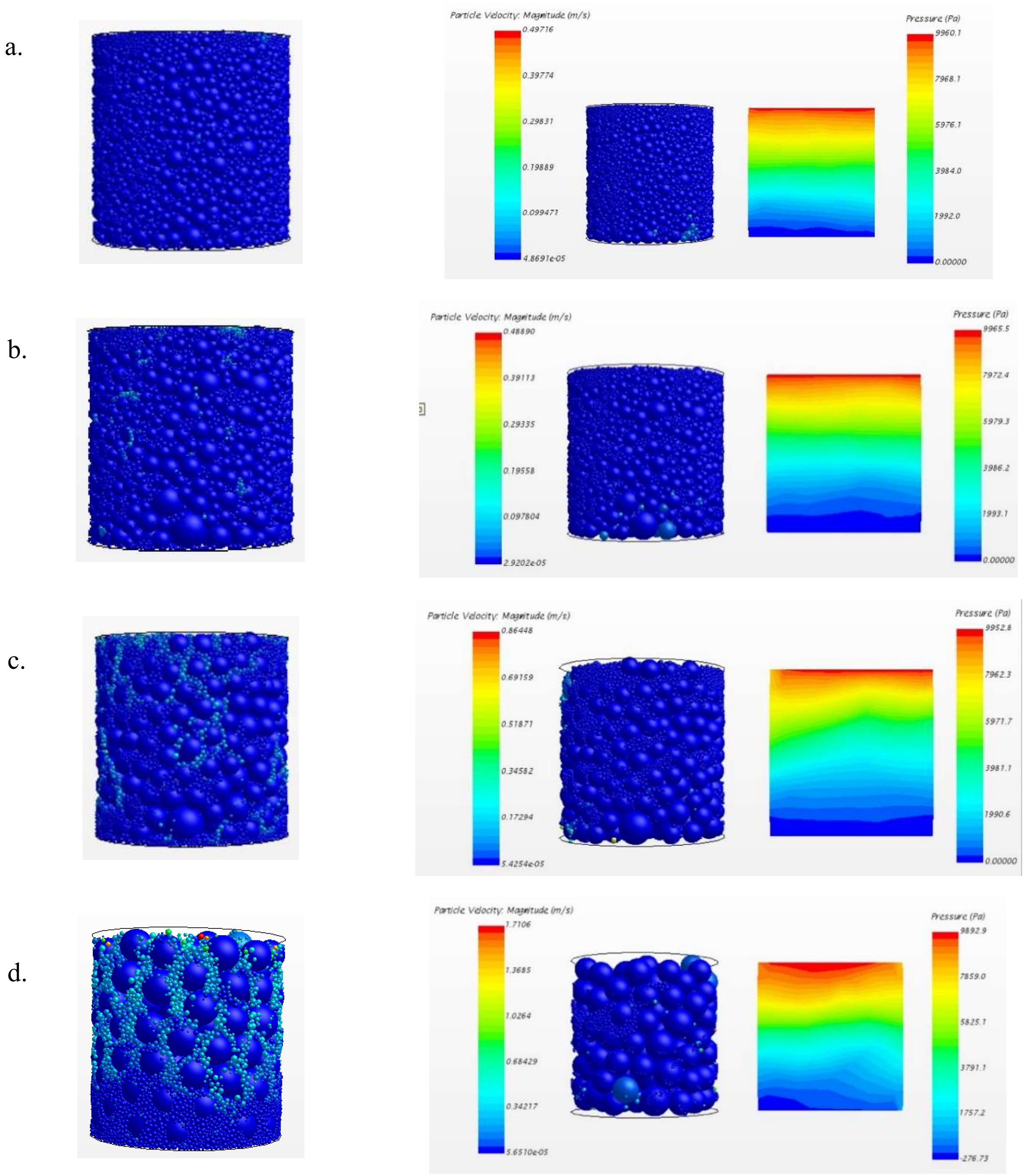

Figure 5-63. The second group of simulation models a) 2-6 mm & 6-30 mm with a fine content of 9.8% and the porosity of 0.325 b) 2-6 mm & 10-35 mm with a fine content of 10.5% and the porosity of 0.328 c) 2-6 mm & 20-40 mm with a fine content of 14.1% and the porosity of 0. 327 d) 2-6 mm & 30-40 mm with a fine content of 15% and the porosity of 0.344

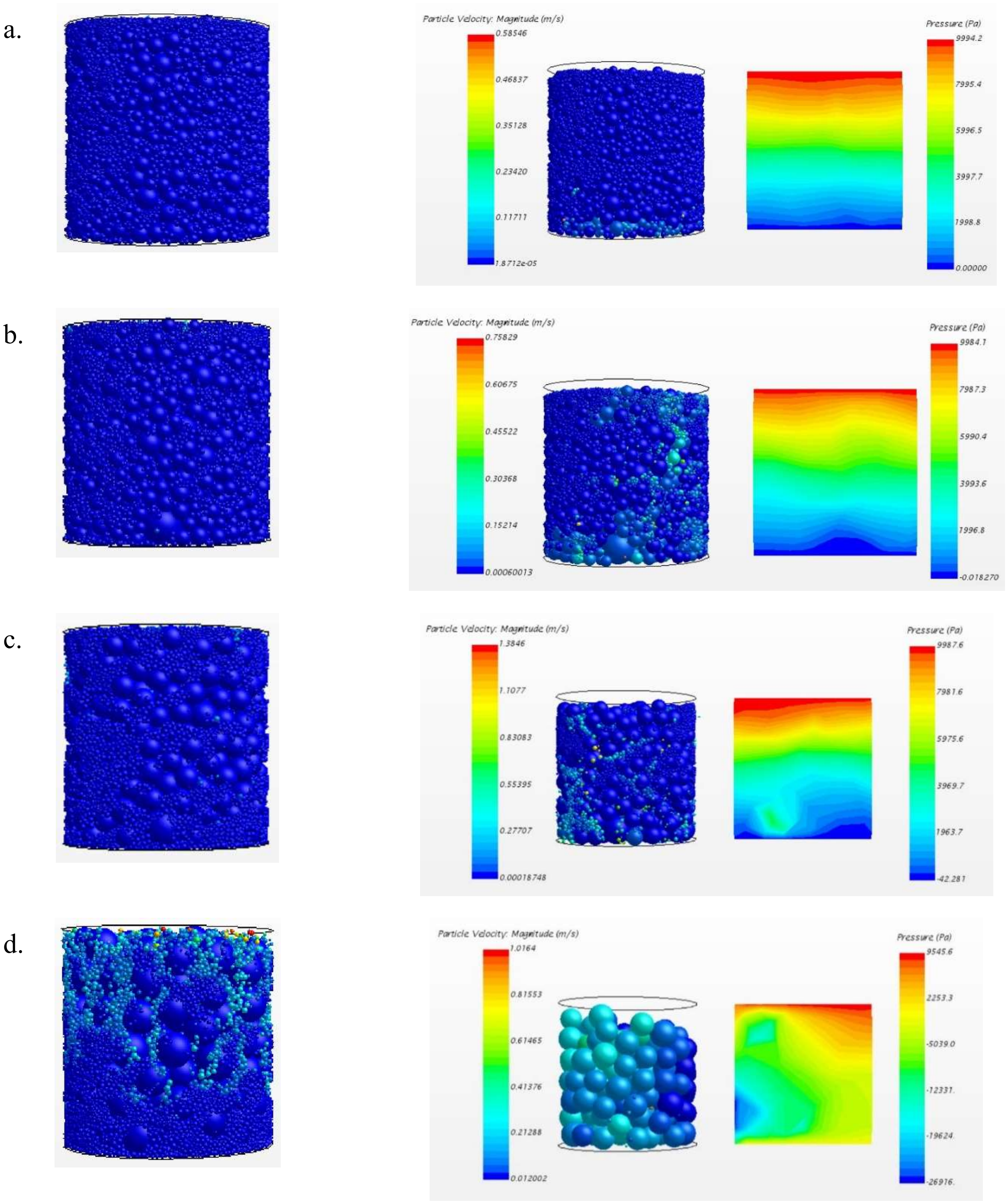

Figure 5-64. The third group of simulation models a) 2-6 mm & 6-30 mm with a fine content of 18% and the porosity of 0.386 b) 2-6 mm & 10-35 mm with a fine content of 17.9% and the porosity of 0.388 c) 2-6 mm & 20-40 mm with a fine content of 23.2% and the porosity of 0.372 d) 2-6 mm & 30-40 mm with a fine content of 20.4% and the porosity of 0.396

Table 5-7. Common criteria to investigate the vulnerability of different to granular soils suffusion.

Criterion	Relationship	Application	Range of Application
Istomina (1957)	$C_u \leq 10$ (internally stable) $10 \leq C_u \leq 20$ (transitional) $C_u \geq 10$ (internally stable)	Sandy gravel	GEO (1993), USDA(1994), USSD(2011)
Kezdi (1969)	$(d_{15c}/d_{85f})_{max} \leq 4$ (internally stable)	All soils	USSD(2011)
Kenney and Lau (1985)	$(H/F)_{min} \geq 1$ (internally stable)	Granular soils	GEO(1993), CDA(2007), ICOLD(1994)
Burenkova (1993)	$0.76\log(h'') + 1 < h' < 1.68\log(h'') + 1$ (internally stable)	Cohesionless and graded soils	
Li and Fannin (2008)	$F < 15, (H/F)_{min} \geq 1$ (internally stable) $F > 15, H \geq 15$ (internally stable)	Granular soils	

C_u = Uniformity coefficient; d_{15} = the diameter of 15% mass percent passing of the coarse part; d_{85f} = the diameter of 85% mass percent passing of the coarse part; H = mass fraction between grain size of d and 4d; F = mass fraction at any grain size d; $h' = d_{90}/d_{60}$; $h'' = d_{90}/d_{15}$; d_{15}, d_{60}, d_{90} the diameter of 15%, 60%, and 90% of mass percent passing, respectively.

Figure 5-65 presents the normalized mass loss for all samples to the total mass of each sample introduced in the above.during the time of the simulation, and Figure 5-66 shows their final values. In terms of normalized mass loss during the time and the rate of increase, seven samples show substantial values of mass loss (more than 2%; G1S4, G2S4, G3S4, G1S3, G2S3, G3S3, G3S2), and five samples reach to a constant value of mass loss without an increase in the value (lower than 2%; G1S1, G2S1, G3S1, G1S2, G2S2). If we behave more conservative and 1% of mass filing is considered for the decision about the stability, only two samples are stable (G1S1, G1S2)

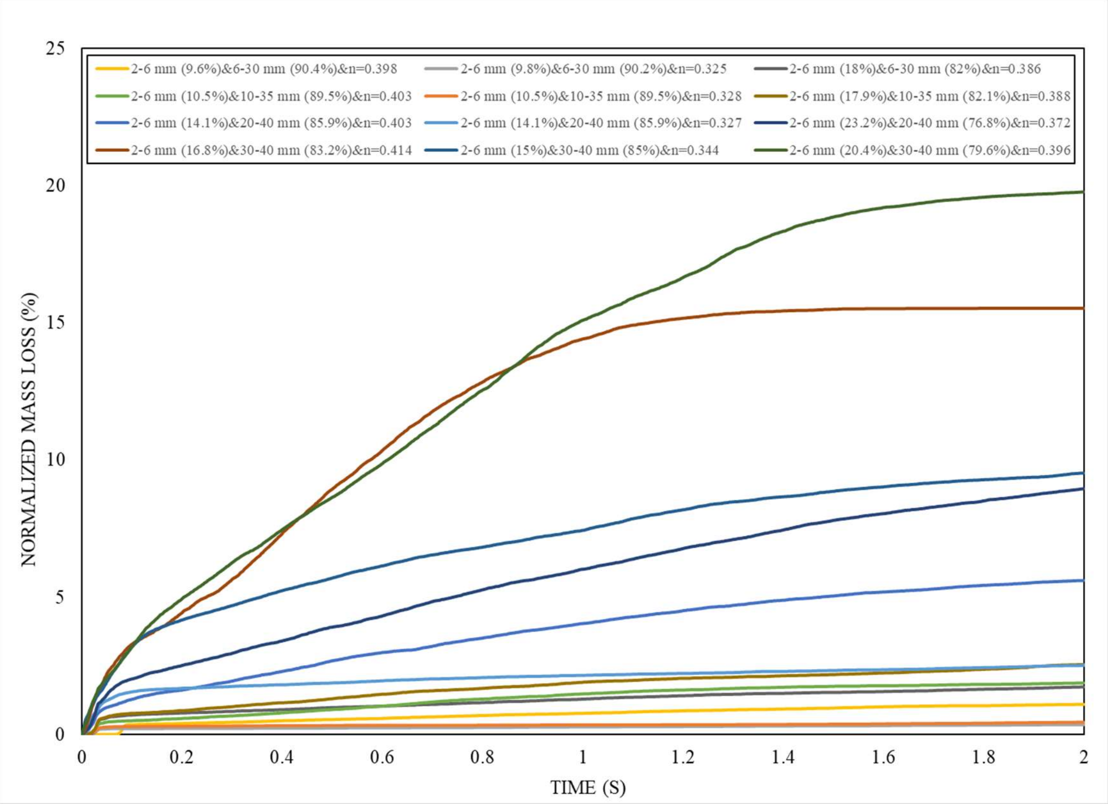

Figure 5-65. Normalized mass loss (%) (mass loss to the total mass of the sample) for five samples considered to check Terzaghi criterion

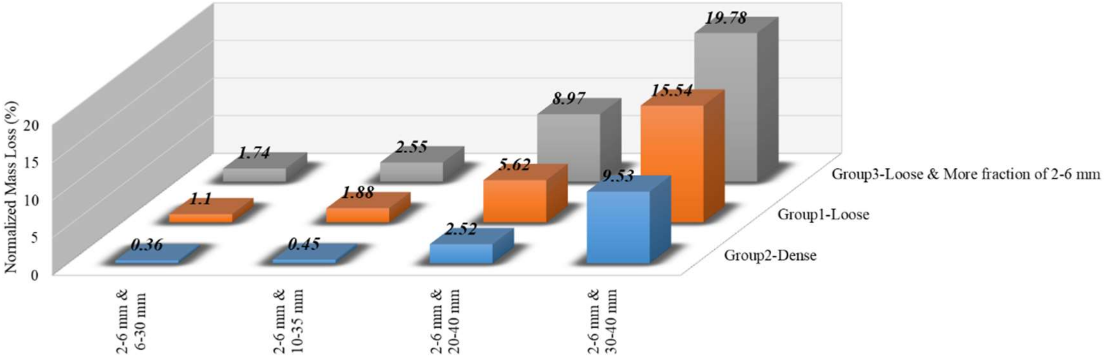

Figure 5-66. The final value of the normalized mass loss (mass loss to the total mass of the sample) at the end of simulations

5.3.4. Istomina (1957) stability criterion

Istomina (1957) proposed a uniformity gradation-based criterion to check the internal stability of sandy gravel soils. He considered the sandy gravel soil in a stable state if the coefficient of uniformity, C_u, is lower than 10. If C_u is between 10 and 20, the soil is considered as transitional and unstable for C_u values larger than 20. Table 5-8 shows the values of C_u for the simulations. Based on the Istomina criteria, all the samples are considered stable, which is far from the results of the simulation. Although the coefficient of uniformity is a useful index in soil classification, but can not detect the gaps between these two diameters (D_{10} and D_{60}) and can not be considered as a representative index to evaluate the internal stability of the sandy gravel soils.

Table 5-8. Comparison of simulation results with Istomina (1957) stability criterion

Sample	C_u	Criterion	Result
G1S1	2.44	S	S
G2S1	2.44	S	S
G3S1	2.7	S	S
G1S2	2.89	S	S
G2S2	2.91	S	S
G3S2	3.04	S	U
G1S3	4.27	S	U
G2S3	4.36	S	U
G3S3	4.83	S	U
G1S4	6.32	S	U
G2S4	6.06	S	U
G3S4	6.52	S	U

5.3.5. Kezdi (1969) stability criterion

Kezdi (1969) proposed a criterion based on the filtering capacity of coarse grain particles to the fine particles in the soil matrix (Zhang et al. 2016). In this criterion, the grain size curve is split into a coarse component and a fine component. For the two components, the $D_{15coarse}/D_{85fine} < 4$, which is initially proposed by Terzaghi (1932), should be satisfied to consider the soil as internally stable. Figure 5-67 shows the values of $D_{15coarse}/D_{85fine}$ for different values of percent passing for all simulation samples. Their maximum values are summarized in

Table 5-9 samples G1S1, G2S1, G3S1, and G3S2 are entirely under the criterion line and can be considered stable based on the Kezdi criterion. For other samples, G1S2, G1S3, G1S4, G2S2, G2S3, G2S4, G3S3, and G3S4, some of the curves are upper than the stability line and can be considered as internally unstable soils. The simulation results show that samples G1S1, G2S1, G3S1, G2S1, and G2S2 are stable. Sample G3S2, which is stable based on the stability criterion, is unstable based on the simulation results.

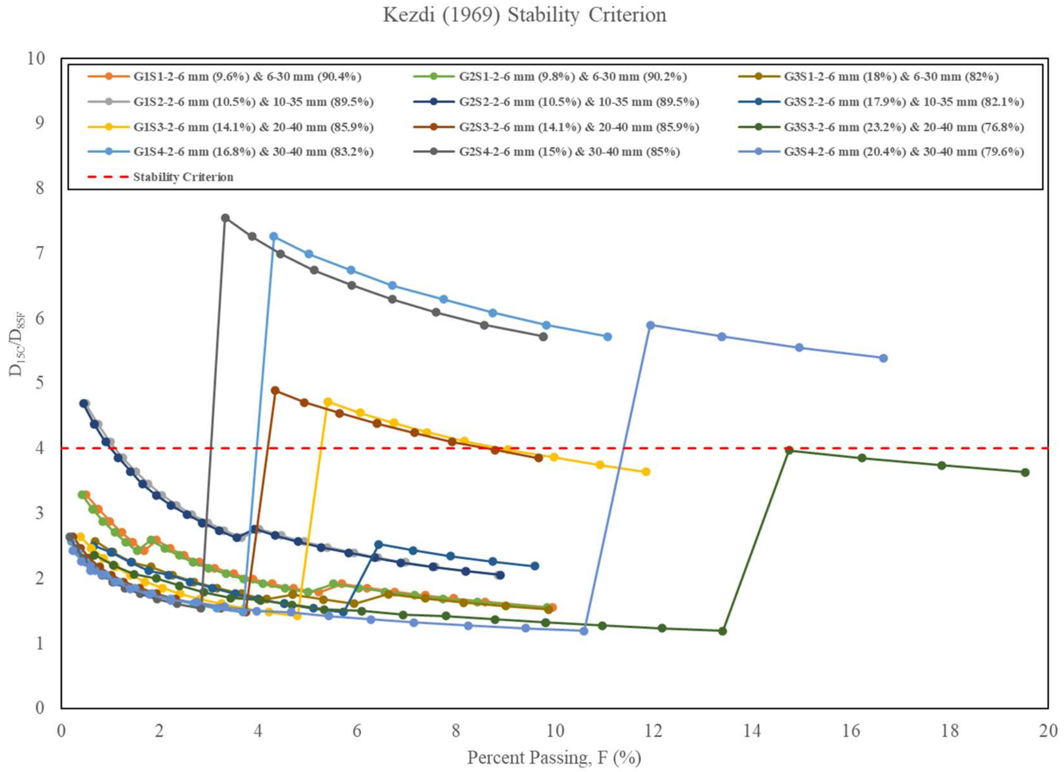

Figure 5-67. Variation of d_{15c}/d_{85f} by considering different values of d to classify fine and coarse parts

Table 5-9. Comparison of simulation results with Kezdi (1969) stability criterion

Sample	D_{15F}(mm)	D_{85B}(mm)	F	(D_{15F}/D_{85B})max	Criterion	Result
G1S1	7.37	2.24	0.50	3.29	S	S
G2S1	7.37	2.24	0.42	3.29	S	S
G3S1	5.76	2.24	0.69	2.57	S	S
G1S2	10.50	2.24	0.49	4.69	U	S
G2S2	10.50	2.24	0.45	4.69	U	S
G3S2	10.50	4.16	6.43	2.52	S	U
G1S3	20.39	4.32	5.40	4.72	U	U
G2S3	20.35	4.16	4.34	4.89	U	U
G3S3	20.34	5.12	14.75	3.97	U	U
G1S4	30.20	4.16	4.31	7.26	U	U
G2S4	30.21	4.00	3.32	7.65	U	U
G3S4	30.20	5.12	11.94	5.9	U	U

5.3.6. Kenney and Lau (1985) stability criterion

Kenney and Lau (1985), with a series of laboratory suffusion test, showed that if the mass fraction of particles between d and 4d (H%) is not larger than the mass fraction of particles smaller than d (F%), the suffusion will happen and the soil is unstable ($(\frac{H}{F})_{min} < 1.3$). Otherwise, the soil is stable ($(\frac{H}{F})_{min} > 1.3$). Kenny and Lau (1986), in their next paper, revised the limit of criterion to 1 ($Unstable$: $(\frac{H}{F})_{min} < 1.0$, $Stable$: $(\frac{H}{F})_{min} > 1.0$).

Figure 5-68 presents the values of $\frac{H}{F}$ for different values of d and Table 5-10 summarizes their maximum values. Based on Figure 5-68, the variation of $\frac{H}{F}$ for six samples (G1S1, G2S1, G3S1, G1S2, G2S2 and G3S2) is larger than one, and the rest are smaller than one and unstable. Based on Table 5-10, the simulation results showed that five samples (G1S1, G2S1, G3S1, G1S2, and G2S2) are stable, and the rest are unstable. With the Kezdi (1969) criterion, three samples are predicted as stable, while with the Kenny and Lau (1985) criterion, five samples are predicted as stable.

Li and Fannin (2008) showed that for the fine content, smaller than 15% Kezdi criterion is conservative, and in contrast, Kenny and Lau's criterion is conservative for fine content greater than 15% (Figure 5-69). This is way samples G1S2 and G2S2 are predicted as unstable by the Kezdi criterion.

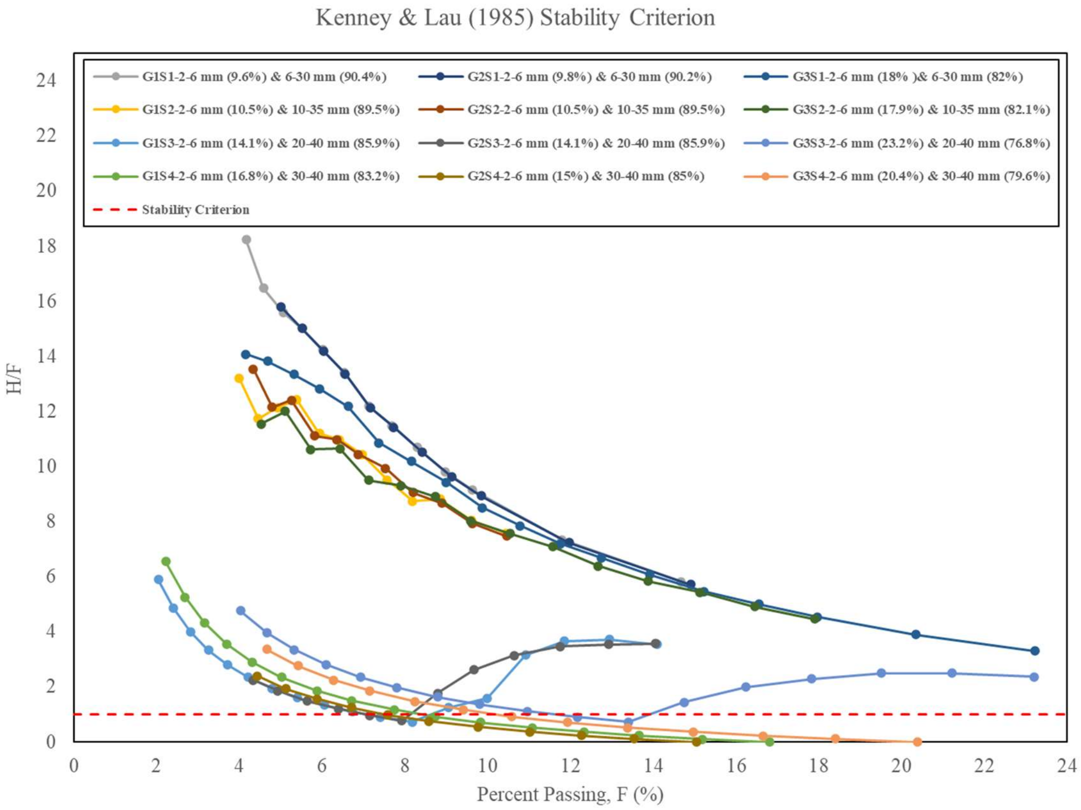

Figure 5-68. Variation of H/F by considering different values of particle size to determine H and F

Table 5-10. Comparison of results with Kenney and Lau (1985) stability criterion

Sample	H	F	$(H/F)_{min}$	Criterion	Result
G1S1	85.33	14.67	5.81	S	S
G2S1	85.10	14.90	5.71	S	S
G3S1	76.77	23.23	3.30	S	S
G1S2	79.16	10.45	7.58	S	S
G2S2	78.17	10.46	7.47	S	S
G3S2	79.91	17.90	4.46	S	U
G1S3	5.93	8.17	0.73	U	U
G2S3	6.13	7.93	0.77	U	U
G3S3	9.81	13.40	0.73	U	U
G1S4	0.00	16.81	0.00	U	U
G2S4	0.00	15.05	0.00	U	U
G3S4	0.00	20.38	0.00	U	U

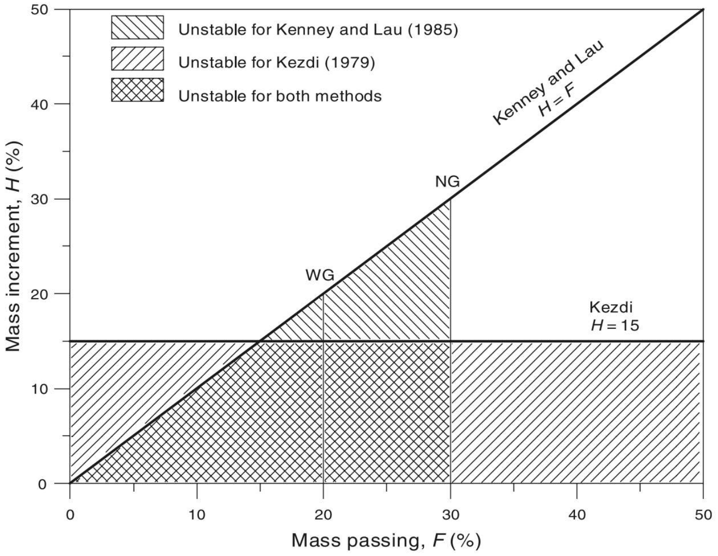

Figure 5-69. Comparison of Kezdi and Kenny and Lau criteria (reprinted from Li and Fannin (2008))

5.3.7. Burenkova stability (1993) criterion

Burenkova (1993) developed a testing procedure to determine the soil fractions in non-uniform soils that built the soil skeleton and loose particles inside the internal voids. He described the heterogeneity of the soils by two ratios called the conditional factors of uniformity ($h' = d_{90}/d_{60}$; $h'' = d_{90}/d_{15}$; d_{15}, d_{60}, d_{90} the diameter of 15%, 60%, and 90% of mass percent passing, respectively) and classified the tested soils in four regions on a semi-logarithmic plot (Figure 5-70).

Zone II shows the points corresponded to the non-suffusive soil skeleton. Zones I and III shows points that can be suffusive under certain hydraulic boundary conditions. Zone IV is the artificial soil samples. The non-suffusive zone can be explained by the following relationship, which is Burenkova criterion:

$$0.76 \log(h'') + 1 < h' < 1.68 \log(h'') + 1 \qquad \text{5-3}$$

Table 5-11 summarizes the results of numerical simulations compared to the Burenkowa criterion. Based on this criterion, only samples G1S1, G2S1, and G1S2 are stable, and others are unstable. The simulations results show that G1S1, G2S1, G3S1, G1S2, and G2S2 are stable and others unstable. The Burenkova criterion results are more conservative than other criteria and predicted two sound samples as unstable ones.

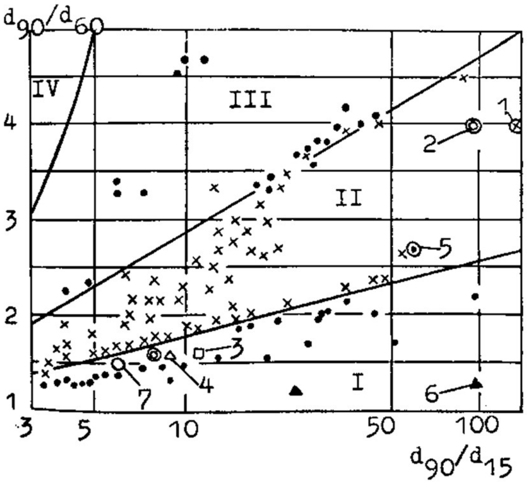

Figure 5-70. Classification of tested soils based on conditional factors of uniformity (reprinted from Burenkova (1993))

Table 5-11. Comparison of simulation results with Burenkova stability (1993) criteria

Sample	D_{15}(mm)	D_{60}(mm)	D_{90}(mm)	h'	h"	Low margin	High Margin	Criterion	Result
G1S1	7.45	14.67	19.70	1.34	2.64	1.32	1.71	S	S
G2S1	7.39	14.52	19.73	1.36	2.67	1.32	1.72	S	S
G3S1	5.57	13.04	17.46	1.34	3.13	1.38	1.83	U	S
G1S2	9.93	16.85	23.59	1.40	2.38	1.29	1.63	S	S
G2S2	6.95	17.09	22.58	1.32	3.25	1.39	1.86	U	S
G3S2	5.58	14.79	19.31	1.31	3.46	1.41	1.91	U	U
G1S3	7.03	22.85	28.36	1.24	4.04	1.46	2.02	U	U
G2S3	7.25	23.25	28.59	1.23	3.94	1.45	2.00	U	U
G3S3	5.15	21.75	25.59	1.18	4.97	1.53	2.17	U	U
G1S4	5.74	32.50	36.98	1.14	6.44	1.61	2.36	U	U
G2S4	5.91	32.16	36.81	1.14	6.22	1.60	2.33	U	U
G3S4	5.44	31.82	35.09	1.10	6.45	1.62	2.36	U	U

5.3.8. Li and Fannin stability (2008) criterion

Li and Fannin (2008) compared the efficiency of the Kezdi (1969) and Kenny and Lau (1985) criteria for granular soils and discussed their range of applications. As mentioned in the above, they discussed the range of application of each criterion and concluded that for the fine content, lower than 15% Kezdi criterion is conservative. Although, Kenny and Lau's criterion is conservative for fine content greater than 15% (Figure 5-69). Based on their discussion, they proposed a new criterion (similar to Kenny and Lau (1985)) which limits the Kenny and Lau criterion to fine content lower than 15%. For fine content higher than 15%, if H(%) (the mass fraction of particles between d and 4d) is greater than 15%, the sample can be considered stable. Table 5-12 presents the result of Li and Fannin's criterion is same as the Kenny and Lau criterion. The criterion predicts five samples as stable successfully (G1S1, G2S1, G3S1, G1S2, G2S2). There is only one sample that is predicted as stable but is unstable based on the results (2.55% of normalized mass loss). Other samples are considered as unstable, based on the results of the simulations.

Table 5-12. Comparison of results with Li and Fannin stability (2008) criterion

Sample	H	F	$(H/F)_{min}$	Criterion	Result
G1S1	85.33	14.67	5.81	S	S
G2S1	85.10	14.90	5.71	S	S
G3S1	76.77	23.23	3.30	S	S
G1S2	79.16	10.45	7.58	S	S
G2S2	78.17	10.46	7.47	S	S
G3S2	79.91	17.90	4.46	S	U
G1S3	5.93	8.17	0.73	U	U
G2S3	6.13	7.93	0.77	U	U
G3S3	9.81	13.40	0.73	U	U
G1S4	0.00	16.81	0.00	U	U
G2S4	0.00	15.05	0.00	U	U
G3S4	0.00	20.38	0.00	U	U

5.3.9. Conclusion

In this chapter, CFD-DEM was utilized to study several real applications of erosion. In the first application, the effect of different contributing parameters on erosion function derived from numerical simulations of Erosion Function Apparatus (EFA) was investigated. In the next, numerical modeling of the infilling process was pursued, and the effect of several parameters on the mass of infilling and its percentage was investigated. Finally, two aspects of internal instabilities, including contact erosion and suffusion, were examined by checking several standard criteria to investigate internal stabilities. In the following, a summary of conclusions from these simulations is provided.

5.2.9.1. CFD-DEM simulation of Erosion Function Apparatus (EFA)

The increase of the mean diameter of particles, coefficient of rolling resistance, and friction coefficient increases the critical velocity and critical shear stress and shifts the erosion functions toward the zones with more resistance against erosion.

Cohesion significantly affects erosion functions. Critical shear stress and critical velocities increase with the increase of cohesion, and the overall erosion function curve shifts to the zones with more resistance towards erosion. There is a linear relationship between critical shear stress and the cohesion between the particles. The relationship between critical velocity and cohesion is quadratic.

The abrasion of suspended particles on the settled particles depends on the ability of suspended particles to trigger incipient motion in settled particles. The erosion rates become higher by increasing the size of suspended particles and their concentration in the fluid. In 0.75 m/s and 3 m/s velocities, the values of erosion rates are close, while in velocities between these two ranges, the difference becomes highlighted.

The effect of dry density on the erosion function is minimum between the parameters which were investigated.

5.2.9.2. Infilling modeling

By increase of mean grain size in particles, the mass of infilling tends to decrease, although, in lower densities, these values are lower.

Although in shallow depth (h=0.3 m), the mass of infilling is zero, in higher depths (0.6 m to 1.5 m), the depth of the hole and its slope does not affect the mass of infilling.

The increase of the static friction coefficient and the coefficient of rolling resistance leads to lower values of the mass of infilling. Cohesion between the particles significantly affects the mass of infilling.

5.2.9.3. CFD-DEM modeling of contact erosion

After validation of the drag force model and the boiling simulation in CFD-DEM, nine numerical samples are constructed to test the efficiency of the numerical simulations in contact erosion modeling (four models with constant mean grain size and five models with grain size distribution). The results proved the efficiency of CFD-DEM in the simulation of contact erosion, and the comparison of the results verified the accuracy of the Terzaghi filter criterion.

5.2.9.4. CFD-DEM modeling of suffusion

After validation of the drag force model and the boiling simulation in CFD-DEM, 12 numerical samples are constructed to simulate the efficiency of the CFD-DEM simulations in suffusion modeling. Results showed the migration of small particles through the voids in the soil matrix in unstable samples. Five criteria for the internal stability of sandy gravel soils are compared with the results of the simulation (Istomina, Kezdi, Kenny and Lau, Burenkova, and Li and Fannin).

Between these criteria, Kenny-Lau and Li- Fannin criteria show the best predictions. Burenkova and Kezdi's criteria show conservative results, and Istomina criterion predictions are incorrect, especially when the coefficient of uniformity is higher.

6. CONCLUSIONS AND RECOMMENDATIONS

This research's main objective was to numerically study the erosion process on the topics that previously were under investigation experimentally at the soil erosion laboratory (SEL) at Texas A&M University. The first goal was to construct CFD models of three erosion tests (JET, HET, and BET), equipped with the Mech Morphing technique (a dynamic mesh that allows the mesh to deform due to erosion boundary) and compare the results to the experimental results.

The second goal was to compare the erosion functions, critical shear stresses, and critical velocities derived from the CFD-DEM simulation of the numerical samples in EFA tests with the experimental modeling of the EFA test.

The third goal was to study the particles' incipient motion in the CFD-DEM method and compare the acceleration, velocity, drag force, and lift force contributions with the video analysis of the EFA test in the laboratory.

The fourth goal was to investigate the average shear stress on the sample calculated from the Moody chart, average shear stress on the sample from CFD, and average shear stress on the particle.

The fifth goal was to inspect the contributing factors which affect the erosion functions extracted from the CFD-DEM simulation of EFA.

The final goal was to explore the potential and applications of CFD-DEM coupling in simulating the erosion process, including infilling and two types of internal instabilities; contact erosion and suffusion.

6.1. Chapter 1 – Introduction

In the first chapter, an introduction to the research topic, the research objectives, and the research plan to reach this research objective were presented. A summary of each chapter and the contributions of the current research to the new knowledge was also provided.

6.2. Chapter 2 – Background Knowledge

Chapter 2 offered an extensive literature review on the erosion phenomenon, erosion mechanism, erosion progression, and different types of internal erosion. The definition of four different internal instabilities, including concentrated leak erosion, backward erosion, soil contact erosion, and suffusion, was also explained. The control parameters that affect different internal instabilities and geometric criteria for assessing erosion potential were presented.

The erosion tests which numerically simulated in this research (JET, HET, EFA, and EFA), their applications, and their procedure are also explained. For each test, the advantages and disadvantages are also listed. A summary of the constitutive models for soil erosion and the background knowledge of measuring hydrodynamic forces in erosion were presented. A short literature review on the infilling definition and the factors influencing the infilling process were explained.

In the last section of this chapter, A review of the literature of numerical modeling of erosion (continuum and discrete) was provided. The basics of the CFD method equipped with mesh morphing technique and CFD-DEM method were explained. Particle equations of motion, different drag force modelings, two-way coupling model, momentum, mass, and energy transfers between discrete and continuum (fluid) medium, contact model between particles, cohesion modeling, and rolling resistance coefficient were introduced.

6.3. Chapter 3 – Numerical Simulation of Erosion Tests

In Chapter 3, the result of CFD simulations on non-erodible boundaries (CHEN4D code performed by H. C. Chen) on JET, HET, EFA, and BET were introduced. These simulations were extended to simulate the CFD method's tests mentioned above, equipped with mesh morphing technique. To change the boundaries, the erosion functions derived from the EFA was utilized on the boundaries. For each section, the shear stress on the boundaries is calculated, and the results were compared with the experimental results.

6.3.1. Comparison of Shear Stress Magnitudes in Some Erosion Tests by Numerical Simulation on Non-Erodible Soils

Table 3-1 summarizes the comparison of shear stress ranges for the erosion tests simulated with CHEN4D code on non-erodible boundaries. Overall, the shear stresses are in the range of 0 to 200 Pa. The shear stress is reasonably constant in the EFA, in the HET, and the BET along the borehole wall starting at 0.3 m above the rods' bottom. The shear stresses vary dramatically along the soil surface in the JET and the BET at the bottom of the borehole. For these two tests, the shear stress is near zero at the center of the soil surface reaches a peak at some small distance from the center, and decreases beyond that. This significant variation makes the theoretical interpretation of those two tests difficult, yet they are valuable as index erosion tests. The shear stresses evaluated based on the Moody chart give consistently higher values than numerical simulations.

Table 6-1. (REPEATED) Comparison of shear stress ranges in EFA, HET, JET, and BET resulting from CFD simulation

Test			U(ave) (m/s)	Surface condition	CHEN4D		Moody Chart
					Min. Shear Stress (Pa)	Max. Shear Stress (Pa)	
EFA			1	Smooth	3	3	2.6
				Rough	6	8	9
			3	Smooth	20	20	19
				Rough	55	70	81
			6	Smooth	70	70	67
				Rough	150	180	324
HET			2.5	Smooth	15	30	22
				Rough	25	30	57
JET			3	Smooth	2.5	51	-
				Rough	3	85	-
BET	SIDE	Gap (mm)	4.5	Rough	12.5	76.5	-
		150					
		75			0.5	96	-
		25			2.7	119	-
	BOTTOM	150			0	87	-
		75			0	155	-
		25			0	111	-

6.3.2. Comparison of laboratory test results and numerical simulation equipped with mech morphing technique

The final aim of this section was to compare the numerical simulation results of JET, HET, and BET with the experimental results. The erosion function resulted from the EFA test applied as a constitutive law of erosion on the soil fluid interface in a CFD framework with mesh morphing to observe the erosion progression. By this comparison, the CFD method's efficiency with mesh morphing to capture the results of these tests with an input erosion function was presented. In the following, a summary of the results is presented.

Table 3-3 summarizes the numerical simulation results. The findings show that the erosion function obtained from the EFA test for each sample can be reasonably used to produce a similar "scour versus time" plot to what the JET, the HET, and the BET experiments would result. However, the variety of interpretation techniques used for each test to obtain the shear stress in the soil-water interface leads to different erosion functions. Therefore, one must be aware of each test's interpretation techniques to obtain the erosion function (erosion rate versus shear stress). It is also worth noting that for the case of the HET results, the scour values refer to the average diameter of the drilled hole in the center of the sample.

Finally, using an erosion function for the three tests, the evolution of shear stress in the JET, HET, and BET during the test was investigated. For all tests, the peak shear stresses were decreased with time.

Table 6-2. (REPEATED) Summary of the numerical simulation results

	Sample Name	**Roughness**	**Final observed scour (mm)**	**Final Calculated Scour using the EFA Erosion Function (mm)**				**Figure**
				RH = 0 mm	RH = 0.5 mm	RH = 1 mm	RH = 3 mm	
JET	Sand #1	0.14	40	40.8	43.5	43.1	48	Figure 3-15
	Sand #2	0.122	23	13.8	16.8	20	20.3	Figure 3-18
	B-1 (4-6)	0.0024	7	10.8	14.3	17.5	18.5	Figure 3-20
	FHWA S2	0.0031	17	8	10.8	12.8	14.6	Figure 3-22
HET	SH-1	0.1	13.4	12.5	13.5	14	14.2	Figure 3-24
BET	CBH3	0.00038	20[1]	20.31	20.35	20.40	-	Figure 3-27

[1] The scour values shown for the BET are the maximum diameter enlargements in 8'-10' depth of the borehole

6.4. Chapter 4 - Comparison of CFD-DEM Simulation Results with Video Analysis

In Chapter 4, the CFD-DEM method's efficiency in capturing the precise values of velocity and drag forces was ensured by simulation of a validation example and comparing the results with the experimental modeling of the same problem. Finally, it tried to emphasize particles' incipient motion by the meticulous study of accelerations and velocities at the start of motion. To do so, this study was done with a video-analysis of Teflon balls and gravel particles (experimental modeling) and by CFD-DEM simulation of numerical samples with the same mean grain size as the experimental samples.

Determination and comparison of acceleration and velocities with numerical simulation and experimental modeling made it possible to compare horizontal and vertical accelerations' contributions at the start of the motion. More importantly, it enabled to compare the average shear stress calculated from the moody chart, average shear stress calculated from the CFD method, and the shear stress on one gravel of particle. In the following, a summary of conclusions from Chapter 4 are listed:

6.4.1. CFD-DEM model Validation

- A comparison of CFD-DEM simulation results with the results calculated from the particle image velocimetry (PIV) method and positron emission particle tracking (PEPT) methods prove the efficiency of CFD-DEM in capturing the correct average velocities of particles.

6.4.2. Comparison of erosion function extracted from laboratory test and erosion function resulted from numerical simulation

  - Erosion functions extracted from CFD-DEM simulations for granular soils have a good agreement with the experimental results. These results can be used as a complementary section to the CFD simulations with mesh morphing techniques. The erosion function extracted from CFD-DEM simulations can be used as the boundary input for CFD simulations with mesh morphing techniques.

6.4.3. Comparison of the results to the current relationships for the critical velocity and critical shear stress

- Both critical velocities and critical shear stresses calculated from CFD-DEM simulations of the samples are well fitted to the data from former researchers (data from Shields, Casey, US.WES, Gilbert, and white (reported by Vanoni (1975))

6.4.4. Comparison of velocities and accelerations from laboratory tests and numerical simulations

- In the experimental video analysis, almost all the average values of velocities are smaller than 0.1 m/s. for the samples with an average size of 5 mm, the horizontal component is larger than the vertical component (TB, SB, and GB), while for the larger particles (G1 and G2), the values of both components are about similar.

- In the numerical simulations, the average velocity values are proportional to the D_{50} of the particles. For the numerical results, except for G1 particles, all other velocities are smaller than 0.1 m/s.
- In the experimental video analysis, The average horizontal accelerations for all samples are higher than g. for TB, SB, and GB, the horizontal accelerations are higher than the vertical accelerations. At the same time, for the G1 and G2 cases, both components are similar
- With the numerical simulation, the overall average accelerations (horizontal and vertical) are lower than the video analysis calculations.
- The acceleration amplitudes from the experimental analysis are higher than results from numerical simulations, which can be connected to vibration f pump, causing more fluctuations and higher acceleration amplitudes.
- In both cases, for the smaller size of particles (TB, SB, and GB), horizontal components can play a significant role in the start of motion, while for larger particles (G1 and G2), the effect of vertical component (lift) can balance the effect of horizontal component.

6.4.5. Contributions of horizontal and vertical components of fluid force at the start of motion

- Accelerations calculated from the numerical simulation were applied to study the contributions of horizontal and vertical fluid force components in the incipient motion of particles. Results indicated that in small particles, the horizontal component plays the primary rule, while, in large gravel particles, the vertical component's contribution also highlighted its rule.

6.4.6. Comparison of shear stress calculated from the moody chart and the fluid forces

- The values of shear stress on the sample calculated from the CFD method, assuming an interface with a roughness of $D_{50}/2$ instead of the soil sample, are similar to the moody chart values.
- The local shear stress in the gravel particles is larger than the average shear stress calculated from the moody chart, and CFD method, and this difference can be magnified in the larger particles.

6.5. Chapter 5 - Numerical Simulation of Erosion Using CFD-DEM Technique and Applications

In Chapter 5, a more profound study of numerical simulation of erosion using CFD-DEM was investigated. The effect of several physical properties on erosion function extracted from CFD-DEM simulations of EFA was investigated.

6.5.1. CFD-DEM simulation of Erosion Function Apparatus (EFA)

- Increasing particles' mean grain size increases the critical velocity and associated critical shear stress. The overall shape of erosion function shifts to the right (more resistant to erosion), and its downward curvature decreases.
- By increasing both coefficients of rolling resistance and static friction coefficient, critical velocity and its associated critical shear stress increases and leads to an erosion function, which shifted to the zones with more resistance toward erosion. The increase of these two coefficients can stand for more angularity and friction between particles and less rounded shape of particles.

- Cohesion significantly affects erosion functions. Critical shear stress and critical velocities increase with the increase of cohesion, and the overall erosion function curve shifts to the zones with more resistance towards erosion.
- The relationship between critical velocity and cohesion is quadratic.
- There is a linear relationship between critical shear stress and the cohesion between the particles. The cohesion is approximately 37 times of critical shear stress. Cohesion is a macro parameter, while critical shear stress is a micro parameter. Although the final cohesion of a sample results from small micro adhesions between particles, its emergence depends on the action of sample particles together, and this mobilization increases the final value of cohesion. Critical shear stress is the required shear stress to detach one particle from the surface, which depends on the interaction between particles and micro adhesion forces between particles, which are significantly smaller than cohesion.
- The abrasion of suspended particles on the settled particles depends on suspended particles' ability to trigger incipient motion in settled particles. By increasing the size of suspended particles, the effect of abrasion on the erosion function would be more. However, this difference becomes more highlighted in fluid velocities between 0.75 m/s and 3 m/s. In the velocity of 0.75 m/s and lower, suspended particles' kinetic energy is low to affect the motion of settled particles. In the velocity of 3m/s and more, the possibility of abrasion between the suspended particles and settled particles are lower.
- With a higher concentration of suspended particles in the fluid, the erosion rates become higher. In 0.75 m/s and 3 m/s velocities, the values of erosion rates are close, while in velocities between these two ranges, the difference becomes highlighted.

- The effect of dry density on the erosion function is minimum between the parameters which were investigated.

6.5.2. Infilling modeling

- By increasing the mean grain size of particles, the mass of infilling (kg) and percent of infilling to the hole volume decreases. Although the vales are dependent on the value of upstream porosity (more porosity provides more mass of infilling and its percent to the volume of the hole), the percent of infilling can reach about one third by increasing the mean diameter of particles from 2 mm to 5 mm.
- The infilling mass is zero with a shallow depth because the scour hole's geometry allows the velocity field to reach the end of the scour hole, and induced shear stress can erode the particles out of the hole. For higher scour depth (more than 2 cm; scaled 0.6 m), the mass of infilling does not affect. Although due to the increase of volume due to the increase of depth, the percent of infilling to the volume decreases.
- The slope of the hole also does not affect the mass of infilling.
- With the increase of rolling resistance and static friction coefficients, the mass of infilling and the percent of infilling to the hole volume decreases. The increase of these two coefficients can be attributed to the more angular shape of particles with more friction between the particles.
- The bold effect of cohesion on the resistance against erosion was highlighted in the EFA modeling, and again here, its significant effect on decreasing the mass of infilling was represented.

6.5.3. CFD-DEM modeling of two internal instabilities in erosion, contact erosion and suffusion

In the last section of Chapter 5, coupled CFD-DEM's capability in capturing the proper mechanism of soil-flow interaction in soil contact erosion and suffusion was introduced. To do so, coupled CFD-DEM was first validated with a boiling condition example in granular soils to ensure the proficiency of the method in capturing the correct behavior of soil particles interacting with seepage forces. Then, several drag force models (numerical and experimental) compared with the current methodology to ensure the accuracy of drag force models, which is the cornerstone of coupled CFD-DEM modeling.

By constructing 21 numerical samples, the adequacy of standard criteria in assessing the internal stabilities of sandy gravel samples was investigated. The following conclusions are drawn from this section:

- Both Di Felice and Schiller-Naumann, the drag force model, capture acceptable results compared to other experimental and numerical results. The Di Felice drag coefficient values are higher and can consider the effect of enhanced drag on a particle due to the presence of other particles around it.
- The quicksand condition happens in a coupled CFD-DEM sample when the hydraulic gradient reaches to near one, which is compatible with a sudden decrease in coordination number (average value of contacts per particle) and buoyancy state of soil particles at the top of the sample.
- In soil sample with two separate diameters, when the gap ratio (D_{coarse}/D_{fine}) is smaller than 4, the normalized mass loss (mass loss to the mass of fine part) of particles is lower than 1% (stable). When it is more than 5, the normalized mass loss is higher than 1%

(unstable). In the case of a gap ratio of 4, when the sample has lower porosity (n=0.4), it is stable, and when it has higher porosity (n=0.44), it is unstable. The same conclusions can be drawn with the samples with grain size distributions. When $D_{15coarse}/D_{85fine}$ is higher than 4, the normalized mass loss with time is increasing with a rate (unstable), while for values lower than 4, the rate is not progressive, and its rate of increase tends to be about zero with time (stable). These findings perfectly conform to the Terzaghi filter criterion in the design of dams and levees.

- By increasing the porosity of samples, the fine contents in the samples,
- Although the Istomina criterion is successful in determining stable samples, it is very unsuccessful in determining unstable samples, which goes back to the application of only the uniformity coefficient in the assessment of stability. The coefficient of uniformity is a useful index in soil classification, but can not detect the gaps between these two diameters (D_{10} and D_{60}) and can not be considered as a representative index to access the internal stability of the sandy gravel soils.
- The Kezdi stability criterion ($D_{15coarse}/D_{85fine} < 4$) is successful in the correct assessment of internal instability in three samples but still is conservative for samples with fine content under 15%.
- Kenney and Lau stability criterion is very successful in the evaluation of internal stabilities in sandy gravel samples. For fine contents higher than 15%, this criterion is conservative.
- Burenkowa stability criterion is the most conservative stability criterion between the five stability criterion studied in this research. Still, the criterion is successful in the evaluation of internal stability.

- Li and Fannin's stability criterion results are the same as the Kenney and Lau criterion, which is evident because Li and Fennin criterion tries to improve the Kenney and Lau criterion for fine content higher than 15%.

6.6. Recommendations on Further Research

- Due to very high computational costs and long-running time of JET and HET and BET, although several initial models were tested, the simulations were stopped to concentrate on more important topics related to erosion. By improving the computational efficiency of hardware, their simulations are recommended to pursue.
- Measuring accelerations and velocities pursued in this dissertation by comparing the results of experimental modeling (video analysis) and numerical simulations. In the first stages of this dissertation, an accelerometer was programmed to be located in a gravel shape particle to measure the accelerations in the incipient motion of particles. Due to the vibration of the EFA and the presence of water, the accelerometer is needed, which was expensive and out of this research's financial borders. Although this money was a lot for university oriented research, it would be little money for other private agencies. Several research types are pursued in this area (Shan et al. 2015). But still, this branch of research on erosion can be interesting to pursue.
- In this research, modeling of EFA was performed, and the physical properties of granular soils, which can affect the soil's erosion function, were investigated. Still, investigating contributing factors that affect the erosion function in fine-grained soils is more controversial, especially chemical properties and cohesion. Briaud et al. (2019) experimentally studied the erosion function's physical properties for fine-grained soils.

Numerical simulation (CFD-DEM) of fine-grained soils is far more complexed than granular soils. The shape of clay particles, the interaction between them, and the chemical properties between the clay minerals are very complexed to model. Still, by improving the molecular dynamics and new models and improving the computational efficiency of computer hardware, simulation of fine-grained samples could be reachable.

- In this research, only spherical particles with a diameter distribution were simulated. The effect of the shape of particles was tuned by a combination of the coefficient of rolling resistance and coefficient of static friction. The angularity of particles can be modeled to investigate their effect on the incipient motion of particles and erosion function of samples.
- Backward erosion is one of the phenomena in erosion which its simulation started in this research, but due to high computational cost, despite several initial results, their simulation is halted. Several significant research pieces have been done in recent years (Tran et al. 2017, Froiio et al. 2019). However, still more focus on this area can shine more light on this complicated topic in the internal instabilities of the dams and levees.
- The minimum size of fine particles in the suffusion simulations was chosen as 2 mm to prevent more computational cost. Several researchers focused on the simulation of the even smaller size of particles but with smaller samples. A broader range of particles with sample size near the experimental modeling is recommended. In this way, the comparison of the experimental and numerical simulations makes more sense.

REFERENCES

1. Abdelhamid, Y., & El Shamy, U. (2014). Pore-scale modeling of surface erosion in a particle bed. International Journal for Numerical and Analytical Methods in Geomechanics, 38(2), 142-166.
2. Abdelhamid, Y., & El Shamy, U. (2015). Pore-scale modeling of fine-particle migration in granular filters. International Journal of Geomechanics, 16(3), 04015086.
3. Abdelhamid, Y., & El Shamy, U. (2016). Pore-scale modeling of fine-particle migration in granular filters. International Journal of Geomechanics, 16(3), 04015086.
4. Adel, H. D., Bakker, K. J., and Breteler, M. K. (1988). “Internal stability of minestone,” in Proceedings of International Symposium on Modelling Soil-Water-Structure Interactions, Balkema, Rotterdam, 225–231.
5. Allen, H. S. (1900). L. The motion of a sphere in a viscous fluid. The London, Edinburgh, and Dublin Philosophical Magazine and Journal of Science, 50(306), 519-534.
6. Ambuj Dwivedi, Bruce W. Melville, Asaad Y. Shamseldin, Tushar K. Guha, (2011), “Flow Structures and Hydrodynamic Force during Sediment Entrainment”.Water Resources Research, Vol. 47. W01509.
7. Arneson, L. A. (2013). Evaluating scour at bridges (No. FHWA-HIF-12-003). United States. Federal Highway Administration.
8. Arnold, H. D. F. (1911). Limitations imposed by slip and inertia terms upon Stokes's law for the motion of spheres through liquids... Taylor & Francis.

9. ASTM. (2015). Standard practice for thin-walled tube sampling of fine-grained soils for geotechnical purposes. Annual Book of ASTM Standards.
10. Bendahmane, F., Marot, D., & Alexis, A. (2008). Experimental parametric study of suffusion and backward erosion. Journal of geotechnical and geoenvironmental engineering, 134(1), 57-67.
11. Benedict, S.T., 2003, Clear-water abutment and contraction scour in the Coastal Plain and Piedmont Provinces of South Carolina, 1996-99: U.S. Geological Survey Water Resources Investigation Report 03-4064, 137p. http://pubs.usgs.gov/wri/wri034064/
12. Benedict, S.T., and Caldwell, A.W., 2009, Development and evaluation of live-bed pier- and contraction-scour envelope curves in the Coastal Plain and Piedmont Provinces of South
13. Brauer, H. (1973). Impuls-, Stoff-und Wärmetransport durch die Grenzfläche kugelförmiger Partikeln. Chemie Ingenieur Technik, 45(18), 1099-1103.
14. Briaud, J. L. (2008). Case histories in soil and rock erosion: woodrow wilson bridge, Brazos River Meander, Normandy Cliffs, and New Orleans Levees. Journal of Geotechnical and Geoenvironmental Engineering, 134(10), 1425-1447.
15. Briaud, J. L. 2013. Geotechnical engineering: unsaturated and saturated soils, John Wiley and Sons, New York, USA.
16. Briaud, J. L., Bernhardt, M., Leclair, M. 2012. The pocket erodometer test: development and preliminary results. Geotechnical Testing Journal, Vol. 35, No. 2, Paper ID GTJ102889.
17. Briaud, J. L., Chedid, M., Chen, H. C. & Shidlovskaya, A. (2017). The borehole erosion test. Journal of geotechnical and geoenvironmental engineering, Vol. 143(8).

18. Briaud, J. L., Chen, H. C., Govindasamy, A. V., & Storesund, R. (2008). Levee erosion by overtopping in New Orleans during the Katrina Hurricane. Journal of Geotechnical and Geoenvironmental Engineering, 134(5), 618-632.
19. Briaud, J. L., Gardoni, P., & Yao, C. (2013). Statistical, risk, and reliability analyses of bridge scour. Journal of Geotechnical and Geoenvironmental Engineering, 140(2), 04013011.
20. Briaud, J. L., Shafii, I., Chen, H. C., & Medina-Cetina, Z. (2019). Relationship Between Erodibility and Properties of Soils. Transportation Research Board.
21. Briaud, J. L., Ting, F. C. K., Chen, H. C., Cao, Y., Han, S. W., & Kwak, K. W. (2001). Erosion function apparatus for scour rate predictions. Journal of geotechnical and geoenvironmental engineering, 127(2), 105-113.
22. Briaud, J. L., Ting, F. C. K., Chen, H. C., Gudavalli, R., Perugu, S., Wei, G. 1999. SRICOS: Prediction of scour rate in cohesive soils at bridge piers, Journal of Geotechnical and Geoenvironmental Engineering, Vol. 125(4), pp. 237-246, April 1999, ASCE, Reston, Virginia.
23. Briaud, J. L., Ting, F. C. K., Chen, H. C., Gudavalli, S. R., Perugu, S. B., & Kwak, K. (1999). Maximum Scour Depth at Bridge Piers in Sand and Clay are Equal. IABSE REPORTS, 97-108.
24. Briaud, J.-L., Chedid, M., and Shidlovskaya, A. (2016). “The borehole erosion test.” Proc., 8th Int. Conf. on Scour and Erosion, CRC Press/A.A. Balkema, Leiden, Netherlands, 12–15.

25. Briaud, J.L., Chen, H.C., Cao, Y., Han, S.W., Kwak, K.W., (2011), "Erosion Function Apparatus for Scour Rate Predictions". Journal of Geotechnical and Geoenvironmental Engineering, Vol. 127(2).
26. Briaud, J.L., Govindasamy, A.V., Shafii, I., (2017), "Erosion Charts for Slected Geomaterials". Journal of Geotechnical and Geoenvironmental Engineering, Vol. 143(10).
27. Burenkova, V.V. (1993) Assessment of Suffusion in Non-Cohesive and Graded Soils. In: Brauns and Schüler, Eds., Filters in Geotechnical and Hydraulic Engineering, Balkema, Rotterdam, 357-360.
28. Butt, H. J., Graf, K., & Kappl, M. (2013). Physics and chemistry of interfaces. John Wiley & Sons.
29. Canadian Dam Association CDA, 2007. Geotechnical Considerations for Dam Safety. Technical Bulletin. Canadian Dam Association, Moose Jaw, Sask.
30. Centers for Disease Control and Prevention (CDC). (1994). Flood-related mortality - Georgia, July 4-14, 1994. Atlanta.
31. CFGB (1997) Internal erosion: typology, detection, repair. Barrages and reservoirs. No:6, Comite´ Francais des Grands Barrages, Le Bourget-du-lac Cedex.
32. Chang, D. S., & Zhang, L. M. (2013). Extended internal stability criteria for soils under seepage. Soils and Foundations, 53(4), 569-583.
33. Chen, C. J., & Chen, H. C. (1984). Finite analytic numerical method for unsteady two-dimensional Navier-Stokes equations. Journal of Computational Physics, 53(2), 209-226

34. Chen, H. C., & Chen, C. J. (1982). The finite analytic method, Vol. 4. Institute of Hydraulic Research., Univ. of Iowa, Iowa City, Iowa.
35. Croad, R.N. (1981). Physics of Erosion of Cohesive Soils, PhD Thesis, Department of Civil Engineering, University of Auckland, NZ.
36. Crowe, C. T., Schwarzkopf, J. D., Sommerfeld, M., & Tsuji, Y. (2011). Multiphase flows with droplets and particles. CRC press.
37. Culbertson, D. M., Young, L. E., and Brice, J. C. (1967). “Scour and fill in alluvial channels.” Open-File Report , U.S. Geological Survey.
38. Cundall, P. A. (1971). A computer model for simulating progressive, large-scale movement in blocky rock system. In Proceedings of the International Symposium on Rock Mechanics, 1971.
39. Dennis, S. C. R., & Walker, J. D. A. (1971). Calculation of the steady flow past a sphere at low and moderate Reynolds numbers. Journal of Fluid Mechanics, 48(4), 771-789.
40. Di Renzo, A., & Di Maio, F. P. (2004). Comparison of contact-force models for the simulation of collisions in DEM-based granular flow codes. Chemical engineering science, 59(3), 525-541.
41. Di Renzo, Alberto and Di Maio, Francesco Paolo. 2004. “Comparison of contact-force models for the simulation of collisions in DEM-based granular flow codes”, Chemical Engineering Science 59 pp. 525-541.
42. Edwards, C., Lottes, S. A., & Majumdar, P. (2013, November). Three-dimensional mesh morphing methodology for scouring around bridge piers based on computational fluid dynamic solution. In ASME 2013 International Mechanical Engineering Congress and

Exposition (pp. V07BT08A033-V07BT08A033). American Society of Mechanical Engineers.

43. Engineers, U. A. C. O. (2002). Coastal engineering manual. Engineer Manual, 1110, 2-1100.
44. Fannin, J. (2008). Karl Terzaghi: from theory to practice in geotechnical filter design. Journal of geotechnical and geoenvironmental engineering, 134(3), 267-276.
45. Farimani, A. B., Ferreira, A. D., & Sousa, A. C. (2011). Computational modeling of the wind erosion on a sinusoidal pile using a moving boundary method. Geomorphology, 130(3-4), 299-311.
46. Fell, R., & Fry, J. J. (2007). The state of the art of assessing the likelihood of internal erosion of embankment dams, water retaining structures and their foundations. Internal erosion of dams and their foundations, edited by: Fell, R. and Fry, JJ, Taylor and Francis, London, 1-24.
47. Foster, M., Fell, R., & Spannagle, M. (2000). A method for assessing the relative likelihood of failure of embankment dams by piping. Canadian Geotechnical Journal, 37(5), 1025-1061.
48. Froiio, F., Callari, C., & Rotunno, A. F. (2019). A numerical experiment of backward erosion piping: kinematics and micromechanics. Meccanica, 54(14), 2099-2117.
49. Galindo-Torres, SA., Scheuermann, A., Mühlhaus, HB., Williams, DJ. (2013). "A micro-mechanical approach for the study of contact erosion." Acta Geotechnica: 1-12.
50. Geotechnical Engineering Office GEO,1993. Review of Granularand Geotextile Filters. GEO Publication No. 1/93. Civil Engineering Department, Ho Man Tin, Hong Kong.

51. Guo, Y., & Yu, X. (2018). Analysis of surface erosion of cohesionless soils using a three-dimensional coupled computational fluid dynamics–discrete element method (CFD–DEM) model. Canadian Geotechnical Journal, 56(5), 687-698.

52. Guo, Y., Yang, Y., & Yu, X. B. (2018). Influence of particle shape on the erodibility of non-cohesive soil: Insights from coupled CFD–DEM simulations. Particuology, 39, 12-24.

53. Hanson, G. J. 1990. Surface erodibility of earthern channels at high stresses. Part II – Developing an in situ testing device. Transactions of the ASAE, Vol. 33, Issue 1, pp. 132-137.

54. Hanson, G. J. 1991. Development of a jet index to characterize erosion resistance of soils in earthen spillways. Trans. ASAE. General Edition, Vol. 34(5), pp. 2015-2020. ISSN 00012351.

55. Hanson, G. J., & Hunt, S. L. (2007). Lessons learned using laboratory JET method to measure soil erodibility of compacted soils. Applied engineering in agriculture, 23(3), 305-312.

56. Heimann D.C., Sprague L.A., Blevins D.W., 2011, Trends in Suspended-Sediment Loads and Concentrations in the Mississippi River Basin, 1950–2009, National Water-Quality Assessment Program, Scientific Investigations Report 2011–5200, U.S. Department of the Interior, U.S. Geological Survey.

57. Hofland, B., Battjes, J.A., Booij, R. (2005). Measurement of fluctuating pressures on coarse bed material, Journal of Hydraulic Engineering, Vol. 131(9), pp.770-781.

58. Honjo, Y., & Veneziano, D. (1989). Improved filter criterion for cohesionless soils. Journal of Geotechnical Engineering, 115(1), 75-94.

59. ICOLD, E. D. (1994). Granular Filters and Drain.

60. ICOLD. (2013). “Internal erosion processes and engineering assessment,” in ICOLD Bulletin on Internal Erosion of Existing Dams, Levees and Dikes, and Their Foundations, Vol. 1, ICOLD, Paris, France.

61. Ihme, F., Schmidt-Traub, H., & Brauer, H. (1972). Theoretische Untersuchung über die Umströmung und den Stoffübergang an Kugeln. Chemie Ingenieur Technik, 44(5), 306-313.

62. Indraratna, B., Dilema, E. L. G., & Vafai, F. (1996). An experimental study of the filtration of a lateritic clay slurry by sand filters. Proceedings of the Institution of Civil Engineers-Geotechnical Engineering, 119(2), 75-83.

63. Indraratna, B., Nguyen, V. T., & Rujikiatkamjorn, C. (2011). Assessing the potential of internal erosion and suffusion of granular soils. Journal of Geotechnical and Geoenvironmental Engineering, 137(5), 550-554.

64. Istomina, V.S., 1957. Filtration Stability of Soils. Gostroizdat, Moscow, Leningrad (in Russian).

65. Itasca, C. G. I. (2008). PFC3D (Particle Flow Code in 3 Dimensions), Version 4.0. Minneapolis: ICG, 3.

66. Jenson, V. G. (1959). Viscous flow round a sphere at low Reynolds numbers (< 40). Proceedings of the Royal Society of London. Series A. Mathematical and Physical Sciences, 249(1258), 346-366.

67. Johnson, K. L., & Johnson, K. L. (1987). Contact mechanics. Cambridge university press.

68. Kanitz, M., & Grabe, J. (2019). Multiscale investigation of suffusion with coupled CFD-DEM-Influence of different drag force models. 2nd International Conference on the Material Point Method for Modelling Soil-Water-Structure Interaction, At Cambridge, United Kingdom.
69. Ke, L., & Takahashi, A. (2012). Strength reduction of cohesionless soil due to internal erosion induced by one-dimensional upward seepage flow. Soils and Foundations, 52(4), 698-711.
70. Kenney, T. C., & Lau, D. (1985). Internal stability of granular filters. Canadian geotechnical journal, 22(2), 215-225.
71. Kenney, T. C., & Lau, D. (1986). Internal stability of granular filters: Reply. Canadian Geotechnical Journal, 23(3), 420-423.
72. Kezdi, A. (1969). Increase of protective capacity of flood control dikes. Department of Geotechnics, Technical University of Budapest, Report, (1).
73. Khosronejad, A., Kang, S., Borazjani, I., & Sotiropoulos, F. (2011). Curvilinear immersed boundary method for simulating coupled flow and bed morphodynamic interactions due to sediment transport phenomena. Advances in water resources, 34(7), 829-843.
74. Kim, H., Chen, H., & Briaud, J. (2016, October). Numerical simulation of scour infilling in overset grid. In Scour and Erosion: Proceedings of the 8th International Conference on Scour and Erosion (Oxford, UK, 12-15 September 2016) (p. 95). CRC Press.
75. Kuwano, R., Kohata, Y., & Sato, M. (2012, August). A case study of ground cave-in due to large scale subsurface erosion in old land fill. In ICSE (Vol. 6, pp. 265-271).

76. Li, Maoxin, and R. Jonathan Fannin. "Comparison of two criteria for internal stability of granular soil." Canadian Geotechnical Journal 45, no. 9 (2008): 1303-1309.
77. Liebster, H. (1927). Über den widerstand von kugeln. Annalen der Physik, 387(4), 541-562.
78. Lim, S. S. (2006). Experimental investigation of erosion in variably saturated clay soils. PhD Dissertation, The University of New South Wales, Australia.
79. Maali, A., Pan, Y., Bhushan, B., Charlaix, E., (2012), "Hydrodynamic Drag-Force Measurement and Slip Length on Micro structured Surfaces". Physical Review E 85, 066310.
80. Moffat, R., & Fannin, R. J. (2011). A hydromechanical relation governing internal stability of cohesionless soil. Canadian Geotechnical Journal, 48(3), 413-424.
81. Monnet, J., Plé, O., Nguyen, DM (2012). Internal Erosion in Dikes alongside Roads and Railways. 2nd International Conference on Transportation Geotechnics (ICTG).
82. Norouzi, H. R., Zarghami, R., Sotudeh-Gharebagh, R., & Mostoufi, N. (2016). Coupled CFD-DEM modeling: formulation, implementation and application to multiphase flows. John Wiley & Sons.
83. Richards, K. S., & Reddy, K. R. (2007). Critical appraisal of piping phenomena in earth dams. Bulletin of Engineering Geology and the Environment, 66(4), 381-402.
84. Schiller, L., and Naumann, A. 1933 "Ueber die grundlegenden Berechnungen bei der Schwerkraftaufbereitung", VDI Zeits., 77(12), pp. 318–320.
85. Shafii, I., Briaud, J. L., Chen, H. C., and Shidlovskaya, A., (2016), "Relationship between Soil Erodibility and Engineering Properties". 8th International Conference on Scour and Erosion, Oxford, U.K.

86. Shafii, I., Zhang, Z., Briaud, J. L., 2018. Measurement of Hydrodynamic Forces on Gravel Particles in the Erosion Function Apparatus. The 9th International Conference on Scour and Erosion, Taipei, Taiwan.
87. Shan, H., Shen, J., Kilgore, R., Kerenyi, K., (2015), "Scour in Cohesive Soils". US Department of Transportation, Federal Highway Administration. Publication No. FHWA-HRT-15-033.
88. Sherard, J. L., & Dunnigan, L. P. (1989). Critical filters for impervious soils. Journal of Geotechnical Engineering, 115(7), 927-947.
89. Sherard, J. L., Dunnigan, L. P., & Talbot, J. R. (1984). Basic properties of sand and gravel filters. Journal of Geotechnical Engineering, 110(6), 684-700.
90. Sherard, J. L., Dunnigan, L. P., & Talbot, J. R. (1984). Filters for silts and clays. Journal of Geotechnical Engineering, 110(6), 701-718.
91. Shields, A. (1936). Anwendung der Aehnlichkeitsmechanik und der Turbulenzforschung auf die Geschiebebewegung. PhD Thesis Technical University Berlin.
92. Shuler, U. (1995). How to deal with the problem of suffusion. Research and development in the field of dams, Swiss National Committee in Larges Dams.
93. Sun, R., & Xiao, H. (2016). CFD–DEM simulations of current-induced dune formation and morphological evolution. Advances in water resources, 92, 228-239.
94. Tao, H., & Tao, J. (2017). Quantitative analysis of piping erosion micro-mechanisms with coupled CFD and DEM method. Acta Geotechnica, 12(3), 573-592.
95. Terzaghi, K.,1939. Soil mechanics: a new chapter in engineering science. Journal of the Institution of Civil Engineers 12, 106–141.

96. Tomlinson, S. S., & Vaid, Y. P. (2000). Seepage forces and confining pressure effects on piping erosion. Canadian Geotechnical Journal, 37(1), 1-13.

97. Tran, D. K., Prime, N., Froiio, F., Callari, C., & Vincens, E. (2017). Numerical modelling of backward front propagation in piping erosion by DEM-LBM coupling. European Journal of Environmental and Civil Engineering, 21(7-8), 960-987.

98. Tsuji, Y., Tanaka, T., & Ishida, T. (1992). Lagrangian numerical simulation of plug flow of cohesionless particles in a horizontal pipe. Powder technology, 71(3), 239-250.

99. U.S. Army Corps of Engineers (USACE), 1953. Filter Experiments and Design Criteria. Waterways Experiment Station, Vicksburg, Technical Memoran- dum, No. 3-360.

100. U.S. Department of Agriculture (USDA), 1994. Gradation Design of Sand and Gravel Filters. Natural Resources Conservation Service, US Department of Agriculture, Washington, D.C.

101. U.S. Society on Dams (USSD), 2011. Materials for Embankment Dams. Committee on Materials for Embankment Dams, United States Society of Dams, Denver.

102. US Bureau of Reclamation (USBR). (2004). Filters. In Design Standards No. 13: Embankment Dams, Denver.

103. USACE (United States Army Corps of Engineers). (1953). “Filter experiments and design criteria.” No. 3-360, Waterway Experiment Station,Vicksburg, MS.

104. Vanoni, V. A. (2006). Sedimentation engineering: American Society of Civil Engineers, Manuals and Reports in Engineering Practice.

105. Vaughan, P. R., & Hermusla, S. F. (2009). Design of filters for clay cores of dams. In Selected papers on geotechnical engineering by PR Vaughan (pp. 121-135). Thomas Telford Publishing.

106. Von Thun, J. L. (1996). Understanding seepage and piping failures–the No. 1 dam safety problem in the west. In ASDSO Western Regional Conference.

107. Walling D.E., Moorehead P.W., 1989, The particle size characteristics of fluvial suspended sediment: an overview, in Sediment/Water Interaction, Sly P.G., Hart B.T.,(eds), Hydrobiologia 176/177: 125-149, Kluwer Academic Publishers.

108. Wan, C. F., and Fell, R. 2002!. ‘‘Investigation of internal erosion and piping of soils in embankment dams by the slot erosion test and the hole erosion test.’’ UNICIV Rep. R-412, July 2002, The Univ. of New South Wales, Sydney, Australia.

109. Wan, C. F., Fell, R. 2004. Investigation of rate of erosion of soils in embankment dams. Journal of Geotechnical and Geoenvironmental Engineering. Vol. 130(4), pp. 373-380.

110. Wan, C. F., Fell, R. 2004. Laboratory tests on the rate of piping erosion of soils in embankment dams. ASTM Geotechnical Testing Journal. Vol. 27(3), pp. 295-303.

111. Wang, Y., Zhou, L., & Yang, Q. (2019). Hydro-mechanical analysis of calcareous sand with a new shape-dependent fluid-particle drag model integrated into CFD-DEM coupling program. Powder Technology, 344, 108-120.

112. Wensrich, C. M., & Katterfeld, A. (2012). Rolling friction as a technique for modelling particle shape in DEM. Powder Technology, 217, 409-417.

113. White, F. M. Viscous Fluid Flow, McGraw-Hill, New York, 1991.

114. Zhang, D. M., Gao, C. P., & Yin, Z. Y. (2019). CFD-DEM modeling of seepage erosion around shield tunnels. Tunneling and Underground Space Technology, 83, 60-72.

115. Zhang, L. M., Xu, Y., & Jia, J. S. (2009). Analysis of earth dam failures: A database approach. Georisk, 3(3), 184-189.

116. Zhang, L., Peng, M., Chang, D., & Xu, Y. (2016). Dam failure mechanisms and risk assessment. John Wiley & Sons.

117. Zheng, H. C., Shi, Z. M., Peng, M., & Yu, S. B. (2018). Coupled CFD-DEM model for the direct numerical simulation of sediment bed erosion by viscous shear flow. Engineering geology, 245, 309-321.